Development and comparison of HVOF and laser DED methods for depositing TiC-Ni_3Al based coatings

By

Zhila Russell

Submitted in partial fulfilment of the requirements for

the degree of Doctor of Philosophy

at

Dalhousie University

Halifax, Nova Scotia

June 2023

Table of Contents

List of Tables

List of figures

Abstract

Deposition of TiC-Ni_3Al composite coatings by high velocity oxyfuel (HVOF) and directed energy laser deposition (DED) was investigated for enhancements, modifications and/or repairs of steel surfaces with extensive wear and oxidation characteristics. Gelation of sodium alginate was employed as an aid to preposition aqueous suspensions, comprised of micron-sized ceramic-metal particles, into micron-sized spherical 'cermet' feed-stock powders. Spraying a sodium alginate containing ceramic-metal particle suspension, with a suitable air atomizing nozzle, into an aqueous bath was outlined as a solution to produce nominally spherical 'cermet' feedstock for HVOF thermal spraying.

Consequently, dip coating of substrate in colloidal suspension containing ceramic-metal particles, has been suggested as an efficient method for layer-by-layer deposition of preplaced cermet feed stock prior to the laser processing. Processing parameters were identified in the case of both HVOF and DED deposition procedures for optimum structural and mechanical characteristics of fabricated builds. Cermet coatings were subjected to microstructural and mechanical characterization through combination of latest available techniques and results are provided in relation to several processing parameters. Improved wear resistance, hardness, scratch resistivity and corrosion behavior of the coated substrates suggest the effectiveness of proposed routes.

List of abbreviations and symbols used.

$\dot{\gamma}$	Normal shear rate
$\dot{\boldsymbol{\gamma}}$	Shear rate
ρ_c	Density
μ	Frictional force
a	Dimensionless parameter
A_{cn}	Cone area
AE	Acoustic emission
AISI	American Iron and Steel Institute
AM	Additive manufacturing.
APS	Atmospheric plasma spraying
BCC	Body-centered cubic
C	Capacitance
CGSM	Cold-Gas Spraying Method
CLSM	Confocal laser scanning microscope
CNC	Computerized Numerical Control.
COF	Coefficient of friction
CVD	Chemical vapour deposition
D	Laser beam diameter
d	Loss angle
DDL	Direct diode laser
D-gun	Denotation gun
DJ-gun	Diamond jet gun

E	Elastic modulus
EBSD	Electron backscattered diffraction
E_{corr}	Corrosion potential
ED	Energy density
EDS	Electron dispersive X-ray spectroscopy
EIS	Electrochemical Impedance Spectroscopy
FCC	Face centered cubic.
FE-SEM	Field emission scanning electron microscopy
FIB	Focused ion beam microscopy
$F_{PP}\dot{\gamma}$	Normal force for plate-plate geometry
F_z	Normal force on the stylus
G'	Storage modulus
G''	Loss modulus
GTTPJ	Gas tunnel-type plasma jet
$\bar{\sigma}$	Stress
H	Hatch spacing
Hv	Indentation hardness
h	Rheometer Gap
HAZ	Heat affected zone.
HHAVF	High Velocity Air-Fuel
H_{sp}	Scratch hardness
HVOF	High velocity oxyfuel
I	Current

i_{corr}	Corrosion current
ICP-OES	Inductively coupled plasma atomic emission spectroscopy.
k	Geometrical Constant
K	Thermal conductivity
K_f	Dynamic consistency index
L_C	Critical load
LCS	Laser cutting system.
LD	Laser deposition
LML	Laser melting
LPPS	Low pressure plasma spraying
LSA	Laser-supported absorption
LSC	Laser surface cladding
LSM	Laser surface melting
LSP	Laser shock processing
L_x	Scratch cone diameter
L_y	Depth of scratch cone
η	Apparent viscosity
$\eta_\circ$	Viscosity at zero shear rate
$N(\dot{\gamma})$	Normal-stress difference
n_f	Dynamic power-law factor
OCP	Open circuit potential
P	Applied normal force in sliding wear
P_w	Laser power

p	Power law index
PD	Potentiodynamic polarization
PFLD	Powder fed laser deposition.
PVD	Physical vapor deposition
Q	Power generation per unit volume
R_Ω	Resistance
R	Radius of the parallel plate
R_a	Surface roughness
SHS	Self-propagating high-temperature synthesis
T	Time
U	Travel velocity of the workpiece
V	Scanning speed
v	Volume fraction
$\boldsymbol{V}$	Volume loss due to wear
VH	Micro-Vickers hardness
V	Voltage
w	Mass fraction
W	Scratch width
WS	Warm spray
Z	Impedance
z	Step size
Z'	Layer thickness
βa	Anodic polarization slope

βc	Cathodic polarization slope
ε	Strain
η^*	Complex viscosity
Θ	Laser diffraction angle
$\boldsymbol{\Theta}$	Phase shift
λ	Radiation wavelength
λ_t	Response time
τ	Laser interaction times
ω	Frequency

Acknowledgements

I cannot find words to express my gratitude to all who stood by my side in this journey and led me to the finishing point. Those who held me up and stood me tall, no matter how impossible this day seemed. I thank my professor, mentor, spiritual father and a true friend, Dr Kevin Plucknett for all he has done and his endless patience with me. Secondly, I would like to dedicate this success to my kind and loving husband Glenn, who trusted me with his whole heart and carried me through the roughest road in life. Moreover, I'm thankful to my three beautiful boys Hayden, Suat and Kal-El who unwearyingly allowed their mother to reach her dreams.

It is most appropriate to dedicate my deepest regards to the personnel within the Department of Mechanical Engineering at Dalhousie University, who supported me every day of my experience as a graduate student; Mark MacDonald, Albert Murphy, Peter Jones, Brian Kennedy, Graham Muirhead, Kate Hide, Donna Laffin, and Prof. Dominic Groulx; thank you all for your kind support. In addition, support provided by John MacDonald is especially acknowledged, for his assistance with the design and construction of the dip coating unit.

Moreover, I would like to especially thank Dr Mazzanti and Dr Corbin for their scientific discussions and wise guidance at every stage of the projects. Technical discussions and support provided by researchers at Boeing (Marc Froning, Mark Pollack, Ryan Glam, and Stephen Gaydos) are also gratefully acknowledged.

Finally, I would also like to thank the NSERC funded network *Holistic Innovation in Additive Manufacturing* (or HI-AM) and Boeing Research & Technology for supporting this research, both physically and financially.

Chapter 1. Introduction

1.1. Background Information

Engineering components serving under harsh environmental conditions are invariably tailored to meet the required functional constraints. However, design and development of a new alloy is a costly task that often requires complex manufacturing routes to be developed. Alternatively, advanced coatings deposited by various techniques have been developed to accommodate for such requirements [1–3]. Ceramic-metal composites, often referred to as 'cermets', are commonly used in applications where high wear and corrosion resistance is required in such coatings. The presence of ceramic and metallic phases simultaneously provides high strength and stiffness, while retaining good toughness, which has resulted in the use of these materials in many applications. Over the past 80 plus years, hard metals and refractory materials based on tungsten carbide (WC) and titanium carbide (TiC) have been researched extensively [2,4–8]. WC based ceramic-metal composites (traditionally termed 'hard metals'), typically with Co, CoCr, or Ni-based metal binders, have been used traditionally in a wide range of abrasion and erosion wear-resistant applications [9–12] and have also recently been implemented as replacements for hexavalent chromium in the aerospace industry [13]. However, WC-based cermets suffer from several limitations, notably a high density (typically between 12 to 15 g/cm^3, depending upon the binder content n=and composition), which is an issue for applications where mass is a critical component [14]. As a consequence, increasing recent attention has been focused on relatively lightweight cermets based on TiC and the closely related titanium carbonitride (Ti(C,N)), with associated cermet densities typically ranging from 6

to 7 g/cm^3 [15]. TiC has been demonstrated to exhibit high electrical conductivity and a stable chemical response in acidic media [16,17]. Due to its excellent mechanical properties, TiC itself has been widely used as the reinforcing phase in composite materials due to superior hardness (3.17 GPa), high melting point (3340 °C), high elastic modulus (~420 GPa), low density (4.92 g/cm^3), and excellent corrosion resistance [11–15].

In addition to the binders traditionally used for WC, there has been recent interest in further improving the binder properties, which has resulted in a variety of developmental alloys being examined. Among these, the nickel aluminide intermetallic compounds NiAl and Ni_3Al have been used commonly as high temperature materials due to their ability to retain strength and stiffness at high temperature, high melting point, good oxidation/corrosion resistance up to 1400 °C, and excellent wettability to substrates [23–25]. Ni_3Al as metallic matrix offers exceptional combination of high strength and thermal stability with low specific weight and high thermal conductivity (76 W/mK), [23,26,27].

The production of TiC based coatings has been investigated using a variety of deposition techniques, including chemical vapor deposition (CVD), physical vapor deposition (PVD), electroplating, and thermal spray [28–38]. In particular, thermally sprayed high hardness coatings are suited for many wear and corrosion scenarios. Thermal spray coatings can present excellent adhesion and cohesion properties for such applications, and consequently have been the subject of numerous studies, such as investigation of the bond strength between the metal and the ceramic matrix, minimizing residual stress, and developing low porosity coatings [39–44]. During the process of thermal spraying, the feed stock particles are melted and sprayed onto the surface of substrate. High-velocity oxy-fuel (HVOF) is a thermal spray coating process that offers manufacture of components with high

temperature operating capabilities [45], and is particularly suited to cermet-type formulations.

The deposition of exceptionally dense, crack-free, and non-porous metal-ceramic coatings, with a much wider thickness range is possible through laser directed energy deposition (DED) [46–50]. Laser processed protective coatings offer excellent metallurgical bonding, combined with very low compositional dilution (of the coating and/or substrate) and low heat input to the component. Due to the use of a highly focused beam, laser cladding creates a relatively small heat-affected zone (HAZ) compared to other related processes, such as welding. Laser cladding and directed energy deposition (DED), with a coaxial powder nozzle has thus been used in many industrial applications to apply composite coatings onto substrates of interest [51–53].

The main challenge in both the HVOF and laser DED processing routes, relates to the requirements of the powder feeding system and nozzle, which usually demand a precise particle size and morphology for the feedstock powder, while the resultant mechanical properties that can be achieved for the bulk composition are retained [54]. There is consequently a drive to produce novel powders with the aim of achieving excellent mechanical performance. This has resulted in decreasing powder grain size (e.g., ultra-fine powder constituents, with a size of less than 15 μm) [55]. With such a reduction in grain size the flowability of the powder is decreased, which causes problems with control of the feedstock during processing [56–60]. Moreover, the formulation of micron (or sub-micron) sized feedstock materials with the required packing characteristics, and minimal final levels of porosity is a difficult and costly task, which plays a major role in determining the feasibility of the thermal coating processes [61,62]. Therefore, the manufacture of complex

ceramic structures (including coatings), advances with emphasis on identification and resolving of issues arising from such feedstock materials [63]. With this in mind, the present thesis is focused on advancing developments in both HVOF and laser DED processing, notably in terms of novel materials and feedstock preparation.

1.2. Thesis Motivation

The research presented within the current thesis has been conducted with the parallel objectives of designing and manufacturing novel TiC-based coatings/clads via both HVOF and laser DED. In particular, an emphasis has been placed upon development of novel feedstock preparation/application routes for both approaches. In each case, the feasibility of performance enhancement, modification, and/or repair of tool steel substrates is evaluated. The wear and corrosion characteristics were explored in relation to state of the powder production and feed delivery system, with the further objective of improving the properties of these coatings in comparison with current commercial solutions.

1.3. Thesis Structure and Research Contributions

The thesis starts with a literature review that outlines the development of HVOF and laser DED processing methods for depositing cermet coatings, including the latest developments in material design for feed stock purposes. Furthermore, the basic properties that are required, and how they are measured, is also discussed. This initial literature review is provided in Chapter 2 and helps to set the scene for the subsequent research.

Initially, TiC-based cermet feedstock, with a Ni_3Al metallic matrix, was manufactured through a gelation approach using sodium alginate, from a colloidal suspension. Cermet feedstock powder with desired size, morphology, and flow capabilities was then obtained by controlled spraying of sodium alginate/TiC-Ni_3Al suspension into a chelating bath followed by drying and heat treatment. This feedstock was then applied to HVOF processing. The details surrounding the design and manufacture of this feed stock have been presented in Chapter 3. Mr. Tyler Stewart and Mr. Peter Grey primarily examined the applicability of the intended route through microstructural and chemical analysis of single droplet gel/cermet particles. Formulation of the feed stock powder, spraying procedure and heat treatment process were developed by the thesis author and Mr. William Sparling. In depth rheological characterization of the cermet/gel suspension were performed by the author, under the guidance of Dr. Gianfranco Mazzanti. The thesis author drafted the final manuscript, which was subsequently edited by Drs. Mazzanti and Plucknett.

The fabricated powders outlined in Chapter 3 were subsequently utilized in the fabrication of TiC-Ni_3Al based HVOF coatings, deposited onto steel 4130 substrates. A comparison was made between the gel-based feedstock and a more conventional agglomeration and sinter equivalent. The HVOF coated substrates were then subjected to a range of microstructural, mechanical, and electrochemical characterization techniques. The details of this study and the results of such evaluation in relation to processing parameters are presented in Chapter 4. The thesis author facilitated and performed the manufacture of thermally sprayed TiC based HVOF coatings from both gel-based feedstock and a more conventional agglomeration and sinter equivalent, with assistance from Mr. Marc Froning (Boeing Research & Technology), who conducted the actual HVOF thermal spray

deposition. Microstructural and mechanical characterization of the fabricated coatings was then completed by the author, and the results of analysis were employed by her for the draft of the subsequent manuscript. The prepared manuscript was reviewed and edited by Dr. Plucknett.

The comparatively low yield of the proposed production route discussed in Chapter 3, along with concerns relating to the capability of the available powder feeding system when depositing novel and complex compositions, resulted in further development of a feedstock delivery process by preplacement of the feedstock for laser DED processing. Dip coating was proposed as an appropriate and efficient method for layer-by-layer deposition of preplaced feed prior to laser DED processing. Successfully preplaced coatings were subjected to DED and processing parameters were identified for optimum structural and mechanical characteristics of coatings. The research relating to this study is provided in Chapter 5. Design and the assembly of the projected feedstock delivery system was completed by the thesis author, with assistance of the technical support team within the Department of Mechanical Engineering of Dalhousie University. Notably, additional support was provided from Mr. John Mc Donald in terms of the design and implementation of the electrical control system for the dip coating apparatus. For the cladding process, the preplacement development for the feedstock powder was performed by the thesis author, while the laser processing of the prepared specimens was performed by Dr. Greg Sweet and Dr. Addison Rayner. Metallographic preparation and subsequent microstructural analysis of the fabricated cermet clads, along with the analysis of the subsequent findings, was performed by the author. The thesis author also drafted the associated manuscript, which was further reviewed and edited by Dr. Plucknett.

The impact of the proposed feedstock preplacement technique upon the mechanical enhancement of D2 tool steel, via laser DED cladding of TiC-Ni_3Al based composites, was consequently quantified through a series of micro-scale hardness testing techniques. The results for this part of the study are presented in relation to laser processing parameters in Chapter 6. Sample preparation, initial design and implementation of the designed mechanical testing procedures, and data analysis and documentation were performed by the thesis author, who also drafted the subsequent manuscript. Notably, repetition of microhardness measurements were performed by Achillis David while the EBSD analysis was completed with the assistance of Dr Mark Amegadzie. The final manuscript review and editing were performed by Dr. Plucknett.

Chapter 7 presents the results of electrochemical measurements performed on the fabricated laser DED clads, generated under a range of processing parameters. Electrochemical measurements, as well as the collection and analysis of the data, were performed by the thesis author and a subsequent manuscript was drafted by her. This manuscript was then reviewed and edited by Dr. Plucknett.

Chapter 8 presents the overall conclusions of these various studies, with a focus upon how the developments and observations relate to the initial research objectives. Comparison is made between the HVOF and laser DED approaches, and also with current commercially produced coating solutions. Finally, a series of recommendations are also presented in this chapter, in relation to future research paths that might be followed to further develop these studies.

Chapter 2. Literature review

The background information relating to the objectives of the current study is presented in this chapter. Development of wear and corrosion resistant TiC-Ni_3Al cermet coatings and a brief overview of existing coating deposition methods, particularly HVOF and DED, is discussed. In addition, the microstructures and associated failure modes of such coatings are also reviewed. Procedures that are subsequently used to characterize the mechanical behavior of the fabricated coatings and approaches to conduct proper measurements are discussed in detail.

2.1. Advances in deposition of TiC based cermet coatings.

Fabrication of TiC based coatings has been investigated through variety of deposition techniques including chemical vapor deposition (CVD), physical vapor deposition (PVD), electroplating, thermal spray, laser melt injection, and laser cladding [28–38]. Very hard coatings with excellent adhesion and cohesion properties for applications with extensive wear requirements, have been subjected to numerous studies, to maximize the mechanical integrity of the manufactured parts [39–44]. In particular, thermal spraying has been traditionally used in deposition of a variety of cermet compositions. It is a well-established technique for applying wear and corrosion resistant coatings that and have the capability of depositing a wide spectrum of feed stock materials (powder or wire), with diverse chemistries including metals, ceramics, alloys and cermets [64–69]. As outlined in the 'Handbook of Thermal Spray Technology' [70], thermal spraying can be viewed as a high-speed heat treatment where the mass of the feed powder experiences a desired temperature

cycle within a given period of time, which is referred to as the dwell time. Consequently, the particles of the feed stock material are melted (or partially melted) by a heat source and then invariably sprayed by a stream of pressurized gas onto the surface of prepared substrate simultaneously. Figure 1 presents a summarized list of currently available thermal spraying technologies. Based on the utilized heat source, thermal spray processes are further categorized into plasma arc, electric arc, kinetic, and flame-based processes. In particular, carbide coatings processed via high velocity oxy fuel (HVOF), with a flame as the heat source, have demonstrated low residual stress, high hardness and bond strength, and a lower volume of porosity among the outlined methods [71,72].

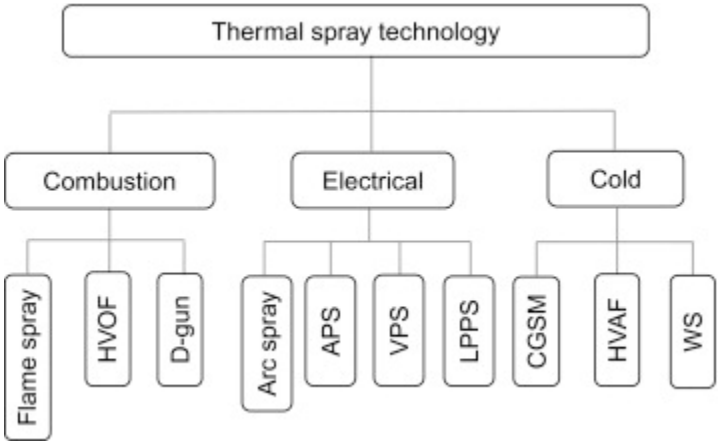

Figure 1. Classification of thermal spray coating systems [70].

More recently with the arrival of high-powered lasers, the deposition of exceptionally dense and crack-free cermet coatings, with a much wider thickness range and shorter processing time became possible [5,73–76]. From the literature it was shown that laser processing routes can significantly reduce the operational costs as a result of reduced

fabrication steps and material loss [77]. Several studies have reported successful production of cermet coatings with excellent metallurgical bonding and very low rates of dilution at low heat input to the component. Laser cladding and directed energy deposition (DED), with a coaxial powder nozzle have been used in many scientific investigations and industrial applications to apply cermet coatings on substrates of interest [51–53]. Chen et al, reported fabrication of TiC reinforced Ni-based composite coatings by coaxial laser cladding with a resultant hardness of 520 $HV_{0.3}$, which was about 2.5 times harder than the as-received substrate [78]. Subsequently, similar work by Zhao et al reported hardness valued in the range of 1308 $HV_{0.5}$ when 5wt% TiC was incorporated in production of cermet coatings in the presence of 30wt% B_4C which were 4.38 times harder than the starting surface [79]. Compared to processes involving highly focused beams, such as welding, laser cladding creates a relatively small heat-affected zone (HAZ). The narrow HAZ in laser cladding prevents crack formation and decreases the impact of heat on the substrate mechanical properties.

The common challenge in both deposition routes, be it thermal spray or laser cladding, relates to the requirements of the powder feed system and nozzle, which usually demands a precise particle size and morphology for the feedstock powder while mechanical properties of the bulk composition are retained [80–82]. In recent years, production of novel powders with the aim of achieving excellent mechanical performance has resulted in decreasing powder grain size (e.g., ultra-fine powder with size of less than 15 μm). With such a reduction in grain size the flowability of the powder is decreased, which causes problems with the controlling of the feed [83,84]. The following sections outline specific progress in the thermal spray and laser deposition technologies used in the present thesis.

2.2. High velocity oxyfuel HVOF thermal spray

The high velocity oxy-fuel spray (HVOF) spraying technique is a comparatively newer addition to thermal spray processes which was introduced by Browning and Witfield in the early 1980s, using a rocket engine. Design HVOF uses a combination of oxygen with one or more fuel gases including propane, hydrogen, and propylene [85]. In thermal spraying, the particles of the feed stock material are melted by heat source and sprayed by a stream of pressurized gas onto the surface of a prepared substrate. High-velocity oxy-fuel (HVOF) coatings, also known as high-velocity flame spray, is a thermal spray coating process that offers potential manufacture of components with densities of ≥95% of theoretical and adhesion strengths ≥69 MPa, which are also capable of operating at high temperatures [86,87]. In comparison to the alternatively used plasma spray technique, tensile quenching is minimized due to the reduced amount of heat experienced by particles and the coatings therefore exhibit much lower levels of internal residual stress [88]. Additionally, the impact of particles onto the substrate at high velocities results in the generation of compressive peening stresses that overlay the previously generated tensile quenching stresses, which consequently allows the fabrication of maximum coating thickness within the desired mechanical constraints [88–91].

The mechanical and physical properties of HVOF sprayed coatings are strongly influenced by the size and the microstructure of the deposited feed stock material. However, at the point of impact on the substrate, the state of the particles within the molten feed material are largely affected by operational factors, such as their velocity and degree of melting, which is controlled by several key process parameters including the total gas flow rate, the fuel/oxygen ratio, stand-off distance, and powder size distribution [92]. Further progress

in HVOF technology has been acquired in assessing the effects of these key processing factors in terms of optimizing the operating performance of coatings. Here, a further aim relates to optimization of the combustion response, minimizing fuel consumption, and increasing the particle acceleration.

2.2.1. HVOF technologies and equipment

A schematic representation of a typical HVOF spraying setup is presented in Figure 2. The basic HVOF system shown consists of a gun, powder feed unit, air and gas supply unit, and a flow meter [93]. The physical constraint of the deposition is often controlled through a computer numerical control (CNC) system which is often equipped with robotic arm.

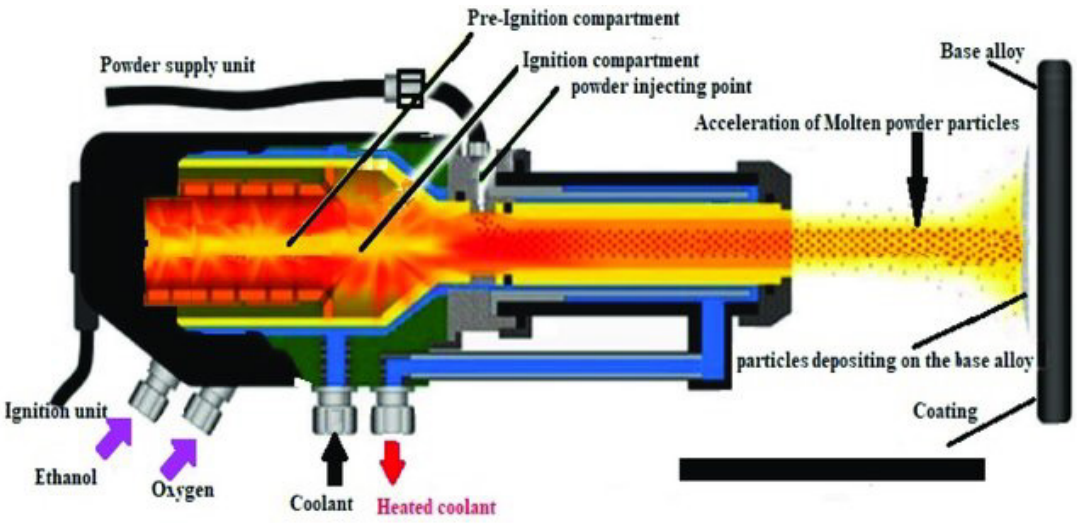

Figure 2. Schematics of a typical HVOF spraying setup [93].

The parameters of the thermal spray process are selected by the operator, which dictates the particle velocity and the temperature of the flame jet. In HVOF spraying processes, the fuel gas (typically propylene or hydrogen) is fed to the air cap along with oxygen, where it leads to high-temperature combustion gases. Depending on the torch design and the fuel being used, the temperature of the combustion jet may reach anywhere between 2300 and 3000°C. The injected air from the annular inlet orifice, in contrast to the exhaust gases, expands through the nozzle to reach supersonic velocity (i.e., 550–850 m s^{-1}), resulting in the formation of a diamond pattern within the exiting flame jet [94].

The feed stock powder is fed from the powder feed unit via a carrier gas, to the gun, where combustion occurs. Powder feeding units for thermal spray applications are generally selected based on their compatibility with the rest of the thermal spray system and the volume of the feed canister. Once powder particles are injected at the central inlet nozzle, via an inert career gas (e.g., nitrogen or argon), the transfer of heat between the gas and the powder particles, and the momentum generated in the process results in further acceleration and heating of the particles. Therefore, as a consequence, the expanding gas jet transfers the partially melted particles toward the prepared surface of the substrate. Fast cooling and solidification of the molten feed stock on the substrate then leads to the formation of thin layer of coating with relatively low levels of porosity [95].

More advanced HVOF units are also equipped with CO_2 based cooling systems for fabrication of exceptionally uniform microstructures. A number of these systems also include a continuous thermal surveillance setup, since optical methods are often inadequate

for measurement of temperature in the presence of the bright flame of the spray gun [94,96].

2.2.2. Characterization of cermet coatings fabricated by HVOF.

Grain size, interfacial strength, and the chemical composition of the materials fabricated by thermal spray systems (including HVOF), often vary from their feed stock materials when processed in other forms such as their wrought, forged, and cast counterparts. Thus, standard testing and characterization methods, in addition to specialized preparation routes, have been developed to understand the material response and its critical attributes for this family of coatings. Several characterization techniques are employed to evaluate the physical and mechanical aspects of thermal spray coatings. These methods include examination of intrinsic and extrinsic characteristics of the coatings with regards to the nature of mechanical property measurements for thermal spray fabrication. A summary of frequently performed measurement approaches for assessment of the mechanical and microstructural properties of HVOF coatings and its related execution protocol is gathered in Table 1.

Table 1. Summary of the intrinsic and extrinsic properties typically measured for HVOF coatings.

Attributes	**Characterization techniques**
Metallography & phase identification	OM[1], SEM[2], CLSM[3], EBSD[4], EDS[5], TEM[6], XRD[7]
Porosity	MIP [97][8], XCT[9] [97], BET[10] [98], OM and SEM [99], Gas absorption [97], Electrochemical techniques [100]
Residual stress	Destructive (i.e., hole drill method [101]) and nondestructive (i.e., XRD, ND[11], LBES[12]) testing [89,102]
Adhesion/cohesion	Tension testing [103], Stud-pull test [104], Shear load test [105], Peel test [106], Scratch test [110,111], Interfacial indentation [110]
Hardness Elastic modulus Fracture toughness	Indentation tests (i.e., Knoop or Vickers hardness) [111]
Wear	Pin on disc [112], Taber abrasion [113], Sliding wear testing
Corrosion	OCP[13] &PD[14] [114], EIS[15] [115], Salt fog spray [116]

[1]Optical microscopy, [2]Scannin electron microscopy, [3]Confocal laser microscopy, [4]Electron backscatter diffraction, [5]Energy-dispersive X-ray spectroscopy, [6]Transmission electron microscopy, [7]X-ray diffraction
[8]Mercury intrusion porosimetery, [9]X-ray tomography, [10]Brunauer-Emmett-Teller
[11]Neutron diffraction, [12]Laser beam excitation spectroscopy.
[13]Open circuit potential, [14]Potentio-dynamic polarization resistance, [15]Electrochemical Impedance Spectroscopy

2.2.2.1.Metallographic preparation and Microstructural evaluation of HVOF coatings

Metallographic preparation of HVOF coatings, prior to microstructural analysis, is a detrimental step in relation to gathering accurate and repeatable results from mechanical testing of these materials. However, the heterogeneous nature of these components often makes choosing an appropriate preparation method very complicated. During metallographic preparation of HVOF coatings special attention must be paid to deformation processes particular to every material, including metallic slip, shearing, twinning, polymeric responses, and ceramic fracture modes to the abrading mechanisms of the polishing process [70,117]. This involves preparation of the coating for sectioning which may involve imbedding the specimen in a suitable protective film/resin. Specimens are often sectioned using abrasive blades such as aluminum carbide (ceramics), diamond blades, and waterjet systems. Sectioned specimens then are embedded in appropriate molding material such as epoxy or Bakelite and subjected to sequential polishing using variety of polishing cloths with a wide range of naps, resiliencies, etc. [117–119].

Microstructural characteristics of the solidified layer demonstrate a substantial amount of information on the dynamics of the system and the potential mechanical performance of the final coating. Metallographically prepared cross sections of the thermal spray coatings are usually examined for porosity, cracks and the state of residual stresses, employing a variety of preliminary and advanced microscopy techniques. Important microstructural features which combine to identify the characteristics of the coatings have been highlighted in Figure 3, representing a typical microstructure of the HVOF coating/substrate. In general, the morphology of the HVOF coatings includes splat structure, oxide stringers, pores, cracks, entrapped un-melted particles, various phases, grains, and the bond interface.

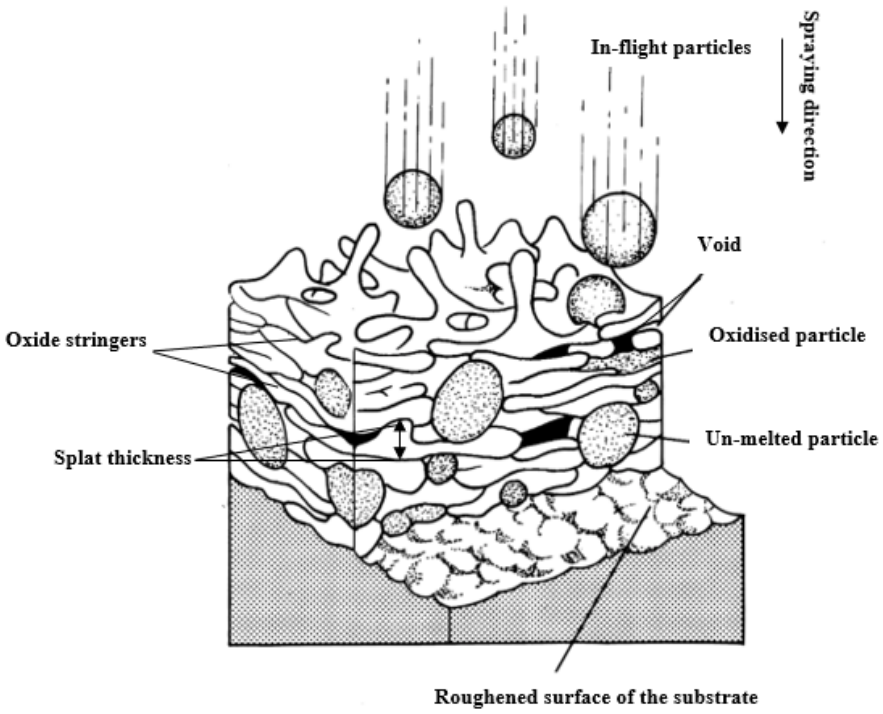

Figure 3. Schematics of common microstructural features observed in structure of the HVOF coatings [70].

HVOF coatings are often characterized by thin overlapping lamellar layers, formed as a result of the spatial interaction of the feedstock and substrate with a defined field of temperature and velocity. A single impacted droplet/particle is referred to as a **'splat**' which solidifies and adheres to other splats to form a continuous layer. The morphology of the molten splats leaving the nozzle, is generally spherical, which spread over the underlying layer upon their impact with the surface of the substrate. Therefore, the cohesion, porosity, and subsequent properties of the deposited coating layer are largely

dependent on the degree of melting of in-flight particles [70]. Moreover, highly anisotropic mechanical properties of coatings are associated with the mechanical structure of the splats. '**Oxide stringers**' or inclusions are referred to as dark contrast and elongated phases that are generally formed parallel to the substrate and are generated as a result of the interaction of any high temperature metallic phases within the coatings and the surrounding atmosphere [120]. Although it has been reported that such inclusions often add to the hardness of the coating, because of the decreased cohesive strength of the coating (due to added brittleness) they are not desired for most applications. The concentration of oxide inclusions may be reduced by elimination of the reactive environment, use of proper feed stock (larger particles form less oxides due to lower surface area to volume ratio), decreasing the process temperature, etc.

Another microstructural feature that significantly affects the mechanical properties of HVOF coatings is the '**porosity**' [89,99,100]. Presence of porosity is often reported in contrast with a high concentration of un-melted and/or resolidified particles, and therefore poor cohesion and other undesirable characteristics of protective coatings such as high surface roughness [70]. Premature cracking, spalling or delamination resulting from inadequate cohesion, leads to reduced hardness and wear resistance of the protective coatings [6,121,122]. In addition, the hard phase removed as a result of excessive wear generally acts as an abrasive 'third body' cutting agent and damages the surface even further. Moreover, fine porosity and interconnection of the pores within the coating results in increased corrosion rates due to contamination of the substrate by corrosive media [123].

2.2.2.2 Mechanical testing of the HVOF coatings

HVOF coatings are generally subjected to mechanical characterization techniques much like other engineered components, using common but specialized measurement approaches according to their qualification requirements for specific applications. Thus, many testing routes have been developed in recent years in relation to accelerating advancement of the thermal spray technologies and HVOF coatings [124–126]. In this section a few of many available techniques that are more commonly used are discussed.

Adhesion is a property of major concern for many types of coatings, as a minimum requirement through the designed life of the fabricated components. Intrinsic factors related to the deposition parameters and extrinsic aspects resulting from post-treatments and the service conditions that are experienced, can influence the adhesion properties of the HVOF coatings [127,128]. Several techniques have been suggested within the literature for the measurement of adhesion or interfacial fracture strength of the HVOF coatings, including: the shear adhesion test, pin test, double cantilever beam (DCB) test, bending test, etc. [129–132]. However, due to the ease of specimen preparation and experimental setup, the tensile adhesion test (standardized in ASTM C633-69) is most commonly used [133,134].

Measurement of hardness in both the macro and micro scale, both on the surface and the cross sections of the thermally sprayed coatings have been reported by many authors [59,135–137]. Due to its capability to differentiate between various presented phases, micro-Vickers hardness has been a popular technique for accurate identification of the hardness properties throughout the microstructure of the coatings (Knoop micro indentation hardness testing is less widely used). In the Vickers indentation technique, a

square-based diamond pyramid with an included angle between opposite faces of 136° is used as an indentation to apply force onto the surface of the specimen. Xie et al, reported the manufacture of WC-based HVOF sprayed coatings exhibiting micro-Vickers hardness values exceeding 1100 HV (Figure 4) [138].

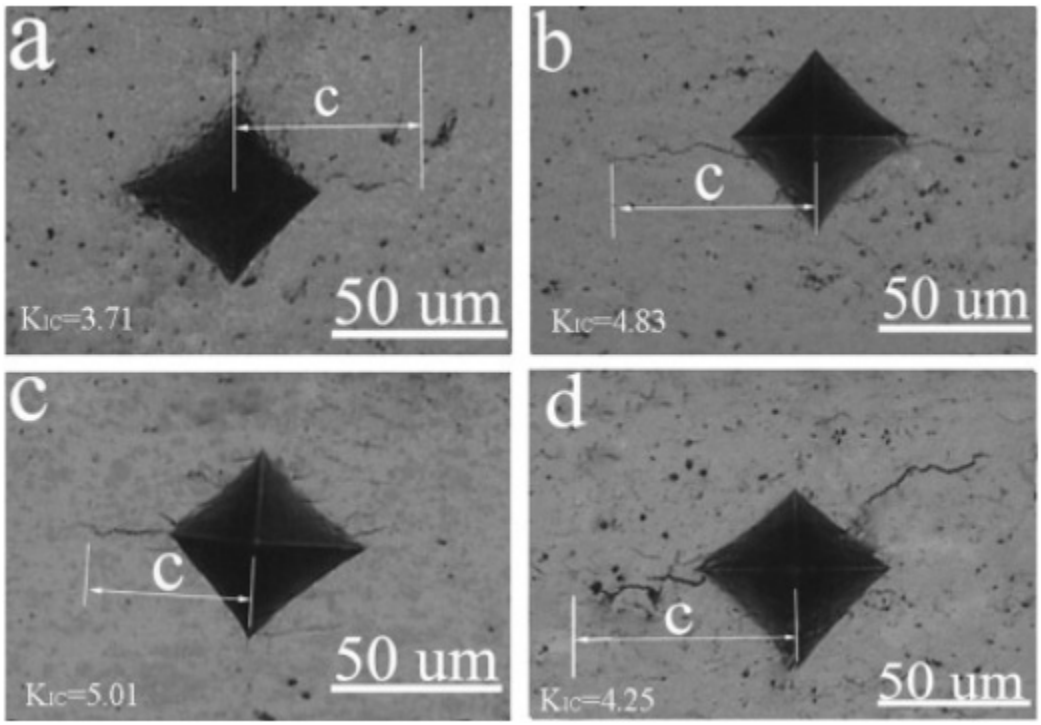

Figure 4. Typical indentations on transverse section with in-plane cracks for four WC based coatings fabricated by HVOF.

The microhardness test can be influenced greatly by the method of which specimen has been metallographically prepared. According to the 'Handbook of Thermal Spray Technology' [70] the measured hardness values of two similar specimens prepared via different polishing routes can vary by over 100 units. The Rockwell superficial hardness

test, under constant applied load, is another common technique used in hardness measurement of HVOF coatings because of its comparative ease and minimal requirements for surface preparation.

Electrochemical methods for determining the corrosion performance of thermal spray coatings have also been specially modified to better understand the heterogeneous response of the component in corrosive media. Both DC and AC testing techniques have been reported repeatedly by authors to assess the complex electrochemical characterization of these systems [139–144]. In DC setups, increasing voltage is applied to the surface of a specimen that has been exposed to corrosive media. The resulting current response is then recorded as an indication of the performance of the coating as a nonconductive barrier. Therefore, properties such as corrosion potential E_{corr}, corrosion current, I_{corr}, cathodic slope, and anodic slope can be utilized for the calculation of corrosion rates [145,146]. In AC corrosion measurements, the fundamentals of the parallel circuits are applied to the specimen where the lag of current response determines the exact phase shift. Thus, the time that takes current to decay from its original value, can be measured as a time constant, τ (Figure 5).

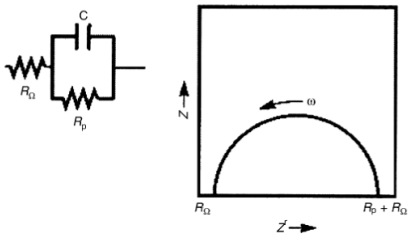

Figure 5. Equivalent circuit of the corroding system shown in Fig. 6 with an electrochemical impedance spectroscopy Nyquist plot [70]

This method, which is also known as electro impedance spectroscopy (EIS), then uses the following equations to compute the values of resistance and capacitance:

Equation 1

$$\textbf{Impedance, } Z = V/I \textbf{ Resistance}$$

Equation 2

$$R = Z \cos \theta$$

Equation 3

$$1/\omega C = Z \sin \theta$$

Consequently, by knowing V, I, θ, and ω, the values of R and C can be determined as an indication of the material's resistance to oxidation attack.

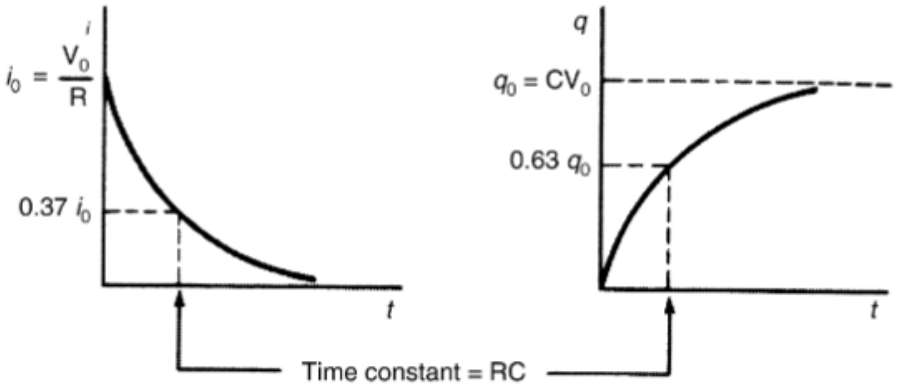

Figure 6. Time constant of a resistive/capacitive (RC) circuit [70].

For the *RC* circuit shown in Figure 5, driving the system from the point of low frequencies to very high frequencies (i.e., 10^{-2} to 10^{5} Hz), the resulting plot is referred to as a 'Nyquist plot', which describes the real versus the imaginary components of impedance that computes the total resistance of the system as Rφ, Rp and C where *Rφ* represents the resistance of the solution or electrolyte, *Rp* is an indication of the resistance of the coating and *C* is the capacitance of the coating. At very low frequencies, the capacitor effectively blocks the current, while at higher frequencies the capacitor acts as a conductor and the current will flow through the capacitor, bypassing the resistance *R* [146].

A simpler way to understand this is through construction of what is commonly known as a 'Bode plot', which plots the log of the impedance versus the log of the frequency, and does not involve the imaginary parts of the impedance (Figure 7) [70,147]. *Rφ* and (*Rφ* + *Rp*) can then be obtained from the horizontal portion of the corresponding log plot at low and high frequencies, independent from the frequency itself.

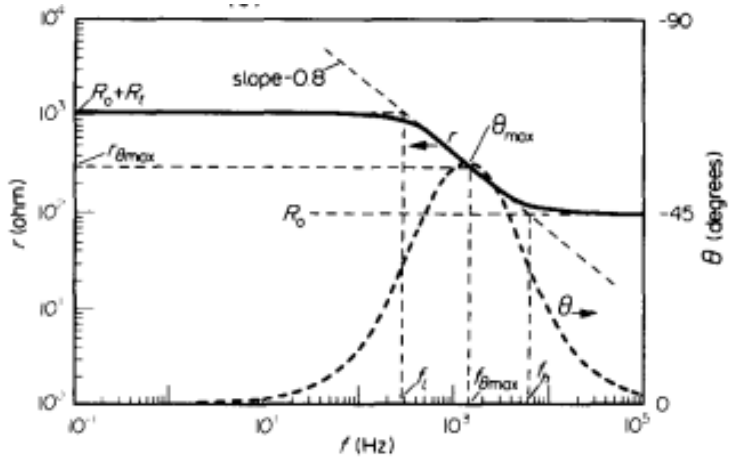

Figure 7. Example of Bode plot [148]

Residual stresses in HVOF coatings (tensile or compressive) are generally caused by differences in temperature and the rate of shrinkage between the hot sprayed coating and the substrate while rapid cooling is in effect. According to Matejicek et al, methods of residual stress measurement in thermal spray coatings can be divided into three main groups [149]; Material removal methods, which includes the hole-drilling technique, deflection measurement or measurement of the curvature and X-ray diffraction.

In the hole-drilling method, a shallow hole is first drilled into the test specimen to a depth approximately equal to the diameter of the hole (typically ranging from 0.8 to 5.0 mm (0.03 to 0.20 in.)). A specially designed three-element strain-gage rosette then measures the associated partial strain relief generated by the presence of the hole [70,150]. Residual stresses that originally existed in-plane, can then be calculated at the location of the hole from the measured strain relief, applying the method described in ASTM E 837, "Measurements of Residual Stresses by Hole-Drilling Strain-Gage Method."

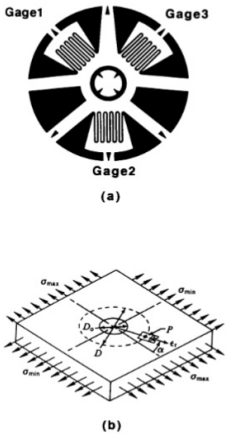

Figure 8. Hole-drilling method for measuring residual stresses [150]. (a) Typical three-element strain-gage rosette. (b) In-plane strain components caused by release of residual stresses through the introduction of a hole.

Measurement of substrate curvature formed due to residual stresses is another very common method which is based on optical or mechanical measurement of substrate curvature. If dimensional variations in both the coating and the substrate are measured after detachment, more information can be recovered. With this approach, stress created by thermal mismatch can be separated from the stress induced by quenching with a simple experimental arrangement and limited requirements for specimen preparation. The highlighted advantages of this method have been related to its direct determination of coating stress, rather than strain, and the *in-situ* monitoring of stress changes during deposition.

X-Ray Diffraction (XRD) is a nondestructive testing route that measures the changes in crystal plane dimensions in different directions, through the shifting in angular position of specific diffraction peaks with respect to the surface of the specimen, which subsequently allows a measure of the stress. Moderate restrictions have been noted in relation to sample preparation and dimensional limits. More detailed information on the XRD stress measurement method is beyond the scope of this document and details can be found in suitable articles [151,152].

2.2.3. Applications of thermally sprayed TiC based HVOF coatings.

Owing to its cost effectiveness and flexibility, HVOF thermal spraying has been adopted extensively in numerous industries. These include aerospace, automotive, industrial gas turbine, marine, and (to some extent) oil and gas [94]. From the literature, aerospace and

industrial gas turbine applications hold approximately sixty percent of the thermal spray market [153] and thus, this industry has been involved in large portion of its developments. Depending on the characteristics of the feedstock material, HVOF technology has been utilized for dimensional restoration and repair, and providing lubricity, thermal insulation, and/or protection from wear and corrosion. Consequently, the principal function of the traditionally applied WC based HVOF coatings is to resist severe wear mechanisms in the aerospace sector. Moreover, the latest innovations in processing of feedstock materials have broadened the range of thermal spray applications even further. A good example of this is the development of a new technology for protecting ceramic powders lacking suitably low or any melting point (e.g., silicon nitride and silicon carbide, which sublime) for thermal spray. Spraying ceramics with no melting point has been achieved by protecting each individual particle with a nanolayer that works as barrier against heat [154]. However, as it has been noted by authors, the buildup of residual stresses as a function of increasing coating thickness still is the biggest challenge in forming high-thickness solid structures, by HVOF spraying due to the buildup of residual stresses [94].

2.2.4. Material design and feedstock processing

Feedstock is generally referred to as materials that are fed into the thermal spray system. Feedstock materials for a thermal spray device are classified into three variants [155]:

(i) powders, (ii) rods and wires, and (iii) solutions and suspensions.

Further classification of feedstock materials is related to their material chemistry and type, material morphology, particle size distribution, and associated spray process. The

following discussion principally refers to powder feedstock since this is the primary component for the HVOF spraying processes.

A prerequisite of any thermal spraying process is the transportation of the feedstock to the heat source and then further to the surface of the substrate. Challenges related to the powder feeding systems refer only to the initial stage of powder transportation, and generally arise from 'spray-ability' of the feedstock powder. Such technical challenges may result in poor quality coatings. Use of high-quality feedstock material is an essential factor for the fabrication of consistently high-quality coatings. The typical powder size used for feedstock in HVOF ranges from 15 to 45 μm. The average speed of the particle and its distribution at the injection point is a critical condition of the feed system. However, the momentum of the individual particles and their trajectory will differ, based on the mass of each particle, which results in variation of final impact velocities and distinction of coating properties [156].

Particle morphology is another significant factor that affects the impingement velocity and temperature, and thus influences the coating porosity content. For example, hollow spherical powders have shown excellent flow characteristics and their low mass allows for consistent melting of particles [157].

A wide range of traditional and commercial powder fabrication techniques are available for preparation of HVOF feedstock materials based on mechanical nature of the various alloys, such as crushing and mechanical milling, atomization, fusion, self-propagating high temperature synthesis (SHS), and spray drying method. Ductile metal feedstocks are often fabricated via water or gas atomization, and utilization of methods such as ball milling and solid impaction are found to be impractical. Subsequently, composite materials can be

fabricated by the process of diffusion sintering which often results in formation of large, agglomerated particles and require further mechanical steps to reduce the particle size.

Mechanical milling has been commonly considered as one of the most feasible methods for preparing a range of metallic, non-metallic, nanocomposite, and nanocrystalline powders within the recommended range of particle size for HVOF. In this technique, ductile metals are mechanically deformed and physically alloyed by mutual impact.

A typical example of mechanically alloyed feedstock powder for fabrication of protective coating via HVOF is mechanically alloyed Ni–Ti–C powders with a particle size range of 8–38 μm for deposition of approximately 250 μm thick onto mild steel substrates [158]. Furthermore, nanostructured feedstock powders for HVOF applications such as nanostructured Cr_3C_2-$Ni_{20}Cr$ coatings, have received much attention, owing to exceptional wear resistance characteristics of the fabricated parts [159].

More recently, fabrication of highly dense coatings with good mechanical properties have also been reported in association with sol gel synthesis technologies [160–162]. A list of available commercial powders processing routes used for fabrication of thermal spray feedstock is presented in Table 2.

Table 2. A summary of available commercial powders processing [163].

Chemical Processes	
	Solid state phase decomposition
	Thermal decomposition
	Liquid phase precipitation
	Gas phase precipitation
Electrolytic Processes	
Mechanical communication	
	Machining
	Milling
	Impact attrition
	Mechanical alloying
	Mechanising
Water Atomization	
Gas Atomization	
Vacuum Atomisation	
Ultrasonic Atomisation	
Micro atomisation Impact	
Plasma Melting	
Centrifugal Method	
	Rotating Electrode
	Centrifugal atomisation
	Spark discharge atomisation

Several commonly utilized feed stock materials for the purpose of the HVOF spraying process are:

- Tungsten Carbide-Cobalt: HVOF tungsten carbide coatings are extremely dense, well bonded and can be applied to a high thickness. HVOF tungsten carbide materials are recommended for applications that are subject to wear [115,135,164].
- Tungsten Carbide-Cobalt/Chrome: HVOF tungsten carbide-cobalt-chrome coatings are more wear resistant in most applications than tungsten carbide coatings and are more corrosion resistant because of the chromium content. HVOF tungsten carbide-cobalt-chrome is recommended for applications with abrasive or sliding wear, which may also be exposed to some level of corrosion. HVOF tungsten carbide-cobalt/chrome coatings are an excellent alternative to hard chromium plating [165].
- Tungsten Carbide-Nickel Superalloy: Spraying a material with HVOF tungsten carbide-nickel superalloy produces a well bonded coating with a high level of wear resistance to abrasive grains, hard surfaces, and fretting [124]. These coatings are ideal for hydraulic rods, ball valves, drilling, and saltwater applications [166].
- Chromium Carbide metal matrix: HVOF chromium carbide coatings have high microhardness and are well bonded [167,168]. These coatings are ideal for providing resistance to solid particle erosion, abrasion, and tribo-corrosion at elevated temperatures [138].
- Stainless Steel: Spraying a material with HVOF stainless steel produces a dense and well bonded lower cost coating. These coatings are used for protection against corrosion, cavitation, and low temperature particle erosion in salvage and repair applications [169].

2.3. Laser cladding

Since the development of high-power gas lasers (e.g., CO_2 lasers) in 1975, laser technology has given rise to the invention and development of unique techniques such as laser welding and laser cladding [170–172]. The development of laser technology was then followed through enhancement of related devices such as powder feeders, cooling systems, hemispherical reflecting devices for re-absorbing the reflected light, etc. Beam deposition processes are referred to as a family of additive manufacturing techniques that employ a focused heat source such as electron beam, plasma arc, or laser beam for the melt and deposition of feedstock powder or a thin metal wire (Figure 9) [173].

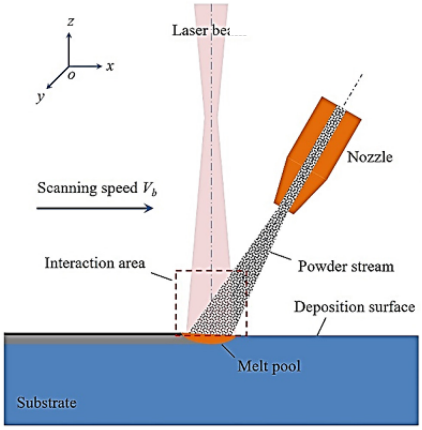

Figure 9. Schematics of laser cladding process, highlighting the process overview [173].

The traditional beam deposition-based techniques such as welding are generally designed for repair, joining, or to apply coatings, while laser cladding is designed to create depositions of complex 3D shapes directly from computer software.

Table 3 illustrates a general overview of the advantages of laser cladding over other, more conventional, processes [174].

Table 3. General overview of the advantages of laser cladding over conventional processes (adapted from reference [174]).

Attribute	Welding	Thermal spray	Laser cladding	CVD	PVD
Bonding strength	High	Moderate	High	Low	Medium
Feed material	Metals	Metals & ceramics	Metals & ceramics	Metals & ceramics	Metals & ceramics
Dilution	High	NA	Medium	NA	NA
HAZ	High	Low	Low	Very low	Very low
Coating thickness	Several mm	50 µm to several mm	50 µm to 2 mm	0.05-20 µm	0.05-10 µm
Repeatability	Moderate	Moderate	Moderate-High	High	High
Cost	Moderate	Moderate	High	High	High

Laser cladding processes produce dense, wear, and corrosion proof structures with smooth and consistent surface finishes. The bonding zone between the substrate and clad layer usually contains a metallurgical bond (vs. the mechanical bond that is more typically obtained through thermal spray) with a smaller heat affected zone (HAZ) in comparison to conventional welding techniques [175]. Depending on the type and amount of material

added to the melt pool, the process can be identified as glazing, laser alloying, or laser cladding [176]. Glazing is generally referred to metallic glass coating, which can provide an environmentally effective surface in terms of wear and corrosion, by alteration of the microstructure(s) without changing the composition [177]. In laser alloying, a small amount of powder is fed into the melt pool to create homogeneous mixing throughout the melt region. The phenomena of dilution by the substrate are thus kept to a minimum with laser alloying, and further addition of material to the surface is required [178]. Reduced dilution, which is the mixing percentage of the substrate to the clad region (compared to laser alloying), reduced thermal distortion, and reduced porosity (particularly in laser cladding by powder injection) are typical advantages of laser cladding compared to other alloying techniques (Figure 10) [174].

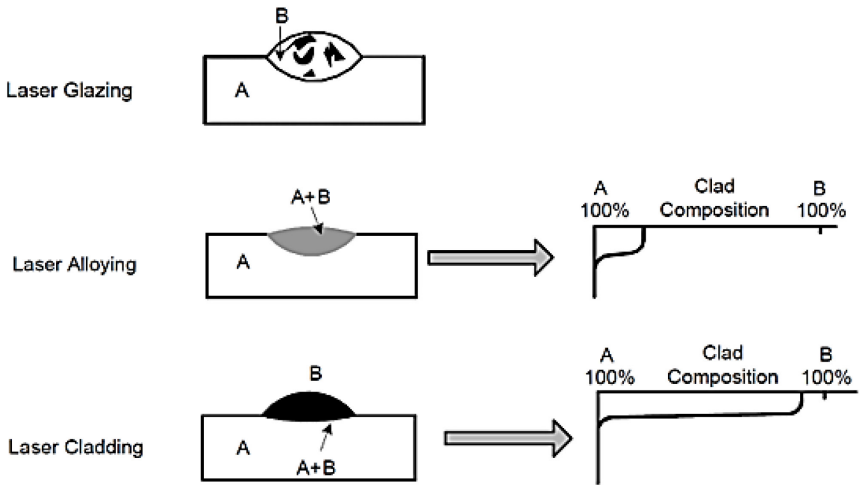

Figure 10. Different microstructures of laser alloying, glazing, and cladding [174].

In laser cladding, a stream of the desired powder is fed into the melt pool created by a focused laser beam as it is scanned across the target surface, leaving behind a deposited

coating of the chosen material [179]; this enables the applied material to be deposited selectively, only where it is required. Laser cladding is often characterized by generation of a fine and homogeneous microstructure, within a dense coating layer. The microstructure of the clad layer is usually designed to promote desirable mechanical characteristics of the surface, such as wear and corrosion resistance. The precise nature of laser beam cladding process has been found to offer flexible technology for repair and rapid design changes in numerus applications such as protective coating of lightweight motors for cars and highly stressed hot work [180,181]. Integration of laser technology into machine tools and manufacturing processes has been a popular research focus in recent years. Additionally, combination of laser technology with complementary techniques such as plasma transferred arc (PTA) welding and inductive heating has made the connection of technical and economic advantages of the individual processes possible. Today's major applications of laser cladding include production of **protective coatings**, **component repair,** and **rapid prototyping** [182].

Laser deposition is an advanced coating technology for improving the surface properties of various components and associated equipment. These coatings exhibit exceptionally dense, crack-free, and non-porous microstructures. Laser coatings offer excellent metallurgical bonding, with very low dilution and (typically) low heat input to the component [183,184]. It has been reported in the literature that there have been many successful applications of coatings that are exceptionally durable, corrosion-resistant, and provide load bearing capabilities [185–188]. These have included using titanium-based alloys, nickel-based superalloys, and cobalt-based alloys, deposited on variety of substrates

mainly steel, aluminum alloys, cast irons and nickel-based alloys [185–188]. An example of such a clad is shown in Figure 11.

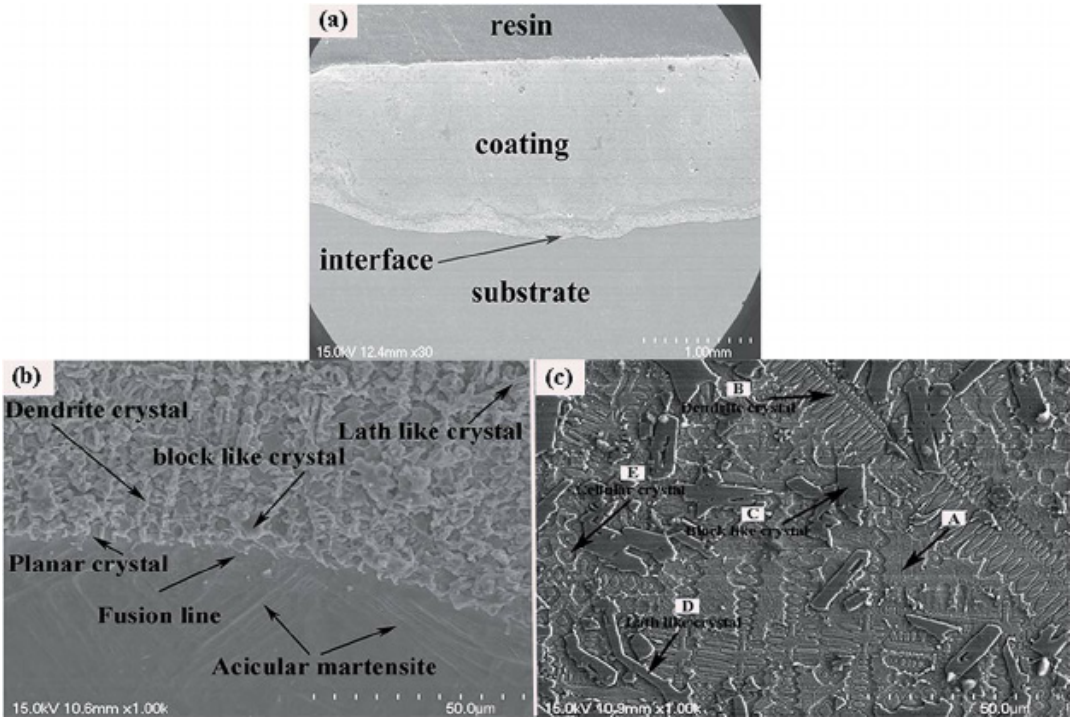

Figure 11. Cross-section SEM micrographs of the laser clad coating: (a) overview, (b) bonding zone and heat-affected zone, and (c) typical microstructure of the NiCrBSiFe composite coating at intermediate region [188].

Thermal control over the kinetics of the deposition makes laser cladding a safe technology to ***repair tooling***, particularly on critical contacting surfaces, while increasing tool life [189,190]. In this respect, a primary application of laser cladding is in the repair of high value components. The low heat input characteristic of the cladding technology is especially beneficial in repair of superalloys, which are highly susceptible to strength loss and physical distortion when exposed to excessive temperature variations. Moreover,

repair of components with an exact desired geometry, and with equivalent microstructure and performance to the original damaged work piece through laser cladding can reduce the overall cost for many repair problems [181,191,192]. This is achieved by elimination of finishing steps and without the drawbacks of conventional repair techniques, such as a large HAZ and high residual stresses [181,191,192]. Furthermore, the costs associated with repairing/replacing a high-volume workpiece such as train tracks, turbine blades, airplane engines, etc. is significant.

Rapid Prototyping is referred to a 'layer-by-layer' approach of laser processing that manufactures mechanical components with homogeneous structure, enhanced mechanical properties, and allows one-step production of complex geometries. The costs of this operation are low with a short manufacturing time. Examples from the literature for rapid prototyping include laser engineering net shaping (LENS), laser additive manufacturing (LAM), laser consolidation (LC), and direct metal deposition (DMD). The concept of layered manufacturing was outlined in 1971 and 1977 through patents from Ciraud and Housholder, but these early ideas did not reach the stage of commercialization without the advent of powerful computers and laser systems [193,194]. The first cladding system was introduced under the name of "selective laser sintering" (SLS) and was acquired by 3-D systems in 2001. SLS uses a wide range of materials, including PVC, polycarbonate, ABS (acrylonitrile butadine styrene), polyurethane, nylon, polypropylene, resin, and polyester. Today, the laser engineering net shaping (LENS) process is used for aeronautical applications by Aeromet which specializes in making parts from titanium parts through powder bed and powder injection mechanisms.

Laser cladding processes are applied in one or two steps, based on the way that the feedstock is supplied. In a two-step process a thin layer of material is deposited onto the substrate and subsequently melted with the laser beam. In the single step method the feed stock is fed continuously into the melt pool generated by the laser beam (Figure 12) [174]. The feed material can be introduced as paste, wire, or powder injection. Among these methods, laser cladding by powder injection has been demonstrated to be most effective due to its high energy efficiency, and it allows for better process control and reproducibility. In laser cladding via powder injection, the powder particles are fed into the heated zone (i.e., the melt pool) to produce a layer of clad on the surface of interest.

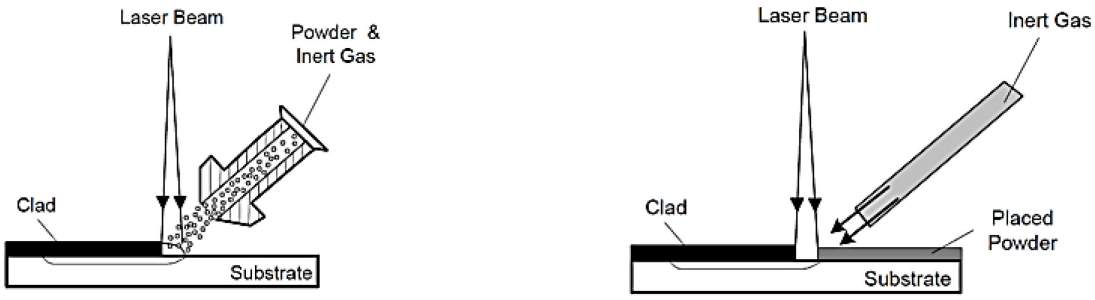

Figure 12. Different methods of laser cladding: a) one-step laser cladding, showing powder injection laser cladding, and b) two-step laser cladding [174].

From the laser cladding history and related documented literature, the development of the cladding technologies and the quality of its process depends upon technological improvement of the involved technologies (e.g., lasers, positioning devices, powder feeders, nozzles, feedstock materials, optimal cladding conditions, etc.) [174,179,195]. The following sections outline a brief review of laser cladding and its related technologies,

covering the fundamentals of laser–matter interaction and the classification of laser material processing under following sections:

- **Cladding technologies**
- **Feed-stock materials**
- **Kinetics of laser cladding**
- **Characterization of classes.**
- **Applications**

2.3.1. Cladding technologies

Characteristics of the clad system are determined by two categories of inputs, namely intrinsic and extrinsic. The intrinsic properties of the feedstock and the substrate are ones such as absorptivity, thermal conductivity, heat capacity, thermal diffusivity, and the actual workpiece geometry. However, the quality of laser cladding is largely dependent on a variety of extrinsic operating parameters and physical phenomena. The main inputs or operating parameters in laser cladding are the lasers, positioning devices, powder feeders and nozzles, as shown in Figure 13 [196]. The physical phenomena or processes occurring as a result of the various input parameters can vary from one clad couple to another. The outputs of the process, which represent the clad quality, include the geometry, microstructure, component integrity (i.e., cracks, porosity, etc.) surface roughness, residual stresses, and dilution [174,197–199]. Thus prior to understanding the characterization of the output of cladding processes, it is essential to understand the mechanics and the

interaction of the processing parameters, as well as the trends in the advancement of their related technologies. The following provides a review of available lasers, powder feeders, and nozzles found suitable for cladding applications according to the available literature.

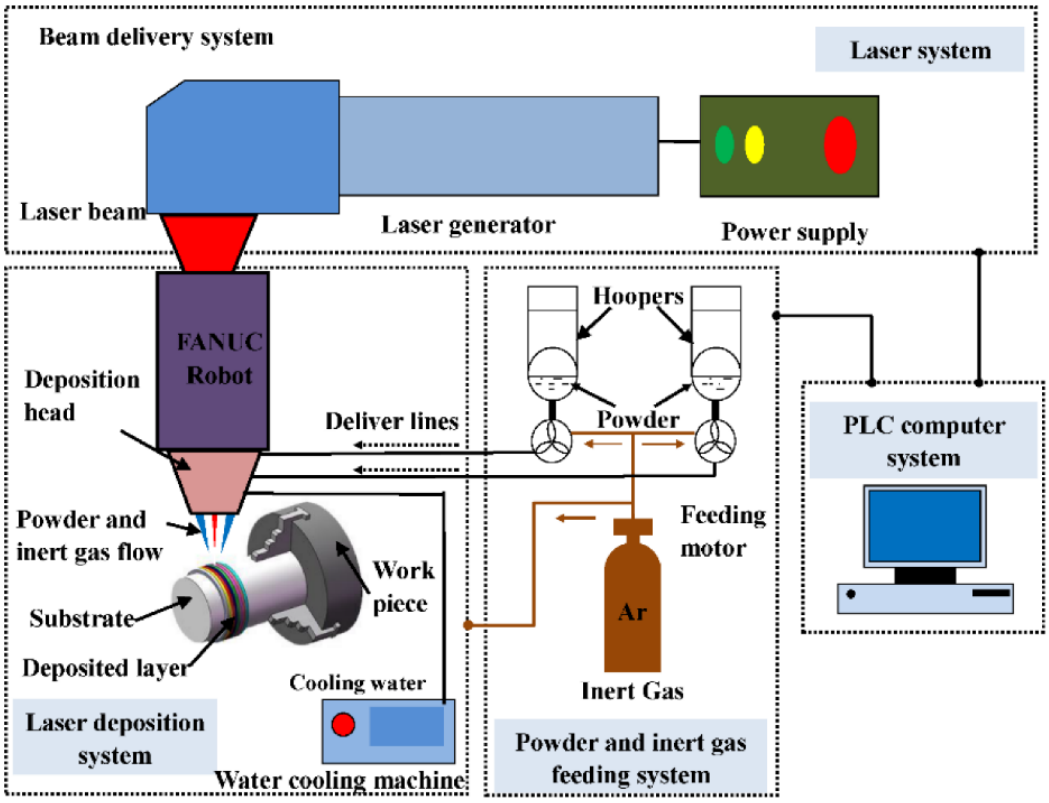

Figure 13. Schematic diagram representing the component of a laser cladding system.

2.3.1.1. Lasers

Characteristics of the laser beam play an important role in laser-material processing, including laser cladding. Laser types can be categorized based on physical and operating parameters which are involved in the laser beam generation. The most common way is to

classify lasers based on the physical state of the active material. According to this criterion, lasers can be categorized as gas lasers, excimer lasers, solid-state lasers, semiconductor lasers, liquid dye lasers, and fiber lasers.

There are many commercially available laser systems, however, CO_2 lasers, lamp-pumped Nd: YAG lasers, diode-pumped Nd: YAG lasers, and high-power diode lasers (HPDL), are most used in the laser cladding process. There are several parameters that indicate the quality of a laser beam, including the beam parameter product (BPP), laser beam mode, energy distribution over the beam spot area, polarization, and 'focus-ability'. Table 4 summarizes characteristics of these four types of lasers which have been widely used in laser cladding.

Table 4. Properties of common lasers employed in the process of laser cladding [174].

Attributes	**CO_2**	**Nd: YAG** Lamp pumped	**Nd: YAG** Diode pumped	**HPDL**
Wavelength (µm)	10.64	1.06	1.06	0.65-0.94
Efficiency%	5-10	1-4	10-12	30-50
Mean Power Density (W/cm^2)	10^{6-8}	10^{5-7}	10^{6-9}	10^{3-5}
Max Power (kW)	45	4	5	6
Fiber coupling	No	Yes	Yes	Yes
In-service life (hours)	1000-2000	200	5000-10000	5000-10000

In laser cladding, the average power, spot size, pulse, beam profile, and laser wavelength, are all factors that are determined by the characteristics of the laser device. CO_2 lasers are traditional high-power lasers that are available with power levels up to several tens of kW [200]. They usually support systems with high power density and excellent beam quality (low "beam-parameter-product" number) [201]. CO_2 lasers have long wavelengths and, unfortunately, consequently result in low absorption of the laser beam by most used metal systems (e.g., steels). Solid state lasers Nd: YAG lasers are characterized by their ability to operate at shorter wavelengths, which improves the absorption characteristics of the laser [174]. However, the low electrical/optical efficiency of this family of lasers makes the equipment bulky and costly to run. HPDL (high power diode lasers) are available up to a maximum of ~6 kW power level. The newest generation of high-power lasers has been especially designed for common end chain applications such as welding, coating, surface treatment, polymer welding, and brazing. These lasers offer the lowest wavelength while benefiting from high electrical/optical efficiency (30-50%). HPDL lasers are generally smaller in size than the other alternate laser technologies of the same kilowatt level [202].

2.3.1.2.Powder feeders

Powder feeders are among the most important pieces of equipment in several industrial applications that involve the transmission of powders, such as thermal spraying, laser cladding, and advanced materials processing. Powder-based laser cladding results are heavily dependent on optimal feeding features of the powder, controlled supply, and metering [203].

Due to the development of numerous powders with distinct sizes, shapes, and other physical and mechanical properties, specialized feeders have been developed to provide flowability and an efficient steady feed stream. In recent years, the production of novel powders, designed with the aim of achieving excellent mechanical performance, has resulted in decreasing powder grain size (e.g., ultra-fine powder with size of less than 15 μm) [182]. With such a reduction in grain size the flowability of the powder is decreased, which causes problems with controlling the feedstock delivery. In general, powder feeders are classified based on their operational parameters [56–60]. The most common types of powder feeders are known as gravity-based, mechanical wheel, fluidized-bed, and vibrating. In laser cladding, the feed rate and the profile of the powder stream is set within the many features of the powder feeder. Feeder systems mainly consist of following parts:

- Stirrer
- Damper
- Vent tube
- Metering disk

The stirrer motor and stirrer are used to maintain powder movement. The adjustable damper regulates the powder feed, while the vent tube equalizes the pressure of the metering disk housing. The metering disk itself, with spreader and suction bars, is used to distribute the powder evenly within the disk groove and to exhaust the powder to the spray gun (Figure 14).

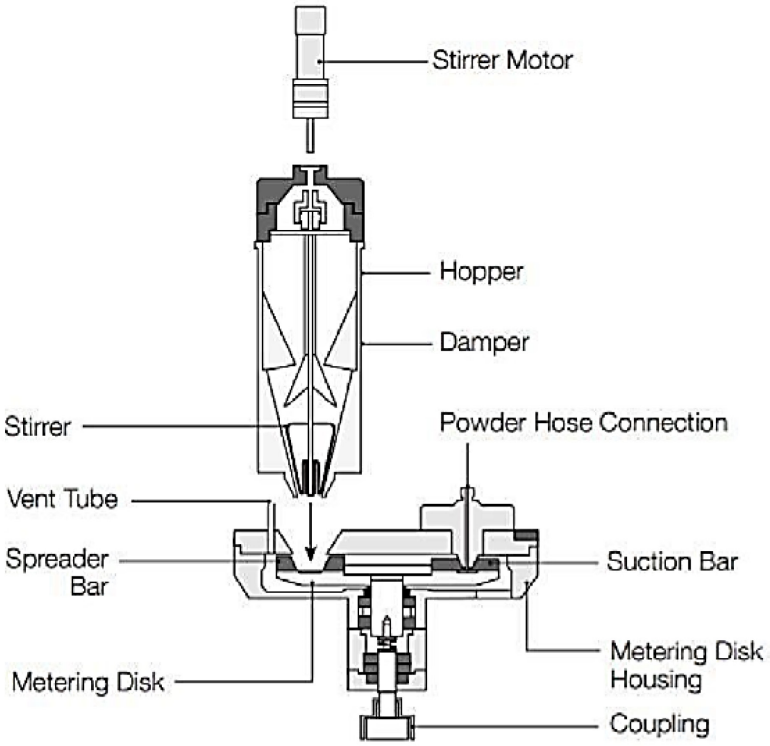

Figure 14. Schematic diagram of a powder feeding system for laser cladding [204].

2.3.1.3.Nozzles

An appropriate nozzle design is the one that provides the minimum distortion of the solid particles per solid surfaces and increases the powder catchment efficiency [205]. In laser cladding through powder injection, the powder delivery nozzles perform in two different configurations: coaxial and lateral. A coaxial nozzle design is more popular due to its independence from the direction of motion; however, experimental work has shown that its powder delivery efficiency, which is the ratio between the deposited powder on the substrate and the delivered powder by the powder feeder within a specified period, is

significantly less than the lateral nozzle design [206]. The major advantage of coaxial powder injection, in comparison to the off-axis powder injection system, is the potential for 3D cladding applications [207].

2.3.1.4.Positioning devices

Positioning devices assist the laser cladding process through translation of a model of the desired part into mechanical work. A previously generated ‘solid’ model is sliced by an appropriate Computer aided manufacturing (CAM) software based on the trajectory planning algorithm, in order to identify the required paths to allow fabrication of the part. Optimal positioning allows enough workspace and maneuverability for the required paths to be followed and determines the appropriate velocity, which is a major process parameter. The positioning device can be a computer numerical control (CNC) table or a robot manipulator with multiple degrees of freedom. The relative velocity and its accuracy are a general input parameter of the positioning devices, which are usually selected based on the size and type of the related process applications. Figure 15 presents the cladding head attached to the robot manipulation system, which was used for a study on the recommended laser-based repair procedures for the worn surfaces of main bearings and crankpin journals in marine diesel engines, as well as for damaged crankshafts (Figure 15).

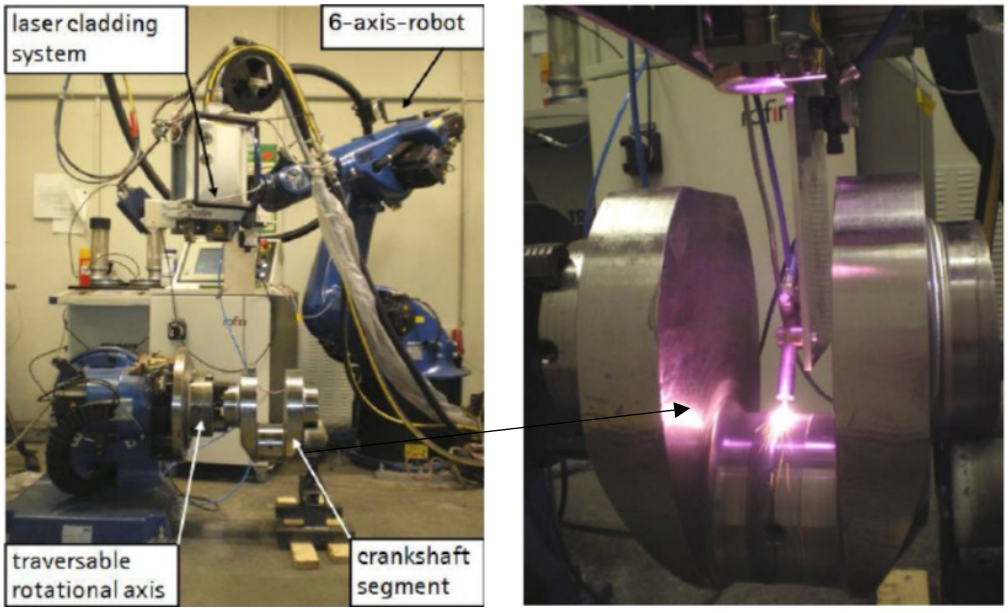

Figure 15. Laser cladding of a crankshaft segment and laser cladding head attached to a robot manipulation system [208].

2.3.1.5.Programming and software

There are number numerical and analytical models proposed for laser cladding that considers heat transfer, melting and crystallization kinetics of the melt pool in relation to processing parameters such as mass feed rate, laser power, and the associated scanning velocity [209–211]. Steady state models are independent of time and simulate key physical reactions (i.e., thermal conduction, thermocapillary, etc.) in relation to the processing parameters. These parameters play an important role in determining the profile of the clad, bonding of the clad to the substrate, compositional dilution, homogeneity of layers, surface finish, defects, etc. However, it is not possible to identify the effects of each parameter on

the characteristics of the final clad but, in general, several constraints are quantified simultaneously to obtain the desired features of the clad layer. The state of the powder when it arrives on the substrate surface was observed in a study on relevant parameters for process control on laser cladding [212]. It was suggested that the particle should be hot enough to adhere to the surface, but not too hot to result in vaporization, followed by ionization and plasma formation. Therefore, the amount of the available energy per unit length of clad, per unit mass of powder, and the time of their interaction are key factors in controlling the state of the powder. These characteristics can be controlled through associated parameters such as the powder mass flow rate and the CNC table traverse speed. There are number of modelling techniques that have been submitted by various researchers for the optimization of such dynamic processes, along with their related process parameters.

While steady state and reported dynamic models do not seem to satisfy the long list of considerations of the various available processing parameters, a lumped model can offer a simplification that can transform complex differential equations to a balance of energy within the process [174]:

Equation 4

$$\boldsymbol{Q_c = Q_1 - Q_{\mathrm{rs}} - Q_{\mathrm{L}} + (n-1)Q_{\mathrm{p}} - Q_{\mathrm{rp}} - Q_{radiation} - Q_{convection}}$$

where Q_c is the total energy that is absorbed by the substrate [J], Q_1 is laser energy [J], Q_{rs} is reflected energy from substrate,16) [is latent energy of fusion [J], n is powder catchment efficiency, Q_p is energy absorbed by powder particles [J], Q_{rp} is reflected energy from

powder particles [J], $Q_{radiation}$ is energy loss due to radiation [J], and $Q_{convection}$ is energy loss due to convection [J] (Figure 16)[174].

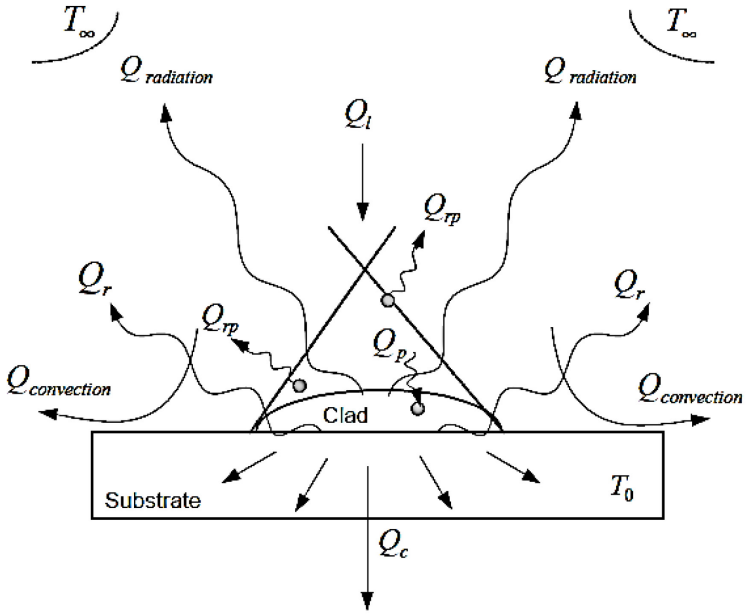

Figure 16. Balance of energy in laser cladding by powder injection [170].

2.3.2. Kinetics of laser cladding

In laser cladding, the substrate absorbs a significant part of the energy that is applied from the moving laser beam (which has a Gaussian distribution intensity). This energy generates a melt pool which ultimately contains powder particles (in the case of powder injection), which also carry part of the energy that has been applied by the laser beam. The heat profile

at time $t = 0$ for a moving laser beam with general strike distribution is described from the literature by the means of heat conduction (Equation 5) [174,213], following:

Equation 5

$$\frac{\partial(pc_pT)}{\partial t} + \nabla.\left(pc_pUT\right) - \nabla.(K\nabla T) = Q$$

where Q represents the power generation per unit volume of substrate [W/m^3], K represents the thermal conductivity [W/m·K], c_p is referred to as specific heat capacity [J/kg·K], ρ represents density [kg/m^3], t is time [s], and U is referred to the travel velocity of the workpiece (i.e., process speed) [m/s].

The dynamics of the melt pool are then further driven by surface tension and the flow of the fluid (i.e., melt) within the surface of the substrate, which is characterized by heat/mass transfer and the momentum of added particles, based on the equation of momentum and the Newton's second law for fluid flow.

2.3.3. Applications of laser processing

Laser beam cladding is an industrially unique process within the field of aero engine and gas turbine repair. Cladding is also a convenient technology for repair and *in situ* modification of design in the tool and die industry. Lightweight, highly stress resistant protective coatings for automobiles and a variety of tools have been widely implemented in production [214]. More recently, laser development focus has been invested in application of the laser technology towards machine tool and manufacturing processes

[174,214]. The new fiber lasers, which are generally distinguished by an extremely high-beam quality, the possibility of rapid beam oscillation, very compact size, uncomplicated adjustability, and moderate costs [215–218]. The current stage of laser cladding technology implementation primarily serves the industries of coating, repair, and rapid prototyping.

With this in mind, the primary applications of laser cladding are for the deposition of wear and corrosion resistance coatings. Laser cladding provides an environmentally friendly alternative to hard chromium plating, as it generates no harmful substances (unlike hexavalent chromium) and provides a wear-protection process that offers controlled adhesion and high-speed coating abilities.

Laser cladding is particularly suitable for the coating of rotating parts, such as crank shafts, cover axles, gear flank, bearings, shafts, tubes, wheels, extrusion screws, etc. and can significantly multiply the operational lifetime of wear resistant parts (Figure 17). Some high-speed installations can apply coatings on components up to 10 m in size and 3500 kg weight, and with diameters of 120 mm.

and this cost is largely elevated by the operational down time needed for the replacement of the damaged gears. It has been shown that laser cladding is highly effective in extending the operating lifetime of these parts, by improving their wear resistance properties.

The heavy-duty gears, which undergo severe abrasive wear, is another large filed where coating through laser cladding is utilized. The replacement of failed gears is usually costly, and the application of a laser clad coating layer that exhibits a fine microstructure and small crystal size, arising from the ultra-rapid kinetics of solidification during the clad process [219].

Figure 17. Pet-food granulate extrusion screws, coated with laser cladding, extended lifetime by ~300% [219].

Improvement of wear properties also arises for titanium alloys, in comparison to traditional/advanced spraying techniques. Titanium alloys are widely used as structural components in the aerospace, chemical, petrochemical, and marine industries, owing to their low density, high specific strength, and exceptional corrosion resistance [174,220]. Laser cladding offers *in situ* repair of high value components such as turbine blades, specialty tools, gas turbine parts, and the component of internal combustion engines [221]. Ultra-high strength steels materials, which are widely used in modern aircraft structures, are highly sensitive to damage caused by corrosion, fatigue, and associated stress corrosion cracking.

This type of damage, in applications with geometrically optimized components, is usually followed by costly replacement of the parts. In such cases, laser cladding has been applied to rebuild material through 'grind-out', with the mechanical properties of the component subsequently restored, with special attention to its fatigue life that can qualify for the minimum safety level. One study proposed that rolling contact fatigue, amongst other mechanisms of wear, between railway tracks and train wheels, can be reduced and repaired by laser cladding using premium wear resistant alloys (i.e., nickel alloy, Stellite 6, maraging steel, and Hadfield steel) as a facing to a much cheaper rail material substrate [221].

The repair of atomizer shafts used in electric power generation, hollow shafts, rotating equipment for the dredging industry, and low-pressure turbine blades for the power industry, are other excellent examples of the repair applications that are made possible by laser cladding (Figure 18) [222–224].

Rapid prototyping and manufacturing (RP&M) have emerged in recent years using several laser processing techniques including stereolithography, laminated object manufacturing (LOM), ballistic particle manufacturing (BPM), selective laser sintering (SLS), fused deposition manufacturing (FDM), and three-dimensional printing (3D printing) [225]. Rapid prototyping was initially used for the fabrication of prototypes made from polymers as communication and inspection tools and functional prototypes made from polymers is already well established in the market [214,226].

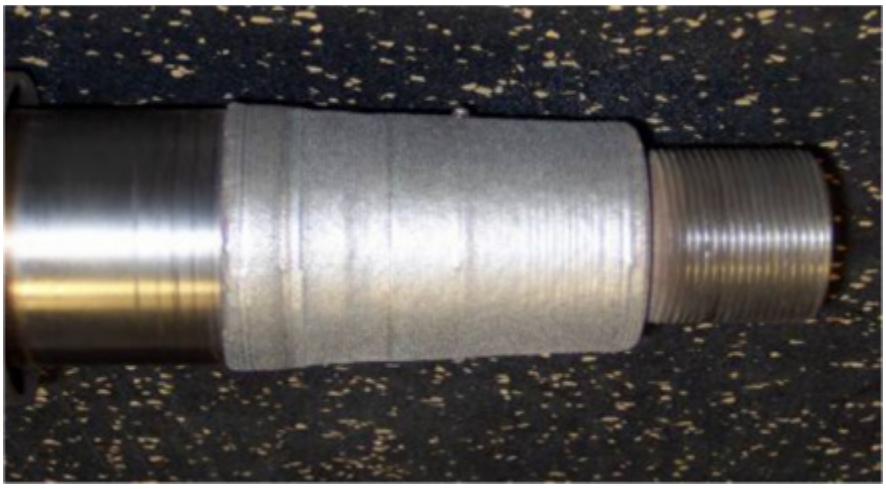

Figure 18. Atomizer shaft with laser cladding deposit [220]

In more recent year rapid prototyping has been used widely for the fabrication of molds and dies by additive and rapid manufacturing, which eliminates the need for most prototype and production tooling. Both metallic and non-metallic rapid prototyping has been attempted using laser deposition technologies. Available approaches in the marketplace for the purpose of the rapid prototyping utilize plastics and non–functional materials to create parts. Laser based systems for rapid prototyping have been introduced as a suitable technology for the creation of functional, near-net shape metal prototypes. A current focus of attention for research topics in the field of rapid prototyping is related to the cost-effective production of parts with consistent geometry and mechanical properties, but at large scale. A number of companies, including Texas Instruments, Inc., Chrysler Corporation, Inc., and Ford Motor Co. have reported the use of rapid prototyping to improve their product development in design engineering manufacturing and marketing aspects [225]. Additionally, rapid prototyping is a promising and powerful technology in

the field of medical science, offering the benefits of prototypes built from functional materials in relatively short periods of time. Although the use of rapid prototyping for medical applications is still at a relatively early stage, the technology has already made impressive strides. Prototyping through laser processing has been already implemented in orthopedic surgery, maxillo-facial and dental reconstruction, the preparation of scaffolds for tissue engineering, and as educational tool in fields as diverse as obstetrics and gynecology, and from forensic medicines to plastic surgery [227].

2.3.4. Material design and feed stock processing

With the rapid advancement of cermet coatings processed using laser cladding, and closely related research activities over past three decades, a wide range of materials have been investigated, including assorted metals, ceramics, glasses, intermetallics, and composite systems [181,185,189,192,199,228–231]. Alloy systems that have been investigated include those based on Ni, Co, Nb, and Ti, along with a range of steel grades. This research in general investigate the basic physical metallurgy applied to laser cladding for each specific material/substrate and the relevant solidification conditions of the cladding process. The phrase ‘clad-ability’ is used to define the viability of the cladding material and the substrate of interest in the “formation of a continuous, high density clad deposit with a uniform or homogeneous microstructure, possessing a strong metallurgical bond to the substrate but with low/specific levels of dilution” [174]. Many studies have shown that the clad-ability of various materials can be determined by identifying the parameters that are used during the cladding process and the chemical interactions of the clad and substrate

materials. Therefore, incompatibility between the substrate and clad material can inhibit the formation of a strong bond between the substrate and the clad material, in which case clad-ability will be nonexistent. The melt pool created by the energy from the laser beam during laser cladding of a powder feedstock onto a substrate, melts a small volume of the substrate itself. Depending on the melting point of the feed powder and the temperature of the melt pool, cladding material can exist in the form of molten droplets or solid particles. Consequently, it is more likely to observe both liquid and solid powder particles in the melt pool surface. Temperature gradients of these surfaces is then generally explained in the literature through the existence of intense convection between the two material systems in relation to the Marangoni effect (mass transfer along an interface between two fluids which can be characterized by the measurements of the surface tension) [232].

Considering laser cladding as a rapid and localized alloying process, arising between the clad material and substrate, typically with dissimilar melting points, the systems of cladding couples generally fit into one of the following three categories of alloying systems:

1. **Eutectic Cladding Process**
2. **Isomorphous Cladding Process**
3. **Complex Multi-Component Alloy Systems**

In **eutectic binary alloy systems,** the melting point of the melt pool is reduced in comparison to the melting point of the pure constituents, due to alloying action and melting of the substrate/clad by compositional dissolution of the constituents within the molten

pool. This reduces the laser beam energy that is required during cladding and, as a result, can increase clad-ability.

In **isomorphous binary alloy systems**, the consequence of alloying at the melting point is very different than in a eutectic system and can result in two distinct scenarios. If the substrate is made of the higher melting point component, the alloying process will result in melting of the substrate interface, by reducing its melting point, and its compositional dissolution into the molten pool. However, this also results in an increase of the melting point for the clad feed and a necessary increase in processing parameters, such as the laser power. If the substrate material has melting temperature lower than the clad feedstock, the alloying will cause an increase in melting temperature of the substrate interface with the melt pool. In this case the requirement for a melt pool with higher temperature usually results in undesired melting of the substrate and higher levels of dilution.

Major industrial applications of laser cladding contain **complex, multi-component alloy systems** in order to produce a hard, wear-resistant coating on a softer and more ductile substrate. Moreover, large temperature gradients between the cladding components are necessary to acquire low solubility which can lead to difficulties in controlling the degree of dilution. Among complex multi-component alloy systems, titanium alloys have broad applications in areas such as aerospace, marine environments, the chemical industry, and biomedicine. As an example, the alloy Ti-6Al-4V has been widely used to produce orthopedic implant materials owing to its superior mechanical and oxidation properties. However, titanium alloys are also known for their poor tribological behavior under severe wear and friction conditions [233,234]. Subsequently, although titanium alloys have been commonly analyzed for the design of medical implants, some researchers have shown that

titanium alloys are subjected to failure due to corrosion-fatigue within the specific environment of body fluids. Further classification of the material couples for the purpose of laser cladding is generally related to the dynamics of solidification. Factors such as mechanical strength, thermal expansion, and the texture of the solidified microstructure are usually characterized in relation to the solidification dynamics of each material within the clad couple. These couples are classified as two main groups: high temperature alloys, and metal-ceramic composites.

High temperature alloys in modern laser cladding are usually Ni, Co, or Fe-based, with smaller amounts of W and/or Mo, as well as C, which promotes formation of metal carbides with the alloy ingredients. In this case, the substrate is generally composed of less expensive low carbon or low alloy steels [199,235–238]. However, it has been reported that the presence of metal carbides and intermetallic compounds can result in hot and/or cold cracking and requires pre- and post-heat treatment through the cladding process [239]. Development of desirable hard and wear resistant surfaces, as a primary intention in laser cladding, has led to an increasing rate of research effort in the exploration of composite systems [174,192,230,240,241]. In the study of metal-ceramic composites for the purpose of laser cladding, the primary objective has focused on limiting the reaction between the ceramic particles and the metallic melt pool. TiC and SiC have been found to offer minimum reaction rates between the ceramic constituents and the molten pool, when used with Al and Ni, respectively [241–243]. In some cases, it has been observed that the reaction between the hard phase and the melt pool can be beneficial to some extent. In this scenario the ceramic phase or added elemental powders such as Mo, Si, C, Zr, and/or Ti, dissolve into the molten pool to form fine particles (e.g., $MoSi_2$, SiC, ZrC, and/or TiC),

that are well bonded to the matrix [241,242,244,245]. In recent years, TiC-based coatings processed by laser cladding have received researchers' attention.

2.3.4.1. Gelation based feedstock technologies.

The earliest developments in processing of ceramics through colloidal routes dates back to 3500 BC, which mainly involved clay-based pottery [246,247]. Later advancement of this approach led to a number of forming methods, such as slip casting, extrusion, filter pressing, and tape casting. Many research activities have focused on understanding the behavior of clay-based systems and characterizing ceramic crystal structures. Clay-based ceramics have an inherently plastic nature, with an aggregated particle network, which provides appreciable yield stress and excellent shape-forming capabilities. Unlike clay-based systems, most ceramic suspensions that serve as feedstock are required to be engineered into a plastic system by incorporating them with organic processing additives, such as polymers and plasticizers. This class of materials can modify the rheological behavior and impart handling strength to 'as-formed' ceramic bodies [248]. Gelation approaches for powder synthesis have the potential to be less expensive and more environmentally friendly but, such systems can only be utilized from a stable (i.e., agglomeration-free), monodisperse colloidal suspensions, with the consequent capability to produce the desired degree of microstructural homogeneity that is required for functional ceramics. Studies have reported that these systems usually lack the desired plasticity, while the manufacture of monomodal particle size is almost impossible [249,250]. Further challenges for these systems have been consequently related to the presence of undissolved

organics of various species within the mixtures and their related decomposition reactions, which can generate defects during subsequent binder removal [247,248,250–252]. Theoretically, colloidal stability can be achieved through careful control of interparticle forces such as the interparticle potential energy, electrostatic forces, stearic forces, and depletion forces. The rheological behavior of such colloidal dispersions is among the most important properties. Rheological measurements are frequently used to observe changes in flow behavior in response to an applied stress or strain. For suspensions of novel composition with unknown rheological behavior, the viscoelastic properties, solids loading capacity, apparent viscosity, and yield stress under shear and compression, can be obtained from simultaneous rheological experiments. This information can thus be effectively used for the design of a specific forming method to be used during ceramics processing. With this in mind, the rheological characterization of TiC based cermet feedstocks within the proposed thesis has been provided in detail.

Sodium alginate is a naturally occurring polymer chain, derived from brown seaweed, and used to increase viscosity and/or form gels used in the food and medical industries [253]. The viscosity of sodium alginate solution is determined by both the concentration and the alginate chain length. The gelation phenomena in sodium alginate rises from α-L-guluronate (G) sections that are chained together on into groups the alginate polymer backbone, known as G blocks [254–258]. When sodium alginate is hydrated, it dissociates into free Na^+ ions and alginic acid. Exposure of alginic acid to divalent or trivalent cations results in bonding of the G blocks and form a box around 3 sides of the cation typically referred to as the “egg-box” model [257,259]. At this stage molecules of alginic acid can

be drawn to and bond with the cation. A schematic representation of this model is presented in Figure 19 [260].

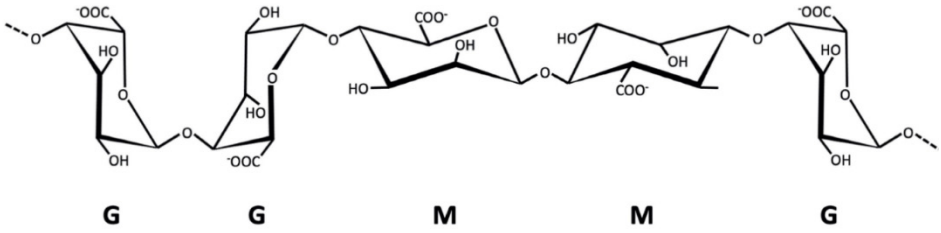

Figure 19. Physical characteristics of chain conformation in alginates.

Gelling agents for alginate generally fall into one of two categories: (i) acid gelation, and (ii) divalent (or trivalent) cation generated polymer cross linking. Gelation can be induced at low and high pHs, and through introduction of organic solvents [255]. Such conditions cause the alginate molecules to denature, forcing the polymer chains to bend and entangle with one another, yielding gelation. This mechanism is less stable than gelation produced through chelation, and as such gelled material will readily degrade when returned to a neutral pH. Acid gelation does not produce a permanent gelled structure, but rather, when acid gelled particles are rinsed with water, the alginate returns to its original state of a long straight polymer chain, and de-binds. By contrast, in chelation, the polymer chains bind to divalent or trivalent cations, crosslinking and creating a gel. This is considerably more stable than acid stabilization and can be washed with deionised water without degradation. Calcium chloride ($CaCl_2$) is the standard chelating agent used in the gelation of most

solutions [254,255,258,261–264], as it is low-cost, highly soluble, chemically stable, and reacts quickly with alginate.

2.3.5. Characterization and analytical methods

Characterization of the clad layer has been studied through microstructural, chemical, and physical analysis of the surfaces subjected to wear, corrosion, range of stress, indentation etc. Measurements of the clad height and its microstructure along the substrate offer valuable information such as roughness of the clad deposit and evaluation of the clad bead quality. Although the mechanical characteristics such as hardness, wear, and corrosion properties of the clad or post cladding substrate can be measured using number of instruments, the study of the microstructure and phase transformations of the cladding feedstock, clad layer, substrate, and its interface with clad layer, are reported as being the most useful information in terms of the material design for specific cladding couples. The following diagnostic parameters for the clad/substrate couple have been reported with advanced microstructural analysis [5,265–271]:

- Dynamics of solidification
- Adherence
- Porosity
- Cracks
- The bonding zones.
- Heat affected zone.

- Presented phases.
- Particle distribution
- Particle size distribution
- Particle geometry
- Chemical composition
- The wear and corrosion mechanisms

Each of the above characterization approaches are possible via one or more types of microstructural analysis of the clad component. Scanning electron microscopy (SEM), transmission electron microscopy (TEM), orientation imaging microscopy (OIM), X-ray diffraction (XRD), optical microscopy (OM), energy dispersive X-ray spectroscopy (EDS), electron backscattered diffraction (EBSD), and electron probe microanalysis (EPMA), are common techniques that are regularly applied in such materials analysis.

The microstructure and properties of laser clad coatings studied by OIM has shown that this technique combines the advantages of SEM observations with information about the crystal/grain orientation and solidification microstructure after laser processing. Using this approach, Ocelík et al. showed that formation of strong epitaxial growth of Co grains on the substrate does not depend on the laser beam scanning speed, based only on a transverse cut of a laser track [272]. They suggested that a longitudinal cross-section at the center of the laser track provides much more information concerning grain size, grain shape and the solidification texture of the coating microstructure formed during laser cladding, as shown in Figure 20 [272].

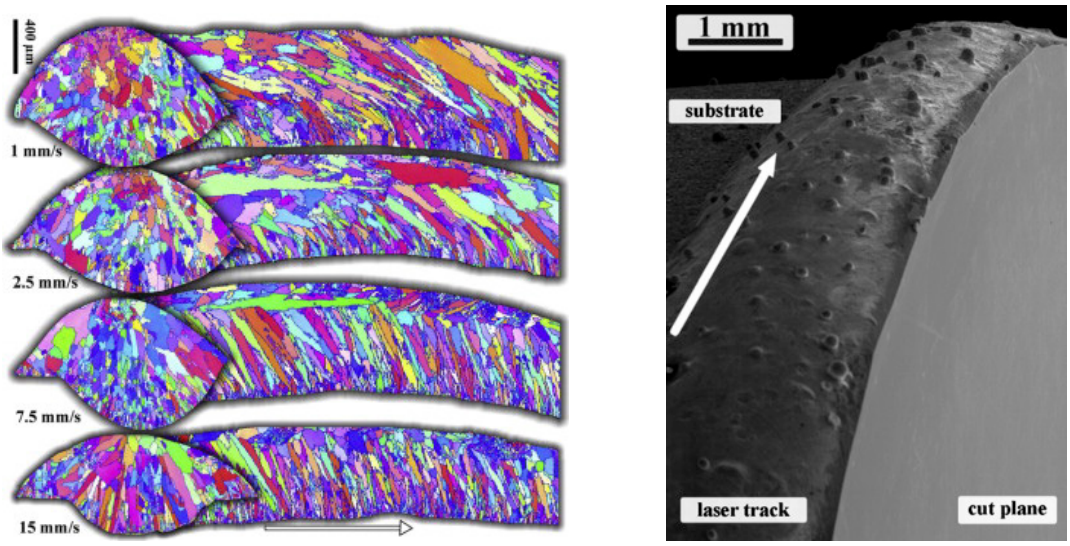

(a) (b)

Figure 20. a) Inverse pole figures with grain boundaries from transverse (left) and longitudinal (right) cuts across single laser tracks formed at four different laser cladding speeds. b) SEM image of a laser clad sample cut in the plane perpendicular to the substrate bar axis and almost parallel to the cladding direction [272].

Characterization of the solidification dynamics by studying the gradient microstructure is particularly feasible with SEM and TEM micrographs, as demonstrated in laser clad TiC-reinforced Ni-alloy composite coatings [273]. In this work, an increase in both the size and volume fraction of TiC particles was reported, along with a change in morphology from small, globular to coarse, flower-like clusters (Figure 21). The same study reported the growth of TiC particle size in relation to its location, which became less effective at higher scanning speeds of the laser beam.

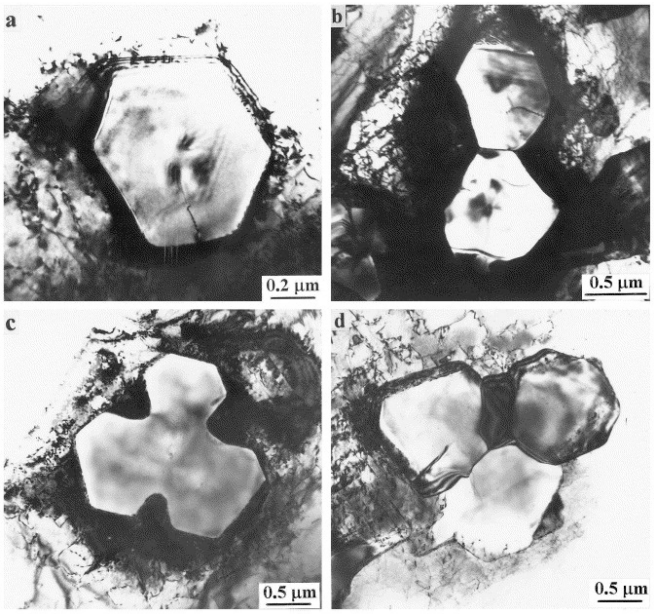

Figure 21. TEM micrographs showing the growing features of TiC particles in different regions of the clad layer, processed at 2000 W laser power and 6 mm s^{-1} scanning speed: (a) at bottom; (b) at lower part; (c) at intermediate part; (d) at upper part [273].

The effect of processing parameters on the quality of the clad is generally explained by its solidification and the represented phase microstructure. Chiang et al reported the presence of dendrites, inter-dendritic eutectics, faceted dendrites, and the retaining of WC particles (Figure 22), in the laser clads of Stellite12 plus WC, using a combination of SEM, EPMA, and EDX. They stated that an increase in laser energy density may result in a decrease of the Co, Cr, and/or W contents of the dendrites, and an increased dilution of Fe [274].

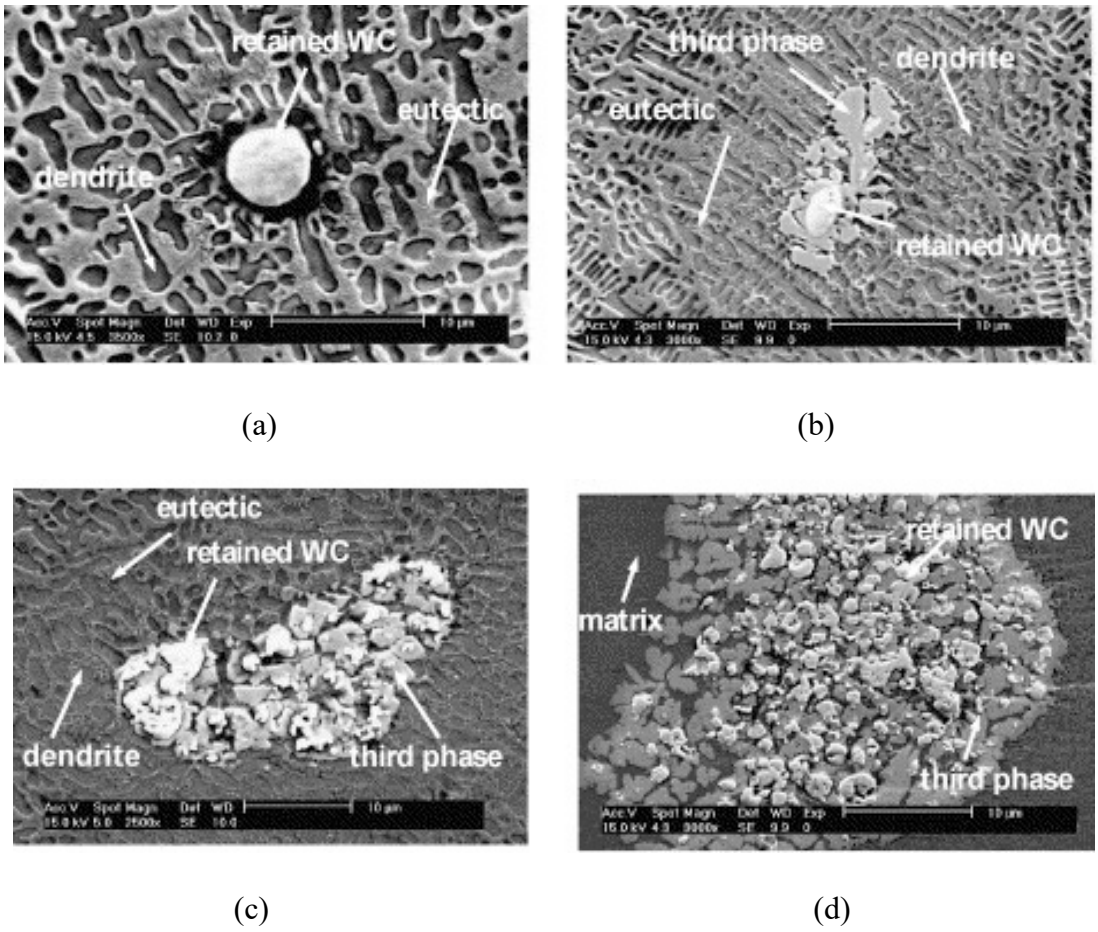

Figure 22. SEM micrographs showing the microstructure of the laser clad 90% Stellite12 plus 10% WC (wt.%) alloy coating obtained at: (a) 28.65 J/mm^2, (b) 38.20 J/mm^2, (c) 45.84 J/mm^2, and (d) 50.93 J/mm^2[274].

2.4. Summary

Selection of deposition techniques including thermal spray and laser cladding has been investigated for fabrication of hard TiC based coatings for applications with extensive wear and/or corrosion requirements. Thermal spraying is a well-established technique used in

deposition of wear and corrosion resistant coatings that have the capability of depositing a wide spectrum of feedstock materials with diverse chemistries such as metals, ceramics, alloys, and ceramic metal composites. In thermal spraying the mass of the feed powder encounters a temperature cycle within an allocated period, namely known as the dwell time. As a result, the particles of the feedstock material are melted (or partially melted) and sprayed by a stream of pressurized gas onto the surface of a prepared substrate. Thermal spray processes are further classified into plasma arc, electric arc, kinetic, and flame-based processes. High velocity oxy fuel (HVOF), with a flame as the heat source, have been used to process carbide with low residual stress, high hardness and bond strength, and a lower volume of porosity among the outlined methods.

Rapid development of lasers with higher power and more advanced wavelength, pulse duration, and beam format, have resulted in advancements of laser processing in recent years. Research efforts have focused on understanding the interaction of the laser beam with the processed material(s), the role of process parameters, the dynamics of non-equilibrium process solidification, microstructural development, and modelling of the process. Today, synthesis of nonequilibrium metallic phases is possible due to the inherent rapid heating/cooling rates arising in laser processing, which cannot be rivalled by other processes.

Most of the laser surface processes, such as laser surface melting (LSM), laser-supported absorption (LSA), laser cutting system (LCS), laser surface cladding (LSC), and laser shock processing (LSP), have shown significant improvement in mechanical properties (i.e., corrosion, wear, fatigue, etc.) of the substrate. Currently, laser cladding competes commercially against several major coating techniques, such as welding, thermal spray,

chemical vapor deposition (CVD), and physical vapor deposition (PVD). However, the high initial and maintenance costs of laser systems prevent them from rapid commercialization via industrial manufacturing. Newer generations of high-power lasers, with high efficiency and low maintenance requirements, are expected to overcome this issue to some extent.

Chapter 3. Gelation-based feed-stock technologies for HVOF thermal spray development: Micro-composite powder preparation and HVOF coating microstructure

Z. Russell[a] , W.A. Sparling[a], T.L. Stewart[a], P. Gray [a], M. Gaier [a], M.J. Froning [c], G. Mazzanti[b,*], K.P. Plucknett [a,*]
[a] Department of Mechanical Engineering, Dalhousie University, 1360 Barrington Street, Halifax, Nova Scotia, Canada (*kevin.plucknett@dal.ca)
[b] Department of Process Engineering and Applied Science, Dalhousie University, 1360 Barrington Street, Halifax, Nova Scotia, Canada (*Gianfranco.Mazzanti@dal.ca)
[c] Boeing Research & Technology, Seattle, USA

Keywords: Sodium alginate, Thermal spray, High velocity oxyfuel, Scanning electron microscopy, Powder metallurgy, Cermets

Abstract

The current study proposes use of the polysaccharide, sodium alginate, as a gelation aid to 'solidify' aqueous suspensions, comprised of micron-sized ceramic-metal particles, into spherical, micro-composite 'cermet' feedstock powders. These feedstock powders, with finely divided ceramic and metallic components, can then be used for the preparation of high velocity oxygen fuel coatings and/or laser deposition cladding. Sodium alginate gelation is typically based on ion exchange, and a variety of gelation agents have been examined in the present work. It is shown that aqueous solutions of CaCl2, Ca-acetate, Al-nitrate, methanol, acetic acid, and 5 % HCl acid are all capable of gelling alginate droplets through a simple cross-linking mechanism. Consequently, spraying a sodium alginate containing ceramic-metal particle suspension, with a suitable air atomizing nozzle, into an aqueous bath of one of the outlined solutions allows the production of nominally spherical 'cermet' feedstock particles. In the present work, TiC-Ni_3Al micro-composite cermet particles have been successfully produced, and then analyzed both before and after a sintering heat-treatment. Furthermore, rheological assessment of the colloidal suspensions

both prior to and during the gelling stage are also described. As a preliminary 'proof-of principle', an initial set of HVOF coatings has also been prepared using the gelled feedstock material, and initial characterization of these coatings is presented.

3.1. Introduction

High velocity oxygen fuel (HVOF) spraying allows for dense coatings to be quickly applied to a wide variety of surfaces. HVOF is used in many industries to produce wear resistant and/or thermal barrier coatings, with the most commonly applied ceramic-metal (cermet) systems being WC-Co and WC-CoCr [275–278], which are often used as replacements for hard chromium plating. To achieve dense, consistent quality coatings, the feedstock powder for HVOF systems must be tightly controlled. A mono-modal, narrow particle size distribution, typically in the 15–40 μm size range, and particles with a spherical morphology are preferable for HVOF, in order to reduce gun clogging during spraying. Furthermore, spherical particles have also been demonstrated to improve flight within the HVOF process gas stream. These criteria help to achieve fully dense coatings, and to reduce inconsistent feed rates, which can lead to variation in coating thicknesses [275–278]. Therefore, the powder production for HVOF applications is often lengthy, costly, and thermally intensive. In simple cases, such as in pure and low alloy content metals, such powders can be produced through inert gas atomisation. However, due to the dispersoid nature of cermets, and the differences in density which normally exist between the metal and ceramic phases, inert gas atomisation is difficult to apply. Instead, operations such as the melt spinning, spray dried agglomeration, or metallic coating of ceramic

particles are employed [275–277], requiring a large initial investment, with a long and energy intensive production path. Therefore, a refined microstructure can be difficult to achieve, although several studies have shown the mechanical benefits of retaining a finely dispersed small ceramic phase [276,277]. Such fine-scale structures can be achieved through approaches such as mechanical alloying [246], whereby even nano-sized ceramic particles can be incorporated into a metallic matrix for each individual particle, with the subsequent potential to create a nano-structured feedstock. The challenge with that approach is then to scale up the overall process to the level needed for production. Consequently, there is still a considerable incentive to find alternative feedstock production techniques for thermal spray. The earliest developments in processing of ceramics by colloidal routes date back to 3500 BCE, which mainly involved clay-based pottery [246,247]. Later advancement of this approach leads to a number of forming methods such as slip casting, extrusion, filter pressing, and dry pressing. Unlike clay-based systems, most ceramic suspensions need to be engineered into a fluid or plastic/paste system through pH control and/or by incorporating organic processing additives. These additives can include dispersants, binders, and plasticizers, and they modify the rheological behavior and impart handling strength to as-formed ceramic bodies and particles [248]. A disadvantage of this approach is that often a binder removal stage is needed. As an alternative, gelation approaches for suspension processing have the potential to be less expensive and more environmentally friendly. However, if the aim is to produce spherical, micro-composite type particles, such systems need to initially be in the form of stable (i.e., no agglomeration), monodisperse colloidal suspensions. There is then the capability to produce the desired degree of microstructural homogeneity that is invariably required for

structural and functional ceramics. It has been reported that these systems usually lack the desired plasticity without suitable process control. Additionally, manufacture of monomodal particle size is almost impossible, and in fact multi-modal powder distributions are often favored [249,250]. Further challenges for these systems have included the presence of undissolved organics of various species within the mixtures and its related uncontrolled decomposition reactions which generate defects during binder removal [247,248,250–252]. Colloidal stability itself can typically be achieved through careful control of interparticle forces, for example through electrostatic, steric, or electrostatic stabilization. The associated rheological behavior of these colloidal dispersions is then a critically important characteristic for subsequent processing approaches.

In considering approaches for gelation processing of suspensions, sodium alginate is a naturally occurring polysaccharide, derived from brown seaweed, and often used to increase viscosity and/or form gels used in the food and medical industries [253]. The gelation mechanism of alginate also works in favour of being able to produce fine spherical gelled particles. It has also already been used in the production of spherical zirconia and silicon nitride particles [12–16], utilising an ion exchange mechanism for gelation, and also for processing SiC bulk ceramics. The viscosity of a sodium alginate solution is dependent on both the alginate chain length and concentration. The gelation mechanism in sodium alginate arises from α-L-guluronate (G) segments, chained together on the alginate polymer backbone into groups, referred to as G blocks [254–258]. When Sodium alginate is added to water, it dissociates into free Na^+ ions and alginic acid. If a molecule of alginic acid is exposed to divalent (or trivalent) cations, the G blocks in the polymer backbone will attempt to bond with the cation and bend the polymer backbone to form a ‘box’ around

three sides of the cation. Additional molecules of alginic acid can then be attracted to and bond with the cation. This gelation mechanism is typically referred to as the “egg-box” model, due to the visual similarity of the bent alginic acid polymer to an egg carton[254–258]. A schematic representation of the structure of the alginate components and this model are presented in Figure 23[260].

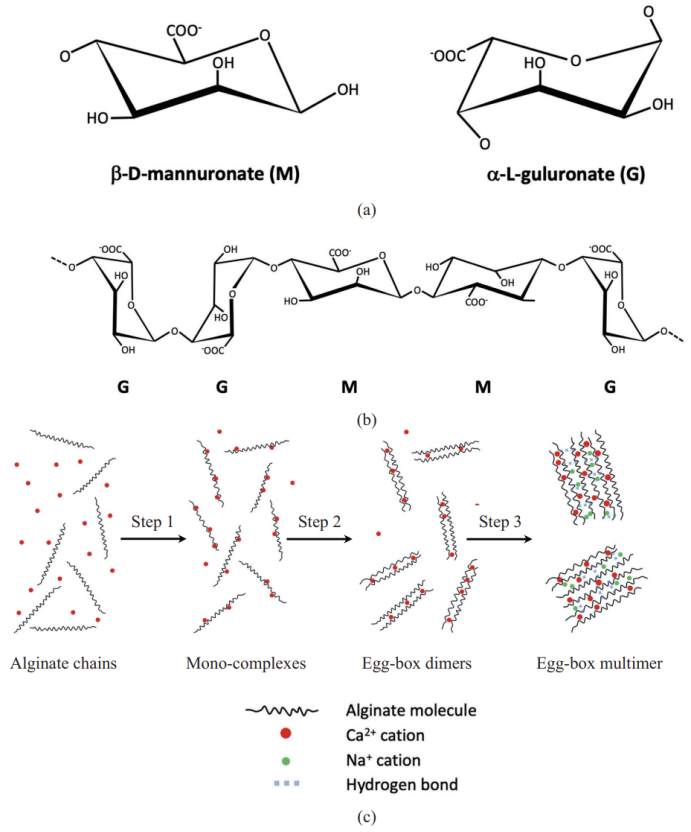

Figure 23. (a) Schematic representation of the structure of the mannonate and guluronate monomer units. (b) Alginate chain structure. (c) Schematic representation of the alginate ion exchange gelation mechanism. Figures adapted from [284].

This process of absorbing metal cations, termed chelation, has been used in the food industry to produce vitamin capsules, candies, and haute cuisine fruit and vegetable “caviar” [255,257,258], as well as in the medical industry for encapsulating bacterial

cultures, or producing cell culture substrates [254,256,257]. Gelling agents for alginate generally fall into one of two categories: (i) acid gelation, and (ii) divalent cation polymer cross-linking. Gelation can be induced at low and high pHs, and through introduction of organic solvents [255]. Such conditions cause the alginate molecules to denature, forcing the polymer chains to bend and entangle with one another, yielding gelation. This mechanism is less stable than gelation produced through chelation, and as such capsules will readily degrade when returned to a neutral pH. Acid gelation does not produce a permanent gelled structure, but rather, when acid gelled particles are rinsed with water, the alginate returns to its original state of a long straight polymer chain, and de-binds. By contrast, in chelation, the polymer chains bind to divalent or trivalent cations, crosslinking and creating a gel. This is considerably more stable than acid stabilization and can be washed with deionised water without degradation. Calcium chloride (CaCl2) is the standard chelating agent used in the gelation of most sodium alginate solutions [254,255,258,261–264], as it is low-cost, highly soluble, chemically stable, and reacts quickly with alginate. In the current study, these sodium alginate gelation approaches are utilised with the aim of producing nominally spherical, micro-composite powders that might be suitable for application in a variety of coating approaches, most notably high-velocity oxy fuel (HVOF) thermal spray, or potentially laser directed energy deposition cladding. A titanium carbide-nickel aluminide (TiC-Ni_3Al) cermet system has been selected for this assessment, based on prior work relating to bulk cermets of similar composition and, consequently, their known performance characteristics in terms of wear and corrosion [16,285–288]. The rheological responses of the aqueous suspensions have been assessed, including the development of a novel approach for dynamic evaluation of

the gelation process. Furthermore, suitable micro-composite particles have been manufactured using an air atomising nozzle system, and these have been successfully gelled. However, the desire to remove as much chlorine as possible has also led to several alternative gelation agents being assessed. Based on this study, preliminary TiC-Ni_3Al HVOF coatings have been prepared using optimised micro-composite powders made by such gelation technology; the wear and corrosion responses of these coatings will be discussed in a future publication.

3.2. Experimental procedures

3.2.1. Raw materials

The TiC powder (lot no. PL20126240; particle size of 1.0–2.0 μm) used in the present study was supplied by Pacific Particulate Materials Ltd. (Vancouver, BC, Canada). The 'Ni_3Al' component was produced through combination of Ni powder (lot no. L10W013; particle size of 2.2–3.0 μm) and an appropriate amount of Ni: Al (50:50 wt%) powder (lot nos. D28X029 and G19X071; each with D50 = 32 μm); both the Ni and Ni:Al powders were supplied by Alfa Aesar (Ward Hill, MA, USA).

The morphologies of the starting powders were subsequently determined using in a field emission gun scanning electron microscope (FEGSEM; model S-4700, Hitachi High Technologies, Tokyo, Japan), with example images presented in Figure 24. It is apparent that the TiC powder is quite angular, with both micron- and nano-sized components, including quite coarse particles, as noted previously [289]. The Ni powder is more equiaxed, but again has some angular surface features. In comparison, the Ni: Al raw

material exhibits a spherical morphology, with numerous satellite particles, that is typically seen for feedstock materials synthesised using a gas atomisation procedure.

The various gel forming agents were acquired from Alfa Aesar (Ward Hill, MA, USA) and/or Sigma-Aldrich (St. Louis, MO, USA) and were reagent grade quality; a summary of the chelating agents examined is provided in Table 5. Organic solvents were all acquired from Fisher Scientific and were of >99.6 wt% purity.

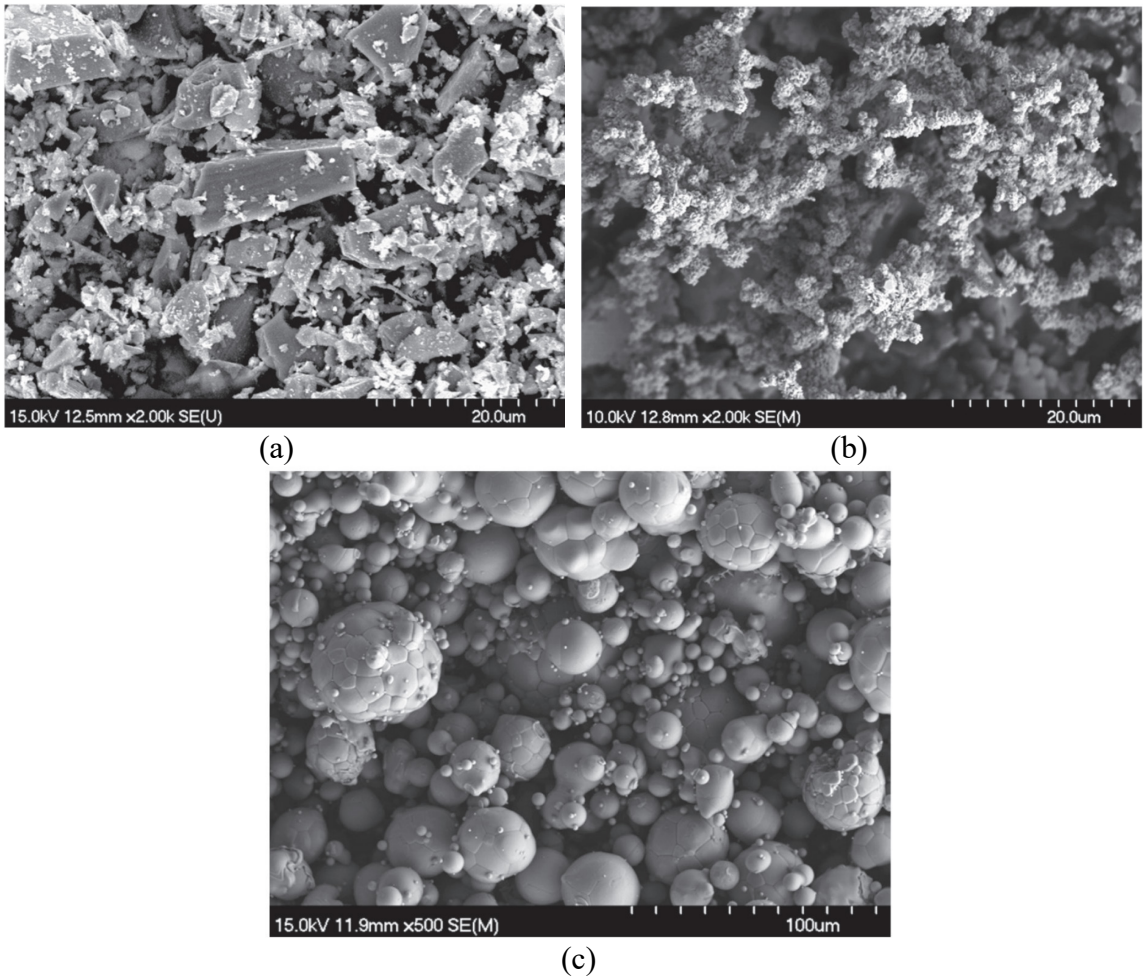

(a) (b)

(c)

Figure 24. Representative FEG-SEM images of the starting powders used for micro-composite particle preparation: (a) TiC, (b) Ni, and (c) Ni: Al.

Table 5. The various gelling agents employed in the present work, along with their initial qualitative performance in terms of particle morphology (droplets pipetted into the gelling agent solution).

Gelling agent	Chemical formula	Abbreviation used (if any)	Concentration	Droplet morphology after gelation
Calcium chloride	$CaCl_2$	$CaCl_2$	0.2 M	Spherical
Calcium acetate	$CaC_4H_6O_4$	Ca-acetate	0.2 M	
Aluminum nitrate	AlN_3O_9	Al-nitrate	0.2 M	
Hydrochloric acid	HCl	HCl	5 %	
Methanol	CH_4O	Methanol	100 %	
Acetic acid	CH_3COOH	Acetic acid	100 %	
Ethanol	C_2H_6O	Ethanol	100 %	
Calcium lactate	$CaC_6H_{10}O_6$	Ca-lactate	0.2 M	Donut/ 'Blood cell'
Isopropyl alcohol	C_3H_8O	IPA	100 %	
Aluminum nitrate	AlN_3O_9	Al-nitrate	0.13 M	
Nickel acetate	$NiC_4H_6O_4$	Ni-acetate	0.2 M	Splat

3.2.2. Preliminary gelation studies

Each of the chelating agents was compared on a molarity and normality basis to evaluate their efficacy. Preliminary investigations involving pipetting droplets of TiC/sodium alginate suspension into aqueous calcium chloride ($CaCl_2$) solutions of various

concentrations. It was observed that a $CaCl_2$ concentration of 3 g/100 ml produced qualitatively spherical particles, which corresponds to a molarity of 0.2 M (or a normality of 0.4 N). Lower concentrations yielded particles exhibited 'tails' or were donut shaped. Higher concentrations resulted in no significant improvement to shape retention, while at the same time increasing the Cl content. All Ca- and Ni-based chelating agents were compared as 0.2 M solutions. Two concentrations of aqueous aluminum nitrate ($Al(NO_3)_3$; henceforth abbreviated as Al-nitrate) solutions were prepared, one 0.2 M (0.6 N) and one at 0.13 M (0.4 N), to investigate whether the charge of the Al_3^+ ion improved gelation. As sodium alginate has been shown to gel in ethanol for culinary applications, alcohols of different chain lengths, along with acetic acid, were also investigated. These organic acids were examined as industrially pure solutions. A 5 % solution of hydrochloric acid (HCl) was also investigated as proof of concept. Solutions of the following compositions were consequently prepared: methanol, ethanol, isopropanol, acetic acid, HCl, $CaCl_2$, calcium acetate (C4H6CaO4; Ca-acetate), calcium lactate ($C_6H_{10}CaO_6$; Ca-lactate), nickel acetate ($C_4H_6NiO_4$; Ni-acetate), and Al-nitrate. For salt hydrates, the concentration of water was determined through thermogravimetric analysis (TGA; Model Q600 Simultaneous Differential Thermal Analyzer, TA Instruments, New Castle, DE, USA) and the concentrations were appropriately adjusted. 2.3. Suspension processing and micro-composite powder production Stable suspensions with an overall cermet composition of 70 vol% TiC with 30 vol% Ni_3Al, where the 'Ni_3Al' is actually comprised of Ni and Ni: Al (50:50 wt%), were created using a solution of 1.6 wt% sodium alginate and water. The sodium alginate solution was initially prepared through blending the alginate in water for 2 min and then degassing the solution. The suspension itself was prepared with 50 wt%

total solids (i. e., TiC and 'Ni_3Al'), with the pH adjusted to 8.5 using a solution of NaOH, and with 0.1 vol% Darvan® C-N added as a dispersant. This suspension stabilization formulation is adapted from a prior study [289]; the general development and mixing procedures for this aqueous suspension are described in detail in that previous work for the same TiC powder. The TiC-Ni_3Al/sodium alginate suspension was then homogenized and degassed, before being sprayed through an atomising nozzle into a water bath containing the gelling agent at a predetermined concentration. In terms of the production of micro-composite powders, the use of air assisted atomisation is an affordable and easily scalable technique for high volume production of micro-droplets, which can in turn be gelled using any number of gelation techniques. In the present work, a TurboTak (Waterloo, ON, Canada), air-assisted atomising nozzle (2 mm diameter) was used, which can finely atomize high-viscosity liquids or suspension by means of compressed air. All experiments were conducted at room temperature (23 ± 2 ◦C). The generated droplet sizes are controlled through simultaneous adjustment of the air pressure and liquid flow rates, as highlighted in Figure 25.

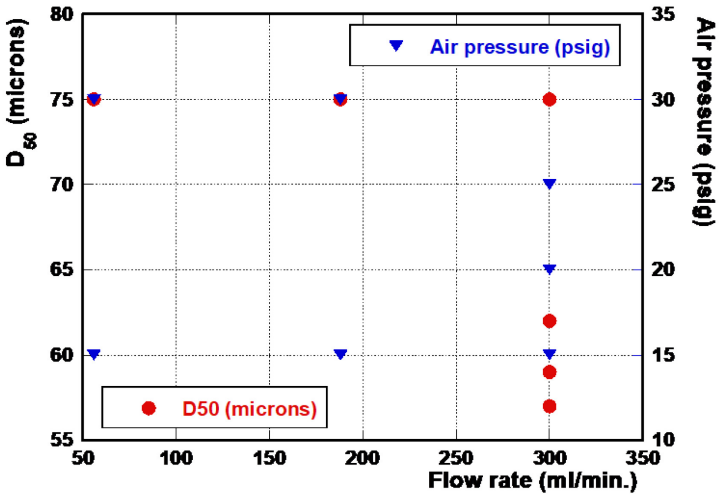

(a)

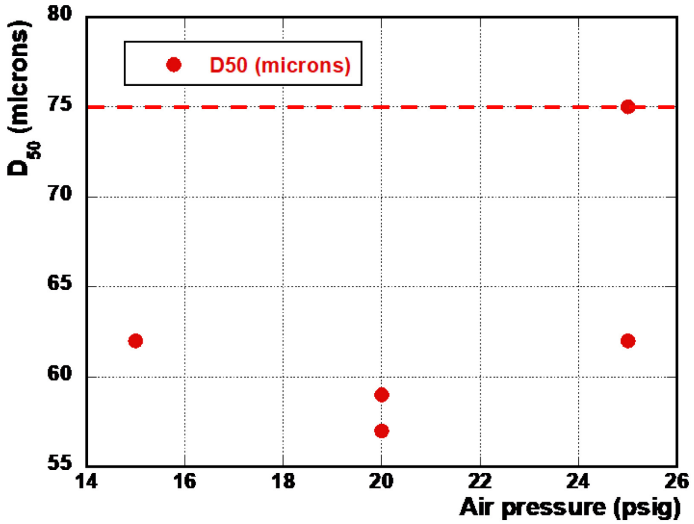

(b)

Figure 25. The generated cermet droplet sizes at simultaneous adjustment of the air pressure and liquid flow rates.

The nozzle itself is composed of a steel cylinder with radially drilled holes, allowing air to enter and disrupt the liquid stream. For the present work, the fine droplets generated from this turbulence are then ejected into a gelling bath; the distance of the nozzle to the bath was roughly 40 cm, and a peristaltic pump was used to pump the liquid. As in traditional gas atomisation techniques, the droplets fall and become more spherical due to the lowered energy associated with a reduced surface area-to volume ratio for a spherical morphology. They then contact the surface of the chelating agent bath and begin to gel; some slight deformation from ideally spherical might be anticipated at this point. A magnetic stir bar in the bath helps to prevent clumping of the particles during gelation but does not yield a significant reduction in inter-particle sticking during drying. The gelled particles were subsequently removed from the bath, rinsed with deionised water, collected using a vacuum filtration system, and then dried overnight in an oven held at 60 ◦C. After drying,

particle clumps were very gently broken apart using a mortar and pestle. Particle size distributions were subsequently measured using a Malvern Mastersizer 3000 (Malvern Panalytical, Malvern, UK). Analysis was performed without ultrasonic vibration so as not to damage the gelled particles. A flow chart of the overall micro-composite powder production process is presented in Figure 26. Simple micro-composite particle heat-treatment operations were also investigated within a differential scanning calorimeter (DSC)/thermogravimetric (TGA) system (model Q600 SDT, TA Instruments Inc., New Castle, DE, USA), to examine melting events and mass loss associated with the gelled particles during heating, and to determine if the mechanical integrity of the particles could be improved through sintering or partial metallic phase melting (which may also improve the powder flowability). These operations were performed with a heating rate of 20 °C/min, in and Ar atmosphere, to various hold temperatures. The micro-composite particles were subsequently examined in a field emission gun scanning electron microscope (FEG-SEM; model S-4700, Hitachi High Technologies, Tokyo, Japan). The micro composite particles were supported on electrically conducting silver paste for imaging in the FEG-SEM, both before and after sintering. Furthermore, cross-sectional imaging, both pre-/post-sintering, was conducted by mounting powders in epoxy resin, polishing, and then gold coating to better examine the degree of bonding within the micro-composite powder. Particle size distribution and chemical composition of the participating powders was analysed using inductively coupled plasma atomic emission spectroscopy (ICP-OES; model Thermo iCap 7400 Dual View, MA, USA), with an internal calibration standard (scandium). Powders were dissolved into solution by a near total acid leach digestion procedure (using HF, HNO_3, $HClO_4$, and HCl) before running on the ICP. Solutions were diluted 10x and up to

7,000x (for higher compositional content in order to keep the readings within the calibration range), in 5% HNO_3.

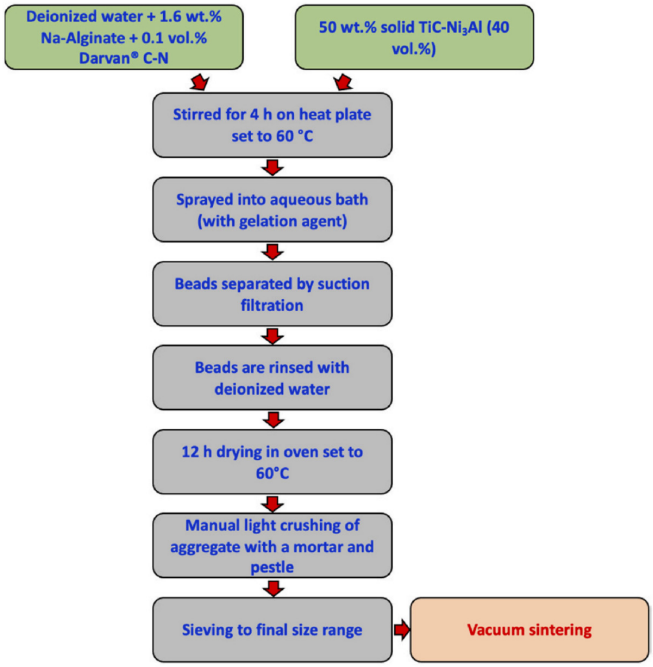

Figure 26. Simplified flowchart of the process applied to produce TiC-Ni_3Al micro-composite particles for HVOF thermal spraying.

3.3. Rheological Characterisation of Suspensions and Gelation Response

Flow and oscillatory rheometry tests (model AR-2000 Advanced Rheometer, TA Instruments, New Castle, DE, USA) were conducted on the cermet-alginate suspensions to characterize their viscoelastic behavior. The tests were done before and after the addition of the gelling agent. A 40 mm diameter parallel plate geometry was used for the rheometric study of the colloidal suspensions, prior to spraying, at 20 °C. The gap was re-zeroed for

each experiment. The upper side of the flat disk had a fixed water trap. A sampling cup with centering capability was specifically designed as an addition to the standard geometry (Figure 27). The inertia of the disk was calibrated with a volume of 1.0 ml of water added to the moisture trap. Liquid samples were introduced on to the plate and left to equilibrate for 5 minutes to minimize residual shear history. The bottom plate of the geometry has a controllable thermal Peltier unit, which allowed the programmed temperature to be accurately maintained for the duration of the experiments within a reasonable range, *e.g.,* 20 ± 0.05 °C.

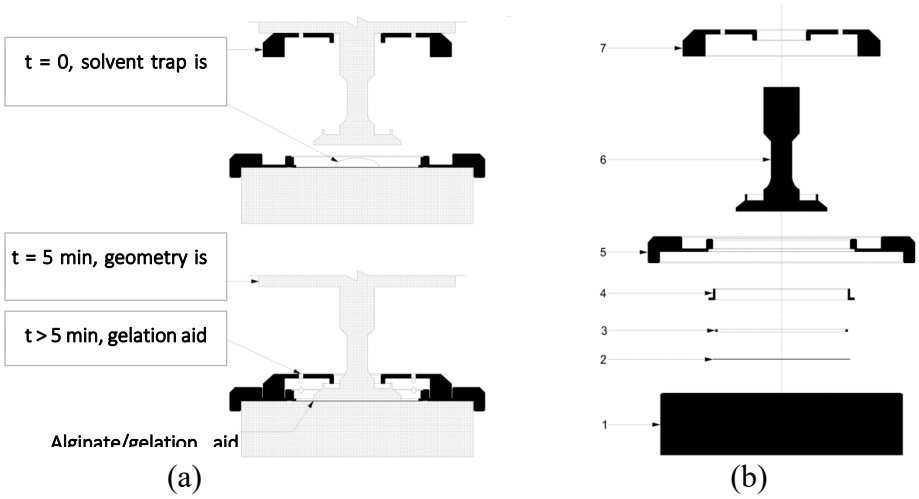

Figure 27. Schematic images of modified lower attachment geometry with solvent trap cover demonstrating a) before and after loading the specimen, and b) detailed diagram of the disassembled trap cover specifying the components of the apparatus: 1. Peltier plate, 2. Base tray, 3. Nitrile O-ring, 4. Sample tray, 5. Sample manifold, 6. Rheometer plate and 7. Solvent trap.

Sodium alginate solutions with 0.1 vol.% Darvan® C-N added as a liquid dispersant, were prepared under atmospheric conditions on a hotplate at 60 °C prior to their rheological measurement or their mixing with the cermet powder blend. The test suspensions for the

rheological studies were prepared with 50 wt.% total cermet solids (TiC and Ni_3Al), as used for the micro-composite powder synthesis described in the previous section. The pH was adjusted to 8.5 using ~5ml of 0.1M NaOH solution per 500 ml of suspension.

The density of the cermet was estimated from the volume fraction ***v*** of ideal mixing of its components:

Equation 6

$$\rho_c = v_{Ni_3Al} \cdot \rho_{Ni_3Al} + \left(1 - v_{Ni_3Al}\right) \cdot \rho_{TiC}$$

Converted to a function of mass fraction ***w*** the expression becomes:

Equation 7

$$\rho_c = \frac{1}{w_{Ni_3Al}/\rho_{Ni_3Al} + \left(1 - w_{Ni_3Al}\right)/\rho_{TiC}}$$

After loading the material onto the sample cup, the disk and the moisture trap cover were slowly lowered, until the disk reached the predetermined test gap (1000 or 1500 mμ). The moisture trap minimized changes due to humidity and evaporation, which are often sources of error during rheological testing of aqueous substances over extended time periods.

3.3.1. Preliminary Flow and Oscillatory exploration

After performing preliminary experiments to establish reasonable boundaries for test parameters, the oscillation frequency was set at 5 Hz and the applied strain to 0.5%, which

were used for most oscillatory experiments. Rheological studies were carried out using a 1000- or 1500-microns gap at 20°C for the cermet/sodium alginate suspensions. The suspension sample volume used was 1.8 mL.

3.3.2. Reported tests: flow and oscillatory.

The tests were performed in two steps: (i) During the first 8 minutes, a shear flow ramp from either 10 s^{-1} or 100 s^{-1} to 1000 s^{-1}, and back, was applied four times. (ii) The oscillatory experiment was then started, allowing for equilibration oscillatory time sweep for 5 minutes sweep on the raw material. (iii) The gelation agent was then added around the sample with minimal disturbance, while the oscillatory time sweep was continued. The measurements from the oscillatory test were recorded for 30 minutes (5 equilibration, 25 gelation), at intervals of 6 seconds. (iv) After the 30 minutes, an oscillatory strain sweeps between 0.2 and 20 % was applied, to evaluate the strength of the gel. The volume of chelating agent added around it, through the centering device shown in Fig. 4, was 3.4 mL of $CaCl_2$ solution.

Through this approach, the rheological responses of the raw suspensions have been gathered and are summarized in terms of the apparent viscosity. For the raw/gelling/gelled the storage modulus (elastic component), G', the loss modulus (viscous component), G'', and the loss angle δ (from its tangent, the ratio of the viscous to elastic responses for a viscoelastic material), as a function of time.

3.4. HVOF Thermal Spraying Trials and Microstructure Characterisation

The gelation-processed TiC-Ni_3Al feedstock powders were deposited using an HVOF system (Model Diamond-Jet, Oerlikon Surface Solutions AG, Pfäffikon, Switzerland) at Boeing Research and Technology (South Park, Seattle, WA, USA). Coatings were deposited onto Ti-6Al-4V alloy panels at thermal spraying 'stand-off' distances of 203, 238, 254, 279 and 305 mm (*i.e.*, 8", 9", 10", 11" and 12", respectively). The substrate materials were first cleaned with acetone and the surface of each panel was prepared by grit blasting with 60 grit SiC particles, in order to increase the surface roughness and hence the adherence between the TiC-Ni_3Al coating and the substrate material. An average coating thickness of 100-150 μm was achieved after 42 passes. The HVOF gun was programmed for a H_2:O_2 ratio of 1300:500 SCFH. The micro-composite feedstock powders then were fed into the HVOF gun at 12 RPM (25 g/min), with 75 SCFH Ar used as the carrier gas.

After coating, the HVOF sprayed samples were sectioned perpendicular to their planar surface, using a precision saw to provide an accurate and clean cut. For imaging of the as-deposited surface, the coated substrates were hot-glued onto stainless steel discs. For cross-sectional imaging, the samples were mounted within a cold-setting epoxy resin and then metallographically prepared for characterization. This was achieved by grinding/polishing with successively finer grades of diamond abrasive to a 0.25 μm final diamond paste particle size. Microstructural characterization of the HVOF deposited TiC-30 vol.% Ni_3Al cermet coatings was subsequently conducted using optical microscopy (OM; Model BX-51, Olympus Corp., Tokyo, Japan) and FEG-SEM (details as before). Compositional analysis was performed in the FEG-SEM using energy dispersive X-ray spectroscopy

(EDS; Inca X-maxN, Oxford Instruments, Concord, MA, USA). The degree of porosity was assessed by adopting the standard black spot test with associated photographic software.

3.5. Results and Discussion

3.5.1. Comparison of Sodium Alginate Gelation Systems

To initially verify that the alternative gelling agents had some degree of functionality, small droplets of a suspension of TiC-Ni_3Al/sodium alginate, produced as described previously, were pipetted into beakers containing individual solutions of each of the various gelling agents. This allowed a preliminary qualitative observation of gelation ability. Solutions containing 0.2 M $CaCl_2$, 0.2 M Ca-acetate, 0.2 M Al-nitrate, pure methanol, pure acetic acid, and 5 % HCl acid produced nominally spherical gelled droplets. In contrast, solutions of Ca-lactate, ethanol, and IPA yielded misshapen, 'donut-like' particles. Ni-acetate produced flattened, 'splat-shaped' structures which due to their lack of strength broke upon impact with the bottom of the beaker. These qualitative results are summarized in Table 5. Based upon these initial observations, only $CaCl_2$, Ca-acetate and Al-nitrate were selected for further study. While methanol and acetic acid performed comparatively well, their high volatility makes them dangerous to work with and the atomising nozzle setup could not be easily recreated in a fume hood. HCl was subsequently eliminated as, though particles gelled well, HCl contained Cl^- ions which are deemed unsuitable for most metallurgical applications, while also presenting some obvious safety concerns. Particles gelled with Al nitrate were similar in nature to the Ca-containing systems. However, during gelation, the

Al nitrate aqueous bath changed color, turning lightly green. This color change was associated with the dissolution of Ni from the solid material in the TiC-Ni_3Al suspension and was confirmed using ICP-OES analysis of the retrieved solution. Roughly 4.5 wt.% of the nickel from the powder had dissolved into the Al nitrate aqueous solution. As such, Al nitrate was deemed unsuitable for use with this specific cermet powder. Ca-acetate was continued as a baseline. Hence, the following results and discussion is based on TiC-Ni_3Al powders produced with these three chelating agents only.

A preliminary series of experiments demonstrated that the mean particle size of the dried particles following suspension spraying through the TurboTak nozzle corresponded well to the particle size suggested by the manufacturer. Additionally, it was generally found that the spray could be greatly increased over the manufacturer's recommended flowrates, which was recommended at 1 to 40 mL/min, without impacting the particle size. Spray gelation trials were performed using both $CaCl_2$ and Ca-acetate containing baths, to verify the accuracy of the performance curve provided by MEGTEK at moderate flow rates of about 300 ml/min. Higher flow rates, up to 500 mL/min, were used to test the operational limit for droplet formation. It is unclear if increased flowrates impact the spherical nature of the particles, since several problems were observed in operation at flowrates greater than 400 mL/min. The back pressure from any blockages that occur at these flowrates resulted in a failure of the friction fit of the tubing and severe vibration of the tubing was seen at these flowrates. These vibrations made the tubing and the apparatus unwieldly. However, low flowrates were also problematic. The peristaltic pump used in this experiment only had two rollers and no accumulator, and thus a severe fluctuation in flowrate was observed.

A typical powder size distribution after spraying and drying of the particles is presented in Figure 28. The distribution is moderately large, with a D_{10} of 17.4 µm and a D_{90} of 187 µm. The distribution is also unimodal though with a slight skew for finer particles. At least part of this skew is likely a result of isolated particle fracture occurring during the crushing of the gelled particles with mortar and pestle to liberate them from one another.

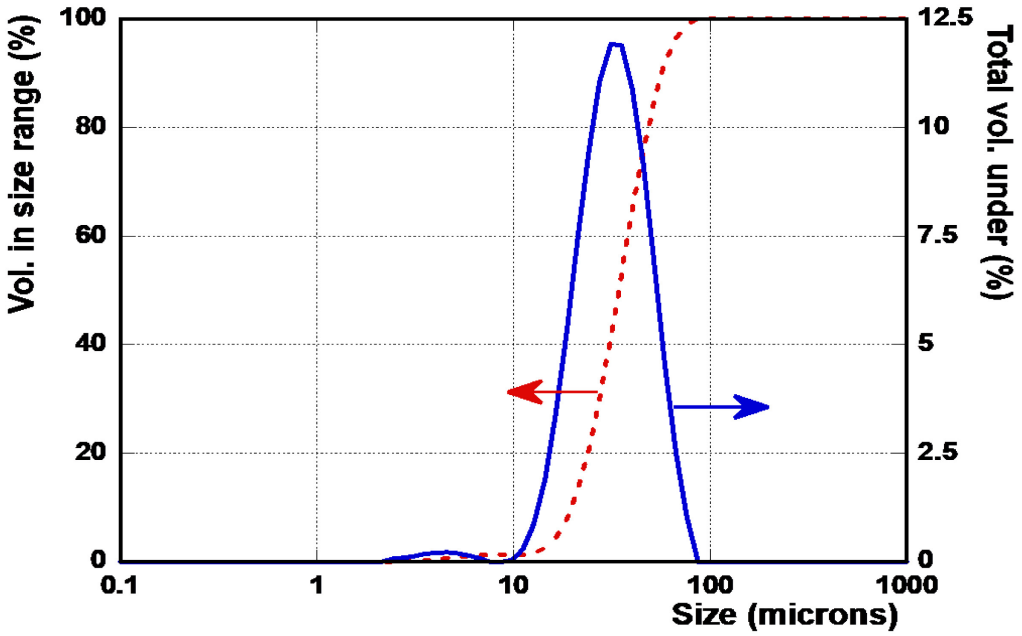

Figure 28. Particle size distribution for TiC-Ni_3Al particles sprayed into a bath of 0.2 M concentration Ca-acetate at a liquid flow rate of 300 mL/min and an air pressure of 0.173 MPa (25 psig).

Example SEM images of gelled and dried particles, sieved to collect the fractions between 45 and 75 µm, as well above and below these limits are presented in Figure 29 and Figure 30; it should be noted that the cermet example prepared with $CaCl_2$ has a higher Ni_3Al

content than for most of the present work, at 40 vol.%. The particles appear somewhat spherical, though are often slightly irregular or oblong in nature. Nevertheless, the particles produced were roughly spherical, and it was possible to then handle and sinter them to increase their mechanical robustness.

The samples that did not pass the 75 μm are quite uniform, as is the fraction collected between 45 and 75 μm. In contrast, the fines that passed through the 45 μm sieve show both intact particles and fragmented material, which is presumably damaged either during the light grinding by mortar and pestle, or during the sieving step itself. However, these particles show a suitable morphology for use in techniques such as HVOF or for laser DED processing.

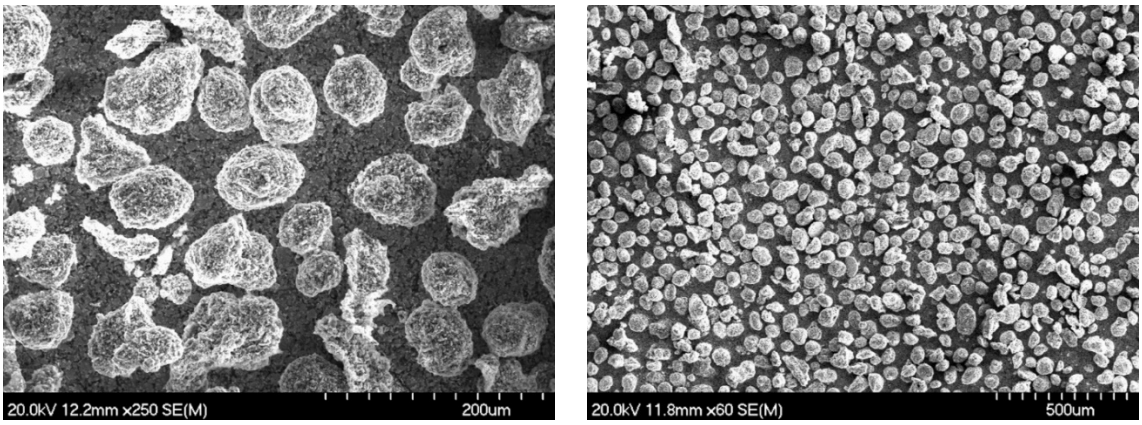

(a) (b)

Figure 29. TiC-Ni_3Al particles produced at sprayed into a bath of 0.2 M Ca acetate at a liquid flow rate of 300 mL/min and an air pressure of 25 psig. The images shown the separated particles sized between 75 μm and 45 μm: (a) high magnification, and (b) low magnification.

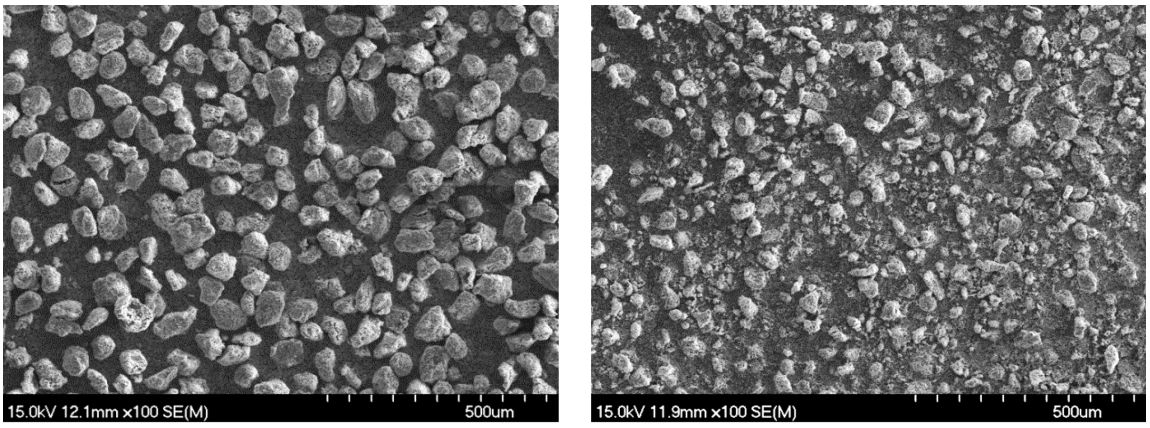

(a) (b)

Figure 30. Examples of fractionated TiC-40 vol.% Ni_3Al particles after gelation with $CaCl_2$, sprayed from a 50 wt.% solids suspension: (a) the +75µm fraction, and (b) the -45µm fraction.

3.6. Rheological Analysis

3.6.1. Alginate suspension before gelation

The apparent viscosity of the 1.6 wt.% sodium alginate in distilled water (without the addition of cermet particles) versus shear rate is plotted in Figure 31. The alginate solution is shear thinning and the presence of a normal stress indicates that it is viscoelastic.

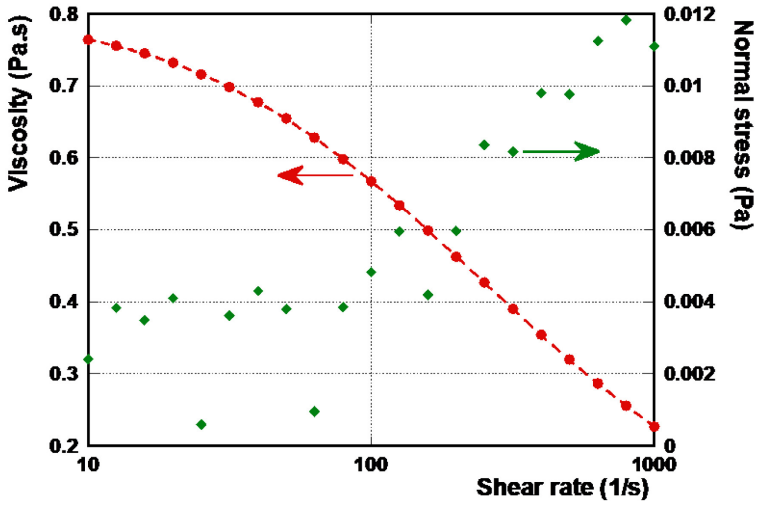

(a)

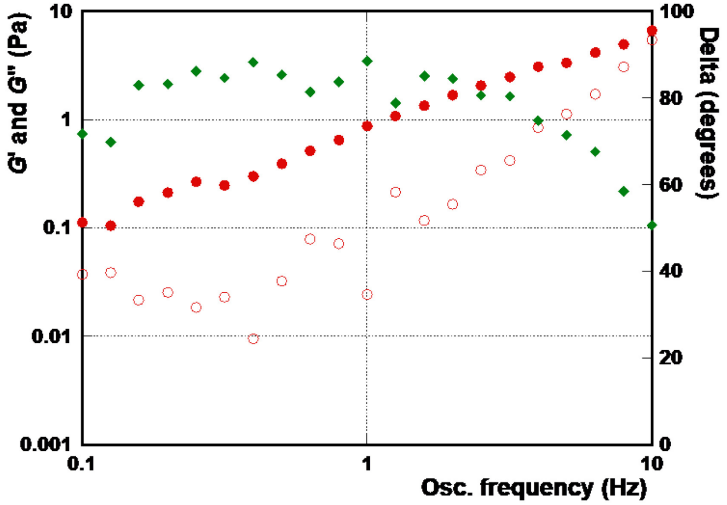

(b)

Figure 31. Rheology plots from 1.6 wt.% sodium alginate in distilled water. (a) Flow viscosity and normal stress vs. shear rate. (b) Oscillatory elastic (G') and viscous (G") moduli vs. oscillation frequency; the secondary axis shows the phase angle, delta.

The flow viscosity η (Pa·s) is described well by the Carreau-Yasuda equation, with negligible infinite shear viscosity:

Equation 8

$$\eta = \eta_o \cdot [1 + (\lambda \cdot \dot{\gamma})^a]^{\left(\frac{-p}{a}\right)}$$

where $\eta_\circ$ is the viscosity at zero shear rate (Pa·s), λ is response time (s), $\dot{\gamma}$ is the shear rate (s^{-1}), p is analogous to the power law index and a is dimensionless parameter that describes the transition from the negligible shear rate region to the power law region.

Table 6. Values of the parameters of the Carreau-Yasuda equation to estimate the apparent viscosity of the cermet suspensions.

Parameter	**Units**	**Value**
η_o	Pa·s	0.810
λ	s	0.00621
a	-	0.888
p	-	0.626

For plate-plate geometries this thrust (the normal force) F_{PP} ($\dot{\gamma}$) (N) is, in fact, the first normal-stress difference $N_1(\dot{\gamma})$ minus the second normal stress difference $N_2(\dot{\gamma})$, as described by Equation 4 [40,41]:

Equation 9

$$\frac{2F_{\mathrm{PP}}(\dot{\gamma})}{\pi R^2}\left[1+0.5\frac{\mathrm{d}\ln F_{\mathrm{PP}}(\dot{\gamma})}{\mathrm{d}\ln(\dot{\gamma})}\right]=(\mathrm{N}_1(\dot{\gamma})-\mathrm{N}_2(\dot{\gamma}))|_{\dot{\gamma}_{\mathrm{r}}=R}$$

The radius of the parallel plate is R (m) and $\dot{\gamma}$ is the shear rate (s^{-1}). The Reynolds number for parallel-plates geometry is given by:

Equation 10

$$Re_{\mathrm{pp}}=\frac{\rho\omega Rh}{\eta}=\frac{\rho\dot{\gamma}h^2}{\eta}$$

Table 7. Rheometry parameters utilised for the cermet suspensions.

Parameter	Symbol	Units	Value
Density	ρ	kg/m^3	2.57×10^3
Apparent viscosity	η	Pa·s	~ 0.1
Gap	h	m	1×10^{-3}
Nominal shear rate	$\dot{\gamma}$	s^{-1}	10^{-1} to 10^3

The oscillatory frequency sweep shows a liquid-like behaviour at frequencies below 1 Hz. Below this value the elastic component is insignificant compared to the viscous component. Above 1 Hz, the elastic component increases faster with frequency than the viscous component. The crossover is close to 10 Hz, however, the liquid-like behaviour is still dominant, since the complex viscosity remains virtually constant, at approximately 0.127

± 0.002 Pa·s. The relationship between frequency, ω, and complex viscosity η^* is described by a power-law regression to characterize the gel properties [290–292]:

Equation 11

$$\eta^*(\omega) = K_f \cdot \omega^{-nf} \ (0 < nf < 1),$$

$$\text{where } \eta^* \text{ is defined by } \{(G'^2 + G''^2)^{1/2}\}/i\omega$$

Constant K_f represents the dynamic consistency index, in this case, whereas exponent nf is the dynamic power-law factor. When the exponent is equal to 1, the system is completely elastic, and η^* decreases with increasing ω. When the exponent is equal to 0, on the contrary, the system is completely viscous, and η^* stays constant regardless ω. The exponent for the alginate solution is very close to zero for frequencies below 10 Hz. These results agree with reported values for sodium alginate media while there was very little work has been done on the rheology of ceramic suspensions [293,294].

3.6.2. Rheology of the Cermet Suspensions

Figure 32 shows the effect of shear rate on the apparent viscosity for cermet suspension with 1.6 wt.% alginate and 50 wt.% solid loads without addition of chelating agent solution. The apparent viscosity of the suspension decreases with respect to shear rate (*i.e.,* it has a pseudoplastic or shear-thinning behavior). These plots show hysteresis as well. The separation between the up and down legs of the hysteresis loops decreased if the rate of change of the shear rate over time was increased, *i.e.,* if more equilibration time was allowed for each step. The fluid behaviour was thus thixotropic. On the other hand, in the

range of higher shear rates (500 to 800 s^{-1}) it was also possible to measure the normal stress. The presence of significant normal forces indicates that the fluid, as expected, was viscoelastic.

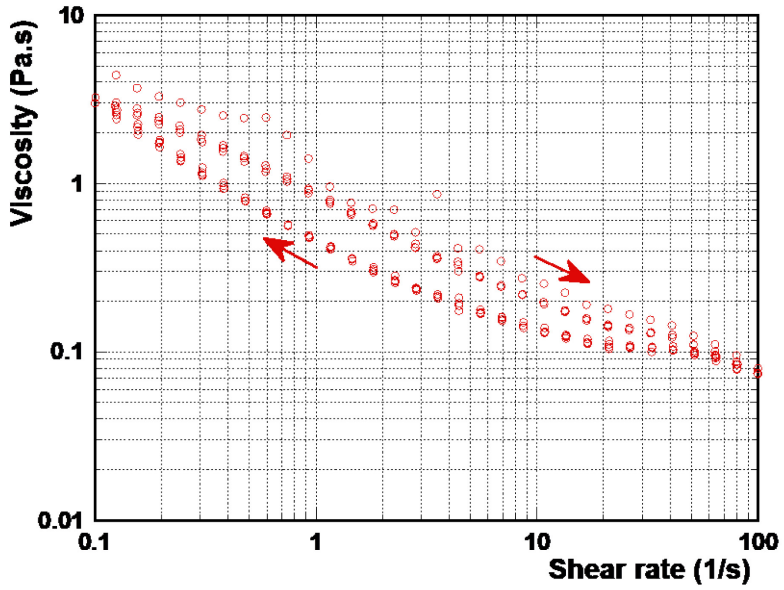

(a)

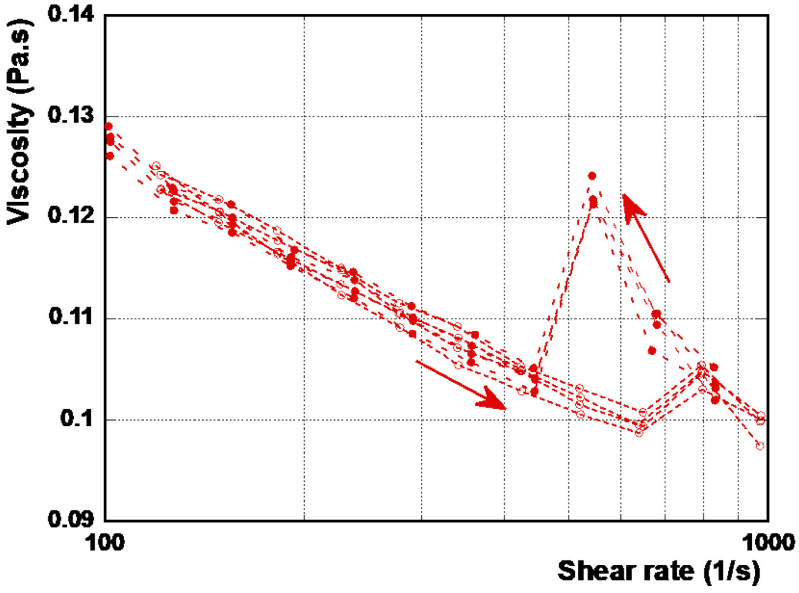

(b)

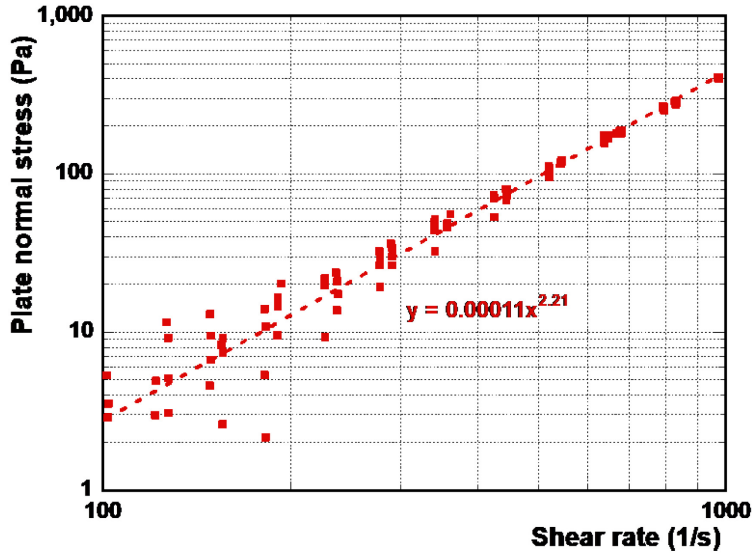

(c)

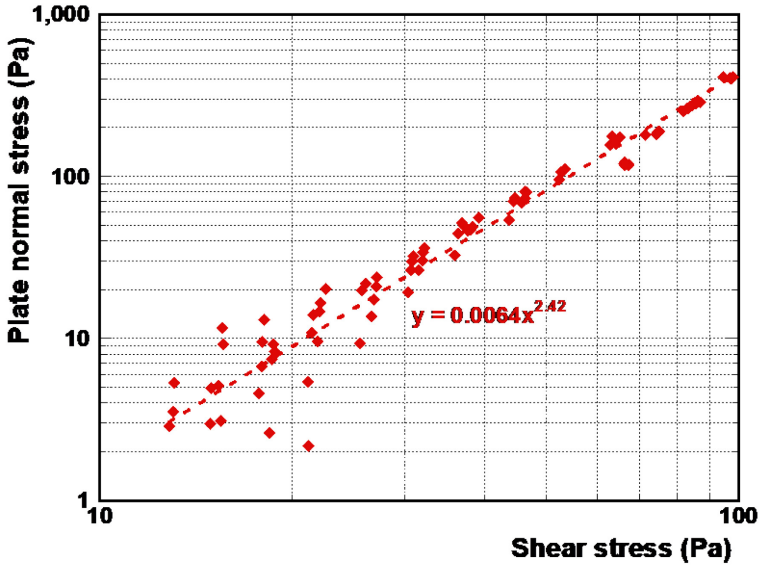

(d)

Figure 32. Flow rheology plots from cermet suspension within the sodium alginate medium stabilized at pH 8.5. (a) The viscosity vs. shear rate response. (b) The associated viscosity vs. high shear rate response. (c) The measured plate normal stress vs. (high) shear rate behavior. (d) The measured plate normal stress vs. (high) shear stress behavior.

The *apparent viscosity* of the thixotropic cermet suspension *changes with time* under any given shear rate. Additional experiments were conducted to explore this time dependence of the suspension and the results are summarized in the plots in Figure 33.

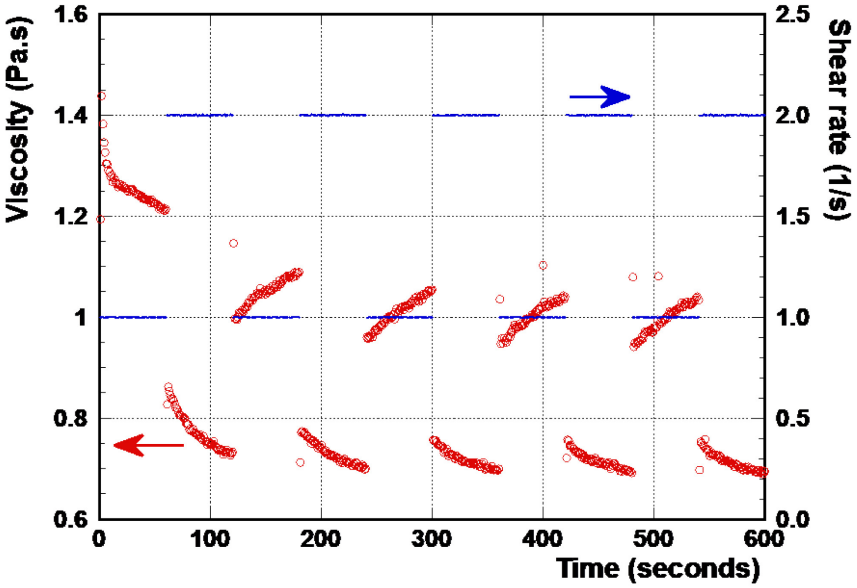

(a)

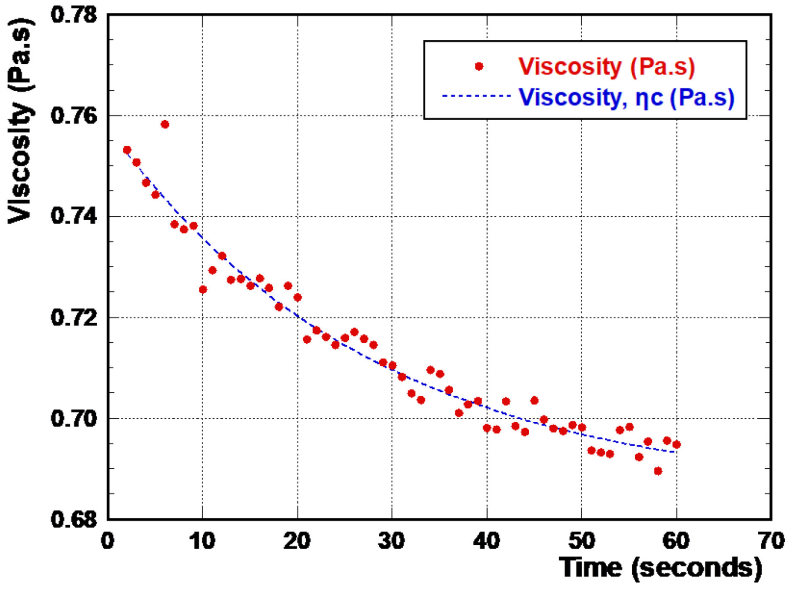

(b)

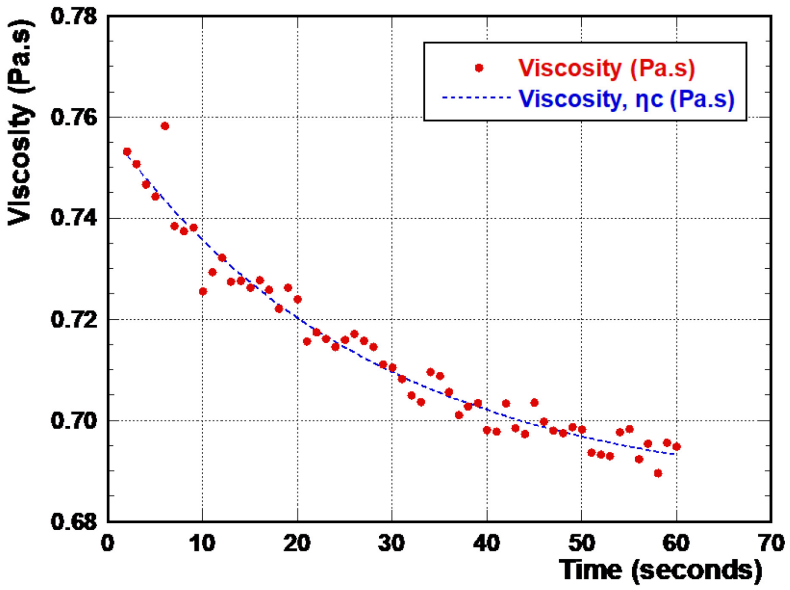

(c)

Figure 33. Apparent viscosity of cermet suspension in the sodium alginate medium stabilized at pH = 8.7, as a function of "time after changing shear rate". (a) Viscosity versus time, as the shear rate is switched alternatively between 1 s^{-1} and 2 s^{-1} every minute. (b) Detail of the viscosity vs. time curve, for the last shear step down from 2 s^{-1} to 1 s^{-1}. (c) Detail of the viscosity vs. time curve, for the last shear switch step up from 1 s^{-1} to 2 s^{-1}.

At short time scales (less than 60 s) the time change of the apparent viscosity follows an exponential function:

Equation 12

$$\eta = \eta_0 + \Delta\eta \cdot \mathrm{e}^{-\left(\frac{t}{\tau_\eta}\right)}$$

Table 8. Characteristics of the time-dependent response of the apparent viscosity of cermet suspensions to change in shear rate.

Variable	units	Shear step down		Shear step up	
η_0	Pa·s	0.940	→1.13	0.760	→0.685
$\Delta\eta$	Pa·s	0.190		-0.0730	
τ_η	s	79.2		27.9	

At longer settling times this behavior is more complicated, as seen in the viscosity data for 240 seconds after the step reduction of the shear rate from 2 s^{-1} to 1 s^{-1}, Figure 34. This response is associated with the magnitude of yield stress that is related to the strength of the particle network.

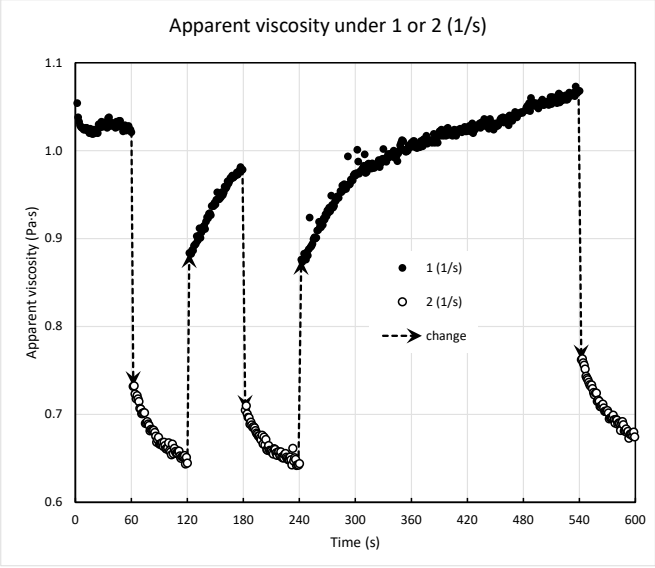

Figure 34. Apparent viscosity of the cermet suspension as a function of time under alternating shear rates (1 and 2 s^{-1}). Initial stabilization was at a sheer rate of 1 s^{-1}.

3.6.3. The gelation process using calcium chloride.

The increase in the moduli of the material due to the gelation process are evident in Figure 12. The elastic modulus (G') is larger than the viscous modulus (G") at all points after the addition of the gelling agent. The Ca^{++} ions rapidly reached the outer perimeter of the material, thus gelling first the most sensitive part of the parallel plate, *i.e.*, the external rim.

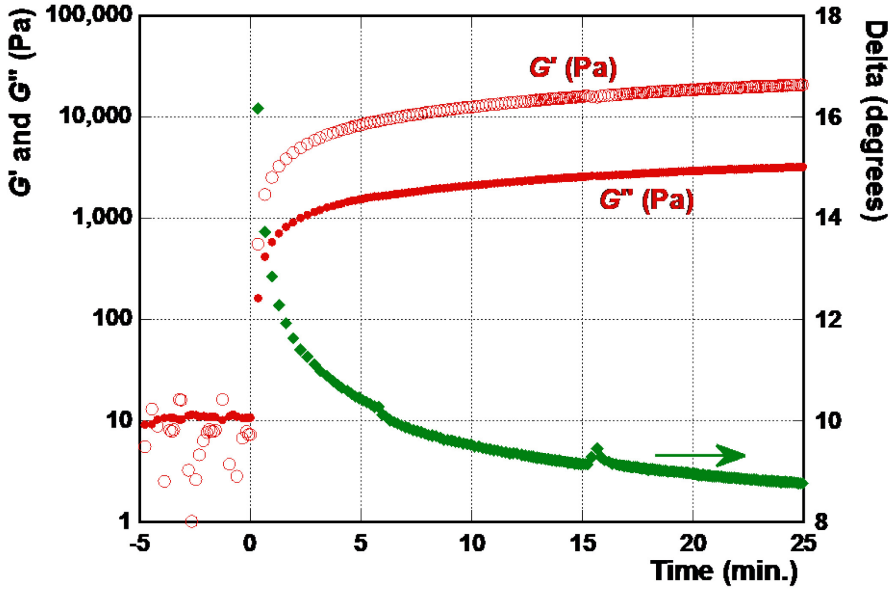

Figure 35. Elastic (G') and viscous (G") moduli as a function of time are plotted on the left y-axis, whereas their relative angle (δ) is plotted in the right axis. The frequency was 5 Hz, and the strain was set to 0.5 %, while the temperature was 20 °C.

During the first five minutes (negative in the plot) the raw material was equilibrated. The $CaCl_2$ solution was then added, and the oscillatory measurements continued. The diffusivity of $CaCl_2$ in water at 25 °C and concentration 0.0 ~ 0.2 M, is 1.12×10^{-9} m^2/s [35].

The suspension of 50% wt.% cermet solids loading has a volume fraction of water volume $v_w \sim 0.86$, estimated from the density of the materials with Equation 13.

Equation 13

$$v_w = \frac{(1 - w_c)/\rho_w}{w_c/\rho_c + (1 - w_c)/\rho_w} = \frac{1}{1 + w_c/(1 - w_c) \cdot \rho_w/\rho_c}$$

The tortuosity was estimated approximately at 1.12 using Pisani's method for spheres [295–297]. Thus, the effective diffusivity in the gel must be lower than $0.86 \cdot 1.12/1.12 \times 10^{-9} \approx 9 \times 10^{-10}$ m^2/s ($\sim 5 \times 10^{-3}$ cm^2/min). The penetration length would be then about 1 mm from the rim of the disc. This narrow ring would be responsible for observed moduli.

3.6.4. Gelled matrix containing cermet particles.

After gelation**,** oscillatory frequency sweep tests were run to explore the viscoelastic characteristics of the cermet suspension gelled with $CaCl_2$. Frequency sweeps and strain sweeps at 20 °C produced results such as those illustrated in Figure 36. From these tests, a strain of 0.2% was found to be high enough to produce a good measurable response, and small enough to maintain the integrity of the gel structure. In a similar manner, a frequency of 5 Hz was chosen as being high enough to provide adequate sampling cycles to evaluate the gel or sol properties, while not disrupting the structure. The elastic and viscous moduli increased very little with the frequency at the 0.2% shear strain (Figure 36a). The complex

modulus was around 2×10^4 Pa. The elastic modulus was about 10 times the viscous modulus, indicating a sol.

After the gelation oscillatory tests, the sol was subjected to an increasing oscillatory shear strain (0.2 to 20%) to examine the tolerance of the structure to deformation. An example of the results is shown in Figure 36b. At strains below 0.5% the sol structure appeared unaffected. Structure deformation starts to happen above 0.5%, with a total collapse of the structure at a shear strain around 2%, which corresponded to an oscillatory stress of about 400 Pa. Measurements were thus restricted to strains below 0.5%.

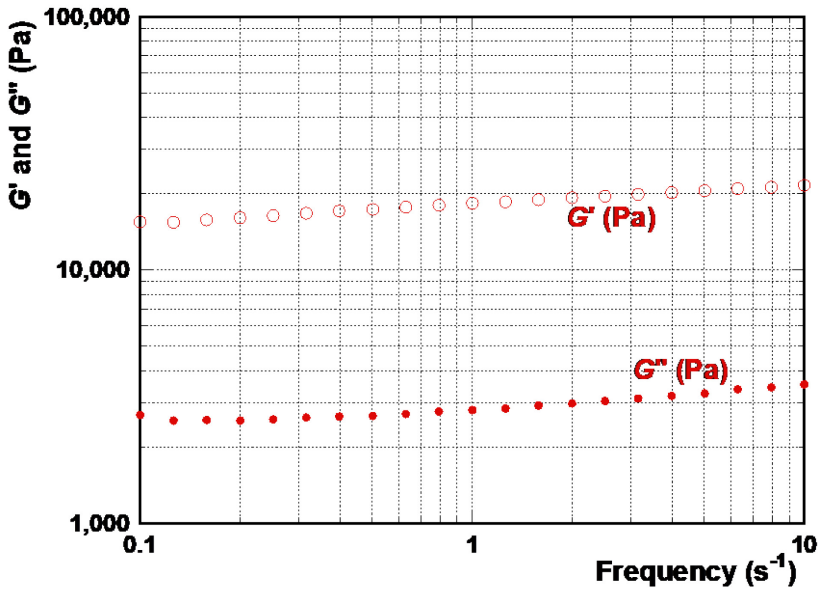

(a)

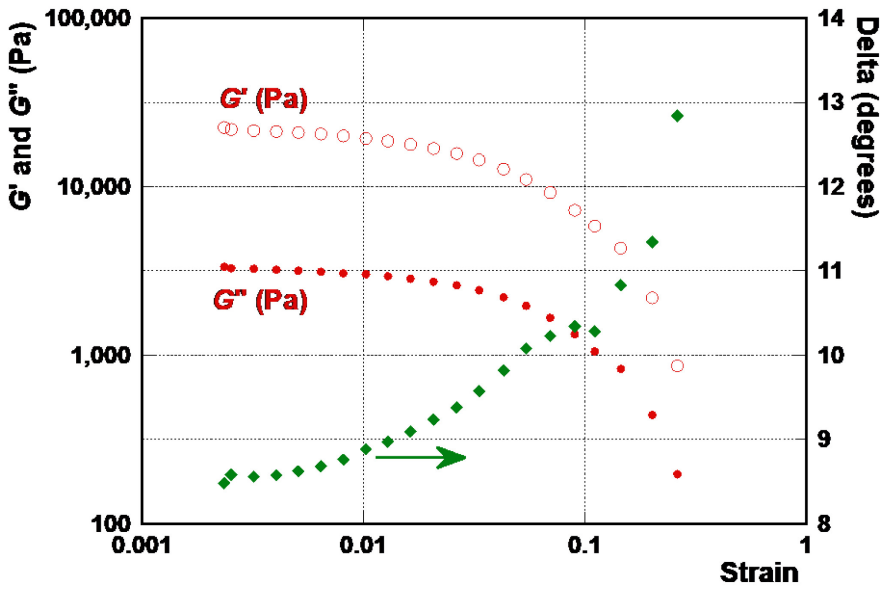

(b)

Figure 36. (a) Elastic (G') and viscous (G") moduli of cermet suspension gelled with $CaCl_2$ as a function of oscillatory frequency, with a constant shear strain of 0.2%, and (b) Elastic (G') and viscous (G") moduli (left y axis) and phase angle (δ) (right y axis) from cermet suspension gelled with $CaCl_2$, as a function of shear strain, keeping the frequency at 5 Hz.

3.7. Preliminary Assessment of HVOF Coating Trials and Morphology

For the initial study of HVOF deposition, the samples were prepared using the $CaCl_2$ ion-exchange chelation approach. In this instance, the TiC-Ni_3Al coating feedstock was prepared with 30 vol.% of the metallic binder phase. The average thickness of the TiC-Ni_3Al HVOF coating vs. the gun stand-off distance for the powder is presented in Figure 37. The reason for the thickness deviation at 203 mm (8") stand-off is not clear at the present time but may relate to particle effectively 'bouncing-off' the substrate.

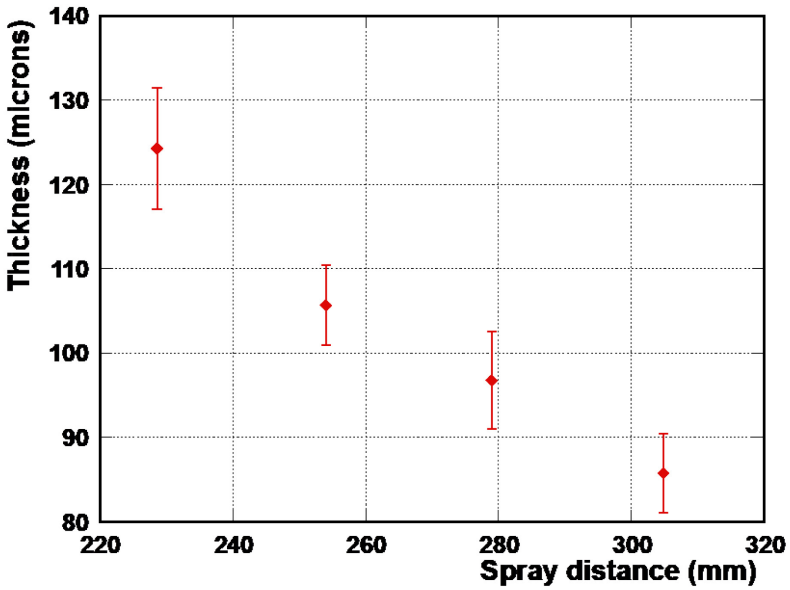

Figure 37. Average thickness of the HVOF deposited TiC-Ni_3Al coatings vs. stand-off distance.

The elemental compositions of the gelation-route feedstock powders, and related HVOF coatings, were assessed using EDS (Figure 38). The result of chemical analyses revealed that the compositions of final HVOF coatings closely resembled the composition of feedstock powder for coatings sprayed at stand-off distances of 203 mm (8"), 229 mm (9"), 279 mm (11"), and 305 mm (12"). Coatings that were sprayed at 254 mm (10") set off distance exhibited the least amount of oxygen contamination, while also showing the highest carbide deposition rates.

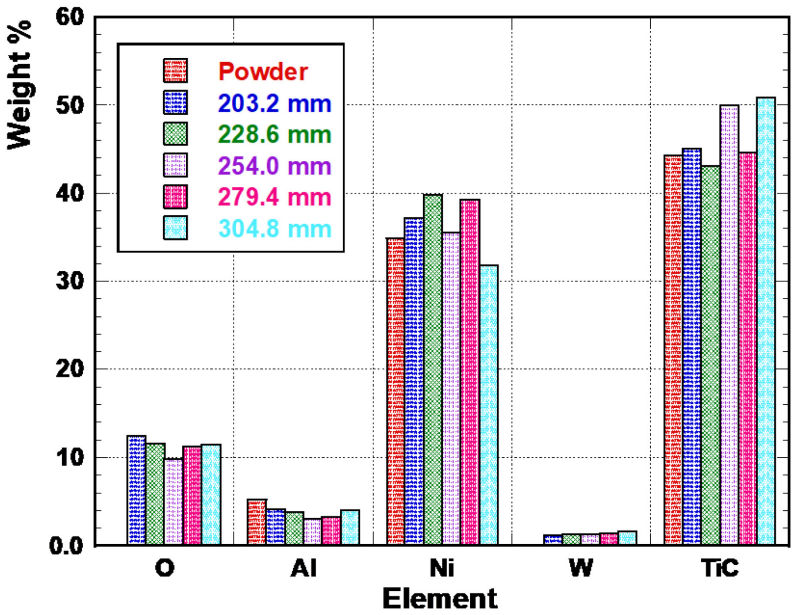

Figure 38. Average elemental composition of TiC based feed-stock powder produced by gelation and resulting coating generated via HVOF for different stand-off distances.

Figure 39 and Figure 40, with the latter at higher magnification, demonstrate representative FEG-SEM micrographs obtained from cross sections of the HVOF thermal spray coatings deposited onto Ti-6Al-4V substrates at various stand-off distances. From the microstructural analysis, it is apparent that there is a general increase in the volume of residual pores with an increasing stand-off distance above 254 mm (10"). The shape of the residual pores (shown in Figure 39) suggests that the coalesced splat/splat boundary is most likely a consequence of metallic bonding and, potentially, also partial re-melting the under-layer upon the arrival of a subsequent droplet. The coatings showed an increase in the thickness of the splats through increasing the stand-off distance, in proportion to the increased porosity. This is believed to be the result of the low flowability of the newly developed powder. Lamellar splat structures,

which are expected for this type of coating, are observed with inclusions of partially melted particles and oxides. Oxide inclusions (dark contrast phase), which are a common characteristic of HVOF coatings sprayed in air, may be beneficial to the mechanical characteristics of the coatings such as hardness and wear resistance. However high concentration of oxides can result in reduced wear and corrosion resistance and cohesive failure of coating, due to their inherently brittle nature. Moreover, EDS analysis confirmed that the internal oxides are mostly formed from Al and Ni (Figure 40. a and b). The formation of oxide particles is related to the intrinsic properties of the material. In addition, un-melted particles are present, following a preferred path distribution of spraying powder, according to their inertia during the thermal spraying process. This can potentially generate porosity, or the particles can become trapped in the body of the coating.

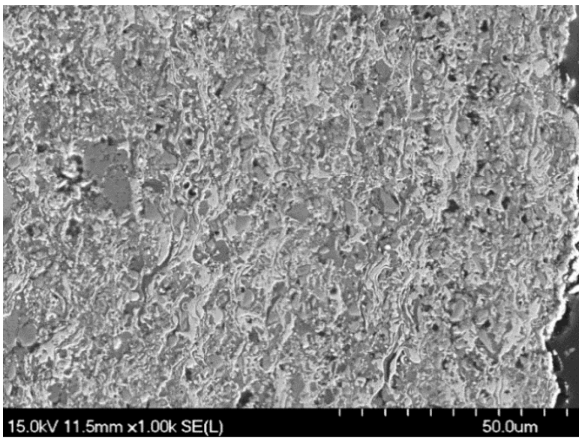

(a)

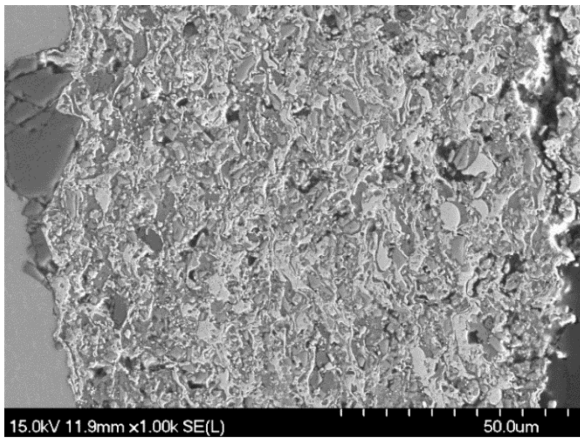

(b)

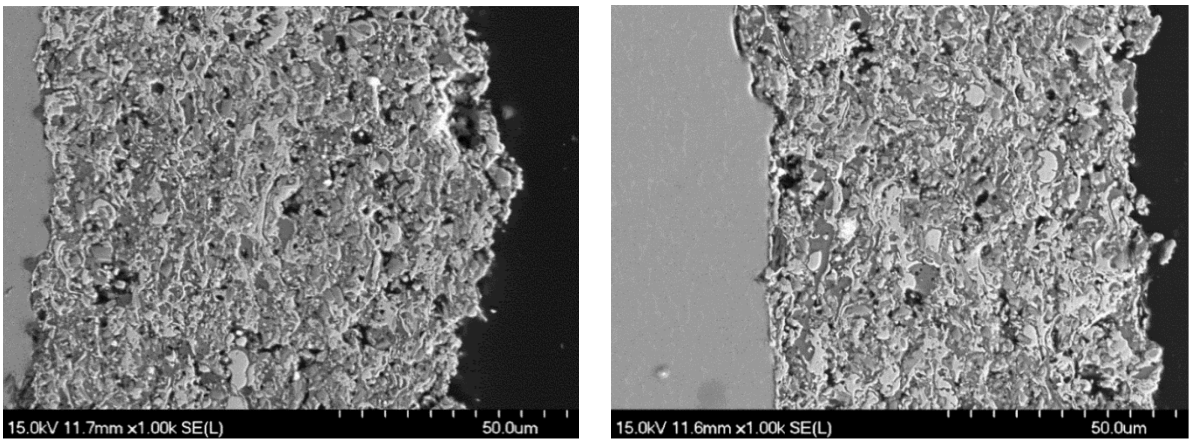

(c) (d)

Figure 39. Representative SEM micrographs obtained from the polished cross sections of HVOF coated TiC-Ni_3Al (30 vol.%) on Ti-6Al-4V substrates, deposited with stand-off distances of: (a) 229 mm, (b) 254 mm, (c) 279 mm, and (d) 305 mm.

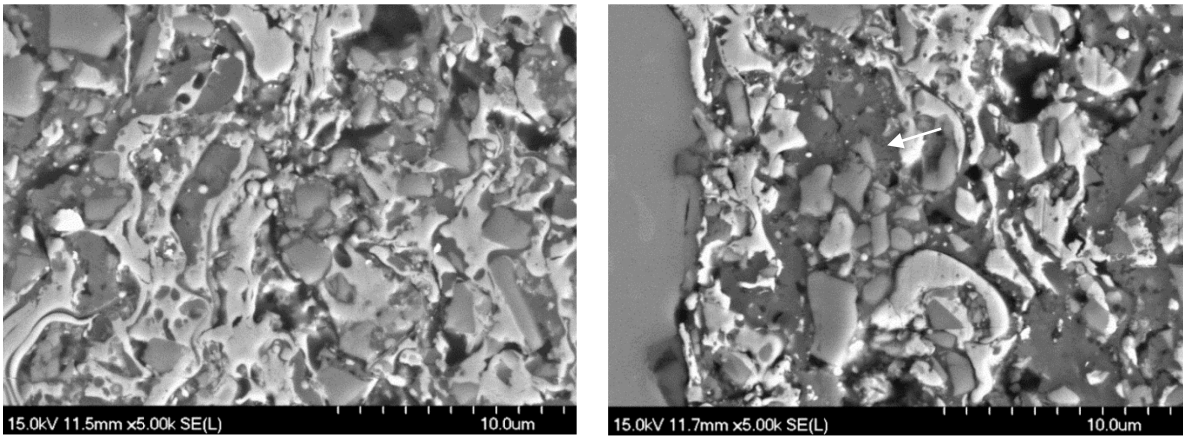

(a) (b)

Figure 40. Higher magnification SEM micrographs obtained from the polished cross sections of HVOF coated TiC-Ni_3Al (30 vol.%) on Ti-6Al-4V substrates, deposited with stand-off distances of: (a) 229 mm, and (b) 279 mm. The SEM images highlight some residual porosity and oxide particles.

3.8. Effects of Pre-Sintering Trials

It is important to note from the initial HVOF trials that without any form of pre-sintering operation (to physically sinter the core of each micro-composite powder particles), the powders had moderately poor flowability during HVOF processing, resulting in clogging of the HVOF spray gun. This relates to the observations in Figure 30 (b), where there is evidence of the particles fragmenting under any form of moderate mechanical loading. To explore simple pre-sintering treatments of the powder as a possible route to improve the flowability, the powder was subjected to high temperature treatment in the TGA instrument.

The sintered powders, however, were prepared only in very small amounts in the TGA and thus were not tested in the HVOF coating process; here the benefit of TGA is that weight changes can be monitored, while the heating cycle can be very carefully controlled.

Powders were heated at 20 °C/min to 690 °C, 925 °C, and 1310 °C; approximately 50 °C above or below notable phase transformations in the metallic binder phase. The Ni:Al (50:50 wt.%) powder, which contributes all of the aluminum to the Ni_3Al formulation, contains the nickel aluminide phases Al_3Ni, and Al_3Ni_2. The eutectic aluminum melts at roughly 640 °C. On the nickel aluminum phase diagram, Al_3Ni is observed to have its solidus at ~854 °C [298,299], but previous experiments had indicated that the solidification onset on cooling occurred closer to ~872 °C in a similar cermet system [260,300]. Significant self-propagating high-temperature synthesis reactions (SHSs) followed both transformations, resulting in a non-convoluted Ni_3Al melting peak in a metallic compact. Slightly aluminum rich Ni_3Al experiences a eutectic at 1360 °C and pure Ni_3Al experiences

a peritectic at 1362 °C. These transformations are registered as one melt peak due to their thermal proximity and the high ramp rate of the DSC/TGA.

FEG-SEM micrographs obtained from the heat-treated powders after they were subsequently embedded in epoxy (Figure 42), reveals that the particles heated to 690 °C, have poor mechanical integrity and are effortlessly removed from the analysed surface during epoxy mount and polishing. The particles heated to 925 °C also suffered from pull out, but to a substantially lower extent, with the particles that were held at 925 °C for 15 minutes appearing to have reduced pull out. The particles heat treated at 1310 °C show significant mechanical integrity as the metallic binder was observed to coat and connect the individual TiC grains. As such, a heat treatment of temperatures up to 1310 °C is recommended.

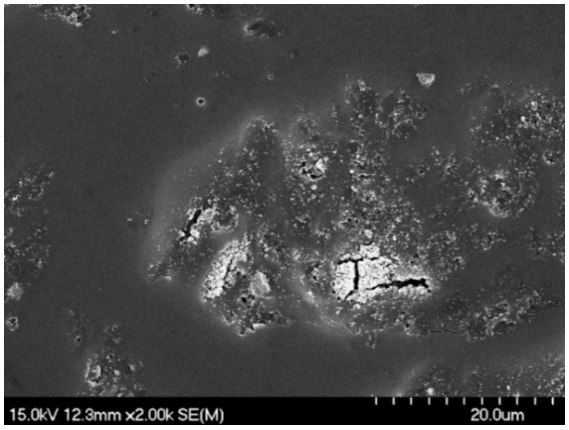

(a)

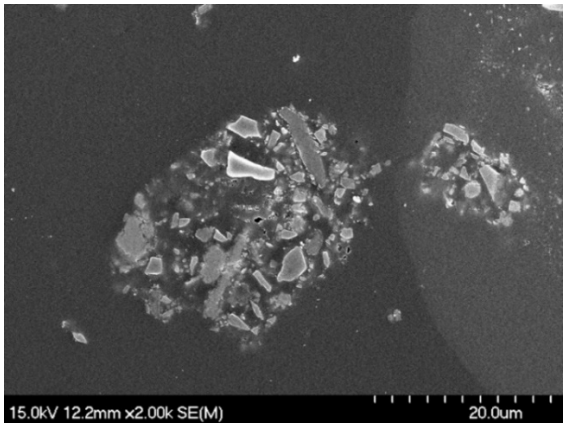

(b)

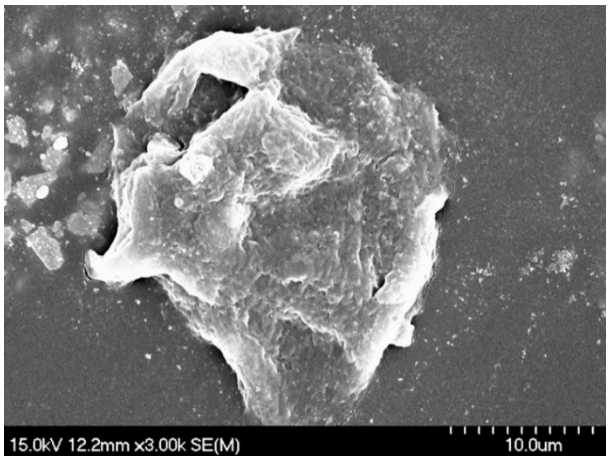

(c)

Figure 41. SEM images show particles sintered with no hold to temperatures of: (a) 690 °C, (b) 925 °C, and (c) 1310 °C. In each case the particle is embedded in cold mounting resin, and lightly 'polished'.

3.9. Conclusions

From this work, it is shown that air atomising nozzles can be employed in conjunction with sodium alginate gelation to produce nominally spherical particles with a mean size below 100 μm. The achieved particles have sufficient mechanical strength in the gelled form that they can be efficiently fractionated into relatively narrow size ranges. These particles can, in turn, be used to produce high quality HVOF thermal spray coatings.

It is also evident that, in addition to calcium chloride, alternative cross-linking agents such as calcium acetate, methanol, acetic acid, and 5 % hydrochloric acid can also be employed to produce gelled particles, at least on the macro scale; however, often these particles are not stable and will readily degrade if rinsed with water.

Finally, it is also noted that particles made via air atomising spray gelation can be sintered to improve their strength for subsequent HVOF processing. However, necking can occur between small particles at elevated temperatures, creating non-spherical feedstocks. The theoretical understanding of interparticle forces through rheological analysis has given some preliminary characterization of the produced powder in one type of gel system, using one of the suggested chelating agents. However, to better understand the interaction of the particles within the gel systems there is a need for further analysis such as direct force measurements, absorbed layer chemistry and solution composition.

Chapter 4. The aqueous corrosion and wear responses of HVOF-deposited TiC-Ni_3Al cermet coatings on AISI 4130 steel substrates

Z. Russell[1], M. Gaier[1], M.J. Froning[2] and K.P. Plucknett[1]*
[1]Department of Mechanical Engineering, Dalhousie University, 1360 Barrington Street, Halifax, Nova Scotia, B3H 4R2, CANADA
[2]Boeing Research & Technology, Seattle, USA

*Contact email: kevin.plucknett@dal.ca

Keywords: nickel aluminides; titanium carbide; potentiodynamic polarisation; reciprocating wear; specific wear rate;

Abstract

The aqueous corrosion and wear performance of TiC-Ni_3Al cermet coatings, deposited by high-velocity oxy-fuel (HVOF) thermal spray onto AISI 4130 steel substrates, is examined in the present work. Two powder feedstock formats were investigated. The first is a conventional agglomerated and sintered powder, which is then compared to a micro-composite powder feedstock fabricated via a novel gelation technology. The HVOF coatings were subsequently examined in terms of their microstructure, corrosion, and wear behaviors. The potentiodynamic polarisation responses of the cermet coatings were assessed in a simulated sea water environment (deaerated H_2O with 3.5 wt.% NaCl). The reciprocating sliding wear responses were also examined, against a WC-Co counter-face sphere. The post-corrosion and worn surface morphologies were subsequently investigated with optical microscopy, scanning electron microscopy, and associated energy dispersive X-ray analysis, with focused ion beam milling used to evaluate the wear track cross-sections. The TiC-Ni_3Al HVOF sprayed cermet coatings demonstrate a combination of high wear and corrosion resistance in comparison to conventional WC-Co and WC-CoCr cermet coatings that were also HVOF deposited and tested under similar conditions.

4.1. Introduction

It is common to require coatings on a variety of metallic substrates to improve the wear and/or corrosion resistance of the underlying material [155]. As a consequence, a broad range of coating and surface treatment technologies have been developed. In particular, the high velocity oxy-fuel (HVOF) thermal spray process has been examined by many researchers and shown to exhibit significant benefits [155,301,302]. The application of HVOF thermal spray coatings offers greater thickness capabilities than techniques such as sputtering or physical vapour deposition, with essentially no restrictions on part size [303]. Repair/rebuilding of damaged or worn parts is also feasible with HVOF [304]. HVOF is therefore applicable to extend the useful working lifetimes, and hence manufacturing economics, of a broad range of materials. Coatings with excellent bonding characteristics and attractive wear and corrosion properties have been developed to optimize the in-service performance of cermet-based, HVOF thermal spray materials [305–308].

The growth in HVOF thermal spray technology applications and advances in feedstock materials has led to the widespread use of ceramic and composite coatings. In particular, the properties of carbide based HVOF coatings have been highly refined, offering excellent component protection. As a consequence, cermet coatings have been deposited onto a wide selection of substrate materials and have been used across a broad range of commercial applications, including in the aerospace and automotive industries [155].

The primary example of these materials is tungsten carbide (WC) based ‘hardmetals’, typically manufactured with Co- or Ni-based metal matrices (WC-Co and WC-Ni, respectively). These coating materials have been widely investigated in recent years as an alternative replacement for chromium electroplating [309,310]. However, there are

concerns due to drawbacks related to the reduction in the fatigue strength of the substrate metal [311]. WC-Co coatings are also heavy, due to the relatively high density of WC (e.g., 15-16 g/cm^3, depending on binder content). A further drawback of WC-Co based coatings is that, although they are hard and wear resistant at ambient temperatures, their range of application is invariably limited to service conditions below ~450 °C due to significant oxidization in air, especially above 600 °C [312,313]. This severe oxidation degradation is also reflected in poor high temperature strength retention for WC-Co [314]. WC-Co coatings also exhibit relatively poor aqueous corrosion resistance[315], although this can be significantly improved with Cr addition[316]. As a potential alternative to WC-Co, 'bulk'-form cermets based on titanium carbide (TiC) offer high mechanical strength, thermal conductivity, and wear and corrosion resistance, while still remaining comparatively lightweight; typically, cermet densities ranging from 5.5 to 6.5 g/cm^3, which are roughly half those of WC-Co based hardmetals. At the same time, TiC-based cermets can also exhibit exceptional fracture toughness behavior [317]. As with WC, a variety of binders have been examined for TiC-based cermets, ranging from simple elemental systems such as Ni [318] or Co [319], through to steels [320,321] and advanced, ductile intermetallics [322,323]. In particular, TiC cermets that utilize a ductile nickel aluminide (Ni_3Al) based binder system have been shown to exhibit excellent high temperature strength retention in their bulk form, to the extent that the materials are stronger at 950 °C than they are at room temperature [323]. Furthermore, recent work has shown that the reciprocating wear resistance of TiC-Ni_3Al cermets can match that of commercial WC-Co hardmetals [285], at less than half the mass, while exhibiting far better aqueous corrosion resistance [324]. Therefore, there is a clear interest in developing these materials in coating

form, for example using HVOF. The properties of HVOF coatings can potentially be modified for the desired applications by altering the characteristics of the feedstock powder, such as the ceramic grain size, binder alloying additions, the content of the metallic phase, etc. The method of feedstock powder production is particularly crucial, to ensure the material produced has the specific required chemical and phase composition, and which also ideally exhibits a spherical morphology, low porosity, and a fine-grained structure. Feedstock powders for HVOF can be produced by a sintering route, followed by crushing and sieving to size [325]. However, cermet powders for HVOF thermal spray can now also be produced by 'atomization' methods from a liquid phase, 'agglomeration and sintering', as well as mechanical and high temperature synthesis [326,327]. Often, they can also undergo an additional plasma heat treatment to fully spheroidize them [3].

The present study investigates the development and performance characteristics of HVOF thermally sprayed TiC-Ni_3Al cermet coatings onto steel 4130 substrates. The TiC-based cermet samples have been prepared with a stoichiometric Ni_3Al intermetallic phase as the binder (at a fixed content of 30 vol.%). Two feedstock powders have been investigated. The first of these is produced through a conventional agglomeration and sintering route. In contrast, the second feedstock powder is manufactured using a novel aqueous spray atomisation and gelation method [160]. This approach was designed to produce nominally spherical particles that are of an ideal size for HVOF thermal spray processing but using a micron-sized ceramic powder to develop these micro-composite feedstock particles. The feasibility of using this gelation-produced feedstock for HVOF coating, and the quality of the coating layer, is evaluated by means of microstructural characterization, and measurement of the electrochemical corrosion and tribological responses. For comparative

purposes, WC-Co and WC-CoCr HVOF coatings with ~30 vol.% metallic phase, were also prepared onto the same 4130 steel substrates.

4.2. Experimental Procedures

4.2.1. Raw Materials and HVOF Feedstock Preparation

A nominally spherical, agglomerated and sintered, TiC-Ni_3Al powder (lot no. AE 10385-SNT; D_{50} = 27.3 μm) was custom manufactured by Oerlikon Metco for the purpose of this study; this powder, and the related coatings, are subsequently referred to as "AS TiC-Ni_3Al", as an abbreviation for 'agglomerated and sintered'. For the gelation-based feedstock, subsequently referred to as "GEL TiC-Ni_3Al", the TiC-Ni_3Al mixture was produced from a TiC source powder (lot no. PL20125339; D_{50} = 1.25 μm [289]), acquired from Pacific Particulate Materials (Vancouver, BC, Canada). The fine TiC was blended with a metal binder mixture, where the Ni_3Al was effectively generated *in-situ* during HVOF thermal spray through reaction sintering of a mixture of Ni and Ni_xAl_y. The Ni powder (lot no. L10W013; 2.2 - 3.0 μm) and Ni_xAl_y powder (lot no. D28X029; D_{50} = 38 μm) were both provided by Alfa Aesar (Ward Hill, MA, USA); the Ni_xAl_y powder exhibited a composition with a 1:1 elemental weight ratio. Appropriate amounts of the TiC ceramic powder were mixed with the corresponding Ni and Ni_xAl_y powders to prepare the final cermet powder blend. Each composition was then ball milled with yttria-stabilized zirconia media in acetone for 24 hours, followed by a 24-hour drying period. The process to fabricate the gelation-based feedstock is discussed in greater detail in a prior publication [160]. However, briefly, the procedure involves the preparation of a stabilized aqueous

suspension, at a solid loading of 50 vol.%; the suspension is adjusted to ~pH = 8.5, with the addition of Darvan® C-N (0.1 wt.%) as a polyelectrolyte dispersant. To promote the gelation process, 1.6 wt.% sodium alginate is added to the suspension as a fine powder, which readily dissolves. The stabilized suspension is then further ball milled for 24 hours, and then sprayed through a system that generates fine aerosol droplets of the aqueous mixture. This spray is directed into a bath of 0.5 M calcium chloride ($CaCl_2$) dissolved in distilled water (25ml/L). Ca^{2+} ions from the $CaCl_2$ then undergo an ion exchange process with the Na^{1+} ions within the solution. The chemical compositions of the HVOF feed-stock powders were determined using inductively coupled plasma optical emission spectroscopy (ICP-OES), and values are presented in Table 9. The mean particle sizes were determined using a Malvern Mastersizer system (Mastersizer 3000, Malvern Instruments, Malvern, UK), and this information is also provided in Table 9.

4.2.2. HVOF Thermal Spraying

The AISI 3140 substrate (150 mm x 38.1 mm x 1 mm coupons) were first cleaned with acetone, and the surface of each panel was then prepared by grit blasting with fine SiC particles (60 grit) to increase the adherence between the cermet coating and substrate. The HVOF gun (Diamond Jet hybrid gun, Sulzer Metco, Westbury, NY), then was programmed for a hydrogen/oxygen ratio of 1300/500 SCFH. Feed stock powders then were fed to the system at 12 RPM (25 gr/min) with 75 SCFH argon as a carrier gas. The fuel gas is mixed with oxygen in the HVOF gun and ejected from a nozzle and form a circular flame, in order to uniformly heat the powder as it exits the gun, with the heated powder then propelled

towards the grit blasted surface of the coupons. The feed-stock powders were subsequently deposited on the steel 4130 coupons at various spraying distances, from 203.2 to 304.8 mm (i.e., 8" to 12") until a satisfactory coating thickness was acquired. The majority of data subsequently presented is for an HVOF spraying stand-off distance of 228.6 mm (9").

Table 9. a) Average chemical compositions of the AS TiC-Ni_3Al and GEL TiC-Ni_3Al feedstock powders, together with their mean particle sizes and b) Average chemical compositions of the AS WC-Co and WC-CoCr feed stock powders

Identification	Production method	D_{50} (µm)	Chemical composition (wt.%)				
			Ni	Al	Ti	C	Other
AS TiC-Ni_3Al	**Agglom. /Sinter.**	27.3	32.83	4.34	Bal.	11.45	0.28
GEL TiC-Ni_3Al	**Gelation**	25.5	34.88	5.24	Bal.	12.38	3.26

(a)

Identification	Production method	D_{50} (µm)	Chemical composition (wt.%)				
			Co	Cr	W	C	Other
WC-Co	**Agglom. /Sinter.**	**47**	**12.26**	**-**	**82.21**	**5.41**	**0.21**
WC-CoCr	**Agglom. /Sinter.**	**53**	**10.54**	**4.7**	**79.14**	**5.37**	**0.25**

(b)

Sprayed samples were subsequently sectioned perpendicular to the deposited surface using a precision saw and then subjected to appropriate mounting and metallographic preparation for characterisation of their surfaces and cross-sections. Microstructural characterization was conducted using scanning electron microscopy (SEM; Model S-4700, Hitachi High Technologies, Toyko, Japan) with energy dispersive X-ray spectroscopy (EDS; Inca X-maxN, Oxford Instruments, Concord, MA, USA) also utilised for compositional analysis in the SEM. Phase analysis of the composition of the fabricated thermally sprayed coatings, as well as the as-received substrate, was identified by means of X-ray diffraction (XRD) investigations, (model AXS D8 Advance, Bruker Corp., Billerica, MA, USA) using Cu Kα radiation with an associated wavelength, λ, of 1.5406 Å.

For corrosion assessment, electrochemical measurements were conducted using a potentiostat/galvanostat (EG & G Model 273A, Princeton Applied Research, TN, USA) combined with an associated frequency response analyzer (Solartron Model 1250, Schlumberger, TX, USA). Corrosion tests were performed using a three-electrode flat cell, with the sample as the working electrode. The counter electrode that was employed was a platinum mesh (Pt), with a saturated calomel electrode (SCE; -0.241 V vs. a standard hydrogen electrode) applied as the reference. The aqueous-based electrolyte was prepared using 3.5 wt.% NaCl addition into distilled water. The test surface area of the working electrode was 1 cm^2 which was modified to approximately 0.3 cm2 for the single-phase Ni_3Al following the approach of Hochstrasser-Kurz [328]for the calculations of the corrosion rate according to the associated ASTM Standard (G102-89: *Standard Practice for Calculation of Corrosion Rates and Related Information*) [329]. Prior to each polarisation measurement, a minimum of 1-hour immersion in the electrolyte was

conducted to determine the open circuit potential (OCP). Each sample then was polarised with scan rate of 0.1667 mV/s, scanning from a potential of -0.3 V (vs. OCP) to +1.0 V (vs. SCE) for all of the examined the compositions. The corrosion current density (i_{corr}) and potential (E_{corr}) were subsequently determined through an instantaneous Tafel-type fit analysis software (CorrView Version 2.8, Scribner Associates, Inc., Southern Pines, SC, USA). This process involves simulating the Tafel curve through fitting four parameters of the Tafel equation, specifically both the anodic and cathodic Tafel slopes (β_a and β_c, respectively), as well as i_{corr}, and E_{corr}. Subsequent refinements to these parameters are then applied, in order to minimise the sum of the differences of the current values for the real and simulated curves. To assess reproducibility, 3 to 5 samples were tested for each of the HVOF samples. Post-corrosion, potential modification of the surface composition was assessed for each sample using EDS analysis within the SEM. Changes in the electrolyte pH values after each test were also measured, using a portable pH meter (model E488, Metrohm Canada Inc., Mississauga, ON, Canada). The post-corrosion electrolyte was also compositionally analysed using inductively coupled plasma atomic emission spectroscopy (ICP-OES; model Varian Vista Pro, CA, USA). To achieve this, the recovered electrolyte was first filtered through a 1.5 μm size membrane filter (ProWeigh®, Environmental Express, Charleston, SC, USA), which allows for the separation of solid material from the filtered solution. The recovered solids were subsequently dried in an oven (model Isotemp™, Fisher Scientific Co., Ottawa, ON, Canada) at 105°C, prior to a 'total acid leach' digestion technique (using a sequence of HF, HNO_3, $HClO_4$, and HCl acids).

The wear response of the thermal spray coatings was evaluated under reciprocating sliding conditions. Wear tests were conducted using a ball-on-flat testing geometry, on a universal

micro-tribometer testing platform (UMT; Model UMT-1, Bruker Corp., Campbell, CA, USA). The counter-face sphere material was a WC-6 wt% Co 'hardmetal' composition, with the spheres being 6.35 mm in diameter. Reciprocating wear tests were then performed under applied loads of 20 to 60 N, in 20 N increments. Dry sliding was carried out at room temperature (21 ± 2 °C) and with a relative humidity of 40-50 %, with tests conducted for 15 minutes at a frequency of 10 Hz. The track length for reciprocating wear tests was 5.03 mm, consequently generating a total sliding distance of 95.4 m for each individual test.

The reciprocating wear responses were subsequently characterized using a combination of SEM, and EDS, together with optical profilometry using a confocal laser scanning microscope (CLSM; VK-X200/X210, Keyence, Mississauga, ON, Canada). This technique was used to measure the depth of each wear and scratch track and to calculate the volume of material that was removed under the evaluated wear conditions for reciprocating sliding, thus allowing the specific wear rate to be calculated.

4.3. Results and Discussion

4.3.1. Feedstock Characterisation

Figure 42 presents typical SEM images obtained from both of the TiC-Ni_3Al feed-stock powders, manufactured through agglomeration and sintering (Figure 42 (a,b)), and gelation (Figure 42 (c,d)). In both cases the feedstock powders are broadly rounded in shape. In the case of the agglomeration and sintered powder, occasional examples of fractured particles are clearly present (highlighted in Figure 42 (b)). While the gelation-based feedstock has a broadly similar morphology, greater evidence of fine particulate matter is apparent, which

is not ideal from the perspective of powder feeding. Furthermore, the gelation-derived feedstock is somewhat more irregular in terms of the overall particle shape, deviating more from spherical.

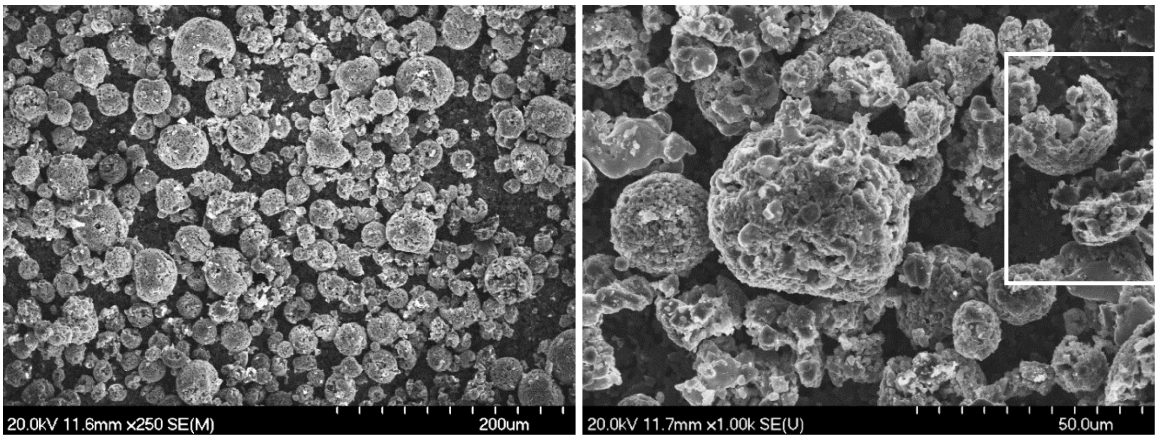

(a) (b)

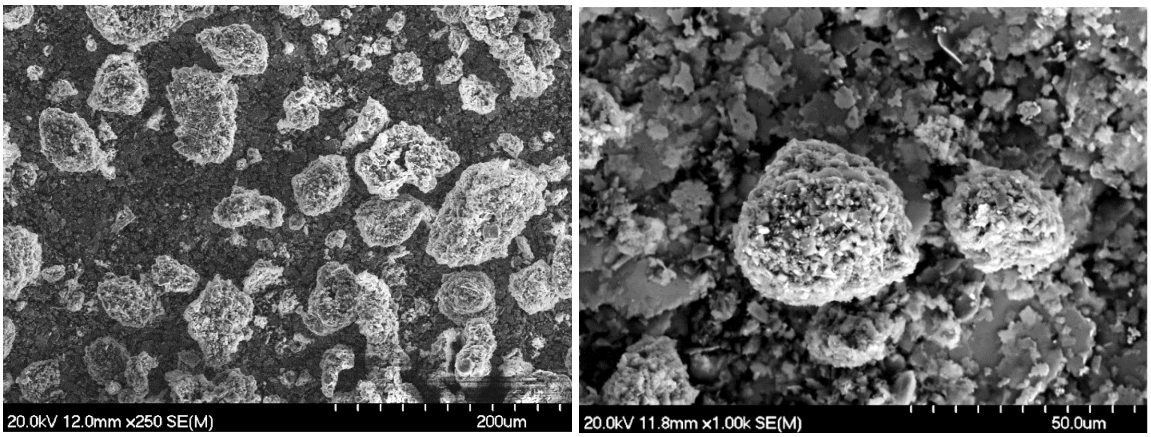

(c) (d)

Figure 42. SEM micrographs obtained from TiC-Ni_3Al feed-stock cermet powder manufactured through: (a,b) agglomeration and sintering (AS), and (c,d) gelation-based (GEL) feed stock technology. Images are shown at lower (a,c) and higher (b,d) magnifications, in each case. Fractured particles are highlighted in (b) for the AS powder.

4.3.2. Coating Morphology and Phase Identification

Micrographs obtained from the cross sections of the as-sprayed HVOF coatings, deposited onto 4130 steel substrates, are shown in Figure 43. Microstructural examination of the manufactured specimens confirmed the successful deposition of coatings using both of the TiC-Ni_3Al feedstock powders (AS and GEL), with well-adhered splats and the presence of a few isolated, globular-shaped pores; to a certain extent, these pores are likely to be ceramic grains pulled out from the coating during metallographic preparation. However, it is also important to note that the powders produced via gelation exhibited a comparatively lower flowability in the HVOF gun, when compared to the conventional agglomeration plus sintering feedstock, which resulted in periodic clogging of spraying nozzle and consequently slightly higher levels of porosity; application of a post-gelation heat-treatment of the feedstock powders, in order to avoid such issues, is described in a prior study [330]. For each of the coatings, a lamellar splat structure is observed, with occasional inclusions of partially melted particles and oxides (dark contrast phase), which are a common characteristic of such coatings when sprayed in air. The shape of the residual pores with both types of feedstock powder suggests the presence of coalesced splat/splat boundaries, which are a consequence of metallic bonding/solidification and then re-melting upon the arrival/bonding of a subsequent droplet.

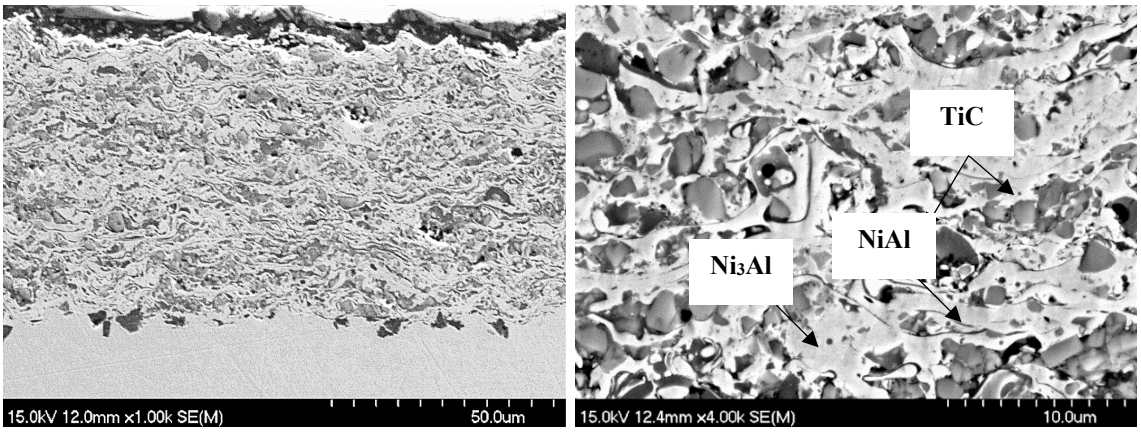

(a) (b)

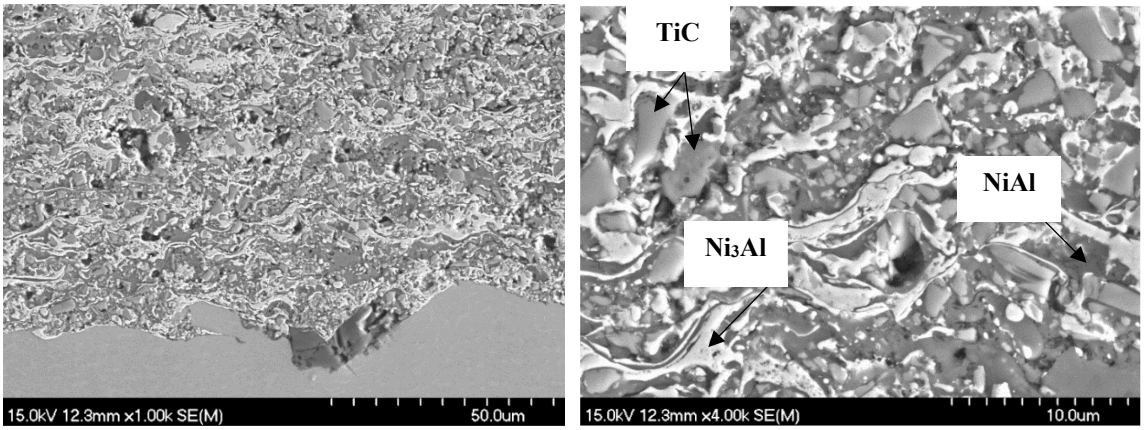

(c) (d)

Figure 43. Representative SEM micrographs obtained from the HVOF-deposited thermal spray coatings prepared from: (a,b) the AS feedstock powder, and (c,d) the GEL feedstock powder. The SEM images are shown at lower (a,c) and higher (b,d) magnifications, in each case.

The results of EDS analysis on the GEL TiC-Ni_3Al coating confirmed that the internal oxides are mostly formed from Al (and possibly Ni), which is known to take place during the interaction of the molten layer/atmosphere with the one deposited beneath, throughout

the deposition of thin lamellar layers (Figure 44). Furthermore, the formation of oxide particles is related to process dwell time and particle temperature. It has been reported that the thickness of these oxide 'stringers' increases with increasing dwell time and particle temperature [70].

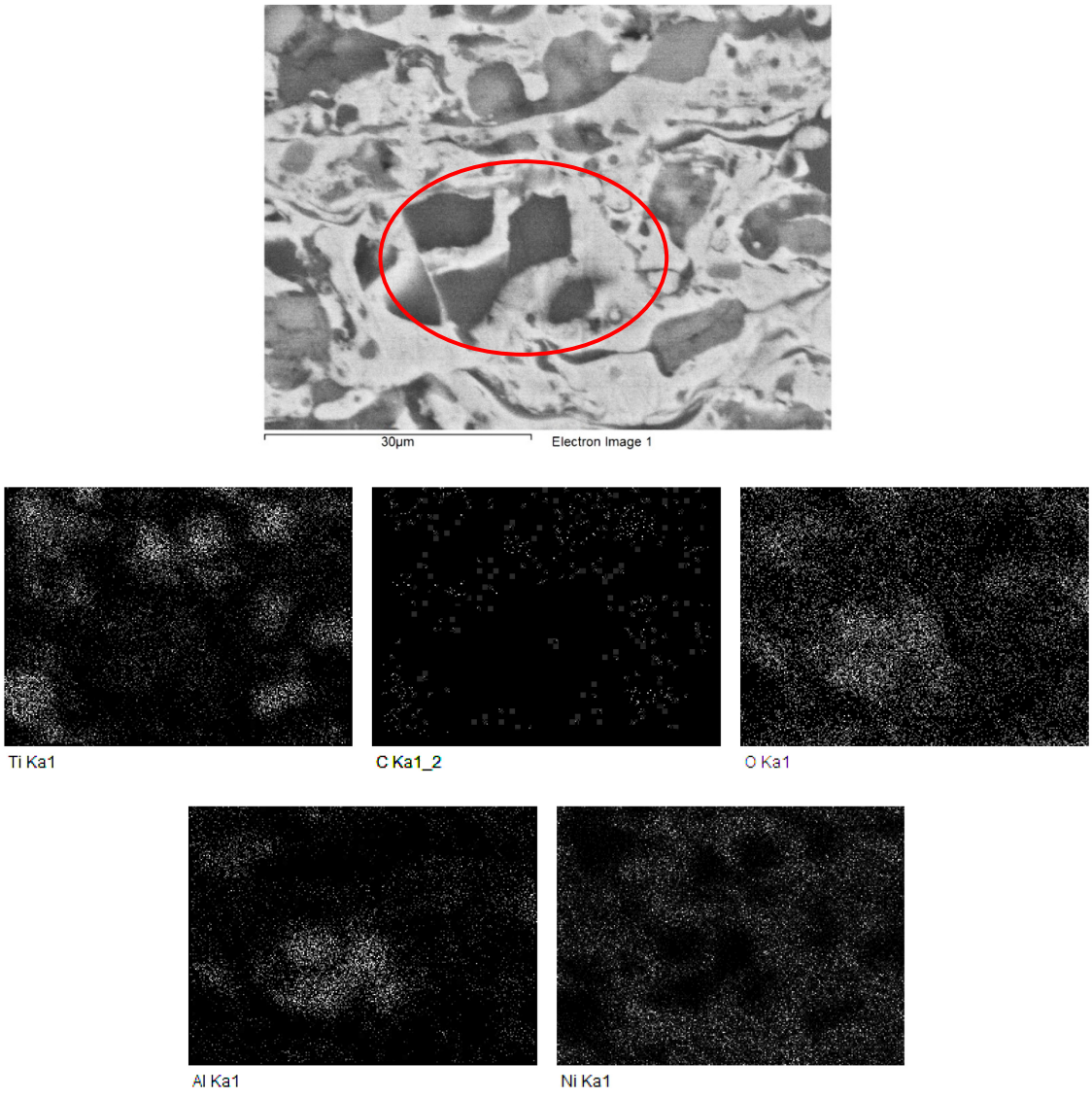

Figure 44. Phase identification from EDS mapping obtained on the cross section of the HVOF Gel TiC-Ni_3Al coating, highlighting Al_xO_y-rich regions (shown circled).

The results of x-ray diffraction analysis on as the as-sprayed AISI steel 4130 substrates, is provided in Figure 45. XRD peaks obtained from HVOF sprayed surfaces at all the stand-off distances confirmed the presence of TiC predominant peaks, while the intensity of the Ni_3Al peaks increased dramatically as stand-off distance was increased. This is attributed to longer in-flight intervals at lower speeds and as a result more time to react. Furthermore, no oxides were detected in the XRD characterization confirming the absence of significant oxidization or decomposition.

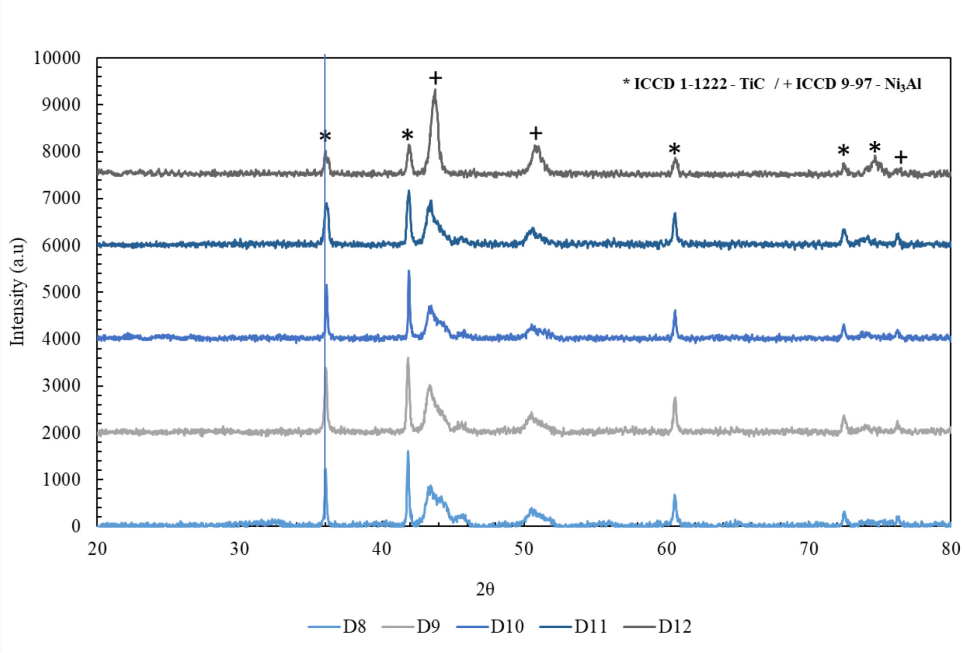

Figure 45. XRD trace obtained from the polished surface of the as-sprayed AISI-Steel 4130 categorized based on the stand-off distance of the HVOF process.

4.3.3. Electrochemical Measurements

Figure 46 illustrates the open circuit potential (OCP) curves recorded from both types of TiC-Ni_3Al cermet coating (AS and GEL) on a 4130-grade steel substrate (Figure 4(a)),

along with examples of the potentiodynamic polarization curves obtained for these coating using an aqueous electrolyte with 3.5 wt.% NaCl, from -0.03 V vs. OCP up to +1 volts vs. reference (Figure 46 (b)). Representative examples of both the WC-Co and WC-CoCr baseline coatings are also shown in Figure 46 (a,b) for comparison to the TiC-Ni_3Al coatings. The corrosion behavior of the TiC-Ni_3Al HVOF coatings is characterized by a true passivity regime, with associated current densities ≤1 μA/cm^2 [331]. Both types of TiC-Ni_3Al feed stock reached their passivation current at a potential of ~200 mV vs. SCE, while coatings sprayed from the gel-based powder also exhibited a trans-passive region at an applied potential of ~600 mV vs. SCE. This type of coating exhibits a visible level of degradation that occurs over the trans passive region, through selective dissolution of the metallic matrix due to galvanic coupling between the ceramic and intermetallic phases. Consequently, broadly speaking, the overall corrosion mechanisms tend to stay the same for essentially all the cermet coatings.

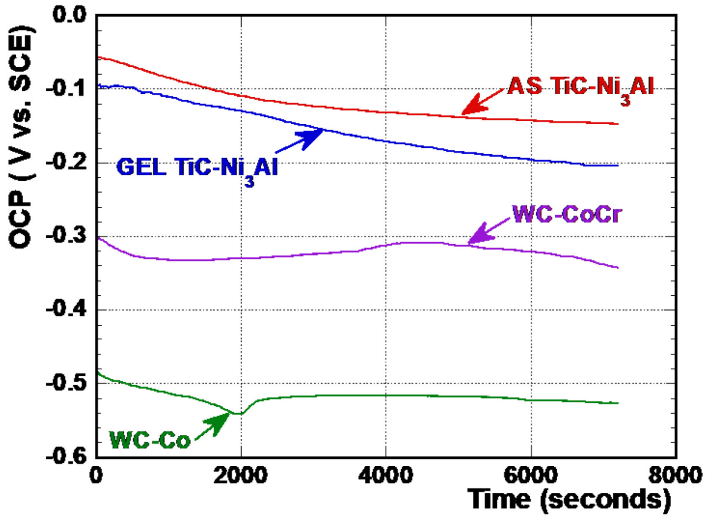

(a)

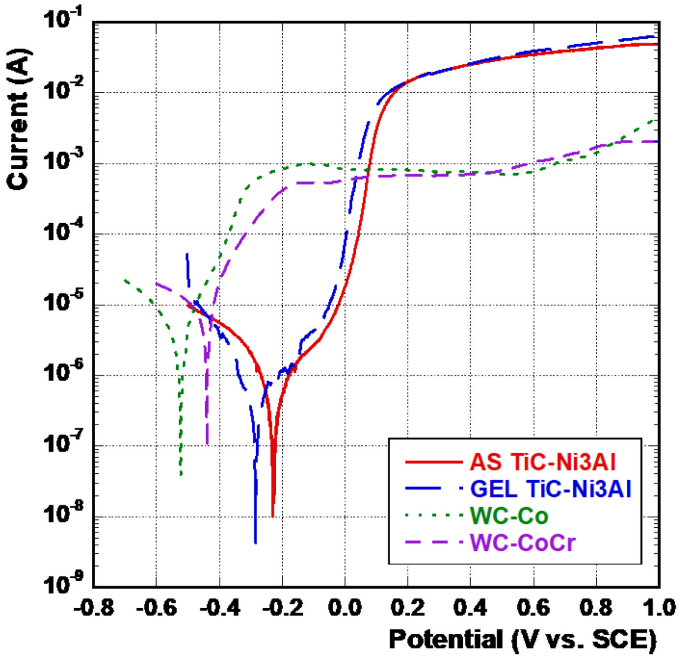

(b)

Figure 46. (a) Representative OCP curves obtained for the TiC-Ni_3Al based cermet coatings, on a 4130-steel substrate, after a 1 h stabilization period in 3.5 wt.% NaCl aqueous media. (b) Representative potentiodynamic polarisation curves obtained for the TiC-Ni_3Al based cermet coatings, on a 4130-steel substrate, after a 1 h stabilization period in 3.5 wt.% NaCl aqueous media. For comparison, WC-based cermet coatings (WC-Co and WC-CoCr) fabricated and tested under the same conditions are also shown.

The average corrosion parameters for each of the cermet materials (presented in Table 10) were determined from the polarisation curves, including the corrosion potential, E_{corr}, the resultant current density at the corrosion potential, i_{corr}, and the current density when passivation arises, i_{pass}. The corrosion rate was then calculated for the exposed surface area following the ASTM standard, G102-89, Standard practice for calculation of corrosion rates and related information, modified solely based on the 'active' material, namely the

Ni_3Al binder for the as-sprayed composition [329]. It is apparent from the potentiodynamic polarisation curves that the TiC-Ni_3Al based cermet coatings offer a greater degree of protection, compared to both the WC-Co and WC-CoCr coatings, with lower corrosion rates. Furthermore, as noted earlier, the TiC-Ni_3Al coatings possess a significantly lower theoretical density and do not contain chromium.

Table 10. Average corrosion parameters for the HVOF sprayed TiC-Ni_3Al coatings in comparison to those based on WC hardmetals.

Coating type and composition	E_{corr} **(± 5 x 10^{-2})**	i_{corr} **(± 1 x 10^{-7})**	i_{pass} **(± 2x10^{-1})**	**Corrosion rate (± 6 x 10^{-4})**	**Corrosion rate - active phase (± 4 x 10^{-3})**
	V (vs. SCE)	**A/cm^2**	**A/cm^2**	**mm/yr**	**mm/yr**
GEL TiC-Ni_3Al	-0.32	2.2 x 10^{-6}	1.9 x 10^{-2}	1.6 x 10^{-2}	4.1 x 10^{-2}
AS TiC-Ni_3Al	-0.27	3.4 x 10^{-6}	1.3 x 10^{-1}	1.4 x 10^{-2}	3.4 x 10^{-2}
WC-Co	-0.52	5.3 x 10^{-6}	6.9 x 10^{-4}	2.4 x 10^{-2}	3.0 x 10^{-1}
WC-CoCr	-0.44	1.8 x 10^{-5}	5.3 x 10^{-4}	1.4 x 10^{-1}	1.4 x 10^{-1}

Figure 47 illustrates examples of the post corrosion cross sections of the TiC-Ni_3Al coatings sprayed using both the agglomerated and sintered and the gelation derived feedstocks. As has been outlined in previous work [315,316,324,328], cermets are generally susceptible to aqueous corrosion through active dissolution of the metallic matrix and subsequent weakening of the nominally ‘three-dimensional’ ceramic network

structure. Microstructural observations for the present coatings show that the oxidation reaction initiates in local sites, such as pores, and becomes galvanically active in the presence of Cl ions in both TiC-Ni_3Al coatings. Further oxidation through galvanic corrosion has resulted in dissolution of the metallic phase at the interface with the carbide grains (i.e., TiC) and loss of the material to the electrolyte prior to eventual passivation of the surface. This was more noticeable in coatings prepared using the gelation technique (GEL TiC-Ni_3Al), which were previously noted to exhibit an undesired flow performance within the HVOF gun during spraying. The SEM micrographs in Figure 47 show that the oxidation attack for both types of powder is initiated on the interface of metallic matrix and carbide grains. However, the extent of attack is highly dependent upon the density of pores and pre-existing surface flaws when both types of feedstock powder are compared.

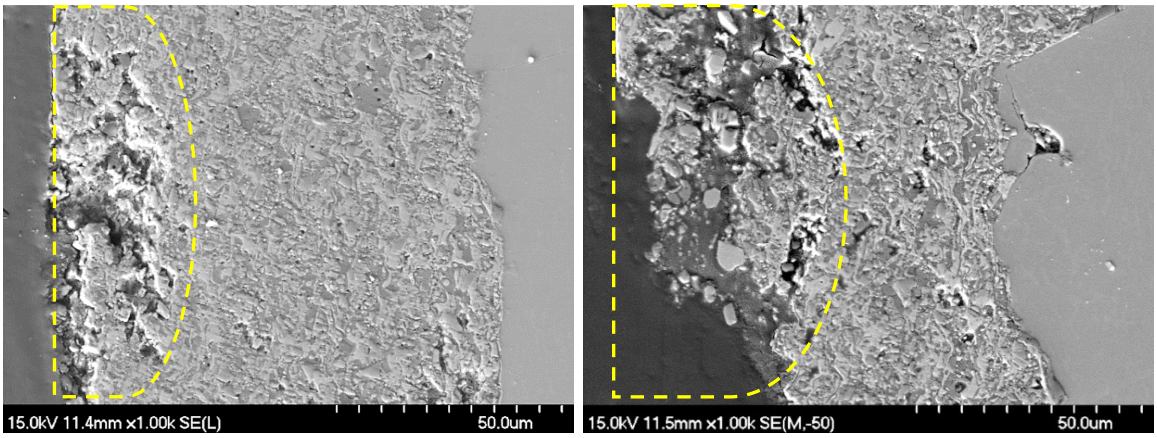

Figure 47. Representative SEM images obtained from the post-polarised surfaces of HVOF thermal sprayed TiC-Ni_3Al highlighting the depth of oxidation during potentiodynamic polarisation tests: (a) AS TiC-Ni_3Al, and (b) GEL TiC-Ni_3Al. The 4130-steel substrate is shown on the left-hand side of both images.

EDS analysis was used to assess the variation of coating composition both before and after corrosion evaluation (Figure 48). The chemical compositions of the post-corrosion surfaces showed an increase in Ti, C, O, and Al. In contrast, Ni was notably depleted post-corrosion; it should be noted that EDS analysis of a non-planar surface is not an optimal evaluation condition, however, this does highlight the general loss of Ni and (to a lesser extent) Al. The EDS analysis has confirmed that a protective oxide layer is formed, which is mostly composed of TiO_{1-x} and Al_2O_3. Moreover, dissolution of the binder leaves behind a carbide skeleton arrangement, which exhibits a much larger exposed surface area in comparison to the as-sprayed coatings.

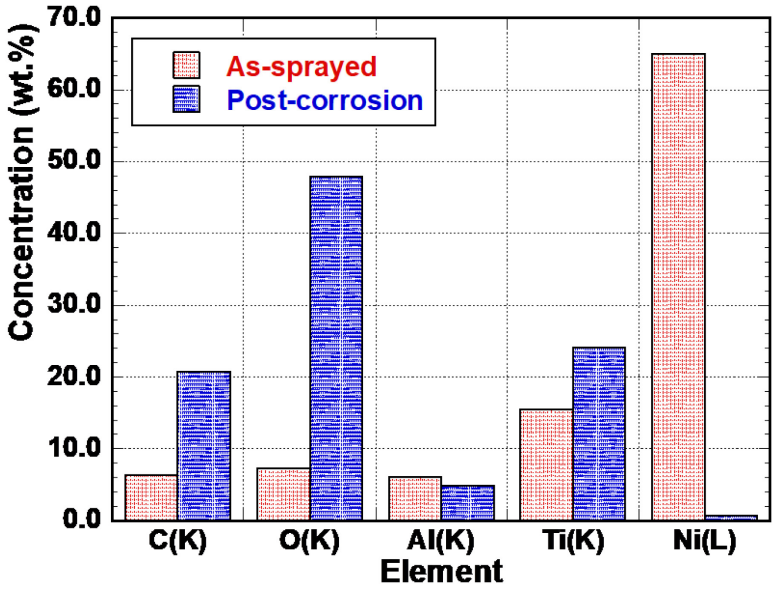

(a)

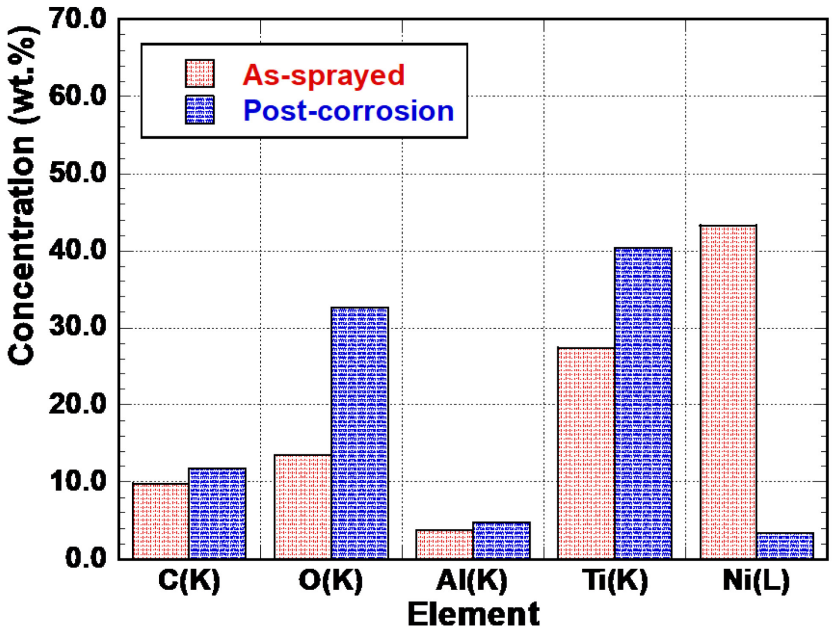

(b)

Figure 48. Results of EDS analysis on the pre- and post-corrosion (i.e., after potentiodynamic polarisation) surfaces of the HVOF thermal sprayed TiC-Ni_3Al coatings for: (a) AS TiC-Ni_3Al, and (b) GEL TiC-Ni_3Al.

4.3.4. Sliding Wear Behaviour

Examples of the dynamic coefficient of friction (COF) curves obtained from the reciprocating wear tests using both types of TiC-Ni_3Al feedstock powder, HVOF sprayed onto 4130 steel substrates, are presented in Figure 49. Both coatings exhibited the least amount of COF fluctuation at the lowest applied load (20 N), over the full duration of the wear tests, with the degree of COF variation increasing with the applied load. Coatings that were sprayed using the agglomerated and sintered TiC-Ni_3Al feed-stock powder exhibited slightly higher variations in COF at the lowest load (20 N), while steady state conditions

were obtained at a relatively faster rate for higher loads of (40 N and 60 N). Typically, steady state is reached once enough volume of the coating has been removed to form a coupled surface, which results in frictional forces without interference from any surface asperities that may be present on either face. This can be further enabled through the formation of a tribolayer. A summary of the mean COF values determined through the UMT-1 software are shown in Figure 49. It is apparent that there is considerable scatter in the TiC-Ni_3Al values, reflecting the developmental stage of coating production. To contrast these values for the COF, bulk TiC-Ni_3Al cermets with broadly similar compositions (i.e., with stoichiometric Ni_3Al contents varied from 20 to 40 vol.%), showed steady state COF values within the range of 0.45 to 0.55 [25], which are notably lower than for the present HVOF coatings. A number of factors may play a role in this difference, notably the anisotropic, splat-type morphology of the HVOF coatings as well as their higher oxide contents, and also the broadly finer grain size noted for the bulk cermets relative to the coatings, which may promote a more rapid tribolayer development. It is also notable that the WC-Co baseline presents the lowest coefficient of friction in this instance, although the wear rates of the four materials are broadly comparable, as shown in Figure 50. When assessing wear, it is important to keep in mind the greater stiffness of the WC-based materials, due to the intrinsically higher elastic modulus of WC relative to TiC (i.e., ~690 GPa [332] vs. ~400 GPa [333,334].)

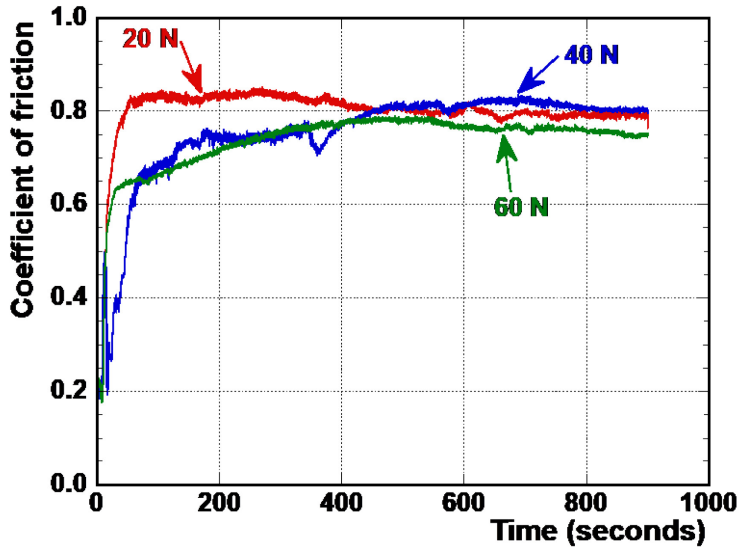

(a)

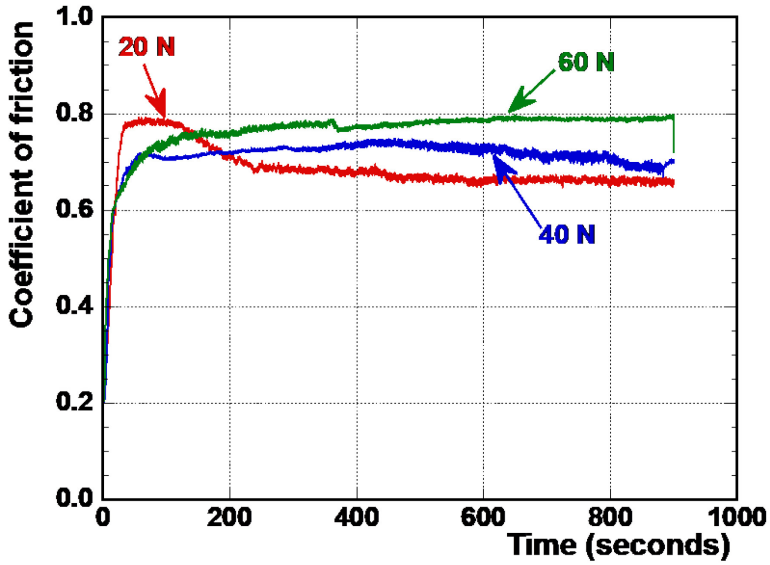

(b)

Figure 49. The dynamic COF responses as a function of applied load for the TiC-Ni_3Al cermet coatings using: (a) AS feedstock, and (b) GEL feedstock.

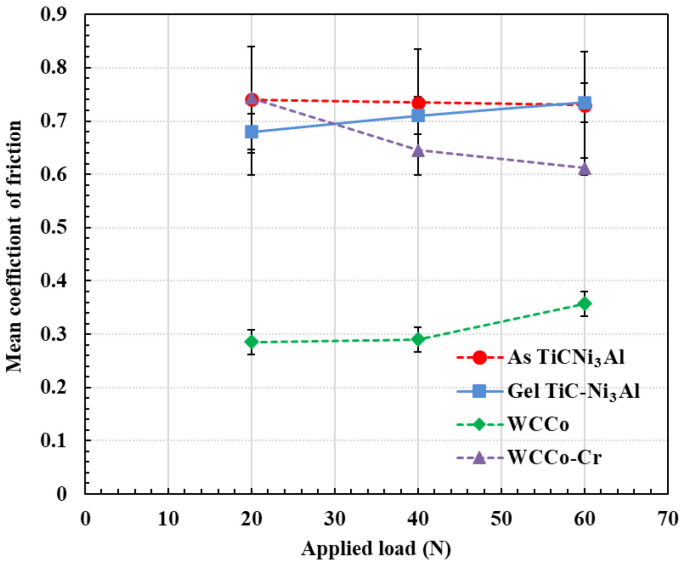

Figure 50. Steady state coefficient of friction values for the TiC-Ni_3Al and WC-based cermet coatings applied onto 4130 steel substrates under 20 N, 40 N, and 60 N applied loads.

The specific wear rates determined for the HVOF sprayed TiC-Ni_3Al and WC-based coatings, deposited onto 4130 steel substrates, under applied loads of 20 N, 40 N and 60 N, are presented in Figure 51. In this instance, the specific wear rate, k_W, for each coating was calculated from the wear track volume using the Lancaster approach:

Equation 14

$$k_W = \frac{V}{PD}$$

where V represents the total volume of material that was removed from the wear track (in mm^3), P is the applied normal force during the test (in N), and D is the total sliding distance for each test (in m). Broadly speaking, lower wear rates were observed for the TiC-Ni_3Al

based cermet coatings fabricated from the commercially produced agglomerated and sintered feedstock powder. The specific wear rates did not show any clear trend with increasing applied load. While there is a moderate degree of scatter, it is notable that these wear rates compare quite closely with bulk TiC-Ni_3Al cermets [285], which were ~0.5 x 10^7 mm^3/Nm, highlighting the promise of these coatings. Furthermore, the bulk cermets exhibited specific wear rates that were largely independent of applied load between 20 N and 60 N; in contrast, the specific wear rates for the GEL TiC-Ni_3Al HVOF coatings do continuously increase within the same range of load.

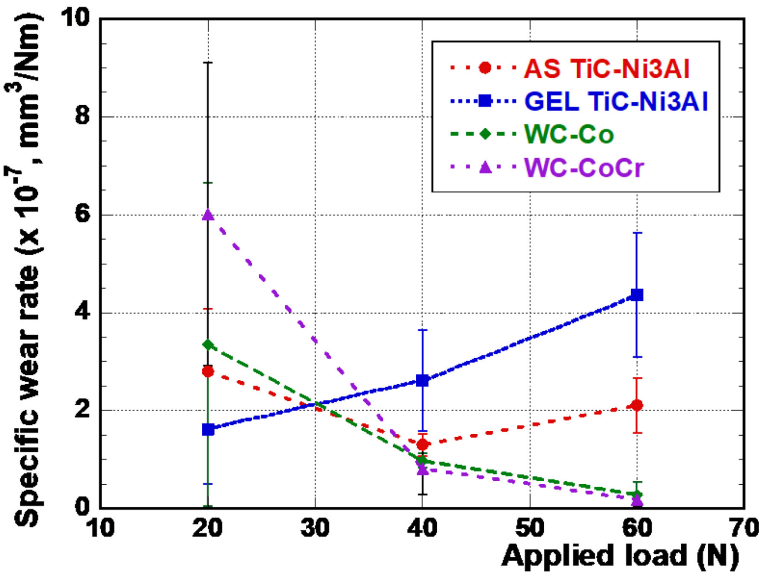

Figure 51. Calculated wear rates for the TiC-Ni_3Al and WC-based cermet coatings applied onto 4130 steel substrates under 20 N, 40 N, and 60 N applied loads.

The type and severity of wear mechanism(s) were identified by subsequent microstructural observations, for example the extent of damage accumulation both within and in the vicinity of the wear track, and the formation/amount of tribolayer that has been generated

during the reciprocating sliding process. Figure 52 shows example SEM images obtained after wear testing, at 40 N applied load, from the surfaces of the TiC-Ni_3Al coatings (both AS and GEL) deposited onto 4130 steel. Figure 52 shows that the formation of a tribo-layer is readily apparent (as it was for all examined loads), and the extent of this formation broadly increased with increasing applied load. Microstructural observations of the worn surfaces show the formation of fine, shallow grooves which are generated in result of two-/three-body abrasion with the indenter tip and wear debris fragments. Additionally, at loads above 20 N some lamellar spallation of the tribo-layer was identified, regardless of the feedstock powder production technique for the TiC-Ni_3Al coatings.

No evidence of microstructural damage in the regions immediately adjacent to the wear track was observed. Prior studies have shown that this lack of damage and, in particular, the absence of evidence of oxidation adjacent to the wear track indicates the frictional forces do not achieve high enough temperatures to generate high temperature oxidation damage [286].

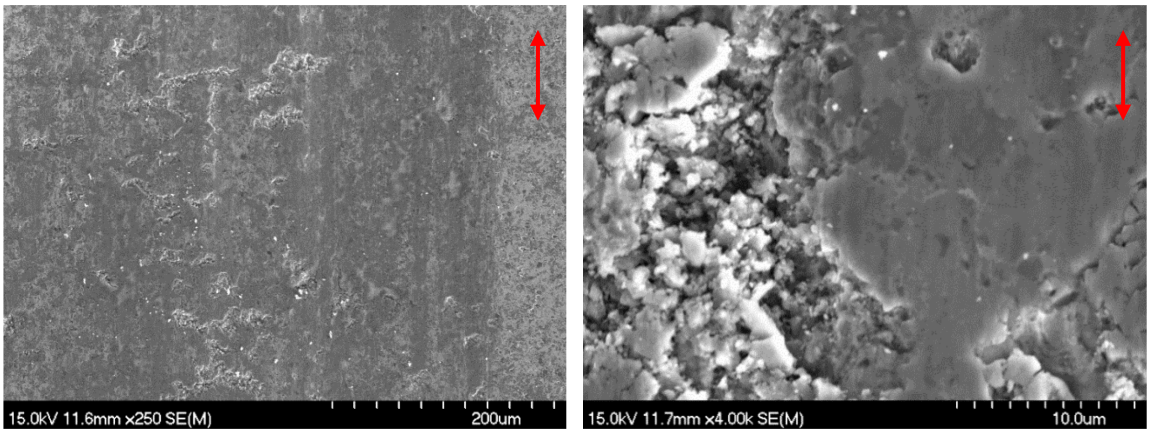

(a) (b)

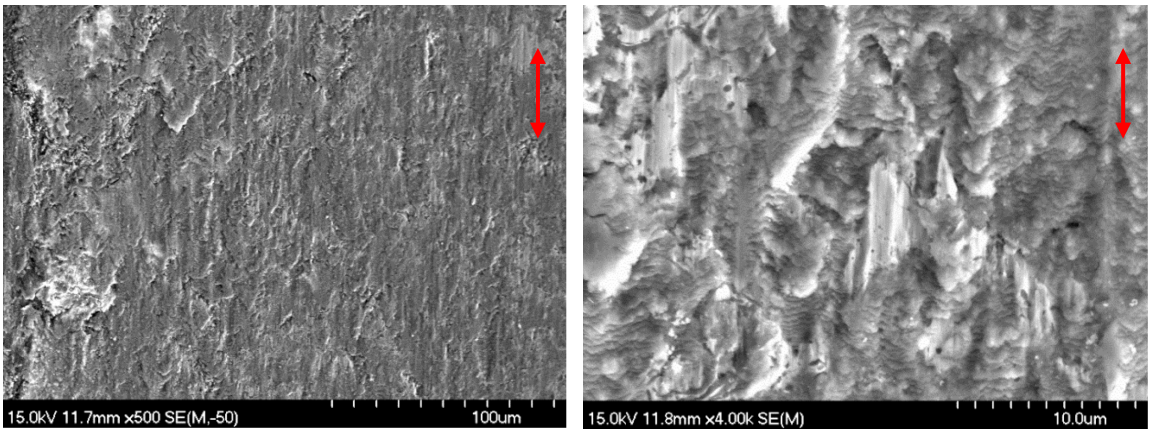

(c) (d)

Figure 52. SEM images obtained from the post wear test surface of HVOF sprayed TiC-Ni_3Al coating on 4130 steel (at 40 N applied load), for the AS-based HVOF feedstock: (a) lower magnification, and (b) higher magnification image of damage. SEM images obtained from post-wear tested (at 40 N applied load) surface of HVOF sprayed TiC-Ni_3Al coating on 4130 steel, GEL-based HVOF feedstock: (c) lower magnification, and (d) higher magnification image of damage. The sliding direction is represented by the red arrows in each case.

Figure 53 demonstrates the tribolayer is greater detail, with associated EDS mapping of the composition within the layer. It is apparent that there is increasing oxygen incorporation into the tribolayer layer with increasing applied load during reciprocating wear. As noted in prior studies on bulk TiC-Ni_3Al and Ti(C,N)-Ni_3Al cermets [285,286], mechanical attrition arises during the wear test, with debris continuously refined under the moving counter face, resulting in an increasing oxygen content through continuous exposure of clean faces on the debris and their subsequent passivation.

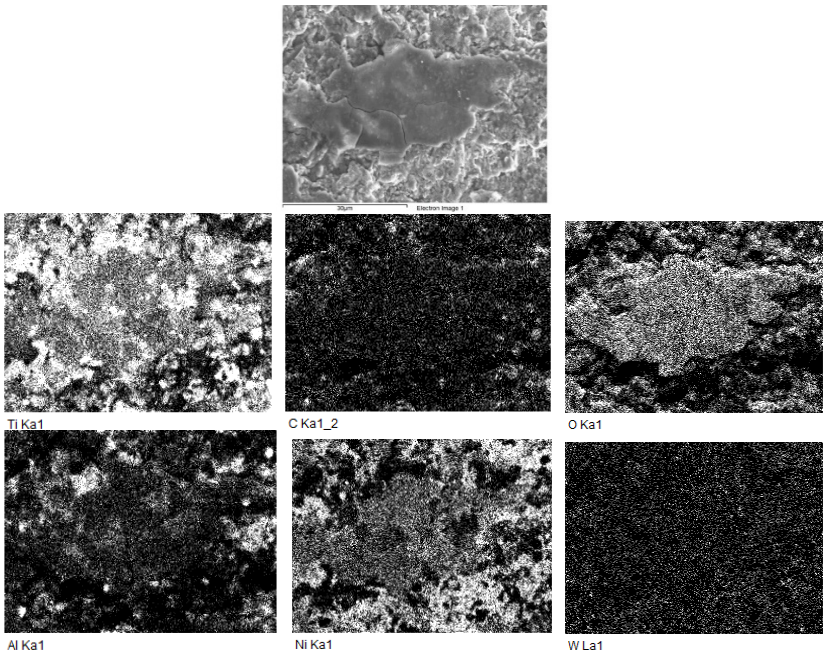

(a)

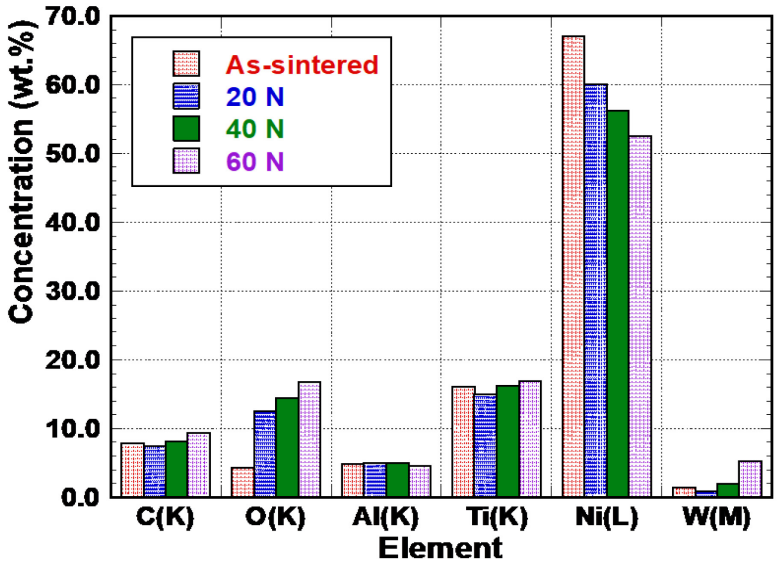

(b)

Figure 53. Phase identification from EDS mapping obtained on the cross section of the HVOF GEL TiC-Ni_3Al coating, highlighting the composition of formed tribo-layer within the wear track.

Cross sectional characteristics of the tribo-layer were confirmed by excision of small volumes of material through FIB milling, as shown in Figure 54(a) for the gel based feedstock powder, to allow observation of the cross-section through the tribolayer and sub-surface region. The use of FIB allows sub-surface damage to be observed without requiring significant sectioning and, in particular, allows the sub-surface observation of different orientations within a single wear track, which is not really feasible with large scale sectioning. In this instance, it is apparent that the sub-surface coating integrity is largely retained, with minimal evidence of cracking (Figure 54 (b)); in this instance, one minor crack may be apparent, which seems to be associated with a porous region within the coating itself. SEM micrographs obtained from cross section of milled wear tracks were characterised by the formation of distinctive pits at point of brittle fracture. These pits are often associated with lamellae spallation and are likely responsible for increased wear rates under higher loads. The SEM and EDS examination of cross sections of the HVOF surface layer, through the wear generated tribo-layer, revealed formation of an intermediate layer containing fine particles of both phases.

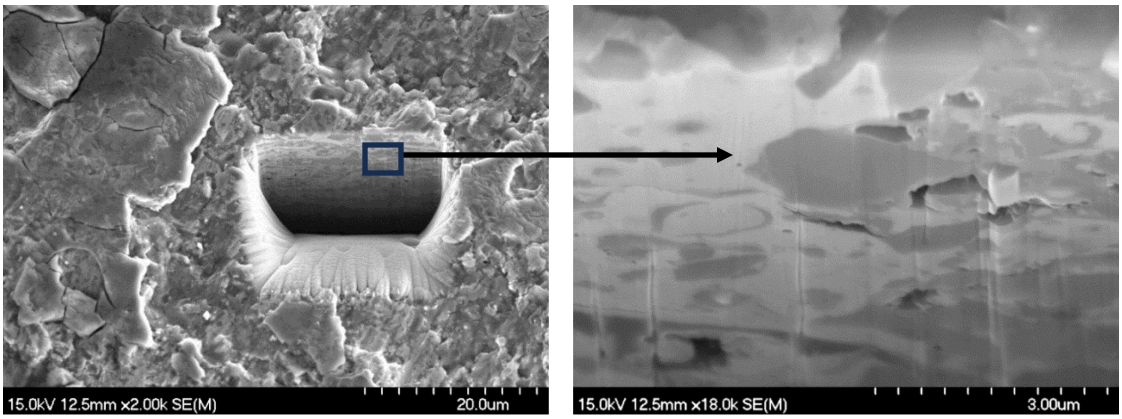

(a) (b)

Figure 54. (a) High magnification SEM image of a FIB generated cross-section for the tribo-layer formed on HVOF sprayed TiC-Ni_3Al coating on 4130 steel substrates at 60 N; the sliding direction is represented by the red arrow. (b) Associated SEM image of the cross-section through the tribo-layer, formed on HVOF sprayed TiC-Ni_3Al coating on 4130 steel substrates at 60 N, for the FIB cut shown in (a), highlighting subsurface integrity and possible minor evidence of lamellar cracking.

4.4. Conclusions

In the present work, initial 'development-stage' TiC-Ni_3Al based cermet coatings have been manufactured through HVOF thermal spray, specifically comparing a novel gelation-based feedstock preparation route to a standardized agglomeration and sintering method. Furthermore, comparison has been made with more conventional WC-Co and WC-CoCr HVOF coatings. The following conclusions can be drawn from the present work.

- Development-stage TiC-Ni_3Al based cermet coatings offer a greater degree of aqueous corrosion protection when compared to both the WC-Co and WC-CoCr

coatings, with the further benefits of significantly lowered theoretical density and an absence of Cr in their overall composition.

- The TiC-based HVOF coatings, regardless of their feedstock production technique (agglomerated and sintered, versus gelation), were found to be superior to the traditional WC-based hardmetal coatings by exhibiting a more noble E_{corr} and lower i_{corr} under similar corrosion testing conditions. However, the full passivation response of the TiC-based HVOF coatings was hindered by physical defects (i.e., residual porosity), associated with the preliminary development stage of the coatings.

- The calculated specific wear rates compare closely with those frequently reported for WC-based coatings. The TiC-Ni_3Al based cermet coatings fabricated using the commercially based agglomeration and sinter feedstock manufacturing route exhibited slightly lower specific wear rates than the gelation-based feedstock, which broadly increased with increasing applied load.
- The formation of a tribo-layer was readily apparent for all of the examined reciprocating wear loads, with a stable response observed for the COF once steady state conditions are achieved. The tribo-layer itself was observed to contain increasing concentrations of O, with increasing load, which is attributed to an attrition/passivation mechanism.

In conclusion, it is demonstrated that TiC-based cermets, with a ductile Ni_3Al intermetallic matrix, offer a viable alternative for the development of high-performance wear and oxidation resistance hard coatings. Furthermore, the advancement of feasible feedstock production techniques is crucial for the design of such alternative coating systems, and this

preliminary work has identified a simple gelation-based technique as being a suitable method for the production of micro-composite powders with a fine-scale internal structure in the final HVOF coatings.

Chapter 5. Evaluation of TiC-Ni_3Al Laser Clad onto Tool Steel Using a Suspension-based Powder Preplacement Approach

Z. Russell[1] and K.P. Plucknett[1*]

[1]Department of Mechanical Engineering, Dalhousie University, 1360 Barrington Street, Halifax, Nova Scotia, Canada (*kevin.plucknett@dal.ca)

*Contact email: kevin.plucknett@dal.ca

Keywords: direct energy deposition; cermet coatings; additive manufacturing; tool steel, gelation, dip coating

Abstract

The effects of various processing parameters were assessed in relation to the geometrical size and microstructure of dense, TiC-Ni_3Al metal-matrix composite (MMC) coatings on D2 tool steel substrates, fabricated using laser direct energy laser deposition (DED). A new powder preplacement approach was applied, utilising *in-situ* gelation of aqueous TiC-Ni_3Al MMC feedstock suspensions, with sodium alginate (Na-alginate) employed as the gelation aid. Dip coating of the steel substrates into the TiC-Ni_3Al based aqueous suspensions, containing either 30, 40, or 50 wt.% solid loadings, was used as an alternative to conventional dry powder preplacement of the feed stock to achieve the maximum powder density after preplacement. Throughout the laser processing stage, partial remelting of steel substrate was employed to explore the possibility of producing a nickel-based matrix. High density, laser processed cermet coatings, with 30, 40 and 50 vol.% Ni_3Al intermetallic contents, were subsequently subjected to both macro- and microstructural evaluation. The volume fraction of reinforcing hard phase (TiC) and dynamics of the solidification front were found effective in controlling the formation and

morphology of these clads. Tensile testing was subsequently conducted on samples prepared from the clad substrates. Partial dissolution of TiC particles in the coating arose during the laser processing and subsequent sub-stoichiometric TiC_x precipitation was noted within a carbon enriched matrix. The clad specimens demonstrated a very low elongation (0.1 % and 0.01 %) and a low toughness (42.73 J/m^3 and 19.29 J/m^3), although exhibiting an excellent tensile strength (404.8 and 333.18 MPa).

5.1. Introduction

Application of composite coatings as a surface treatment for improving the mechanical properties of wear resistant steel parts has received considerable attention in several industrial and research fields, owing to its large economic impact [1–3]. Hard, refractory, titanium carbide (TiC) has been commonly utilised as a suitable reinforcing phase in iron (Fe) based metallic matrix, due to its exceptional physical and chemical properties such as low density (~4.93 g/cm^3), high hardness (~31 GPa) [335,336], high wear resistance [337,338], high toughness [8], high thermal and chemical stability, and low coefficient of friction (COF) [339–342].

Metal matrix composite coatings (MMC), based on TiC, have been investigated through a variety of deposition techniques, including chemical vapor deposition (CVD), physical vapor deposition (PVD), electroplating, and thermal spray [28–38]. Several thermal spray routes have been used traditionally in the manufacture of ceramic-metal composites and thin coatings [115]. The fabrication of thermally sprayed, high hardness coatings with excellent adhesion and cohesion properties, for applications with extensive wear

requirements, has been the subject of numerous prior studies. These include investigation of the bond strength between the metal and the ceramic matrix, minimizing of residual stresses, and development of low porosity coatings [39–44].

More recently, fabrication of both metallic and non-metallic materials has been attempted using laser-based additive manufacturing (AM) deposition technologies, such as laser directed energy deposition (DED) [46–50]. AM approaches have been proposed for the fabrication of forming moulds and dies, as well as their subsequent repair after use, using a range of TiC ceramic-based feed-stock materials [343–345].

The preparation of micron- or nano-sized powder feedstocks with the desired packing properties, homogeneity and low porosity is a difficult and costly task that plays a major role in feasibility of developing AM processes for composite materials [61,62]. In contrast, gelation-based approaches for powder processing have the potential to be less expensive and more environmentally friendly but, such systems can only be utilized from a stable (i.e., agglomeration-free) colloidal suspensions, with the capability to subsequently produce the desired microstructural homogeneity that is required. Furthermore, deposition of the feedstock powder from a slurry (e.g., comprised of powder, water, and a binder), has shown the potential for good bonding between the preplaced powder layer and the substrate [346,347]. Therefore, a non-permanent coating can be deposited in a structured manner that can potentially result in a reduction of material consumption during the fabrication of parts with near net shape geometry that require minimal post processing steps. The physical process of laser cladding with preplaced powder has been investigated by others in attempts to fabricate a low dilution clad layer over a wide range of process parameters [348–350]. In this method, which is also known as the ‘two-step’ laser cladding process, the first step

consists in the deposition of the coating precursor, which can be supplied in different forms (e.g., powder, paste, or wire) onto the substrate material [179], while the second involves the final consolidation of the coating. Preplacing the feedstock material can be accomplished by selected coating techniques to achieve optimum coating quality [134]. Among these, the most frequently applied techniques are spin and dip coating, followed by drying, pyrolysis, post annealing, etc. [351–356]. Dip coating is one of the oldest commercially applied coating processes with its first patent issued to Jenaer Glaswerk Schott & Gen. in 1939 for sol-gel derived silica films [357].

Although the dip coating process can be applied to a wide variety of precursor solutions, it has been found that use of sol-gel type solutions offers the most possibilities to influence the film properties, by modifying the size and structure of the inorganic species in the sol together with the solvent(s) [357–359]. In the standard dip coating approach, the substrate is immersed into the precursor solution at a constant speed followed by a certain dwell time to leave sufficient interaction time of the substrate with the coating solution for complete wetting. Then the substrate is withdrawn vertically from the solution at a certain rate to balance the upward moving flux that takes place during evaporation period. The simplicity of this technique offers a practical *in situ* preplacement tool for a range of substrate and feedstock couples for use in AM [357].

Melting of the preplaced layer by laser irradiation then takes place during the second step, where limited interparticle contact eliminates the conduction factor and powder particles effectively heat up only in their initial, (nominally) fixed position [179]. Once irradiated particles reach the molten state, they can conduct heat to the neighboring particles and propagate through the interface that wets the substrate. As a result of the temperature

gradient between the molten particles and substrate, the solidification of the melt begins. From this point, the melt-liquid interface does not propagate into the body of the substrate unless additional laser power and/or interaction time are provided. The final depth of the melt front is thus representative of the dilution of the cladding material [360,361].

With these factors in mind, the present study has focused upon the development of a novel, gelation-based preplacement technique to facilitate the laser cladding process with ceramic-metal coatings. In this respect, sodium alginate is used as a gelation aid, which gels through an ion exchange mechanism [362] whereby Na^{1+} ions are replaced with Me^{2+}, which cross-links the alginate structure. A variety of metal 2+ (and 3+) ions can contribute to this cross-linking mechanism, with differing efficacies [363], including Ni^{2+} and Al^{3+}. For the present system, in dense TiC-Ni_3Al cermets, corrosion studies have demonstrated Ni^{2+} and Al^{3+} leaching into the electrolyte, opening the potential for low levels of these ions to facilitate cross-linking.

In terms of the material system being examined in the current work, building on the previously outlined studies of bulk TiC-Ni_3Al cermets, the surface enhancement of tool steel substrates has been evaluated via laser DED cladding of TiC-Ni_3Al based coatings. In prior studies it has been shown that TiC based cermets, with various Ni_3Al binder contents, exhibit an excellent combination of mechanical and thermal properties [121,330,364–366]. Significant correlations have been verified between the content of Ni_3Al metallic phase and mechanical characteristics of the fabricated components such as Young's modulus, hardness, bond strength and microstructure [367]. The present article consequently outlines a novel 'two-step' process route for laser DED cladding that utilises a gelation preplacement technique for the feedstock with a ceramic-metal suspension

prepared with a biodegradable gelation agent to aid coating-substrate adhesion prior to laser processing. The suggested hybrid manufacturing route offers a potentially simple and low-cost method for the fabrication of TiC-based coatings, with a range of preferred microstructural and mechanical characteristics.

5.2. Experimental procedures

5.2.1. Raw materials

A fine, commercially available, TiC powder (lot no. PL20126240; D_{50} = 1.0 - 2.0 μm) was utilised in the current work, supplied by Pacific Particulate Materials Ltd., Vancouver, BC, Canada. In order to produce a Ni_3Al binder that is evenly distributed within the powder feedstock mixture, Ni_xAl_y powder (lot no. D28X029; D_{50} = 32 μm) with a 1:1 elemental weight ratio, is combined with an appropriate content of Ni powder (lot no. L10W013; particle size of 2.2 - 3.0 μm) to obtain the final Ni_3Al stoichiometry; these two precursors were both supplied by Alfa Aesar, Ward Hill, MA, USA. The D2 tool steel substrate material was supplied from McMaster-Carr (Elmhurst, IL, United States). Inductively coupled plasma optical emission spectroscopy (ICP-OES; model Thermo iCap 7400 Dual View, MA, USA), with an internal calibration standard (scandium), was employed for compositional analysis of the tool steel. The elemental compositions of the steel substrate, with respect to the ASTM A681 standard for tool steels, are summarized in Table 11.

Table 11. The standard compositional ranges for the alloys used as steel substrates.

Substrate grade	Elemental composition (wt.%)								
	C	Cr	Mn	Mo	Si	V	P	S	Fe
D2	1.40-1.60	11.0-13.0	0.10-0.60	0.70-1.20	0.10-0.60	0.50-1.10	-	-	Bal

5.2.2. Suspension preparation and dip-coating procedures

Colloidal suspensions with nominal Ni_3Al intermetallic matrix compositions varying from 30 to 50 vol.% (with TiC making up the balance), and with solid loadings ranging from 30 to 50 wt.% in distilled water with 1.6 wt.% Na-alginate, were prepared as preplaced feedstock material prior to laser cladding (as summarized in Table 12). Additional specimens were prepared from preplacing the feed stock powder without presence of gelling agent (e.g., Na-alginate) to examine the impact of gelation on quality of the fabricated clads.

For initial homogenization, each composition was ball milled for 24 hours, with yttria stabilized zirconia media and acetone as the suspension medium. Ball milling was then followed by a 24-hour drying period. The dried powders were subsequently individually sieved through a -75 μm stainless steel mesh. X-Ray diffraction analysis (XRD; model AXS D8 Advance, Bruker Corp, Billerica, MA, USA) was employed for identification of the possible crystallographic phases that were present in both the dried powder mixtures and the subsequently processed laser DED clads. The dried cermet compositions were then added into solutions of distilled water with either 0, 1.6, or 3.2 wt.% sodium alginate (Na-alginate); 0.1 wt.% Darvan® C-N is also added as a dispersant in each case, to form a stable

suspension. The pH value of the homogenized mixture then was adjusted to ~8.5 using solutions of NaOH and HNO_3, and the suspensions vacuum degassed. A flow chart representation of the overall process is presented in Figure 55.

Table 12. Summary of the colloidal suspensions prepared as preplaced feed stock material prior to laser cladding.

ID	Ni_3Al content (vol.%)	TiC content (vol.%)	Suspension	Solid loading (wt.%)
140-30-1.6	30	70	1.6 wt.% Na-alginate	40
140-40-1.6	40	60	1.6 wt.% Na-alginate	40
140-50-1.6	50	50	1.6 wt.% Na-alginate	40
150-30-1.6	30	70	1.6 wt.% Na-alginate	50
150-40-1.6	40	60	1.6 wt.% Na-alginate	50
150-50-1.6	50	50	1.6 wt.% Na-alginate	50
160-30-1.6	30	70	1.6 wt.% Na-alginate	60
160-40-1.6	40	60	1.6 wt.% Na-alginate	60
160-50-1.6	50	50	1.6 wt.% Na-alginate	60
150-30-3.2	30	70	3.2 wt.% Na-alginate	50
150-40-3.2	40	60	3.2 wt.% Na-alginate	50
150-50-3.2	50	50	3.2 wt.% Na-alginate	50
150-30-0.0	30	70	Distilled water	50
150-40-0.0	40	60	Distilled water	50
150-50-0.0	50	50	Distilled water	50

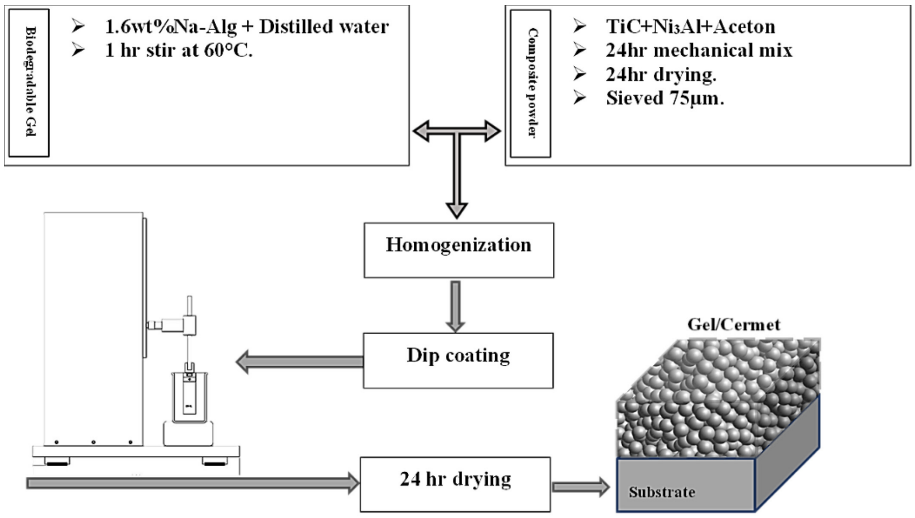

Figure 55. Process flowchart for preparation of colloidal suspensions and dip coating for a TiC-Ni_3Al cermet powder mixture in a 1.6 wt.% sodium alginate aqueous solution.

Preplacement of the cermet coating via dipping the substrate in a viscous mixture was achieved using a linear driven stage, designed, and built with capability of operating at controlled velocities for a wide range of sample sizes and shapes (Figure 56). An open-source Arduino board was used to assure precise setting of withdrawal speeds, which ranged from 0.05 to 5 mm/s. Prior to dip coating, the steel substrate coupons, with dimensions of 75 x 50 x 5 mm (L x W x H), were cleaned with acetone and subjected to SiC bead blasting of their surfaces. The cleaned substrates were then immersed in and subsequently withdrawn from the suspension in a direction parallel to the flat surface of the plates, followed by drying. The thickness of the preplaced coating after drying was measured by CLSM and was determined to be 0.04±0.01mm for specimens after one dipping process.

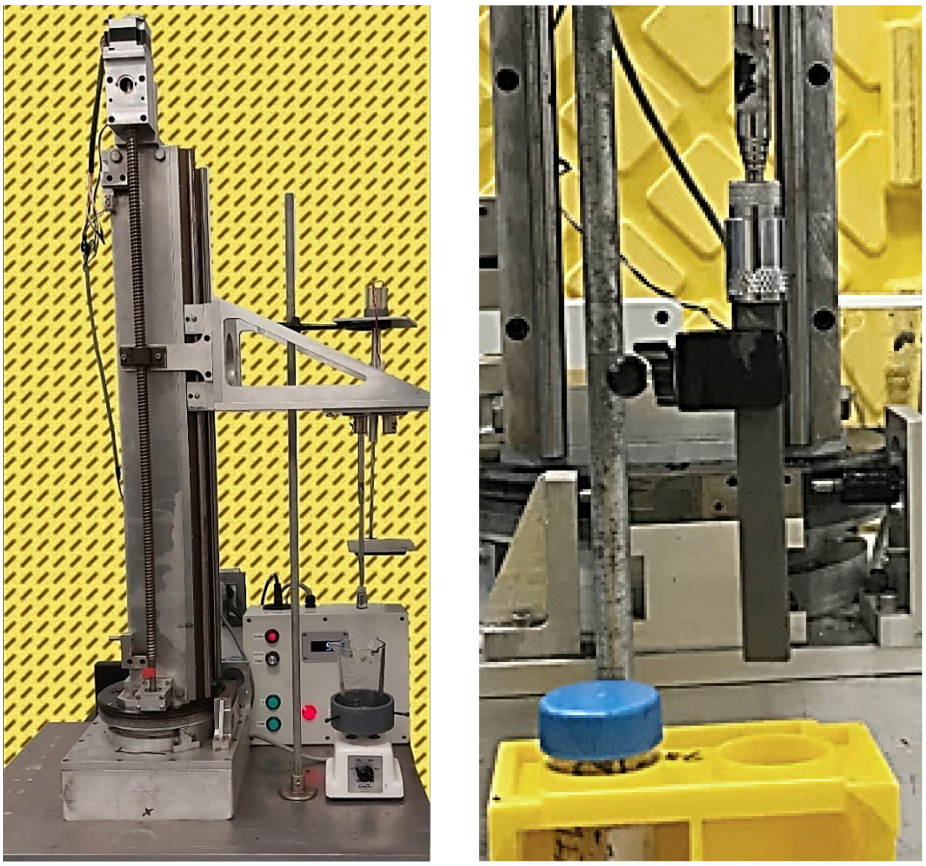

Figure 56. The assembled dip coating unit and enlarged example of dip coated specimen.

Additional samples were machined with appropriate dimensions for tensile testing according to ASTM E8/ E8M. Dimensional details of tensile specimen machined for testing coated and as received D2 steel substrate is provided in Figure 57.

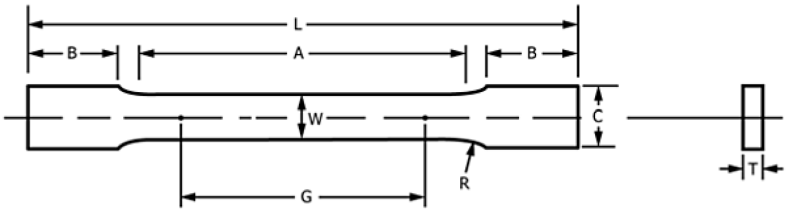

Dimensions	Values (mm)
Gauge length (G)	50.00 ± 0.1
Width (W)	12.5 ± 0.2
Thickness (T)	6.35 ± 0.01
Radius of fillet (R)	12.5
Overall length (L)	200
Length of reduced parallel section (A)	57
Length of grip section of grip section (B)	50
Width of grip section (C)	20

Figure 57. Rectangular specimens for tensile testing of coated and as received D2 steel substrate [368].

The effects of the substrate temperature upon the degree of cross-linking were examined by precooling or preheating substrates prior to the dip coating step, while further specimens were subjected to the preplacement by dipping at room temperature. Moreover, the role of Ni addition as cross linking agent was examined by substitution of Ni_3Al with SS316 as the binder metallic phase.

5.2.3. Laser cladding

An Optomec 500 MTS-Ca laser DED system (Optomec Inc., Albuquerque, NM. US) was employed for the processing of preplaced coatings on the steel substrates (Figure 58). The DED laser (ytterbium-doped fiber laser (IPG Photonics; λ=1070nm)), with a maximum operational laser power of 1 kW and focusing optics tuned for a spot size of ~700 μm, was operated in continuous mode for all trials. Initially, a series of single-track clads that were processed at various laser powers, P, and laser scanning speeds, V, were analysed for measurements of the related bead diameters. A five-axis CNC vertical machining center, integrated with the laser system, allowed cladding at various scanning speeds by alteration of the work piece (i.e., substrate with preplaced coating) velocity.

(a) (b)

Figure 58. The Optomec 500-CA DED system utilized for fabrication of presented builds: (a) an example of the steel substrate location and clamping system, and (b) the DED operational chamber.

The DED chamber itself was prefilled with an Ar environment, while an Ar shielding gas was also delivered through a nozzle at 10 l/min to further protect the DED melt pool from possible oxidation. The dip-coated steel coupons were processed under laser powers, P, of 250, 300, and 350 W, while scanning speed, V, was varied between 58 and 116 mm/min., for each of the evaluated laser powers. The laser beam was effectively moved over the preplacement coated substrate at specific interaction time, τ(s), defined following:

Equation 15

$$\tau = \frac{D}{V}$$

where D is the laser beam diameter [mm] and V the laser scanning speed [mm/s] [369]. Additionally, the dog bone tensile samples, which were coated on both sides, were subjected to laser power of 350 W at 6.77mm/s laser scan speed at their center point with dimensions of 10x50 mm (Figure 59).

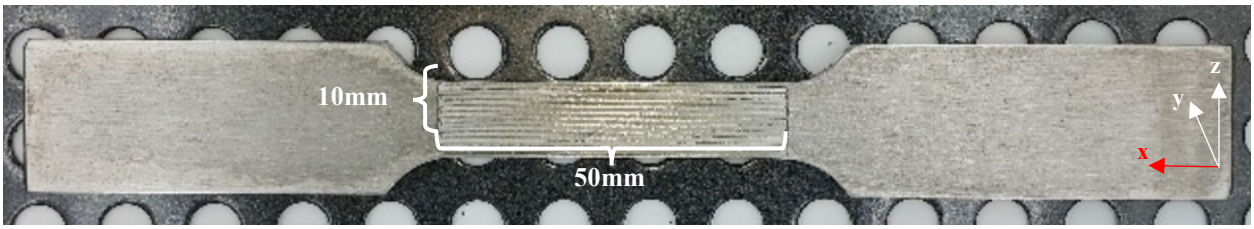

Figure 59. Example of dog bone testing samples prepared for tensile measurement of TiC-Ni_3Al cermet coatings on D2 steel, (x axis denotes the direction of laser scanning); note that samples were coated on both sides.

5.2.4. Post-cladding characterization

After DED processing, the clad specimens were sectioned perpendicular to their planar surface, using a precision saw. They were then resin mounted, prior to grinding and polishing down to a final 0.25 μm final diamond paste particle size. Metallographic specimens were all subjected to preparation procedure outlined by ASTM E3-11 for preparation of metallographic specimen [368].

The overall surface plane view of the clads and three-dimensional measurements of the single tracks were conducted using a confocal laser scanning microscope (CLSM; model VK-X2000, Keyence, Mississauga, ON, Canada). Clad microstructural characterization was also performed by using field emission scanning electron microscopy (FE-SEM; model S-4700, Hitachi High Technologies, Tokyo, Japan). Chemical composition analysis was performed in the FE-SEM using energy dispersive X-ray spectroscopy (EDS; Inca X-maxN, Oxford Instruments, Concord, MA, USA); EDS analysis is used to analyze the clad zone in order to measure the degree of dilution, instead of using a more conventional method that measures the dilution by clad dimensional characteristics [179]. Crystalline phase analysis in the composition of the fabricated clads as well as the as received and laser remelted substrate was revealed by means of X-ray diffraction (XRD) analyses, (XRD; model AXS D8 Advance, Bruker Corp., Billerica, MA, USA) using the Co K_α radiation and a wavelength, λ, of 1.5406 Å.

5.3. Results and discussion

5.3.1. Feedstock powder characterization

The elemental compositions of the as-received powders are provided in Table 13. In each case it can be seen the powders correspond to the manufacturer's specifications. The morphologies of the as-received powders utilised in the present study are shown in Figure 60; here, the TiC-Ni_xAl_y-Ni cermet composition was prepared by mixing the powder blend via ball milling with zirconia media in acetone for 24 hours, and the constituent Ni_xAl_y-Ni precursors are then (ideally) used to produce the intermetallic Ni_3Al binder phase in the subsequent process.

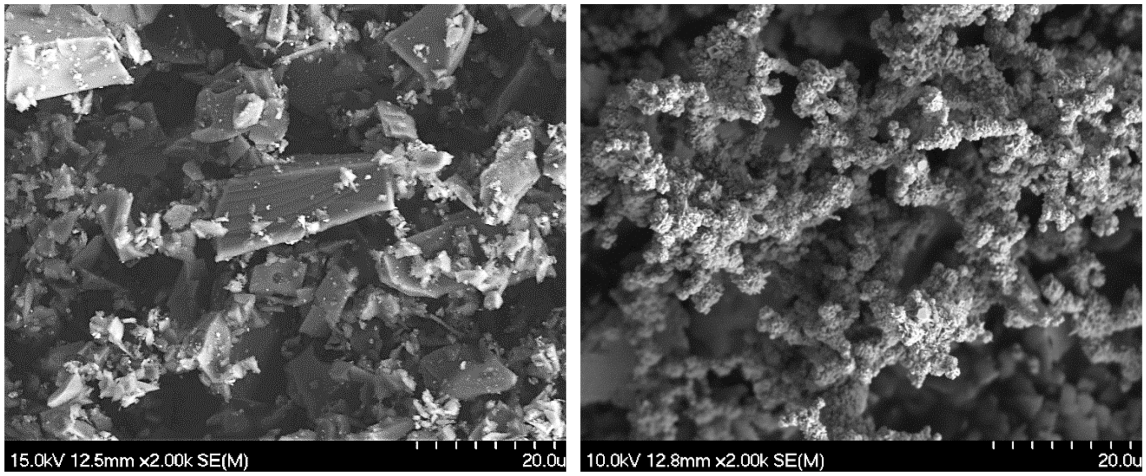

(a) (b)

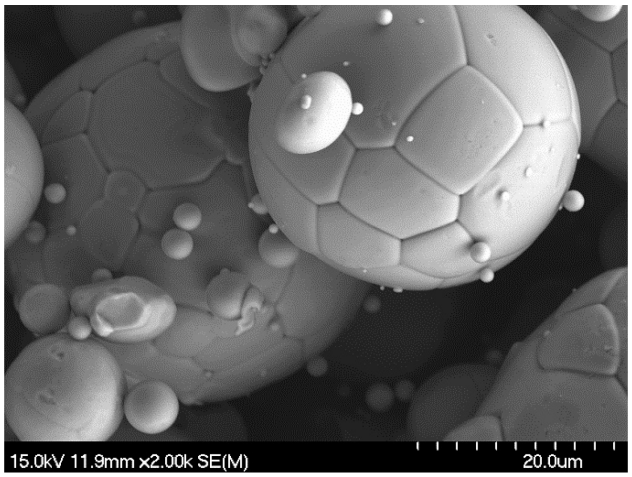

(c)

Figure 60. Representative SEM images of the morphologies of the as received powders utilised in preparation of TiC-Ni_xAl_y-Ni cermet composition: (a) TiC, (b) Ni, (c) and Ni_xAl_y.

Table 13. The elemental compositions of the as received powders utilised in prepration of the TiC-Ni_xAl_y-Ni cermet composition for preplacement trials measured by ICP-OES.

ID	Elemental composition (wt.%)										Particle size (µm)
	C	Ti	O	Al	Si	Cr	Mn	Fe	Ni	Mo	
TiC	25.68	74.32	-	-	-	-	-	-		-	1-2
Ni_xAl_y	-	-	-	49.8	-	-	-	-	50.01	-	32.0
Ni	-	-	-	-	-	-	-	-	99.9		2.3-3.0

Figure 61 presents an XRD trace of the starting powder blend prior to the preplacement stage of the cladding process. Distinct peaks are observed for TiC and Ni, while various nickel aluminide phases have been identified, although that the X-ray trace for the Ni_xAl_y

powder is complex, with Ni_2Al_3 and Ni_3Al present but with a slight shift (this may possibly arise from lattice strain induced during the ball milling stage).

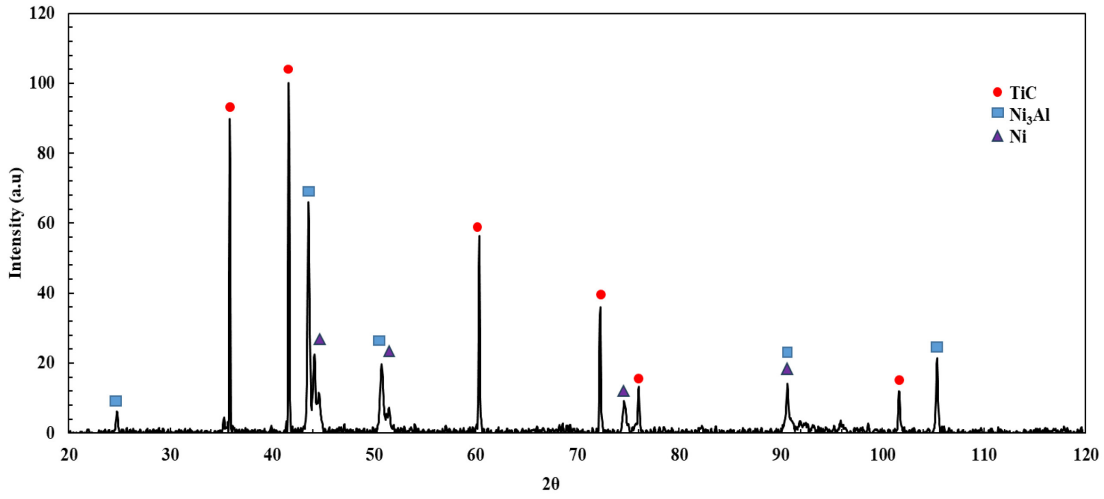

Figure 61. X-ray diffraction peaks of the dried starting TiC carbide and Ni_xAl_y/Ni blend after ball milling but prior to the suspension preplacement stage.

5.3.2. Single droplet and dip-coating behavior: Evaluation of preplacement for the TiC-Ni_3Al coatings

The extent of potential cross-linking was examined through control of substrate temperature prior to dip coating. Sodium alginate is widely used in food-based applications and is an example of an aqueous gelling system that is (typically) cross-linked through an ion exchange mechanism, for example where Ca^{2+} ions (from a $CaCl_2$ source) replace the Na^{1+} ions in the sodium alginate. Notably, a variety of divalent and trivalent cations have been shown to facilitate cross-linking, and hence gelation, in sodium alginate containing systems [370–372]. Among these cations, Ni^{2+} has been shown to be an effective divalent

ion option, as has Al^{3+} [363,371,373]. For the present case, the expectation is therefore that over a period of time, Ni^{2+} and/or Al^{3+} are slowly released from the aqueous powder mixture to the local environment (on a sub-μm length scale) where a degree of localized cross-linking of the sodium alginate can then arise. Further confirmation of this potential mechanism was justified by conducting ICP-OES measurement on the post dip coating and solutions (Table 14).

Table 14. Results of ICP-OES measurement on elemental composition of the post gelation coating and post dip mix for cermet coatings fabricated with 30 and 40 vol.% Ni_3Al metallic binder phase.

ID	Elemental composition mg/kg							
	Al	Co	Fe	Na	Ni	Ti	W	C
30 vol.%Ni_3Al_TiC_ Solid coating	75501	2786	646	6956	93611	502424	15119	16.77
40 vol.%Ni_3Al_TiC_Post dip solution 1	43.2	48.3	58.7	4104	72.8	0.2	<0.5	0
40 vol.%Ni_3Al_TiC_Post dip solution2	5.5	0.1	2.1	3556	88.9	0.2	<0.5	0
30 vol.%Ni_3Al_TiC_Post dip solution	57.3	0.1	0.1	1556	0.1	0.2	119	0

The result of ICP OES analysis on post experiment solution on the filtrate and solution verified the presence of free Ni^{2+} and Al^{3+} ions, which consequently can be anticipated to have been involved in the cross-linking reaction with sodium alginate. This can also be factored into the improved quality of the coatings when the solid loading increases from 30 to 50 wt.% cermet feed in suspension, due to the greater availability of cross-linking ions. Figure 62 demonstrates images of dip coated D2 steel coupons, after drying, with

TiC-Ni_3Al formulations prepared either in the absence of sodium alginate or with sodium alginate included in the suspension.

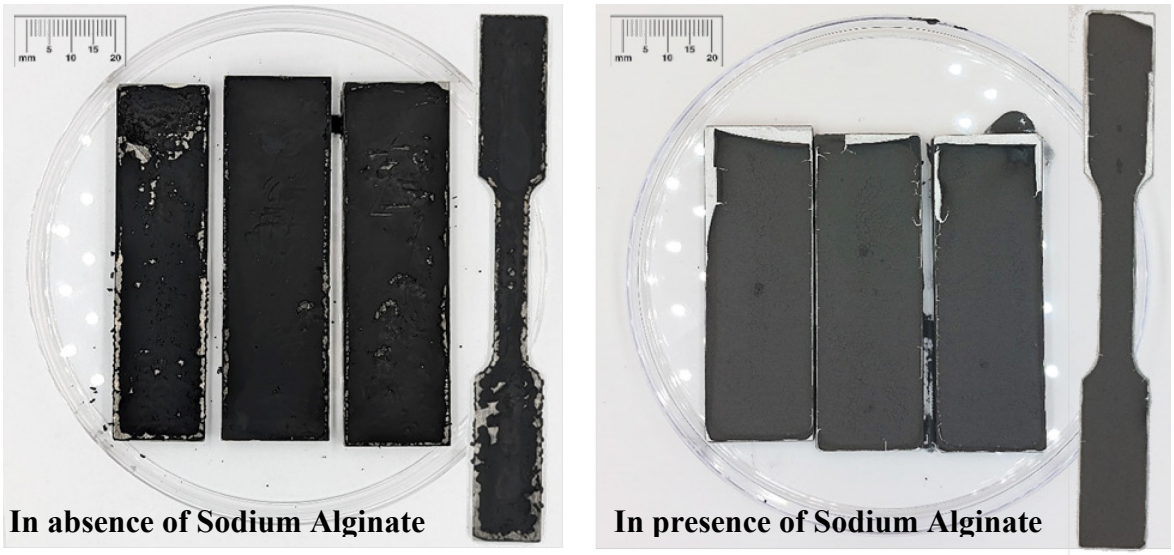

(a) (b)

Figure 62. Dip coated specimen at various dimensions with TiC as the ceramic phase, prepared with: (a) 40 vol.% Ni_3Al metallic phase in distilled water and (b) 40 vol.% Ni_3Al metallic binder phase in 1.6wt% sodium alginate solution.

Without sodium alginate present the dipped specimen did not form a uniform and cohesive coating structure. Instead the dry films tended to crack and fall off the substrate as there was no sodium alginate within the composition (Figure 62 (a)), and hence no mechanism for corss-linking and increasing the coating coherency. When a mixture of Ni_xAl_y and Ni was used as the metallic binder phase, in conjunction with sodium alginate, the dip coated surface was uniform, and largely crack-free. In this instance, cracking within the preplaced cermet films was eliminated with addition of sodium alginate to the mixture prior to the ball milling step (as shown in Figure 62 (b)). To assess the effects of temperature on this process, which also will affect the rate of water evaporation, the ageing response of

suspension droplets was assessed. Figure 63 shows CLSM 3D images of the droplets, prepared with nominal 30, 40, and 50 wt.% TiC-Ni_xAl_y-Ni solids loadings, on D2 substrates that were cooled or heated to various temperatures. During the formation of the gelled films, the inorganic TiC-Ni_3Al precursors are concentrated onto the substrate surface by gelation of the alginate polymer containing suspension medium, driven by cross-linking, continuous drying, condensation, and evaporation. Further characterization of the experimental ageing of droplets over a period of 120 hours was then conducted using the CLSM. Figure 63 presents 3D CLSM reconstructions of the of aqueous suspension droplets, as deposited, with 30, 40 and 50 wt.% solids loading, where the D2 steel substrate plates are: (i) precooled (to -2 ± 2 °C), (ii) preheated (to 60 ± 2 °C), and (iii) held at room temperature (23 ± 2 °C).

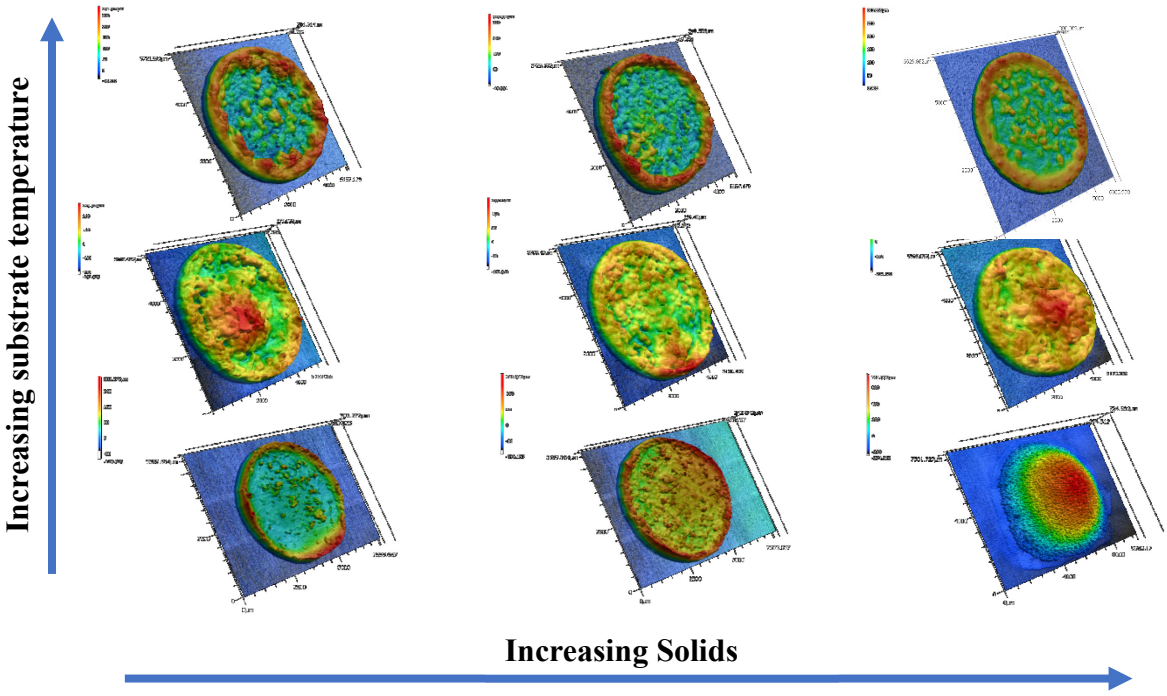

Figure 63. As-deposited suspension droplets on precooled D2 steel substrate with 30, 40 and 50 wt.% solid loading.

Adequate levels of gelation on the surface of the substrate were confirmed to play the main role in the physical and the mechanical qualities of the preplaced films. The results of cyclic topographical observation of the cermet/gel droplets revealed that cross linking and gelation eventually takes place due to condensation and drying of the gel. Studies of the influence of temperature on sodium alginate gelation are, unfortunately, quite limited. However, Jeong and colleagues recently showed in a study of Ca^{2+} gelation of sodium alginate that temperature has a significant impact on gelation behavior and subsequent properties [374]; gelation at low temperature, in that instance 5 °C, resulted in higher gel strengths while simultaneously a greater water content was retained, and the gels had lower densities. EDS analysis on microstructure of the green coating was also used to further verify its chemical composition. Figure 64 represents the results of EDS mapping and recorded average elemental composition of the green TiC-Ni_3Al 30 vol.% gel/cermet coating after 24 hours of drying. EDS mapping demonstrated homogeneous dispersion of the cermet elements while 8.48 wt.% O was detected within the composition of the green coating. Results of EDS measurements on compositions with 40 and 50 vol.% Ni_3Al indicated that the amount Ni in the final coating was increased as the wt.% solid loading of the colloidal suspension. This infers a potential maximum amount of Ni^{2+} ions are needed for gelation, above which excess Ni does not enter the liquid medium and remains in the coating.

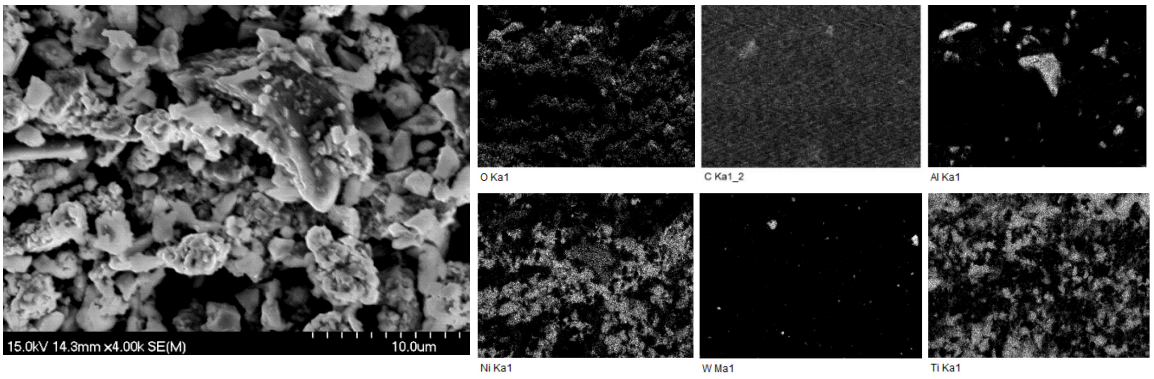

Element	Weight%	Atomic%
C	49.91	75.73
O	8.48	9.66
Al	1.64	1.11
Ti	17.66	6.72
Ni	21.61	6.71
W	0.70	0.07

Figure 64. EDS mapping of dried green gel/cermet coating microstructure, highlighting the average elemental composition in units of weight% and atomic%

5.3.3. Macro-scale evaluation of the laser clads

5.3.3.1. Characterization of single track clads

Metallographic examination of cross sections of the single track clads and their interfaces with the substrate were examined to assess the clad quality of the laser DED tracks. This stage of the work was performed to refine the processing conditions for preparation of clad layers (i.e., multi-track clads). Figure 65 illustrates the top view of single-track clads laser processed at 300 W with $\tau = 0.8$ s and 0.6 s respectively (Figure 65 (a,b)). Both tracks were

constructed from same the cermet composition with variation of carrier media for dip coating procedure.

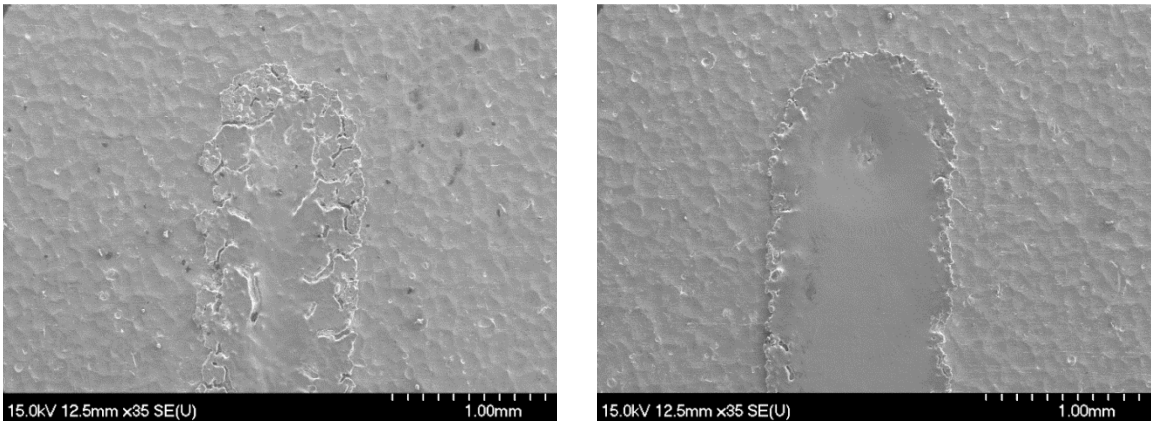

(a) (b)

Figure 65. SEM images of the of single-track clad layers prepared from: (a) 50 wt.% solids TiC-Ni_3Al in distilled water, and (b) 50 wt.% solids TiC-Ni_3Al with 1.6 wt.% sodium alginate in distilled water. The Ni_3Al content was 40 vol.% in both cermet formulations.

As it is shown in Figure 65 (a), absence of Na-alginate in carrier media resulted in fabrication of a porous clad layer with minimal bonding to the substrate. These specimens did not survive the sectioning process for the cross-sectional image analysis. In contrast, regardless of laser processing parameters, clads were fabricated successfully at various degrees of bonding to the substrate.

Figure 66 shows representative SEM images obtained from the cross sections of TiC-Ni_3Al (40 vol.%) single track clads, formed onto D2 steel, and fabricated at increasing laser powers (left to right) and laser scanning speeds (top to bottom). It was observed that, for a laser power of 300 W, a scan speed of 50.8 mm/min was required to produce a successful single-layer deposit with the desired bonding to the substrate across the clad width. From

these SEM images, it is possible to see that both the laser power and scanning speed play a crucial role in clad formation, the extent of bonding, and the overall clad quality/microstructure. For DED conditions of τ = 0.9 s and 250 W laser power (Figure 66 (a)), only limited bonding was observed between the preplaced coating and the substrate, although the clad layer could not be easily removed from the substrate and showed some degree of adherence. However, as shown in Figure 66 (b), increasing the laser power to 300 W for the same value of τ, clearly effects the extent/kinetics of melt pool generation in a positive manner, with the formation of a well bonded layer. It is also apparent that shorter beam interaction times (i.e., τ = 0.5 s), as shown in Figure 66 (c) and (d), appear to be insufficient to create a homogeneous melt pool, which resulted in reduced wetting of the coating and poor substrate interfacial bonding at 250 W, with a moderate improvement at 300 W. Consequently, these preliminary evaluations indicate that increasing laser power increases the probability of forming a high quality clad, but it is not the only effective parameter. For a given value of τ, sufficient heat to melt a given volume of the substrate may be provided by laser energy. However, in reality, this is determined not only by the laser power but also by the scan speed (V).

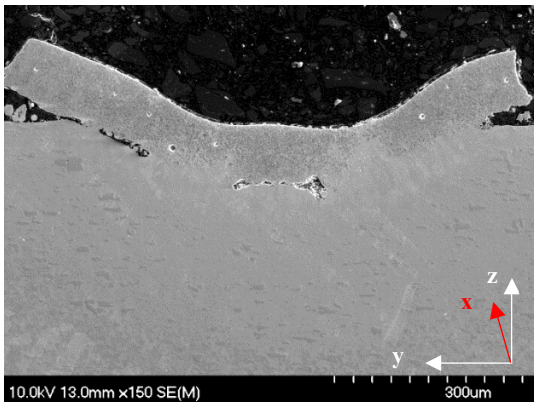

(a)

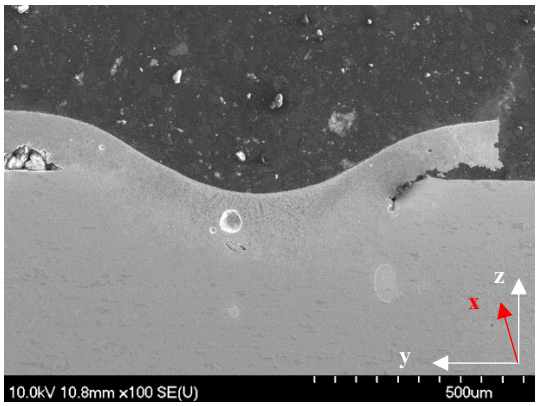

(b)

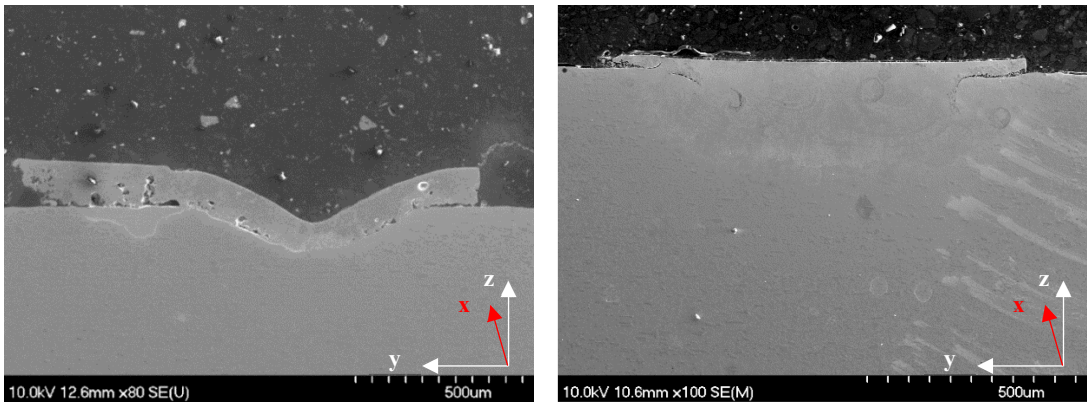

(c) (d)

Figure 66. Cross sections of TiC-Ni_3Al (40 vol.%) single tracks, clad onto D2 steel substrate with laser powers of: (a) 250 W, and (b) 300 W, both at $\tau = 0.9$ s. Cross sections of TiC-Ni_3Al (40 vol.%) single tracks, clad onto D2 steel substrate with laser powers of: (c) 250 W, and (d) 300 W, both at $\tau = 0.5$ s. In each case, the x-axis denotes the direction of laser scan during DED.

5.3.3.2. Characterization of the multi-track clad coatings

The preliminary single track clads showed that a high-density layer can be produced on the surface of the substrate, that is well bonded and, in most cases, contains no microcracking. The geometric characteristic of the fabricated multi-track clads, obtained with various processing parameters, was subsequently verified through a series of measurements determined from both macro- and microstructural analysis. Figure 67 provides an example from a transverse section of a well adhered clad/substrate pairing, for AISI D2 tool steel, with a variety of measurement parameters outlined schematically.

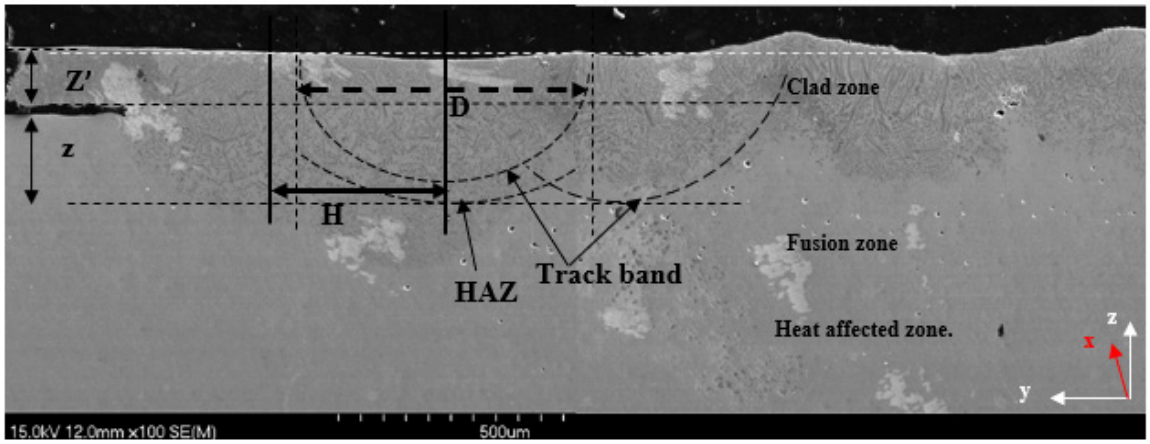

Figure 67. The macrostructure of a transverse section of the clad surface of D2 steel, for a sample processed at P = 300 W and τ = 1.2 s. Note that the x-axis aligns with the direction of laser scanning.

As shown in Figure 67, the corresponding cross-sectional structure for multi-track clads was divided into four distinct regions, based on the respective thermal background and solidification kinetics of the clad/substrate regions. The top layer of the clad, which consists of the deposited coating (nominally) above the surface of the substrate, is referred to as the 'clad zone'. The height and width of clad zone are denoted as (*Z'*) and (*D*), respectively, where *Z* represents the combination of the clad height above and below the surface of the substrate. The clad height above the surface is given by *Z*', while volume below the clad zone is referred to as the 'fusion zone', which describes the depth of the coating below the original surface of the substrate, and here is indicated as *z* also subsequently referred to as the '*z*-step'. The fusion zone is followed by a narrow layer in the form of a 'heat affected zone' (HAZ), where the substrate has been affected by the large temperature gradients during laser DED heating/cooling and will likely exhibit some microstructural distortion.

To describe the structure of the solidified melt pool across the printed track in relation to the processing parameters, definition of the laser specific energy, E, (in J/mm^3) is proposed [195,375,376]. In this respect, E is defined as the energy per unit area scanned by the laser beam per unit time. The value of E can be calculated following [377]:

Equation 16

$$E = \frac{P}{V.H_s.Z'}$$

where P, *V, and Z'* were defined earlier, and H_s is referred to hatch spacing of the adjacent laser raster track. Figure 68 presents correlation graphs that were constructed from the results of calculated E values for each fabricated clad versus its build parameter conditions. It is apparent that an increase in scanning speed generally leads to a decrease in E, while an increased laser power exhibited the opposing behavior. During laser processing, a significant portion of the energy is absorbed by the substrate, which will have a Gaussian distribution intensity. The melt pool generated by this input laser energy, at time $t = 0$, will have a heat profile as follows [174,213]:

Equation 17

$$\frac{\partial(pc_pT)}{\partial t} + \nabla.\left(pc_pUT\right) - \nabla.(K\nabla T) = Q$$

where the power generation per unit volume of the substrate is denoted by Q [W/m^3], U is the travel velocity of the workpiece [m/s], and t is time [s]; in this instance, the substrate properties are denoted as c_p, the specific heat capacity of the substrate [J/kg·K], while K

represents the thermal conductivity [W/m·K], and ρ is the density [kg/m^3]. From this point, the dynamic response of the melt pool is further driven by surface tension and the flow of the molten pool beneath the surface of the substrate, which is described by heat/mass transfer and the second law for fluid flow [378–380]. In the case of high temperature alloys, such as Ni and Co, or Fe-based with smaller amounts of W and Mo as well as C, it has been observed that the reaction between the hard phase and the melt pool can be beneficial to some extent [241,242,244,245]. In this scenario the ceramic phase or, alternatively, added elemental powders such as Mo, Si, C, Zr, and/or Ti, dissolve into the molten pool to ultimately form fine precipitated particles (e.g., $MoSi_2$, SiC, ZrC, and/or TiC), that are well bonded to the matrix after cooling.

When the applied H_s and Z', as parameters outlining the dimensions of the melt pool, were correlated with the calculated values for E, only the layer thickness expressed a decrease with increased E. Then, computed E values were subsequently correlated with the initial clad composition, ranging from 30 to 50 vol.% Ni_3Al metallic binder. In this instance, an increase in the volume fraction of metallic phase in the cermet blend was observed to lead to an increase in calculated values for E. Based on these observations, at 30, 40, and 50 vol.% metallic binder content, the reduction of scanning speed presents the best correlation with the computed E. On the other hand, as shown in Figure 68 (b), the increase in E is an indication of the normalized alloy density as a percentage of its theoretical calculated density. Furthermore, the ranges for E can be calculated against the volume fraction of the metallic phase and percentage of the achieved theoretical density, which are presented as scatterplots in Figure 69.

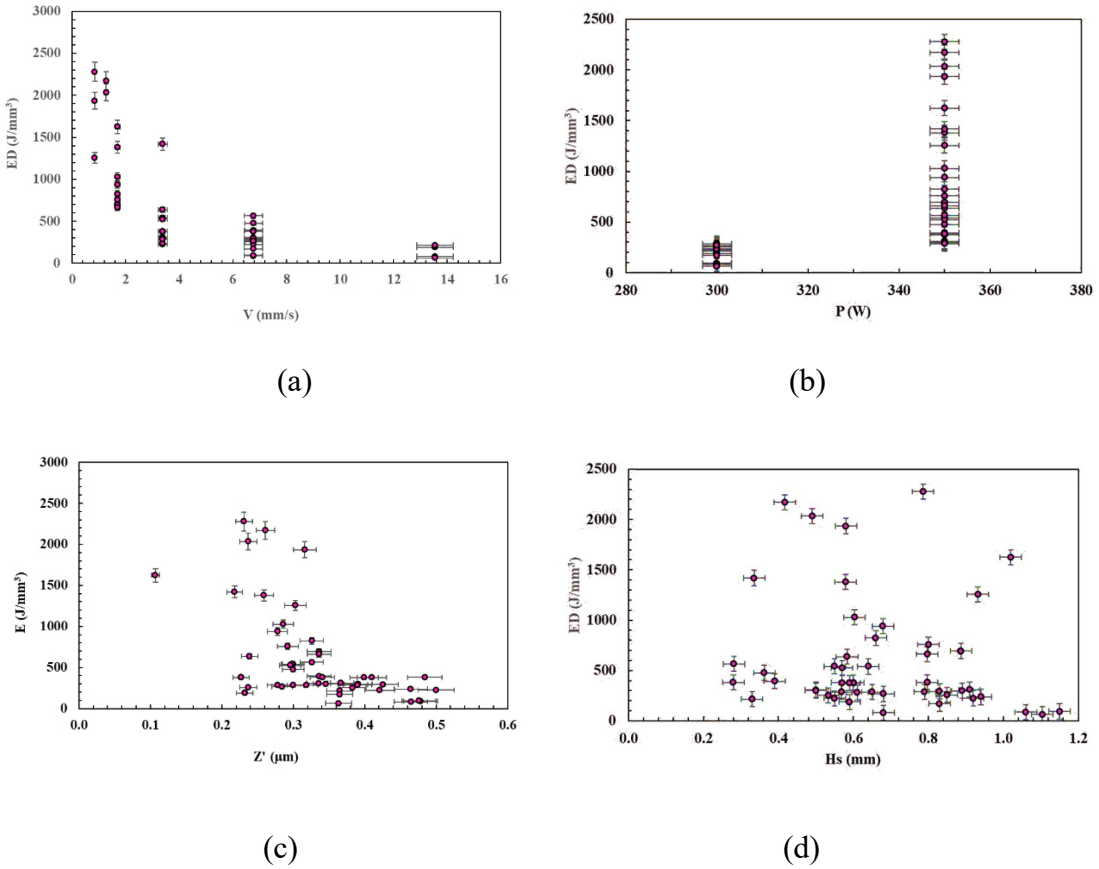

Figure 68. Correlation graphs constructed from calculated E values for: (a) scan speed, (b) laser power, (c) z-step dimensions, and (d) hatch spacing.

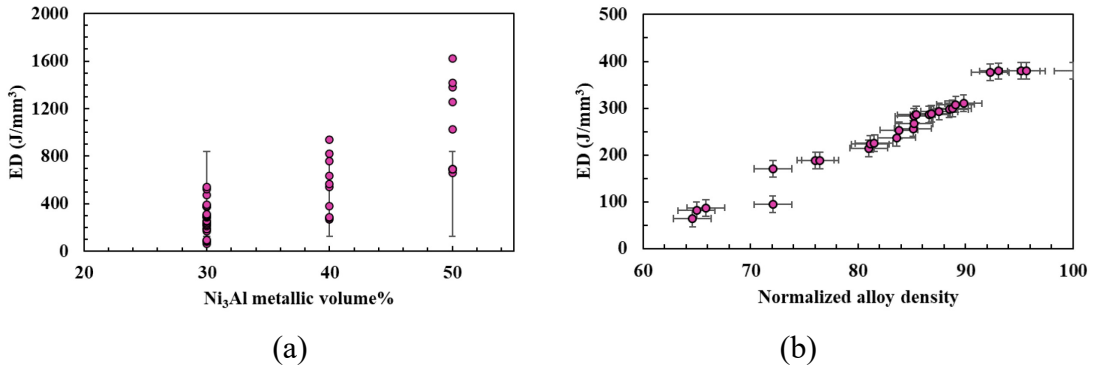

Figure 69. Calculated E values as a function of: (a) the volume fraction of metallic phase in the clads, and (b) the normalized density of the fabricated clad layer.

5.3.4. Compositional and phase analysis

The results of x-ray diffraction analysis on as the as-received substrate (both with and without laser processing), are provided in Figure 70. The as-received substrate consists of α-Fe (ferrite), γ-Fe (austenite), and Fe_3C (cementite) (Figure 70 (a)). The as quenched laser remelts on the other hand, revealed formation of γ-Fe matrix with Fe_3C and Cr_2C_3, while the ferrite (α-Fe) peaks were suppressed (Figure 70 (b)). Similarly, representative x-ray diffraction analyses for TiC-Ni_3Al (40 vol.%) clads laser deposited onto D2 substrates are provided in Figure 71. XRD peaks obtained from coated surfaces at all the scanning speed confirmed presence of TiC particles in the composite. Predominant XRD peaks are composed of TiC, γ-Fe, and $(Fe, Cr)_3C$, which have formed due to the segregation of Cr to grain boundaries and inter-dendritic region of γ-Fe during the fast solidification process. Thus, the dendritic region which becomes depleted from Cr decomposes into $(Fe, Cr)_3C$ during cooling after solidification.

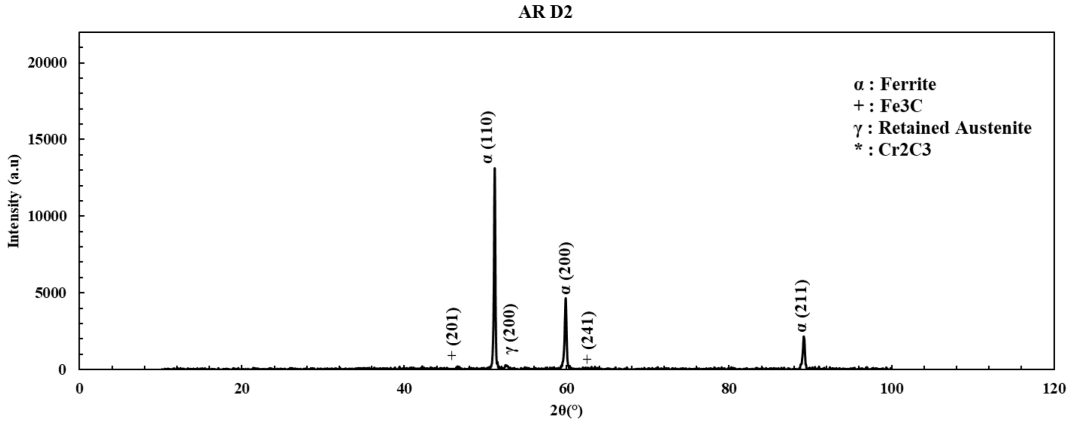

(a)

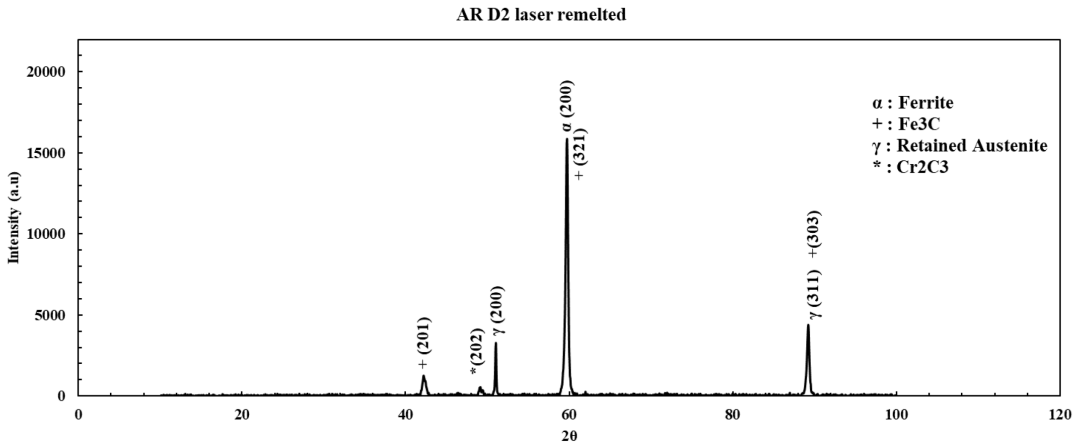

(b)

Figure 70. (a) XRD trace obtained from the polished surface of the as-received D2 substrate. (b) XRD trace obtained from the as-received D2 substrate subjected to a laser remelting step, with P = 300 W and τ = 1.2 s.

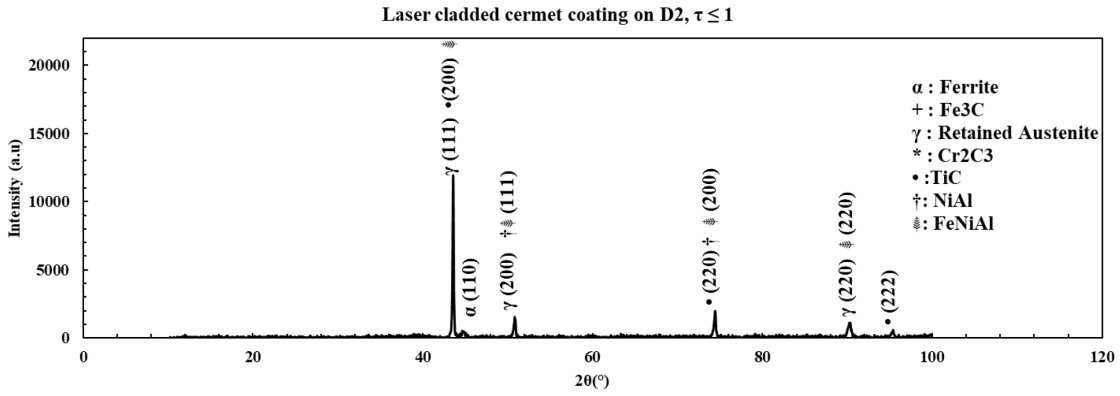

(a)

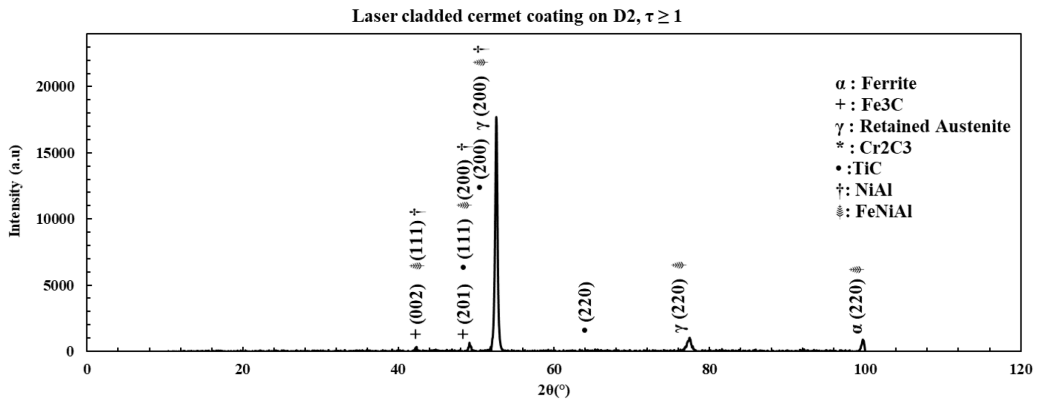

(b)

Figure 71. XRD traces obtained for the TiC-Ni_3Al 40 vol.% coatings clad onto D2 substrate processed at: (a) P = 350 W and $\tau \geq 1$ s, and (b) P = 350 and $\tau \leq 1$ s.

5.3.5. Micro-scale evaluation of the laser DED clads

5.3.5.1. Microstructural analysis of the laser clads

EDS mapping of the TiC-Ni_3Al clads prepared with 30 vol.% Ni_3Al intermetallic phase, produced with a laser power of P = 300 Wand τ = 1.4 s on D2 tool steel, is shown in Figure 72. It is apparent that the dark layer of the coating is primarily concentrated with Ti and C, with minor amounts of Fe. On the contrary, the substrate region below the coating was found to be rich in Fe and Cr, while a low concentration of Ni was detected in both the coating and the substrate region.

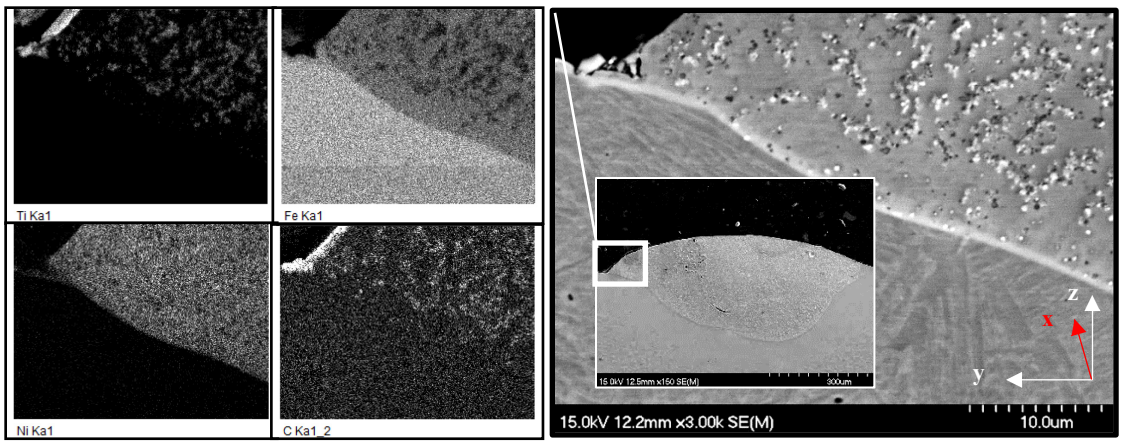

Figure 72. EDS maps for a TiC-Ni_3Al clad with 30 vol.% Ni_3Al intermetallic phase, processed at P = 300 W and τ = 1.4 s. Note that the x-axis denotes the direction of laser scanning in each case.

EDS maps of the TiC-Ni_3Al clad coatings on D2 steel, prepared with 30 vol.% metallic phase (processed at P = 300 W and τ = 1.4 s), are presented in Figure 73; these images show the top portion of the clad zone and the clad/substrate interface in Figure 73 (a) and (b), respectively. EDS mapping shows that the dark contrast particles in the coating layer are composed of highly concentrated Ti and C along with the traceable amount of Ni; whereas, the white matrix region is composed of Fe, Cr, and Ni. Detection of the Ni within the substrate is attributed to the partial dilution of Ni within the initial TiC-Ni_xAl_y-Ni blend or formation of Ti-Ni intermetallic that mixed with the steel matrix.

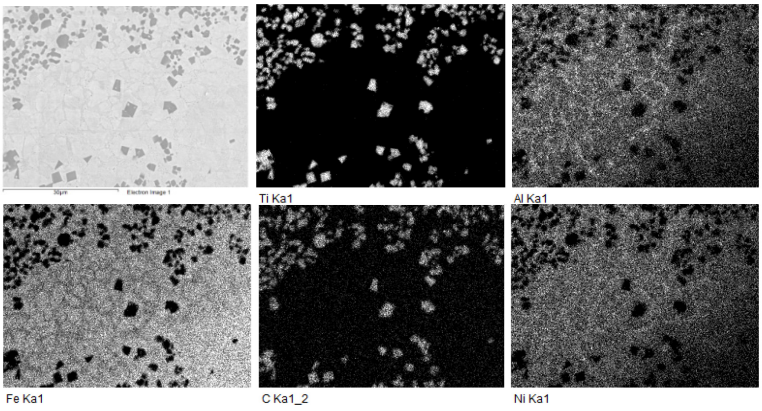

(a)

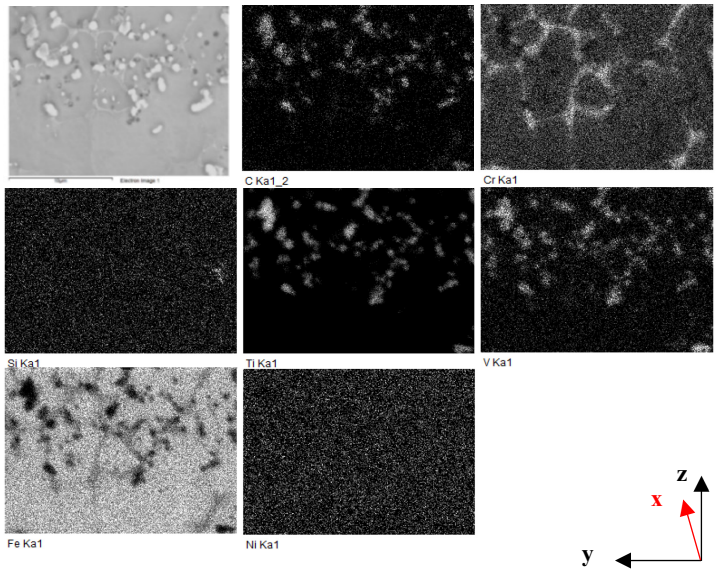

(b)

Figure 73. EDS captures of TiC-Ni_3Al clad coatings on D2 steel with 30 vol.% metallic phases processed at P = 300 W and τ = 1.4 s: (a) at the top portion of the clad zone, and (b) at the clad/substrate interface. Note that the x-axis denotes the direction of laser scanning in each case.

EDS analyses on the clad/substrate interface and through the HAZ area detected a sudden change in the distribution of Fe and Cr, diffusing from the substrate, at the interface (Figure

74). Although this can be generally attributed to elemental diffusion and dilution of the substrate, it can be assumed that given the relatively controlled range of diffusion, this would also likely be quite beneficial to the clad/substrate adhesion.

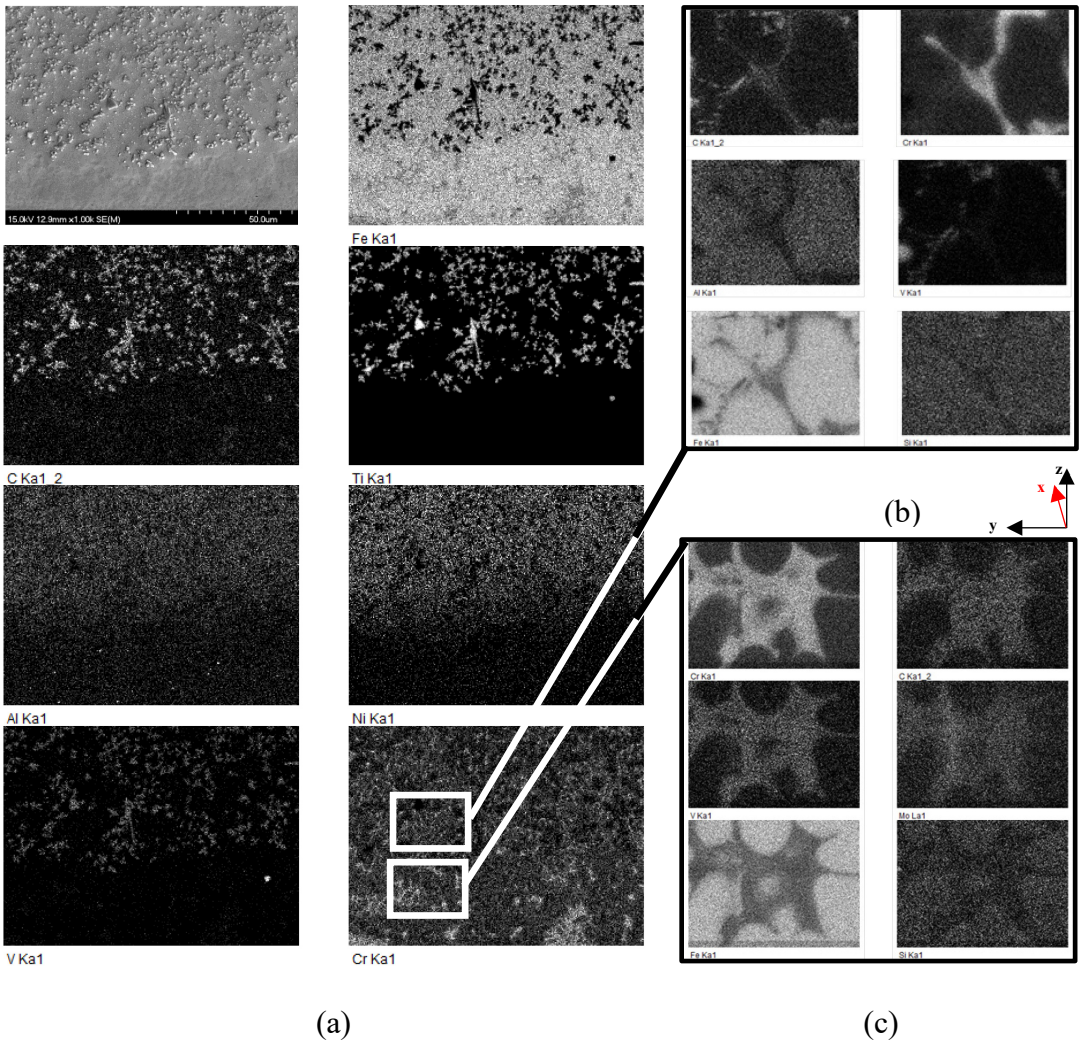

Figure 74. Corresponding EDS mapping from the cross section of the TiC-Ni_3Al/D2 steel substrate clad couple, highlighting the transition in structure from: (a) the clad layer coating, to (b) the clad layer/substrate interface, and (c) the HAZ. The sample was processed at a laser power of P = 350 W and τ = 1.2 s. Note that the x-axis denotes the direction of laser scanning in each case.

Figure 75 represents an example of low magnification CLSM optical micrograph obtained from cross section of TiC with (40 vol.%) Ni_3Al intermetallic clad coatings, onto D2 steel substrates at P = 350 W and τ = 1.12 s laser power.

The low magnification microscopy on etched specimens shows that $(Fe, Cr)_3C$ carbide is mostly present along the grain boundaries of the austenitic metallic matrix while the microstructure of the as received D2 consisted of large carbides in a matrix of tempered martensite [381].

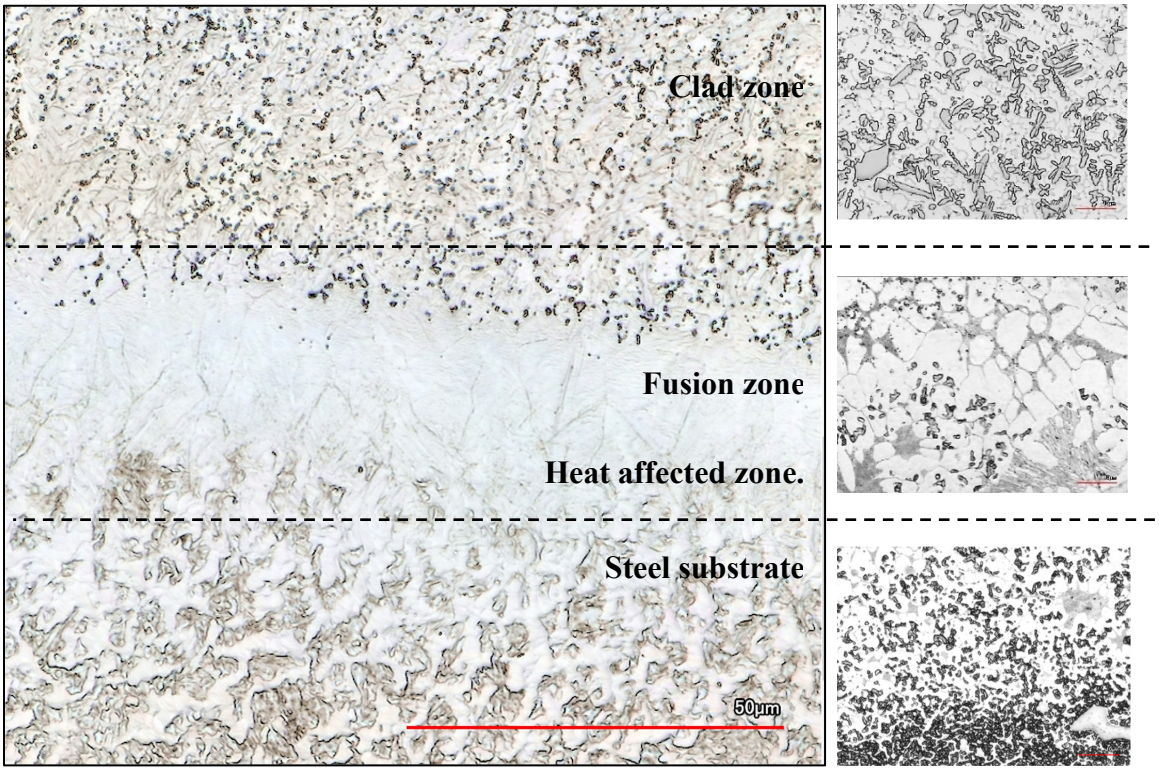

Figure 75. CLSM optical micrographs illustrating the variation of morphology with the TiC-Ni_3Al (40 vol.%) clad on D2 steel, laser processed at P = 350 W and τ = 1.12 s.

Microstructural analysis, in conjunction with the results from phase identification, revealed that the laser DED manufactured clads exhibit a general morphology with the dispersed hard phase within a metal matrix that varies in terms of microstructural characteristics. This variance was seen to strongly depend upon three main factors: (i) the laser processing parameters (i.e., laser power and scanning speed), (ii) the volume content of the introduced metallic phase (i.e., Ni_3Al) within the feedstock, and (iii) the clad depth in relation to clad/substrate interface. Thus, the subsequent microstructural examination of the fabricated clads has been presented in accordance with these factors.

5.3.5.2. Effect of laser parameters on clad morphology

Microstructural analysis shows that at P = 350 W and τ = 0.1 s, a high-density layer is produced at the surface of the substrate, which is well bonded to substrate regardless of the content of Ni_3Al. Figure 76 highlights the three predominant structures observed within the clad layer, which vary in final morphology by means of their kinetics of solidification. Analysis of the microstructure of the present TiC-Ni_3Al based clads revealed that at 350 W laser power, when $\tau \leq 1$ s, both the size and volume fraction of TiC particles significantly varies, transitioning from small globular particles to coarse 'flower-like' clusters. Such an inhomogeneous microstructure was found to result in formation of microcracks with some pores around the un-melted particles. A prior study has reported that variation of TiC particle morphology is largely affected by its location within the clad layer [382].

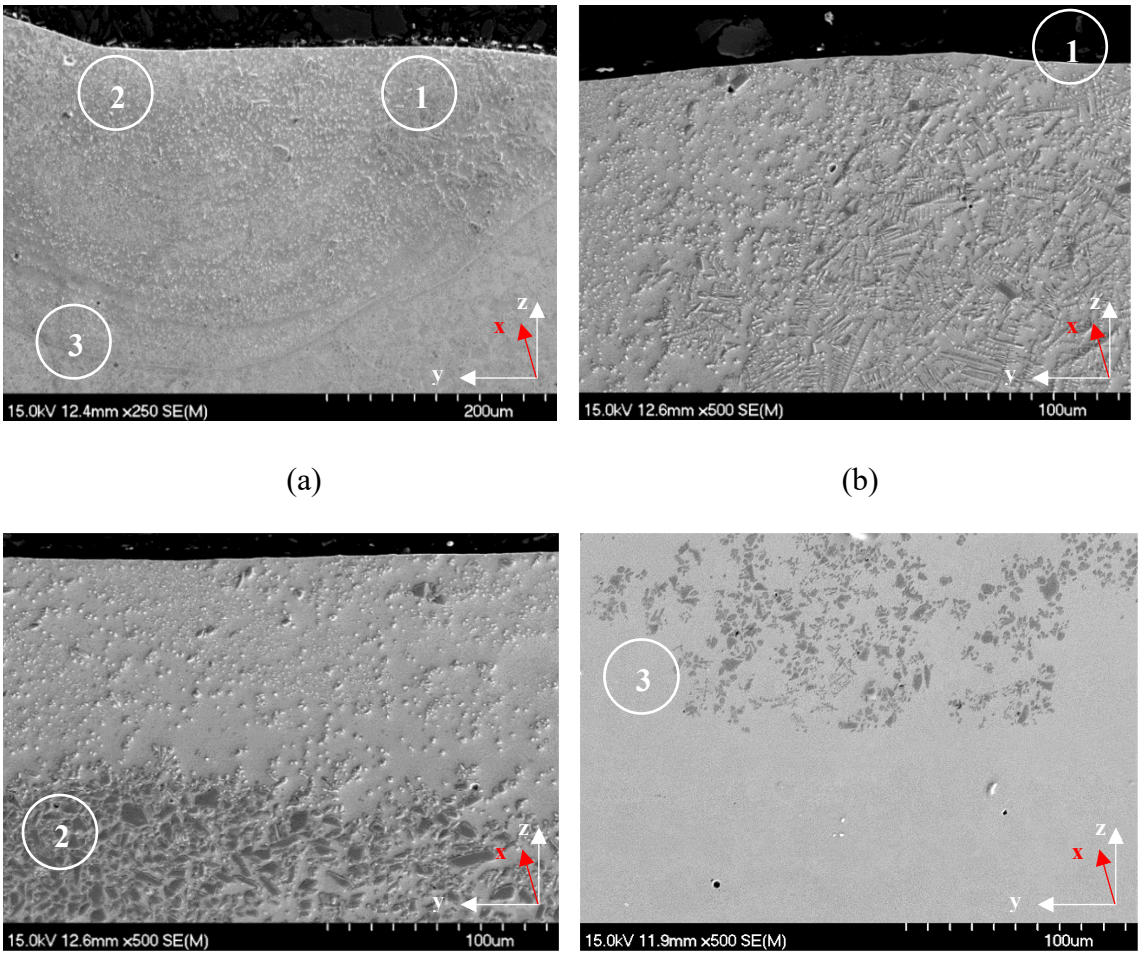

Figure 76. SEM micrographs illustrating the variation of morphology with the TiC-Ni_3Al (40 vol.%) clad on D2 steel, laser processed at P = 350 W and τ = 0.1 s. (a) Low magnification SEM image of the TiC-Ni_3Al/D2 steel substrate clad couple. (b) Low magnification SEM image of the clad surface at the edges of the melt pool. (c) Low magnification SEM image of the clad surface at the center of the melt pool. (d) Low magnification SEM image of the clad/substrate interface at the central access of the melt pool. Note that the x-axis denotes the direction of laser scanning in each case.

From the SEM micrographs shown in Figure 76, it is apparent that the cooling rate is a dominant phenomenon in establishing the localized temperature of the system, which gives rise to the formation of various carbide sizes and morphologies. It is well known that the overall solidification dynamics, degree of dispersion, and size of these carbides are ultimately responsible for controlling the mechanical properties of high-speed and tool steel grades [383–385].

The solidification of the coating material begins at the coating/substrate interface substrate (Area 3), shown in Figure 76 (d). In this region, the crystal's nucleation rate is higher than their growth rate, resulting in formation of a fine, globular microstructure. With increasing distance from the steel substrate, the ratio of the temperature gradient to solidification rate decreases and, consequently, the formation of a dendritic morphology was observed (Area 1, in Figure 76 (b)). The maximum solidification rate is reached within the zone just below the surface (area 2, in Figure 76 (c)), where there are a limited number of large, partially melted reinforced TiC particles. As the TiC based carbides are nearly entirely dissolved, the matrix is enriched with Ti and C, which results in the formation of carbides (visible in the form of white contrast precipitates in Areas 1, 2 and 3). These carbides exhibit minimal dendritic growth and are mainly preserved in the cubic/polygonal morphology. The presence of such isolated, individual particles has been reported to rapidly increase the value of hardness of such composites into a range of 1000-1600 HV [22,53,386,387]. Examples of the morphology obtained from cross section of the TiC-based clads, prepared with same volume content of Ni_3Al intermetallic matrix (40 vol.%), but higher scanning speeds (i.e., $\tau \geq 1$ s) and again clad onto D2 steel substrates at 350 W laser power, are presented in Figure 77.

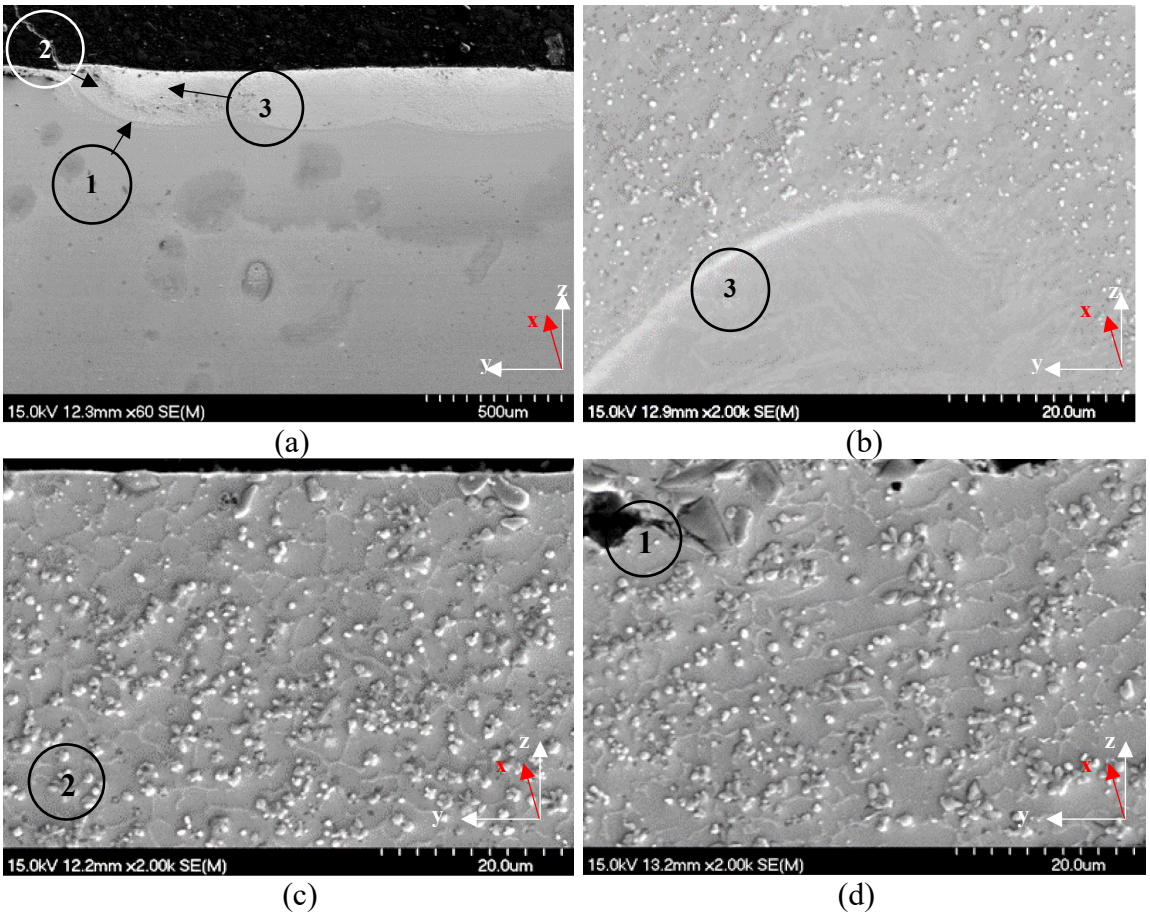

Figure 77. SEM micrographs illustrating the variation of morphology with the TiC-Ni_3Al (40 vol.%) clad on D2 steel, laser processed at P = 350 W and $\tau \geq 1$ s. (a) Low magnification SEM image of the TiC-Ni_3Al/D2 steel substrate clad couple. (b) at the clad/substrate interface at the central access of the melt pool. (c) at the clad surface at the center of the melt pool. (d) at the clad surface at the edges of the melt pool. Note that the x-axis denotes the direction of laser scanning in each case.

As shown in Figure 77 (a), at higher scanning speed, compositions containing 40 vol.% metallic binder, clad layers exhibited dense clads with optimal layer thickness which were well adhered to the substrate. The dispersion of hard phases in the clads with higher scanning speed and same laser power was observed to be homogeneous in all of the clad

zones (i.e., Areas 1, 2, and 3). In contrast, the increase in volume fraction of the binder phase resulted in the formation of clad layers with high levels of dilution and undesired reduction of the clad height. Moreover, it was noted that at higher laser scanning speeds, the variation of the fabricated carbides also becomes dependent on compositional variations introduced by the feed source or caused by the laser processing parameters.

5.3.5.3. Microstructural variations due to the volume content of Ni_3Al metallic binder

Examples of the morphology obtained for partially melted TiC carbide particles within the nominally Ni_3Al intermetallic matrix are presented in Figure 78, for clads prepared with 30, 40, and 50 vol.% Ni_3Al binder, deposited onto D2 steel substrates at 350 W laser power and higher scanning speeds (i.e., $\tau \geq 1$). The dispersion of the hard carbide phase(s) within clads with 30 vol.% Ni_3Al metallic binder composition was observed to be homogeneous through the various clad zones, while minimal dendritic growth was observed (Figure 78 (a)). In contrast, the increase in volume fraction of the binder phase resulted in formation of clad layers with high levels of dilution and an undesired reduction of clad height (Figure 78 (b,c)). At a 30 vol.% Ni_3Al content, a high portion of the reinforcing TiC particles are still present in their primary form (i.e., angular grains, 2-5μm in size), and lower levels of wetting that may be anticipated due to a reduction of the liquid phase appear to have resulted in the formation of some residual pores within the microstructure of the clad coatings. At 40 vol.% Ni_3Al content, partial melting of the larger TiC carbide particles results in the generation of nucleation sites for the crystallization of complex carbides. Complex carbides are generally established in a ternary system that contains a transition element (M), and a B-group element (M′), in addition to carbon, with typical

stoichiometries of $M_2M'C$ or $M_3M'C$ [388]. At 50 vol.% Ni_3Al content, the formation of a coarse dendritic TiC structure (darker grey contrast) was observed, which distinctly changes in terms of its microstructural features when moving towards the mid-section of the clad layer. Moreover, the TiC dendritic structure, which is an indication of constitutional supercooling [389], is uniformly dispersed within a fine lamellar eutectic matrix structure, which also changes when progressing towards the substrate/clad interface. In a study of plasma spray deposition in the Ti-Fe system, it was suggested that spherical TiC particles develop in a semi-solid melt region while, in contrast, a dendritic structure results from solidification of a completely liquid melt pool [62]. In that instance, the semi-solid process zone can be viewed as un-melted particles of TiC within a liquid metal phase. Thus, a decrease in the hard phase content (i.e., a higher Ni_3Al intermetallic volume fraction), leads to a decrease in the rate of nucleation and results in undesired dendritic growth.

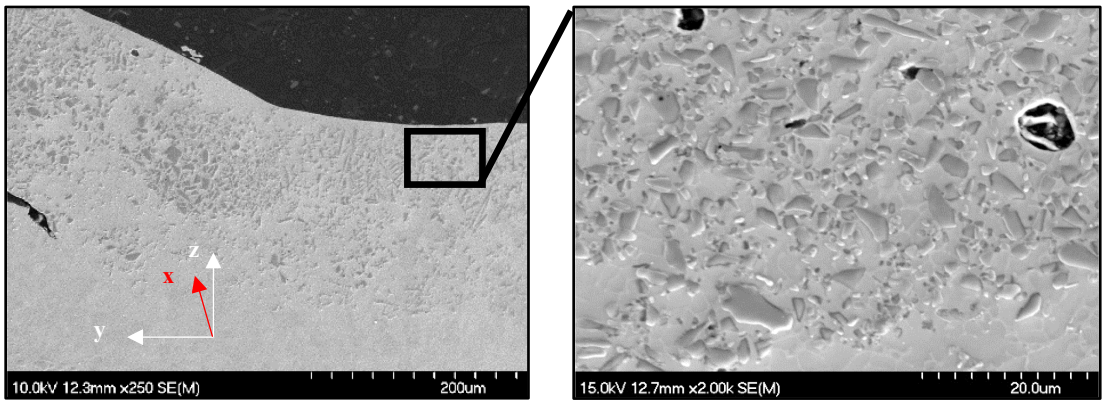

(a)

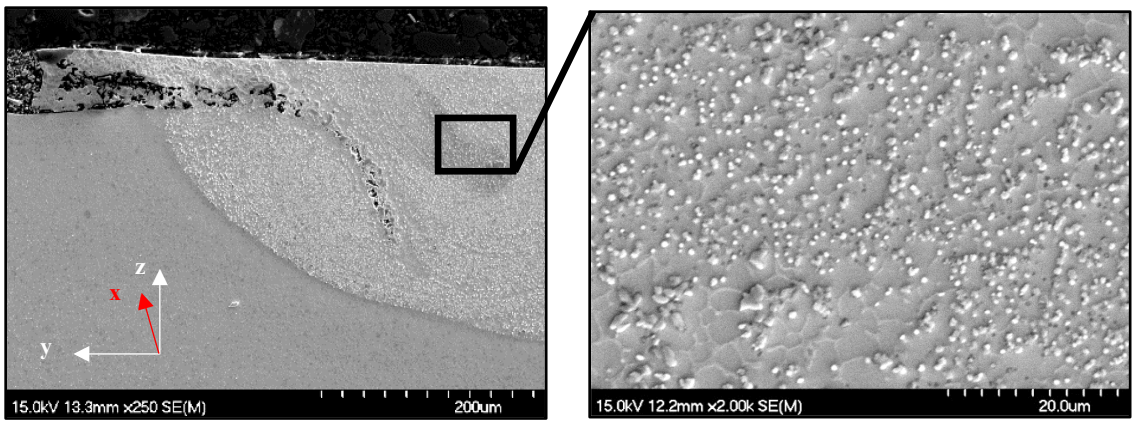

(b)

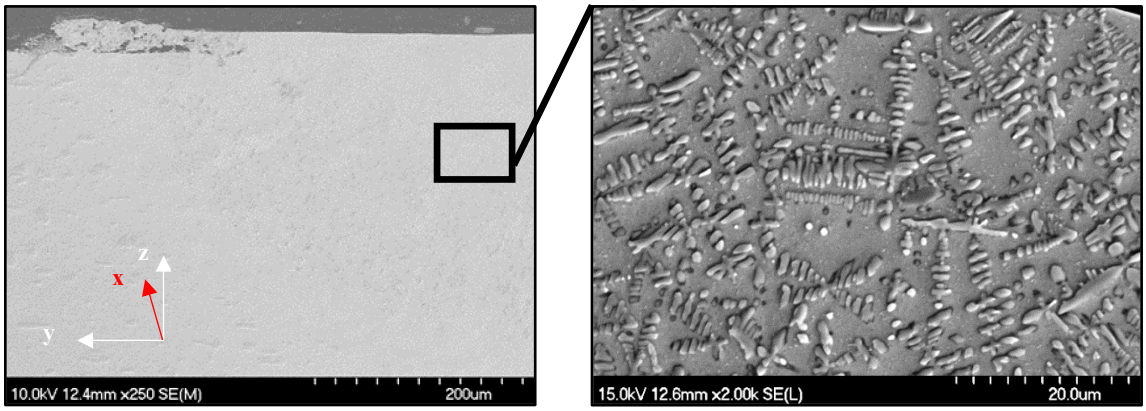

(c)

Figure 78. Cross sectional view of TiC-Ni_3Al based DED clad coatings on D2 steel with: (a) 30, (b) 40, and (c) 50 vol.% Ni_3Al metallic binder. Samples were all laser processed at P = 300 W and $\tau = 0.14$. Note that the x-axis denotes the direction of laser scanning in each case.

5.3.5.4. Variation of clad morphology within the clad depth

Microstructural investigations at higher scanning speed, unsurprisingly, showed that the morphology of the homogeneously dispersed phases within the clad depth, slightly varies in size within the different clad zones. This is proposed to be due to the ultra-rapid heating and cooling rates that arise during laser processing of thin coatings (Figure 79).

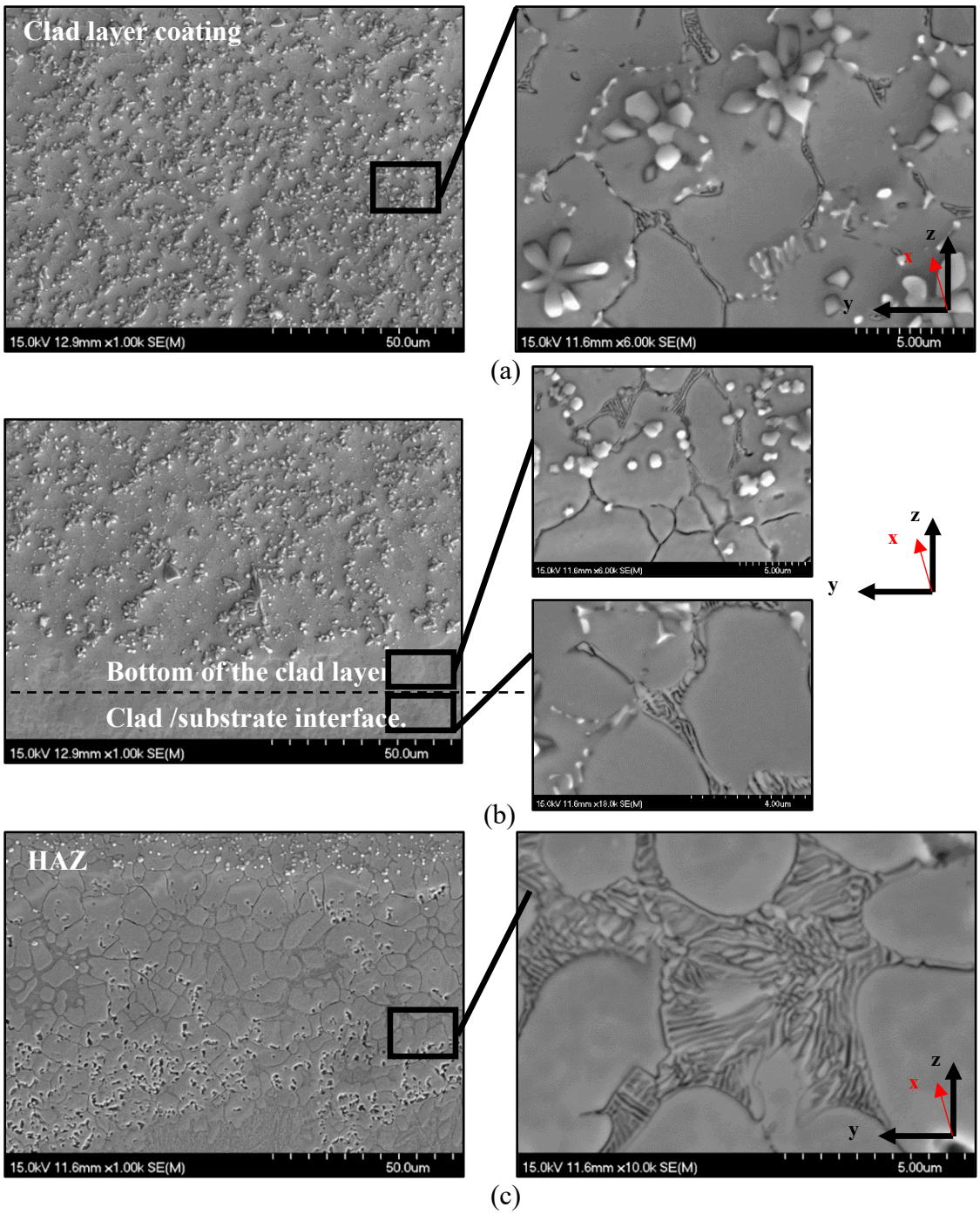

Figure 79. (a) SEM images of the TiC-Ni_3Al/D2 steel substrate clad couple, highlighting the transition in structure from: (a) the clad layer coating, to (b) the clad layer/substrate interface, and finally (c) the HAZ. The sample was processed at a laser power of P = 350 W and τ = 0.2 s. Note that the x-axis denotes the direction of laser scanning in each case.

Figure 80 presents higher magnification SEM images of the carbide microstructures that are consistently observed from the mid-section and the bottom layer of the TiC composite coating, with 30 and 40 Ni_3Al, fabricated at higher scanning speeds (i.e., $\tau \geq 1$s); in this instance the clad conditions were P = 350 W and τ =1.4 s. At 30 vol.% Ni_3Al metallic matrix content, the TiC reinforcing phase developed into nucleation sites for primary V- and Mo-based carbides that precipitate during the laser melting/solidification process. These carbides exhibit a hexahedral structure (with morphologies ranging from blocky to round) which often forms a flower like morphology, resulting from coalescence and partial sintering of TiC based carbide particles.

Primary carbides generally can be identified with a dark core that is known to be composed of Ti, and C and rim structure which generally formed by a mixture of Fe, Cr, V, W, and Mo (along with C) and leading in formation of an octahedron type microstructure surrounded by low index face of TiC cubic crystal (Figure 80 (a), (Areas 1 and 2)). Moreover, Ni is also apparent, but this is likely due to X-ray generation from the immediately surrounding matrix. This is because TiC is partially soluble in Ni, which may result in agglomeration of the nucleated TiC particles toward the mid-section of the clad. Pei and colleagues have confirmed similar microstructures via TEM analyses on laser processed TiC based cermet coatings within a broadly similar Fe, Ni metallic matrix [40]. Therefore, upon solidification, nucleation of TiC occurs from the melt pool, while some MC type carbides decomposed into M_6C carbide by the reaction [40]:

$$MC + \gamma \rightarrow M_6C + \gamma'$$

As it is shown in Figure 80(b), three particles are attached to each other without fully fusing during the fast growth of the solidification front and precipitation of carbides out of the supersaturated melt in the middle and bottom of the clad.

The rod like continuous network, denoted in Figure 80 (a) by (Area 3), are known to be M_2C type carbides, which were mainly rich in Cr and Mo in the present case. The morphology of this type of carbide transformed from rod-like to lamellar as the volume content of the Ni_3Al component was increased. Elemental compositions of the primary hard phase obtained from mid-section of the TiC-Ni_3Al 30 vol.% composite coating on D2 steel, fabricated with P = 350 W and τ = 1.4 s is shown in Figure 81.

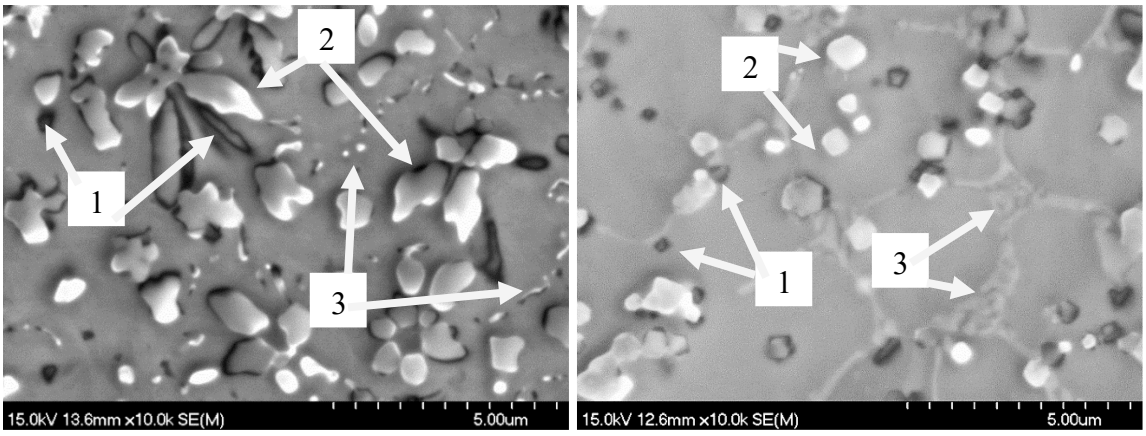

(a) (b)

Figure 80. High magnification SEM micrographs highlighting various carbide microstructures that were repeatedly observed in laser cladding of D2 tool steel with: (a) 30 vol.%, and (b) 40 vol.% Ni_3Al metallic binder, processed at P = 350 W and τ = 1.4 s.

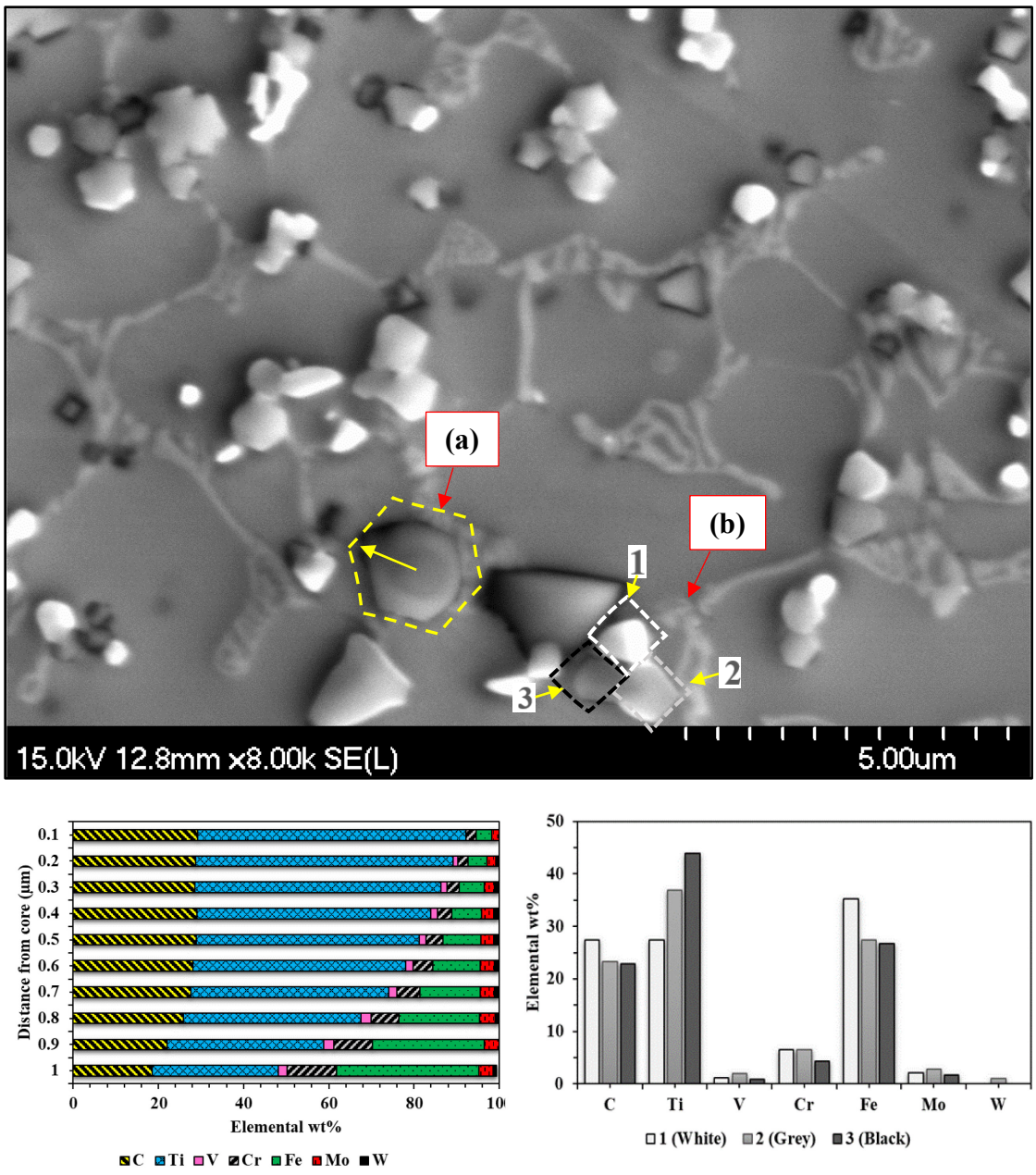

(a) (b)

Figure 81. Elemental compositions of the primary hard phase obtained from mid-section of the TiC-Ni_3Al 30 vol.% composite coating on D2 steel, fabricated with P = 350 W and τ = 1.4 s, in relation to: (a) the center of the grain cross section, and (b) highlighting the elemental composition of three types of carbide structure repeatedly observed during laser processing of the D2 tool steel.

5.3.6. Mechanical testing

Tensile experiments were conducted according to the ASTM E8/E8M standard (*Standard Test Method for Tensile Testing of Metallic Materials*). Tensile properties were evaluated for two different sets of cladding parameters, in addition to the as-received D2; two tests were conducted for each process variant. This was performed for a further examination of the impact of the outlined coating process conditions. Figure 82 demonstrates the tensile testing results obtained for both the as received and cermet clad tensile samples, fabricated onto D2 steel.

Since the lath-shaped martensite generally has high hardness, the ductility of the AR tensile samples is anticipated to be favorable. Nevertheless, it could be seen that both clad specimens possessed a very low elongation (0.1 % and 0.01 %) and a low toughness (42.7 J/m^3 and 19.3 J/m^3), although exhibited an excellent tensile strength (404.8 and 333.2 MPa. The surface microstructure results in a high ceramic content, which is detrimental to the fracture toughness of the material. Toughness may also be impacted by the final surface residual stress, while the roughness can impact the strength. The various grain sizes nucleated in different zones of the melt pool may lead to different extents of the strengthening effect.

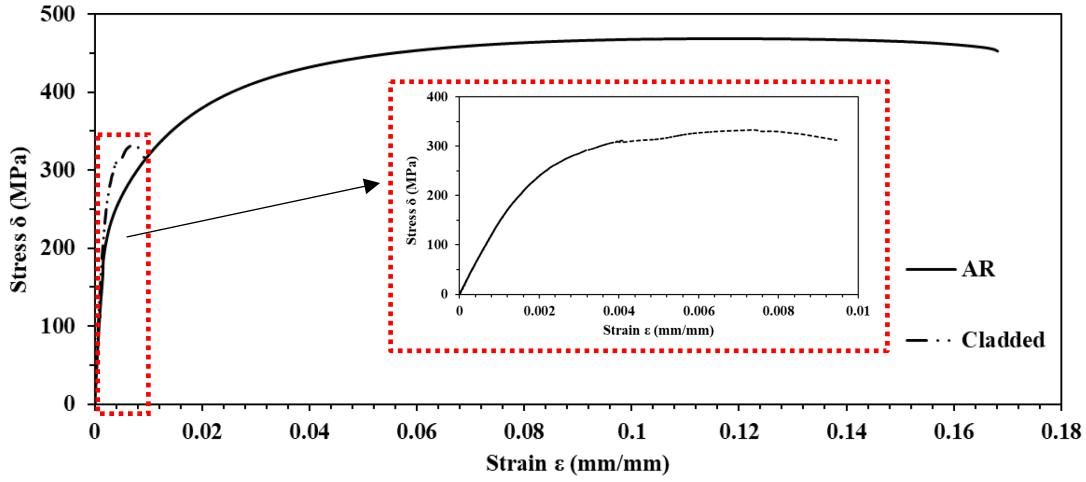

(a)

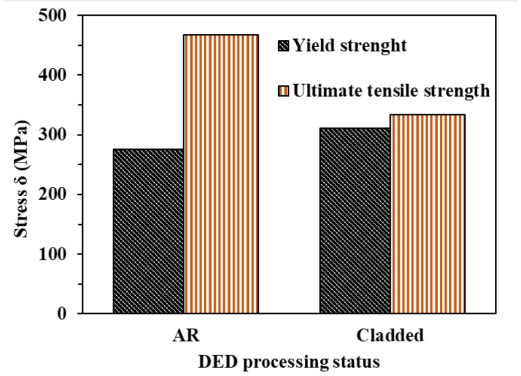

(b)

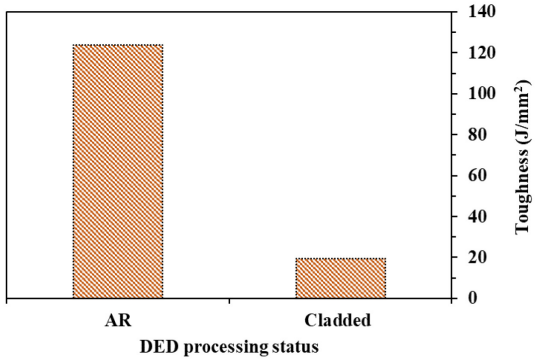

(c)

Figure 82. (a) Typical tensile stress-strain curves for the as-received D2 substrates and the TiC-Ni_3Al 40 vol.% cladded specimens (P = 350 W and τ = 1 s, with E = 297.7 J/mm^3). (b) Reduced strain range plots of the tensile stress-strain curves for the TiC-Ni_3Al 40 vol.% cladded specimens shown in (a). (c) The calculated toughness of the clad and as-received samples.

Localized inhomogeneity within the microstructure may generate moderate to large stress concentration(s), accelerating the expansion of any cracks that might be present. Crack propagation occurs at the locally weak zones (i.e., where there are defects and voids) during tensile testing, leading to premature failure.

The occurrence of martensitic transformation generally accompanies laser processing, creating pronounced residual stresses within the crystalline grains. The stress arising from this phase transformation also brings greater brittleness to the laser processed samples. Fracture morphologies of the as built and DED cermet coated tensile samples fabricated at (E = 297.7 J/mm^3) are shown in Figure 83, while Figure 84, illustrates a comparison between the tensile fracture surfaces of the clad sample and as-received steel substrate. The fracture surface is characterized by the generation of cleavage microcracks, shortly followed by plastic deformation.

Moreover, second phase particle cracks and microcavities generated from ferrite pre-crack tips were detected (Figure 83 (a)). This type of post tensile microstructure has been previously reported by other studies on steel substrates with α-Fe/Fe_3C interface structure [390,391]. The fracture surfaces of the as-received D2 samples exhibited equiaxed dimples in addition to some cleavage planes, indicative of a both ductile and brittle failure. Post fracture cross-sections of the cermet clad specimens demonstrated an obvious “cleavage river pattern”, showing a typical brittle fracture response [383]. This was in accordance with the very low toughness values recorded during the tensile analyses.

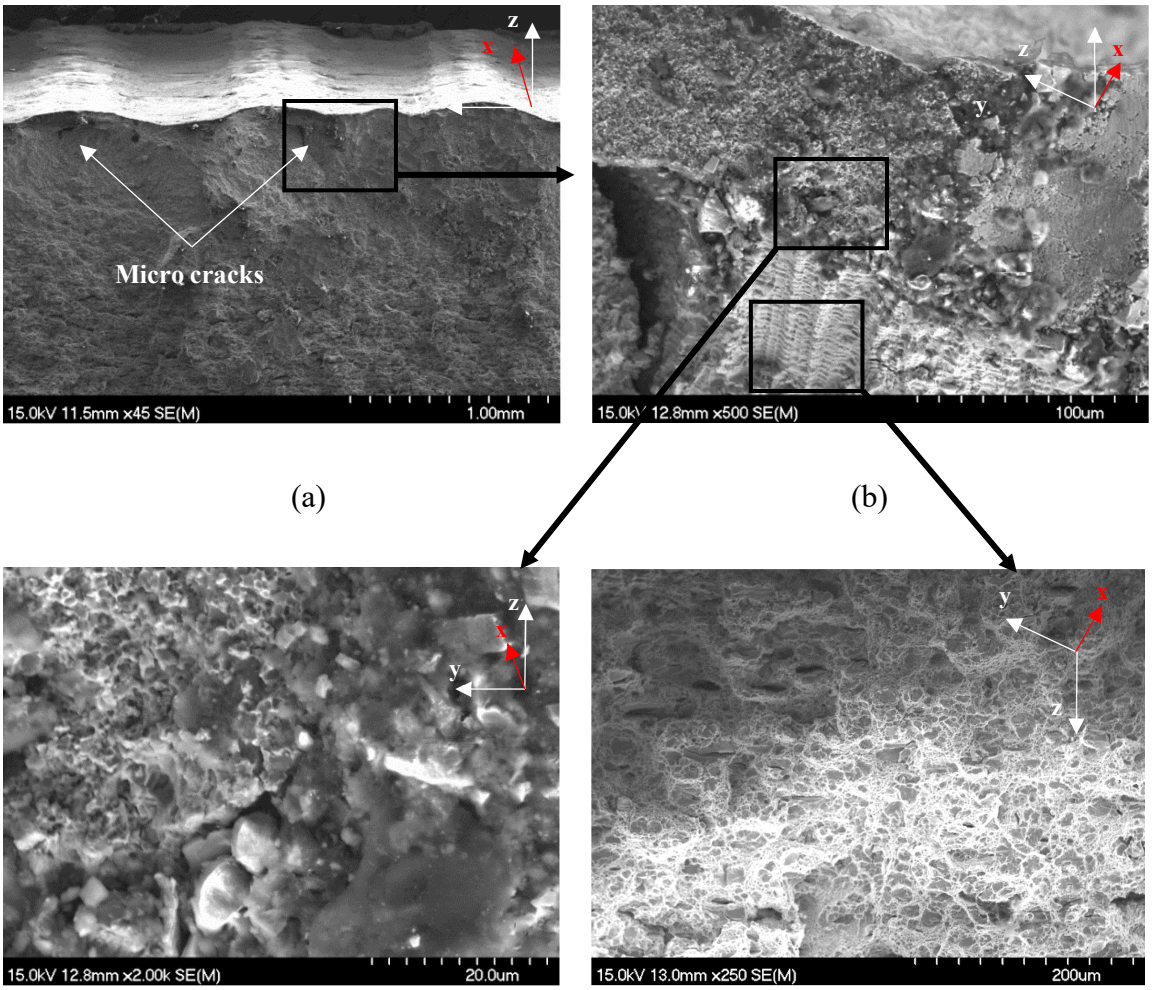

Figure 83. SEM micrographs captured from the tensile fracture surfaces of laser-processed TiC-Ni_3Al 40 vol.% coating on D2 substrate (P = 350 W, and τ = 1 s, E = 297.71 J/mm^3). Images are recorded at: (a) the cross-section of the fracture surface highlighting various locations with respect to the coating/substrate interface, (b) a top (plan) view of the fractured coating/substrate edge, (c) the cross section of the clad layer, and (d) the cross section of the substrate below the clad layer. Note that the x-axis denotes the direction of the laser scan.

5.4. Conclusions

The *in-situ* gelation of aqueous TiC-Ni_3Al feedstock suspensions, with sodium alginate as a gelling agent, was examined for preplacement of feedstock material onto D2 steel substrates and subsequent laser cladding. The feedstock preplacement step was conducted by dip coating, as an alternative to conventional dry powder preplacement. Suspension-based preplacement has several advantages, notably much higher solids contents are possible, in comparison to dry powder placement, while this route also creates the opportunity to use very fine (i.e., sub-micron) particles within the suspension.

When dip coating, it is apparent that when sodium alginate gelation takes place, it improves the quality of the powder coating quite considerably (in contrast to suspensions without sodium alginate). The extent of potential cross-linking during gelation was also examined through control of substrate temperature prior to dip coating; the coating step was thus found to be further improved by precooling the substrate. The presence of divalent and trivalent cations, specifically Ni^{2+} and Al^{3+}, were shown to be an effective cross-linking agent, being slowly released from particles within the colloidal suspension into the local aqueous environment; in this instance, diffusion only needs to occur over a ~1 μm (or less) length scale. The outlined method was confirmed to be effective as an environmentally friendly processing step (sodium alginate is a food-grade biopolymer), while a high powder packing density can then be achieved in the coating.

After the dip coating stage, the optimal processing parameters for laser cladding of dense, TiC-Ni_3Al metal-matrix composite coatings onto D2 tool steel substrates were assessed, and a relationship between the various parameters was analysed. A laser power of 300 W and scan speed of 50.8 mm/min was required to produce a successful single-track/layer

deposit with the desired bonding to the substrate across the clad width from gel-based cermet clads. The real-time cooling rate was found to affect the dilution and morphology of carbides generated in the clad. It was observed that the scan speed affects the dilution and cooling rate, which are the two main factors in establishing the desired carbide morphology and microstructure. Results show that cooling rate has the most dominant effect on the morphology and size of the TiC particles transitioning from small globular particles to coarse 'flower-like' clusters. Ultimately, the extent of heat generated by use of different scan speeds results in varied carbide morphologies and distributions. Microstructural analysis, in accordance with the results of phase identification, demonstrated that the polygonal/cubic morphology of the dispersed hard ceramic phase, within a ferrous/Ni,Al containing metal matrix, varies in characteristics based on three main factors:

Laser processing parameters (i.e., laser power (P) and scanning speed(V)): At 350 W laser power, for $\tau \leq 1$ s, both the size and dispersion of TiC particles significantly varies through the depth of the clad layer, causing inhomogeneity and a possible decline in the mechanical characteristics. In contrast, increasing the scan speed (i.e., $\tau \geq 1$ s), homogeneous dispersion of the hard phase was observed within clads throughout its depth.

The volume content of the introduced metallic phase (i.e., Ni_3Al) within the feedstock: The dispersion of the hard carbide phase in clads with 30 vol.% Ni_3Al metallic binder composition was observed to be homogeneous through the various clad zones, with minimal dendritic growth observed. In contrast, increasing the volume of the binder phase resulted in the formation of clad layers with high levels of dilution and an undesired reduction of the clad height.

The clad depth in relation to clad/substrate interface: Structural investigations at higher scanning speed, showed that the morphology of the homogeneously dispersed phases within the clad depth, slightly varies in size throughout the depth, due to the ultra-rapid heating and cooling rates that arise during laser processing of such thin coatings.

The mechanical characteristics of the fabricated clads were examined through preliminary tensile testing. The clad specimens demonstrated a very low elongation (0.1 % to 0.01 %) and a low toughness (19.3 to 42.7 J/m^3), although exhibited a reasonable tensile strength (333.2 to 404.8 MPa). The low toughness in laser processed tensile parts was attributed to the heterogeneous microstructures and grain size. Therefore, the various grain sizes nucleated in different zones of melt pool may lead to different extents of the strengthening effect.

Chapter 6. Scratch resistance and damage mechanisms arising in TiC-Ni_3Al based laser DED clads on D2 tool steel

Z. Russell, A. David, M. Amegadzie and K.P. Plucknett*

Department of Mechanical Engineering, Dalhousie University, 1360 Barrington Street, Halifax, Nova Scotia, Canada

email: *kevin.plucknett@dal.ca

Keywords: directed energy deposition; laser cladding; cermets; additive manufacturing; wear behaviour; tool steels; hardness

Abstract

TiC-based cermet coatings have been applied onto high Cr-containing, cold work D2 tool steel substrates through laser direct energy deposition (DED). A suspension-based preplacement method was used for first applying the coating feedstock onto the substrate prior to DED laser cladding, by dip coating of the steel substrate into a suspension of TiC-Ni_xAl_y-Ni (with an overall Ni_3Al stoichiometry). Process optimization gives well-adhered, preplaced feed stock material on the surface of the substrate, with a uniform thickness. The preplaced material was then subjected to laser DED processing using various laser powers and scanning speeds, resulting in fabrication of high density clads on the substrates. The subsequent mechanical enhancement of the D2 steel surface was quantified in relation to the laser processing parameters. Hardness profiles were generated by cross sectional micro indentation of the clad layers. Micro-Vickers hardness (VH) values of the cermet coatings have been measured from load–displacement curves under a range of applied normal forces. Results VH of the composite coatings are in the range of 265.7 to 890.3 GPa. As a preliminary assessment of the wear response, a variety of single pass scratch testing

approaches have been undertaken. A qualitative evaluation of interfacial strength between coating and substrate material was also performed by cross sectional scratching of the clad coatings. Failure modes and damage mechanism were examined at different processing parameters by means of acoustic emission (AE) and coefficient of friction (COF) measurements, together with assessment of the post-test microstructures. The scratch hardness (H_{Sp}) of the cermet clad coatings varied within the range of 4.88 to 7.58 GPa, as a function of applied normal force (ranged within 10 - 40 N), which was considerably higher than the D2 substrate (H_{Sp} = 3 GPa under applied force of 10 - 40 N). Mechanical performance of the modified D2 steel surfaces was found to vary considerably, depending on the implemented laser-processing parameters and its resultant solidified microstructure.

6.1. Introduction

Ultra-high strength steels, which are utilised in numerous applications in everyday life, are highly sensitive to damage caused by corrosion, fatigue, and stress corrosion cracking [392–396]. This type of damage, in applications with geometrically optimised components, is usually followed by costly replacement of the parts. Consequently, discovering preventive measures and feasible *in situ* repair strategies have been attractive scientific and industrial pursuits for many years [74,191,397–399]. Enhancement of the functional properties of steel surface by application of ceramic composite coatings has been found to be an effective technique [75,76,400–403]. Ceramic particles invariably have much higher elastic modulus and abrasion resistance in comparison to the majority of metals and typically maintain their mechanical integrity at elevated temperatures. Several deposition techniques have been reported in the open literature, such as chemical and physical deposition (CVD and PVD), mechanical milling plasma-based implantation, sputtering, pulsed electrode surfacing and deposition, laser deposition, etc. [404–412]. However, many of these techniques are generally expensive and require complicated procedures and long fabrication times [413–416], while often leading to fairly thin coatings. Table 15 outlines some examples of high-performance cermet coatings, their associated processing routes, and their measured hardness values, as reported in the open literature [2,417–424]. Since the arrival of laser-based manufacturing technologies, laser hardening has been explored by a number of researchers for modification of the surface properties on hard steels. Increased wear and hardness properties have been reported when the surface was subjected to a high energy laser, where high heating/cooling rates and quenching of the substrate have resulted in the formation of a martensitic structure [425–428]. Laser

cladding has been applied to rebuild material, following removal of the damaged zone through grinding. This allows restoration of both the original dimensions and mechanical properties of the component, with particular attention to the fatigue life that can qualify for the minimum safety level. Laser cladding thus offers *in situ* repair of high value components such as turbine blades, specialty tools, gas turbine parts, and internal combustion engine components [74,221,397,398]. Superior strength, hardness and fracture toughness, in contrast with relatively low production costs, have been extensively used in the fabrication of wear resistant composites [429–432].

Table 15. The hardness of some advanced composite coatings and their related processing routes reported in the literature.

Composition	Processing technique	Hardness	Source
Cr_3C_2/25% Ni–Cr	**High velocity oxyfuel (HVOF), direct diode laser**	HV 1032	[29]
ZrB_2–ZrC/Ni	**Self-propagating high-temperature synthesis (SHS), atmospheric plasma spraying (APS)**	$HV_{0.1}$ 525.02 (± 96.08)	[30]
Al_2O_3	**Gas tunnel-type plasma jet**	HV 1200	[31]
WC–Cr_3C_2/Ni and WC/Ni	**HVOF**	$HV_{0.3}$ 1188 and 1105	[32]
Ni/ZrO_2	**Electroplating**	HV_{25} 600	[33]
TiC/20 wt%Ni (bulk)	**Sintering**	HV 1295	[34]
Ti/TiC	**Laser melting (LM)**	HV 700	[35]
Ti/SiC	**Laser deposition (LD)**	HV 647.5	[36]
Graphene oxide (GO)/TiC	**Powder fed laser deposition (PFLD)**	$HV_{0.1}$ 250-350	[37]

With this in mind, the present study investigates the use of laser-based DED cladding for applying TiC-Ni_3Al based cermet coatings onto D2 cold worked tool steel substrate. A preplacement approach is developed, that is based on the use of an aqueous suspension of TiC-Ni_xAl_y-Ni and sodium alginate. Using a suspension-based approach allows moderately complex-shaped components to be coated, through controlled dipping, which is much more challenging to achieve with dry-powder preplacement approaches. Furthermore, an important benefit of utilising suspension-based preplacement is that the effective solids loading in the dry powder is significantly greater than when using dry powder (typically 3 to 5 times higher). In terms of the examined substrate, AISI D2 steel has been extensively used in the tool and die industry for manufacture of wear resistant parts with a high degree of machinability. However, this family of steels suffers from low surface hardness, and mechanical failure often arises with rapid variation of large forces at frictional contact points [8,433,434]. Damaged surfaces are also susceptible to further degradation of the service parts in corrosion scenarios, due to the generation of localised corrosion sites, particularly under harsh operating environments [435–437]. Surface modification via laser beam technologies has consequently been suggested as an effective technique in improving the mechanical properties of D2 steel [438–441]. While the mechanical properties of the bulk material can be determined via a number of established techniques, a true understanding the failure mechanisms and their progression for more complex structures (i.e., with laser printed surface layers), demands precise micro-testing and observation techniques that are capable of generation and processing wide range of data within short processing times [7,442–444]. Consequently, such micro-mechanical/tribology approaches have been utilised in this work to determine the impact of TiC-Ni_3Al based cermet coatings

on the mechanical performance of the D2 cold worked tool steel substrate fabricated by laser cladding.

6.2. Experimental Procedures

6.2.1. Materials

The present TiC-Ni_3Al cermet formulations were prepared by mixing TiC powders, and the constituent precursors to form the intermetallic Ni_3Al binder phase through a reaction sintering approach; in this instance, a mixture of Ni_xAl_y and Ni were employed. The final Ni_3Al content in the mixtures were targeted from 30 to 50 vol% of the overall cermet composition. The TiC powder (lot no. PL20126240; particle size of 1.0 - 2.0 μm) used in this work was procured from Pacific Particulate Materials Ltd. (Vancouver, BC, Canada), while both the Ni powder (lot no. L10W013; particle size of 2.2 - 3.0 μm) and Ni_xAl_y powder (lot nos. D28X029 and G19X071, respectively; each with D_{50} = 32 μm) were purchased from Alfa Aesar (Ward Hill, MA, USA); it should be noted that the Ni_xAl_y powder exhibited a 1:1 weight ratio between Ni and Al. After weighing the starting materials, each examined cermet composition was ball milled for 24 hours with yttria-stabilized zirconia milling media in acetone, followed by a 24-hour drying period. The dried powders were subsequently sieved through a -75 μm stainless steel mesh screen, to eliminate any potential hard agglomerates. The laser clads were fabricated onto annealed and precision ground D2 tool steel plates supplied from McMaster-Carr (Douglasville, GA, US). The substrate specimens were sectioned into a final geometry of 75 x 50 x 5 mm and

were subjected to abrasive grit blasting with 300 μm zirconia shot prior to preplacement of the cermet feed material, as follows.

Stable, aqueous cermet suspensions with 50 wt.% solids loading were then developed from a solution of 1.6 wt.% sodium alginate and distilled water, with 0.1 vol.% Darvan® C-N added as a dispersant. The suspension pH was then adjusted to a value of 8.5 using a solution of NaOH. The cermet/alginate suspension was subsequently homogenized on magnetic stir plate for an average of 3 hours at 385 rpm and then vacuum degassed. A dip coating apparatus with a linear driven stage was designed and employed for preplacement of feed material on substrate by dip coating method. Precise control of withdrawal speeds at 0.05 mm/s and angle 90° was obtained via a control board interfaced to an Arduino controller. Subsequently, the D2 tool steel coupons were then immersed and withdrawn from the coating suspension, with the long dimension of the coupon oriented parallel to the direction of withdrawal. After dip-coating, the substrates were dried at 20 ± 3 °C for 24 hours prior to laser cladding. The chemical compositions of the coating feedstock mixtures and D2 steel substrate are provided in Table 16 and Table 17, respectively**.**

Table 16. Chemical compositions of the examined clad formulations.

Clad component	**Compositional wt.%**		
	TiC	**NiAl**	**Ni**
Coating: TiC-30 vol.% Ni_3Al	60.23	5.26	14.53
Coating: TiC-40 vol.% Ni_3Al	51.62	13.91	38.44
Coating: TiC-50 vol.% Ni_3Al	43.02	17.39	48.05

Table 17. Standard chemical composition of the D2 substrates used in the present work.

Substrate	C	Cr	Mo	V	Mn	Si	Fe
AISI D2 tool steel	1.55	12	0.8	0.9	0.35	0.25	Balance

6.2.2. Direct Deposition Cladding

Following dip-coating and drying, the preplaced cermet coatings were laser clad onto D2 substrates using an Optomec MTS 500-CA DED system, equipped with a 1 kW ytterbium-doped fiber laser (IPG Photonics; λ = 1070 nm), integrated with a five-axis CNC vertical machining center to control the velocity of the workpiece. The segmented 3D model of targeted clad dimension was generated via Mastercam Mill 2019 software, coupled with the available DED system. A laser spot size diameter (D) of ~780 μm was achieved at a standoff distance set to 7.9 mm, under an argon atmosphere with an oxygen content < 10 ppm. The effect of test parameters was assessed under initial applied values of laser power (P) of 200, 250, 300, and 350 W. Similarly, the scanning speed (V) varied between 58 and 116 mm/min. for each of the evaluated laser powers. The laser beam moved above the preplaced, suspension-coated substrate at pre-determined interaction times (τ), in seconds, as defined in Equation 18:

Equation 18

$$\tau = \frac{D}{V}$$

where D and V were defined previously [44].

6.2.3. Microstructural Characterization

Following laser processing, the clad samples were sectioned perpendicular to their planar surface, using a precision saw, and were then mounted prior to grinding/polishing down to a 0.25 μm final diamond paste particle size (Figure 84). The general appearance of the clads and three-dimensional measurements of the surface was performed on both the as-printed and mechanically tested specimens using 3D confocal laser scanning microscope (CLSM; VK-X200/X210, Keyence, Mississauga, ON, Canada). Microstructural characterization was conducted using optical microscopy (OM; Olympus BX-51, Olympus Corp., Tokyo, Japan) and field emission scanning electron microscopy (FE-SEM; Model S-4700, Hitachi High Technologies, Tokyo, Japan). Compositional analysis was performed in the FE-SEM using energy dispersive X-ray spectroscopy (EDS; Inca X-maxN, Oxford Instruments, Concord, MA, USA). Moreover, EDS analysis is used to analyze the clad zone in order to observe and report the dilution, instead of using a more conventional method that measures the dilution simply by clad dimensional characteristics [445,446]. FE-SEM imaging, in conjunction with CLSM observations were performed on multiple clad layers for verification of the clad dimensions and their related surface roughness. Additionally, electron backscattered diffraction (EBSD) was utilized in the FE-SEM for a more complete understanding of the represented phases, grain morphology, and crystallographic texture of clad cross sections.

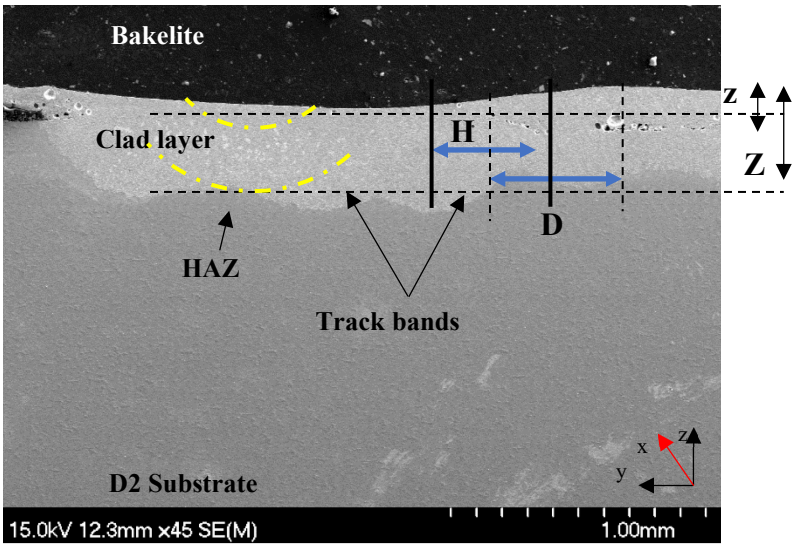

Figure 84. Microstructural representation of the clad dimensions obtained from low magnification SEM imaging on polished clad/substrate cross sections. Note that the x-axis in the lower right-hand corner denotes the direction of the laser scan.

Laser processing parameters are often simplified into a singular energy input for a given build volume. The magnitude of energy output within a specified unit of length value of energy density, *ED*, has been calculated based on volumetric energy density [377], derived from those utilised in laser powder bed fabrication:

Equation 19

$$E = \frac{P}{VH_sZ'}$$

where P is the laser power and V is the laser traverse rate (as before), H is the line hatch spacing of adjacent laser raster tracks, and Z is the layer thickness (z-step size).

6.2.4. Mechanical testing

6.2.4.1. Micro Vickers indentation

Vickers hardness analysis was conducted based on ASTM E2546 and ISO 14577 using an instrumented indentation system (Nanovea® PB1000, Nanovea Inc, Irvine, CA, USA) [107,447]. Indentations were performed by application of a linearly increasing normal load to a fixed final load, prior to unloading to the initial position. The examined operating conditions for the Vickers indentation experiments are listed in Table 18.

Table 18. Micro Vickers indentation parameters applied for the testing of TiC-Ni_3Al based DED clads on D2 tool steel.

Indenter Poisson ratio	0.7		
Indenter elastic modulus (GPa)	1,140		
Sample Poisson ratio	0.238		
Applied force	1 N	3 N	5 N
Loading/unloading rate (µm/s)	15	30	70

Indentation tests were performed on cross sections of the coated specimens, where the coating/substrate interfaces were imbedded perpendicularly in a Bakelite resin disc; both ends of the clad sample were exposed on either side of the Bakelite block, and both faces were subjected to sequential polishing to achieve an average surface roughness of $R_a \leq 10$ nm prior to the indentation procedure. Indentations were then performed in three regions relative to the clad structure; top, intermediate, and near the coating/substrate (zones 1, 2, and 3 respectively), where each is spaced relative to the previous indent at a separation distance determined by multiplying the generated indentation depth by 10 Figure 85.

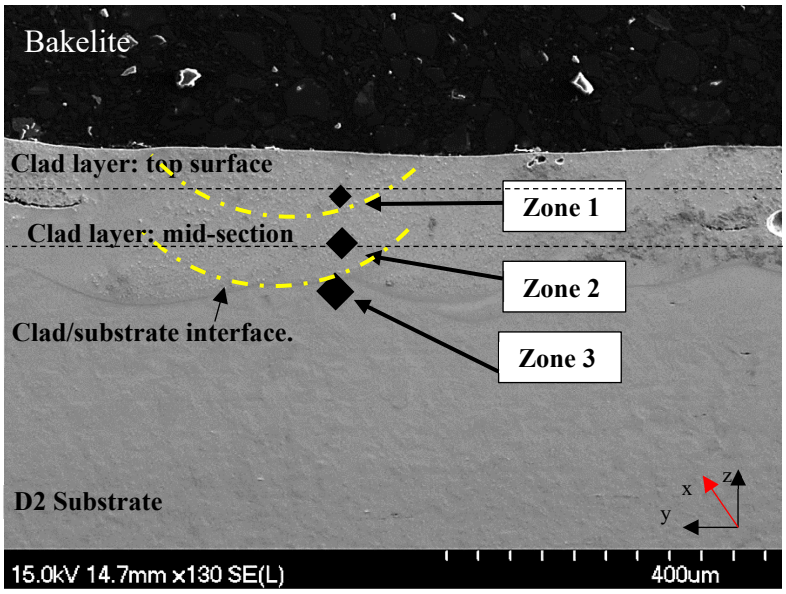

Figure 85. Cross sectional view of the cermet clads highlighting the locations for performed indents in three regions: top (zone 1), intermediate (zone 2), and near the coating/substrate (zone 3). Note that the x axis in the lower right-hand corner denotes the direction of the laser scan.

The indentation hardness (*H*) was subsequently determined from the recorded load-displacement curves, with stiffness recorded continuously during the loading of the indentation. Two specimens were tested from each coating category, with five separate indentations at each load for defined regions: top, intermediate, coating/substrate interface; these are subsequently referred to as zones 1, 2, and 3, respectively. Indentation loads of 1, 3 and 5 N applied normal force were used in each case. Microstructural observations were subsequently performed on the indented surfaces to observe plastic deformation and potential crack formation.

6.2.4.2. Scratch testing

Micro-scratch-hardness tests were performed using a Universal Micro Tribometer (UMT-1; CETR, Campbell, CA, USA), using a diamond stylus with apex angle of 120 ± 5°, and a nominal tip radius of 200 μm. The test was conducted with reference to the standards ASTM G171-03 (*Standard Test Method for Scratch Hardness of Materials Using a Diamond Stylus*) and ASTM C1624 – 05 (*Standard Test Method for Adhesion Strength and Mechanical Failure Modes of Ceramic Coatings by Quantitative Single Point Scratch Testing*) [108,448]. A schematic representation of the experimental setup to assess the scratch properties of the clad coatings is presented in Figure 3. The scratch hardness of a material was determined by producing a 5 mm long scratch on the sample surface under a series of constant loads (5, 10, 20, 30, and 40 N), which were applied in three different directions (x, y, and z) with respect to the laser scanning path for the cermet-based clads. Scratch tracks were generated both vertically and horizontally in relation to the direction of the laser scan, to view and determine possible anisotropic failure mechanisms that can commonly arise during directional and layered processing. Consequently, cross sectional scratches were also utilised, which are generally performed to examine the adhesive characteristics of coating systems [107,109,449]; this procedure was conducted in order to observe the variation of scratch resistance within the respective cross sectional clad zones. A schematic diagram of the generated scratches, with respect to their orientations on the clad specimen, is provided in Figure 86(b). The frictional force (μ) and resultant acoustic emission (AE) signals during each scratch pass were measured continuously during the tests. Each scratch measurement was repeated at 5 locations for each sample, to ensure the reproducibility of the results. A semi-quantitative measure of coating adhesion, the critical

load (L_C), and the generated failure mode(s) were verified by performing a series of microstructural analyses in relation to the obtained scratch data. Subsurface cracking and other possible interlayer events detected by AE were further examined using focused ion beam microscopy (FIB; Model F-2000A, Hitachi High Technologies, Tokyo, Japan), sectioning into the scratch track in order to view the sub-surface cross-sections.

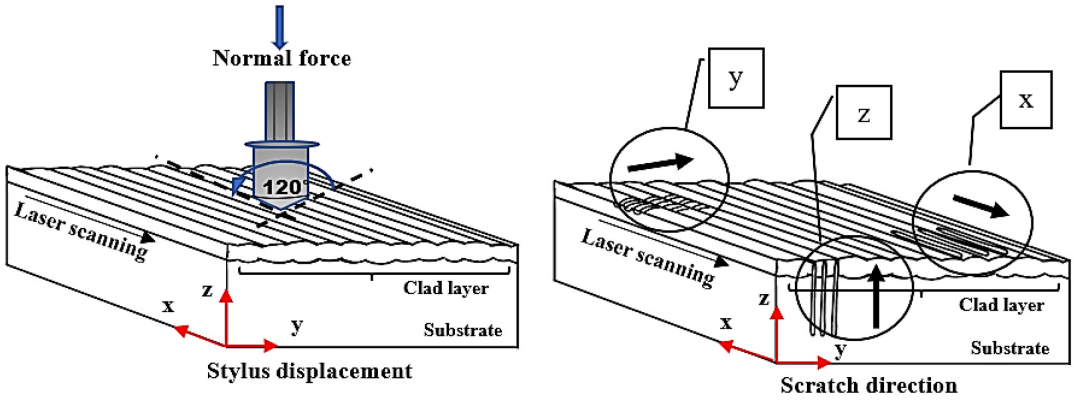

(a) (b)

Figure 86. (a) A schematic representation of the scratch testing procedure, indicating the path of the stylus displacement with respect to the direction of the laser scan during cladding. (b) The relative orientations of the analysed scratch regions, demonstrating the direction of the generated scratches in relation to the direction of the laser scan during cladding: x - parallel, y - perpendicular, and z - normal to the laser scan direction.

Through thickness, stacked CLSM images and associated metrology measurements, along with FE-SEM images, have been used to generate an understanding of the deformation and failure mechanisms of the clad layers in relation to the processing parameters. Examples of confocal images used for profiling the widths of the scratch tracks are provided in Figure

87. In this context, the widths of generated scratch tracks (*W*) were then measured using the CLSM for subsequent calculation of scratch hardness values.

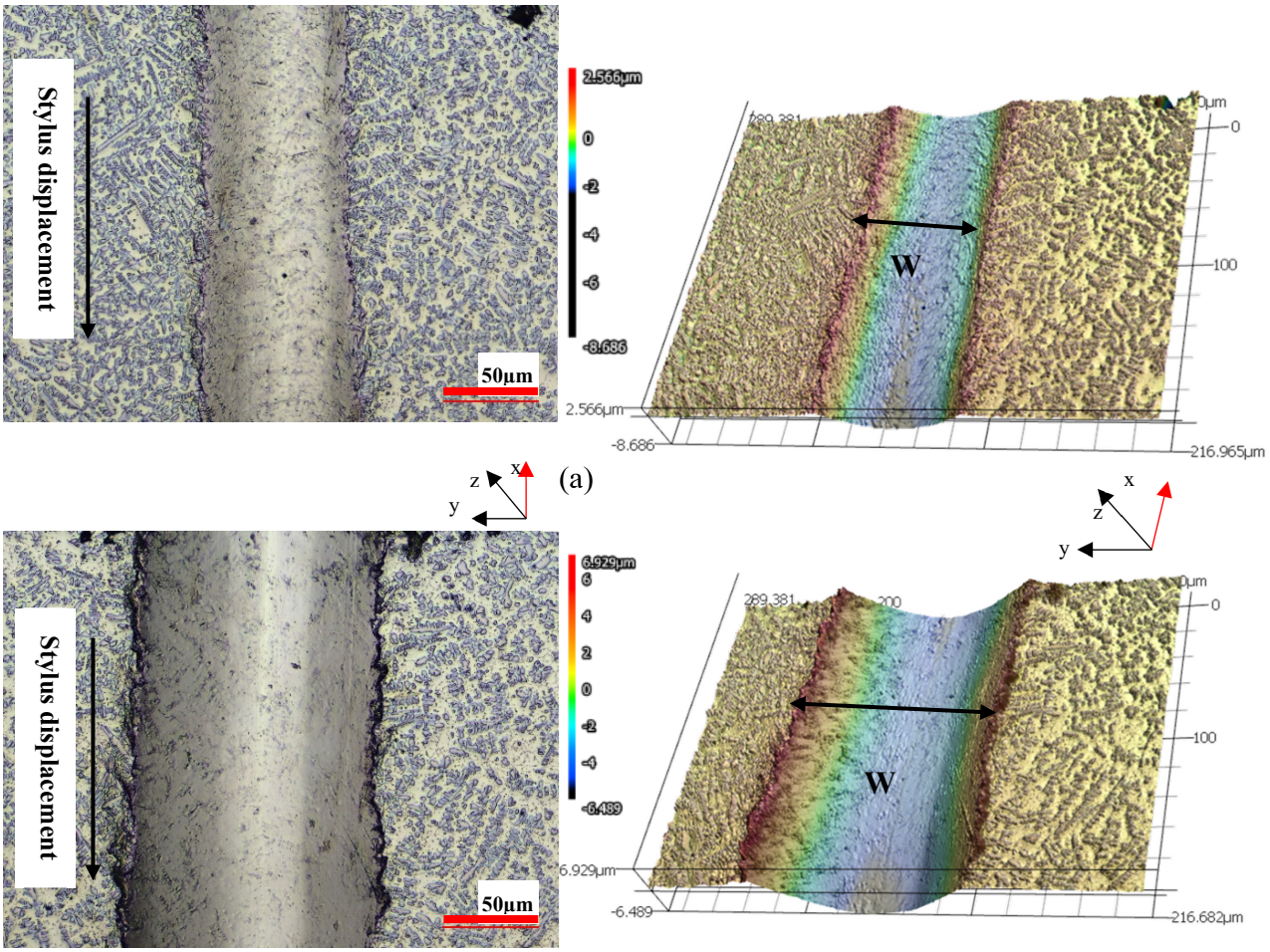

Figure 87. Post-scratch, CLSM generated 3D images for TiC-Ni_3Al (30 vol.%) clads onto D2 steel substrates, (P = 350 W and τ = 0.6 s, ED = 253.14 J/mm^3.) under constant load of: (a) 20 N, and (b) 30 N. Note that the x-axis corresponds to the direction of the laser scan, as shown schematically in Figure 86.

6.3. Results and Discussion

6.3.1. Directed energy deposition laser cladding

A combination of CLSM and FE-SEM was utilised for the assessment of the surfaces and cross sections of the fabricated clads. The laser processing parameters explored for determining optimum laser cladding conditions are presented in relation to the resultant *ED* and surface roughness of the composite clads in Figure 88. Calculated values for *ED* obviously increased when the laser and reaction time increased where, in contrast, lower surface roughness was observed. Similar results have been reported by previous authors working on laser cladding [450,451]. AM components are often represented by the quality of their printed surfaces. Nevertheless, it is well known that laser cladding typically generates high surface roughness and often requires post-processing steps. It is worth mentioning that only sound clad coatings, with the potential for being utilised without any post-processing steps, were included in the measurement of surface roughness values in the present work. Examples of surface morphologies related to various *ED* values are shown in Figure 88 (c, d, e, and f). Macro-characterization of the as-processed samples, by means of CLSM measurements, revealed that successful clad layers were built with the narrow range of 300 to 350 W laser power and 0.84 to 6.77 mm/s laser scanning speed. The surface roughness of the fabricated clads was strongly dependent on the calculated *ED*, where visibly smother surfaces were observed at higher *ED* values (i.e., >150 J mm^{-3}), reaching the lowest roughness (R_a = 3 - 3.5 μm). At lower calculated *ED* values, the resultant clads exhibit an irregular surface, with uneven scan lines and cavities between tracks, as shown in Figure 88 (c).

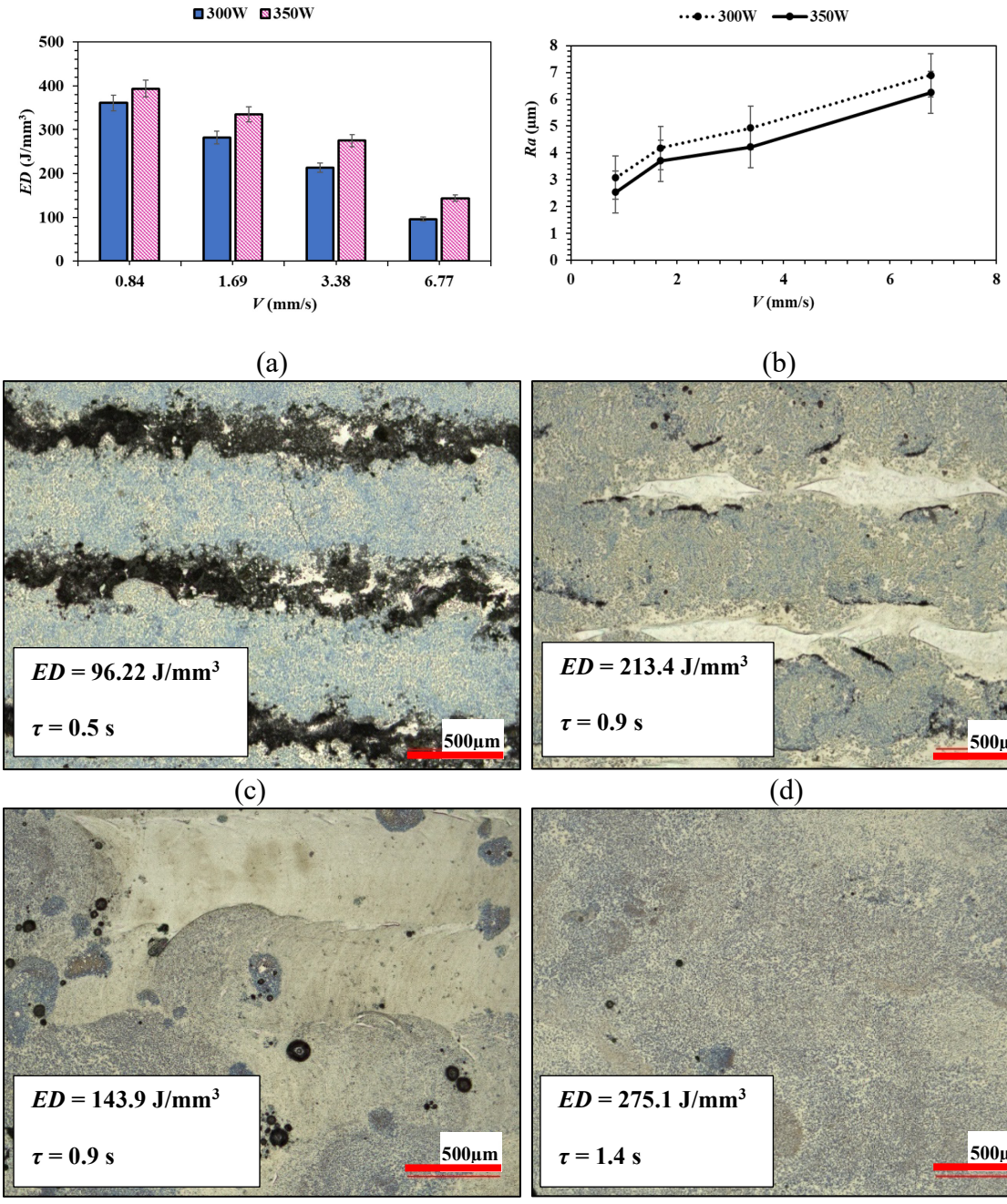

Figure 88. Laser processing parameters explored for determining optimum laser cladding conditions in relation to: (a) the average calculated ED (J/mm^3), and (b) the measured surface roughness, R_a (in μm). Low magnification imaging on examples of resulted surfaces representing clads fabricated at (c) P = 300 W, τ = 0.5 s, (d) P = 300 W, τ = 0.9 s, (e) P = 350 W, τ = 0.9 s, and (f) P = 350 W, τ = 1.4 s.

Figure 89 presents low magnification CLSM micrographs of the transverse cross sections of fabricated clads processed at various laser powers and scanning speeds, resulting in different levels of *ED*. From these (and similar) optical images, it is possible to see that the laser power and scan speed both play a crucial role in clad formation, and clad quality/microstructure. At V = 6.77 mm/s and P = 300 W laser power, with resulting τ = 0.5 s (shown in Figure 89 (a)), a large volume of un-melted particles was observed. However, at a lower scanning speed, V = 3.38 mm/s, presented in Figure 6(b), τ was effectively increased to 0.9 s resulting in the formation of fully remelted and solidified microstructures that contain a minimal number of pores and defects. As shown in Figure 89 (c), increasing the laser power to 350 W, for the same scanning speed, affects the kinetics of melt pool generation in a positive manner, with the formation of homogeneously nucleated hard particles. Subsequently, as shown in Figure 89 (d), at longer beam interaction time (i.e., τ = 1.6 s), formation of dendritic structure is observed.

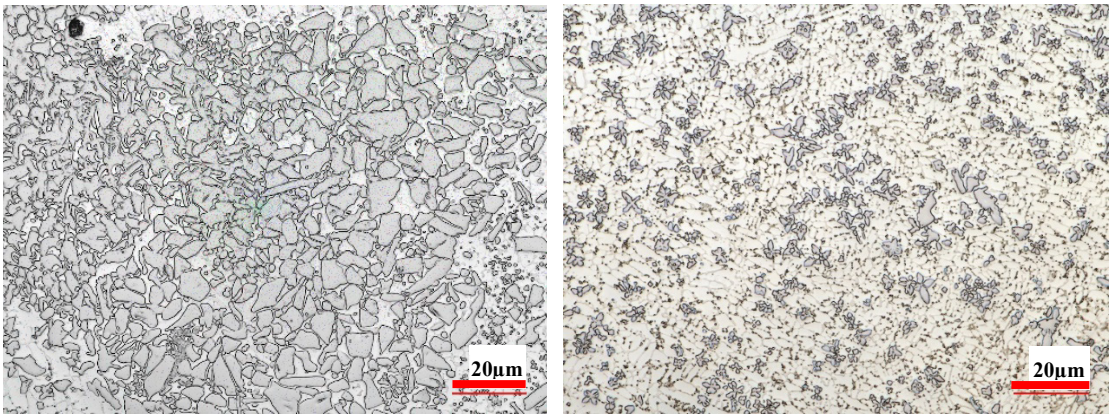

(a) (b)

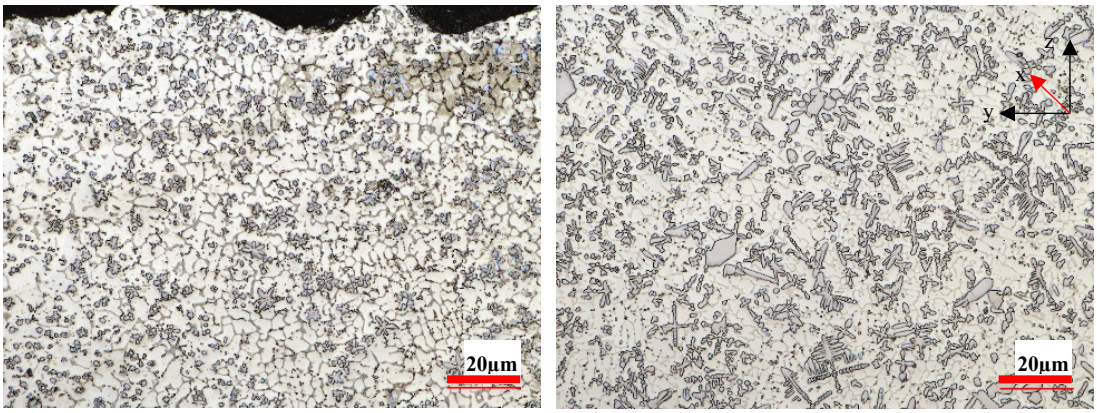

(c) (d)

Figure 89. Examples of low magnification CLSM micrographs obtained from transverse cross section of fabricated clads processed at: (a) P = 300 W, V = 6.77 mm/s, (b) P = 300 W, V = 3.38 mm/s, (c) P = 350 W, V = 6.77 mm/s, and (d) P = 350 W, V = 3.38 mm/s.

6.3.2. Microstructural and phase analysis

Figure 90 presents SEM micrographs obtained from the polished cross section of a laser deposited layer (P = 350 W and τ = 1.4 s), highlighting the main clad zones (top, middle, clad/substrate interface, and the underlying heat affected zone), in respect to the substrate and the central axis of the beam diameter. These cross-sectional SEM micrographs reveal the formation of a high-density clad layer on the surface of the substrate that is well bonded and contains no microcracks. The general microstructure throughout the clad layer exhibits a mix of columnar and equiaxed structure, which can be anticipated to form at different cooling rates. The carbide network consists of M_2C/M_6C and MC carbides in the forms of both columnar and near-equiaxed grain structures, which also change in size and morphology as the distance from the substrate decreases. At the bottom region of the

coating, continuation of the substrate lattice structure presents a heat-affected zone region (HAZ) that can grow into the coating. This type of microalloying can provide a complete metallurgical bond between the coating and substrate. From observations of the morphology generated for P = 350 W and τ = 1.4 s, the levels of residual porosity were reduced essentially down to zero.

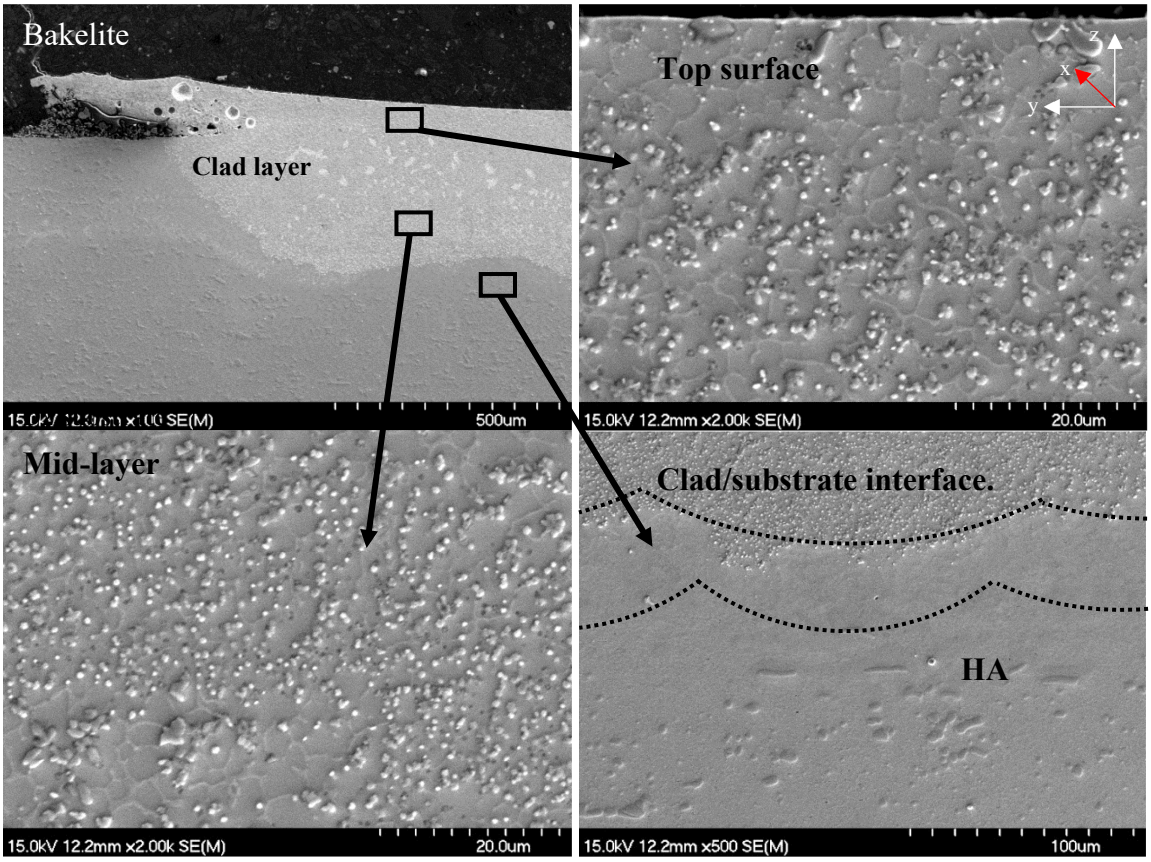

Figure 90. SEM micrographs illustrating the variation of morphology with the TiC-Ni_3Al clad on D2 steel, laser processed at P = 350 W and τ = 1.4 s. Note that the x-axis denotes the direction of the laser scan.

Microstructural evaluation of the clads fabricated at various laser scanning speeds revealed that any size refinement of the hard carbide phase is closely correlated with the laser scan

speed. This is attributed to reduced irradiation time and the resultant energy absorbed into the melt pool. Therefore, an increased solidification rate results in the formation of a finer microstructure and minimal dendritic growth of TiC particles. Similar results have been observed by other research groups, suggesting faster cooling rates due to higher extraction of energy by the substrate and therefore formation of a finer microstructure, results from use of increased laser scanning speed [452–454]. The average distribution of the solidified phases and their chemical compositions within the TiC-Ni_3Al clad on D2 steel (P = 350 W and τ = 1.4 s), with respect to depth from surface was verified through combined EBSD and EDS analysis; this information is provided in Figure 91. As demonstrated in Figure 91 (a), discrete chemical phases are contained through the depth of the clad layer. This figure shows that NiAl is homogeneously distributed in the form of equiaxial grains. The top portion of the clad demonstrates the presence of the preplaced feed stock constituents of TiC, Ni and Al, in addition to a moderate Fe content (~70 wt.%). With the exception of Mo, which was only detected at the clad/substrate interface, high concentrations of the main D2 alloying elements, namely V and Cr (~5.8 and ~5.5 wt.%, respectively) were also detected near the surface of the clad layer. The middle portion of the clad cross-section was found to maintain the approximate elemental composition of the top of the clad, with a homogeneous dispersion of the hard phases. Compositional analyses on the clad/substrate interface, slightly above the HAZ, demonstrated the presence of a higher Fe content (~83 wt.%), while the concentrations of Ti, C, Ni, Al, and V were simultaneously reduced. The average content of C through the depth of clad layer was relatively constant, which with the recorded decrease for the Ti content, resulted in an increase in C:Ti ratio as the clad depth increases.

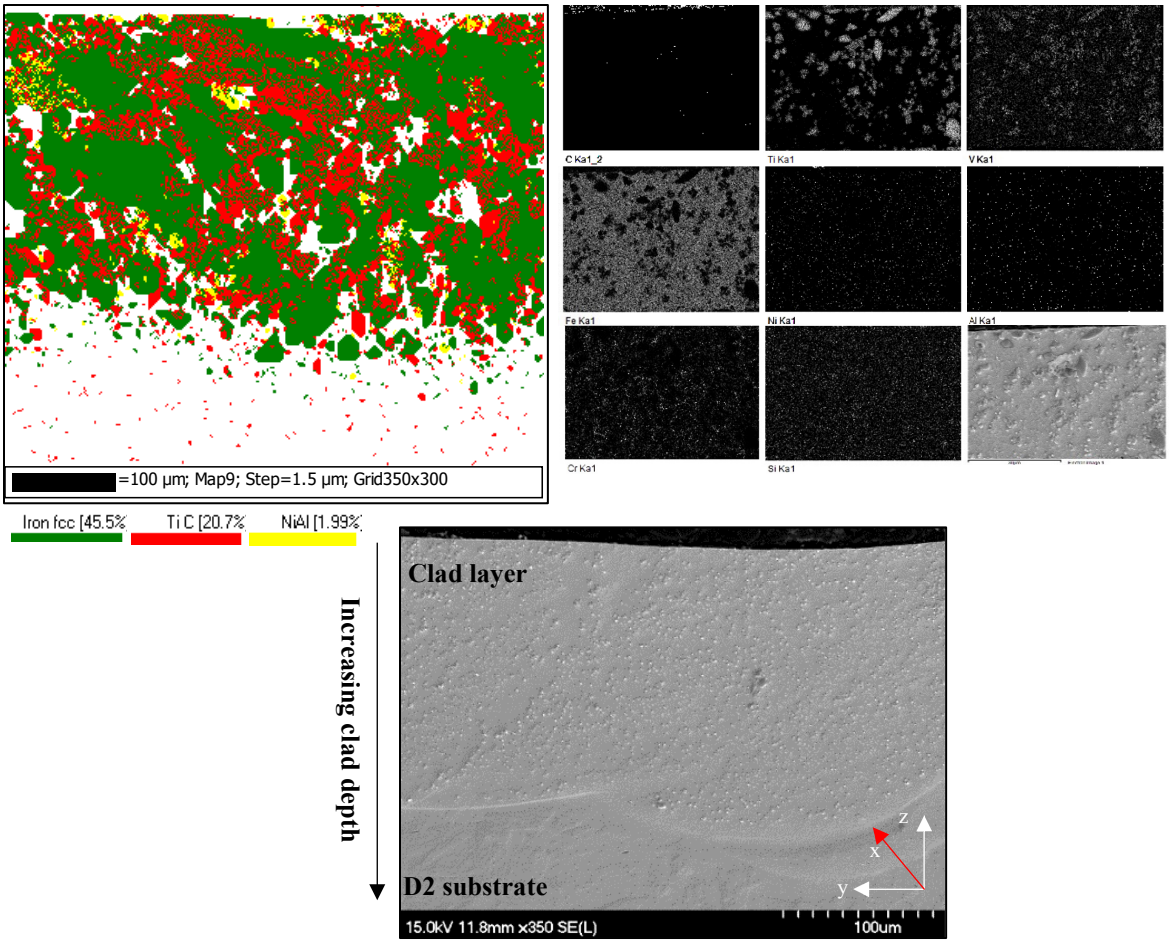

(a)

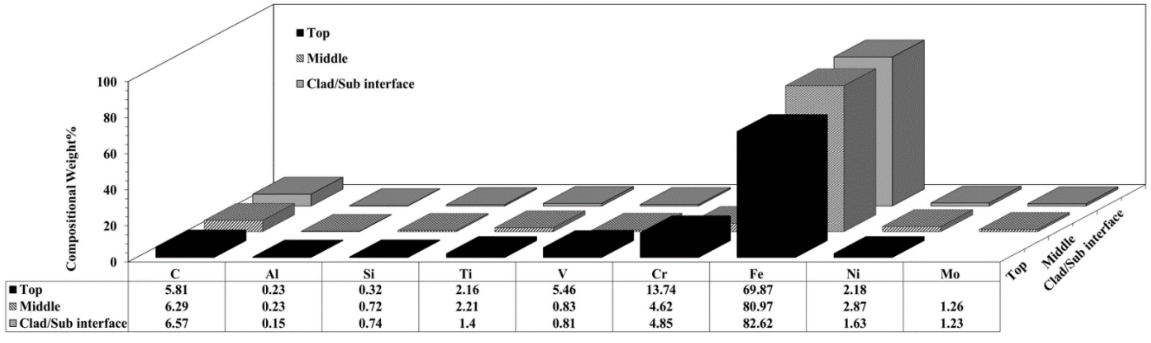

	C	Al	Si	Ti	V	Cr	Fe	Ni	Mo
Top	5.81	0.23	0.32	2.16	5.46	13.74	69.87	2.18	
Middle	6.29	0.23	0.72	2.21	0.83	4.62	80.97	2.87	1.26
Clad/Sub interface	6.57	0.15	0.74	1.4	0.81	4.85	82.62	1.63	1.23

(b)

Figure 91. Elemental distribution of TiC-Ni_3Al (30 vol.%) clad on D2 steel (P = 350 W, τ = 1.4 s), demonstrating: (a) EBSD analysis (left) and EDS mapping (right), and (b) variation of the chemical composition through the depth of the clad layer.

The phases present through the depth of the clad structure were verified by high magnification SEM and compositional EDS analysis (Figure 92). The cross-sectional morphology and compositional variation indicated that within each clad zone, there are three distinct phases: metallic matrix (region A), primary carbides (B), and secondary hard phases (C), as shown in Figure 92 (a). The metallic matrix (A) is formed during the fast solidification of Fe solid solution, supersaturated with up to 0.85 wt.% Ti, 0.18 wt.% Al, and 1.82 wt.% Ni, in addition to Cr and V (3.79 and 7.23 wt.%, respectively). In the mid-clad zone, the elemental concentration of the metallic matrix exhibited an increase in Fe, Cr, Ni, and Al, while the concentrations of Ti and V were reduced. At the clad/substrate interface, the elemental composition of the metallic matrix was characterized with further reduction of the initial TiC-Ni_3Al cermet components while the concentration of Fe and its alloying elements was increased further toward the composition of the as-received D2 substrate. The primary carbide phase, which is denoted as (B) in Figure 92(a), was composed of 60.5 wt.% Fe, V, Ti, Cr, Si, Al, and Mo near the top surface of clad cross section. At the mid-section of the clad layer, no Mo or Al were detected in the structure of primary carbides, while reduction of the Ti, C, Ni, V, and Si concentrations coincided with a significant increase in Cr content. No traces of the original cermet composition (i.e., Ti, C, Ni, or Al) was detected within the composition of the primary carbide phase at the clad/substrate interface and (B) was mainly composed of Fe, C, Mo, V, Si, and Cr with lower concentration, in comparison to those recorded for middle of the clad layer. The microstructure of secondary carbides occurring at various clad depths (i.e., top, middle, clad/substrate interface) are denoted with (C) in Figure 92 (a).

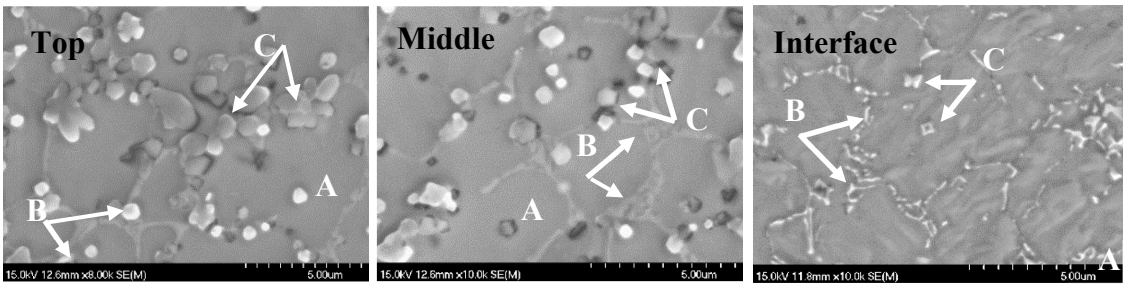

(a)

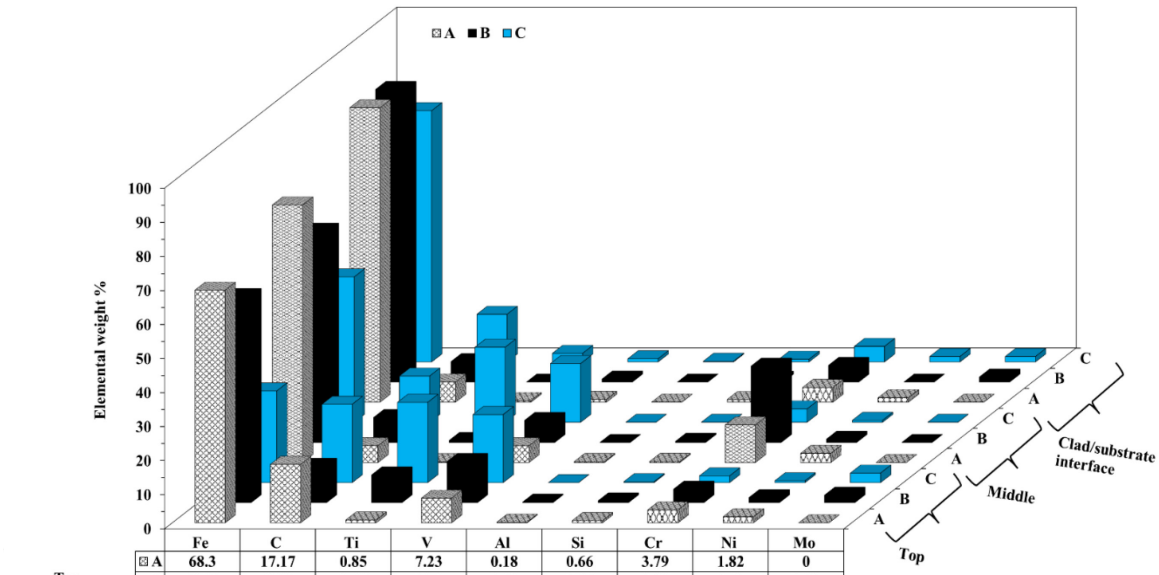

		Fe	C	Ti	V	Al	Si	Cr	Ni	Mo
Top	A	68.3	17.17	0.85	7.23	0.18	0.66	3.79	1.82	0
	B	60.53	10.73	8.17	12.1	0.18	0.56	3.98	1.53	2.22
	C	26.92	23	23.56	19.98	0	0.29	1.98	0.55	2.81
Middle	A	75.59	4.94	0.24	4.92	0.27	0.3	11.04	2.7	0
	B	62.03	7.31	0.56	6.46	0	0.31	22.37	0.96	0
	C	42.67	13.58	22.02	17.23	0	0	3.92	0.58	0
Clad/substrate interface	A	86.44	5.89	0.47	0.82	0	0.77	4.32	1.3	0
	B	85.89	6.01	0	0.88	0	0.83	4.9	0	1.49
	C	73.75	14	2.53	0.94	0.21	0.79	4.57	1.61	1.61

(b)

Figure 92. Representative FE-SEM micrographs obtained from polished cross sections of the TiC-30 vol.% Ni_3Al coating laser clad onto D2 steel (with an applied laser power of 350 W, at τ = 1.4 s). (a) The phases identified in the clad layer, namely the metallic matrix (A), primary carbides (B), and secondary carbides (C) arising at the top and middle of the clad, and the clad/substrate interface. (b) The results of the corresponding EDS analyses of the phases outlined in (a).

6.3.3. Microhardness Evaluation

Figure 93 presents examples of the Vickers indentations obtained within Zone 1 (top of the of clad), Zone 2 (mid-section of the clad), and Zone 3 (near the substrate/clad interface), under an applied load of 5 N. Laser scans were used to generate an accurate profile of the indents, to help assess the type of deformation within the indent at various depths under the applied loads. The indented depth, at constant load, exhibited an increase when moving from the surface of the coating towards the substrate, highlighting reduced hardness.

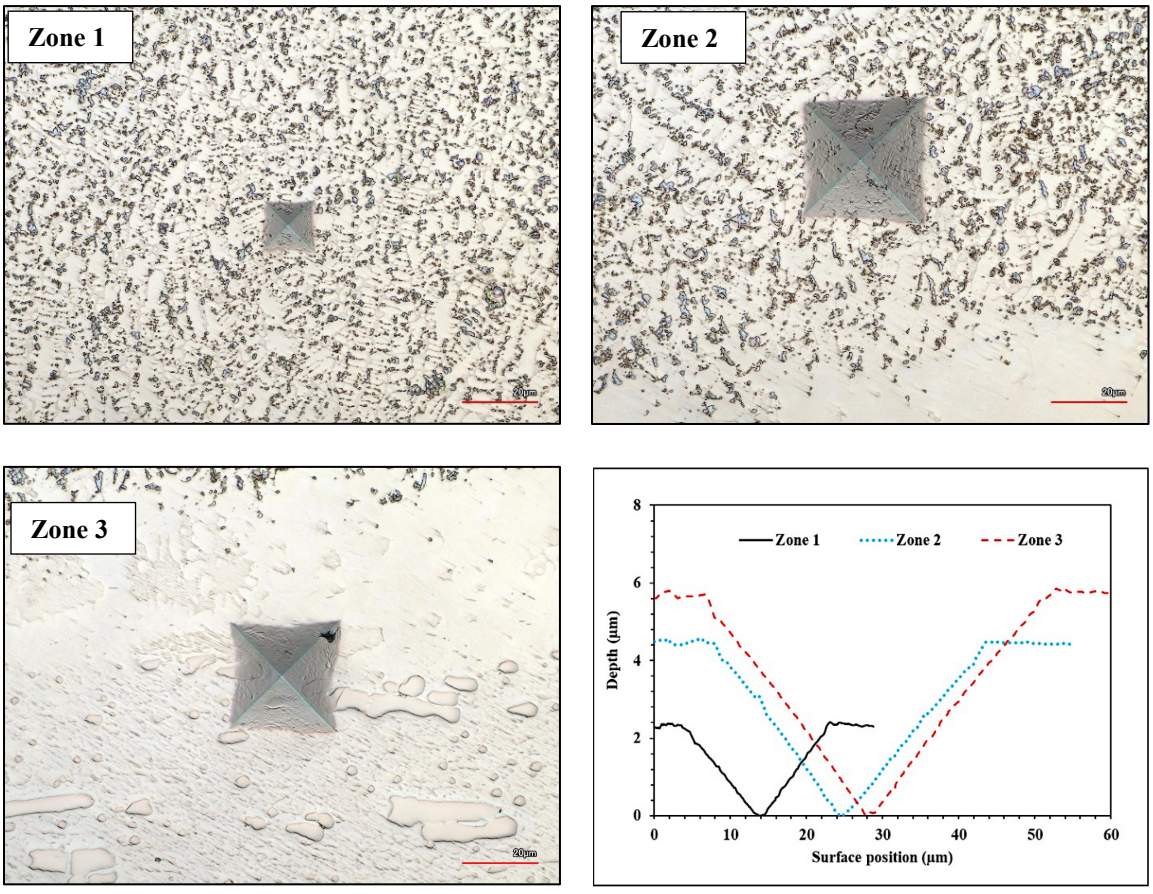

Figure 93. CLSM images and associated 2D cross-sectional profiles for the indents obtained using an applied load of 5 N within zones 1, 2, and 3.

Figure 94 presents SEM micrographs obtained from indentations imprints on cross sections of the clad coatings on D2 steel, in relation to its location to the surface of the clad notably for: Zone 1, which is referred as the top portion, and Zone 2, which is located at the mid-section of clad layer. The images also highlight the corners of the indentation at higher magnifications. According to the microscopy results, the indents exhibit clear boundaries with sharp edges and no extended damage outside of the indentation area. However, a few isolated microcracks, which appear to show a clear crystallographic directionality with the cubic carbide (white arrows), were observed at higher magnifications within the hard phase of the composite clads.

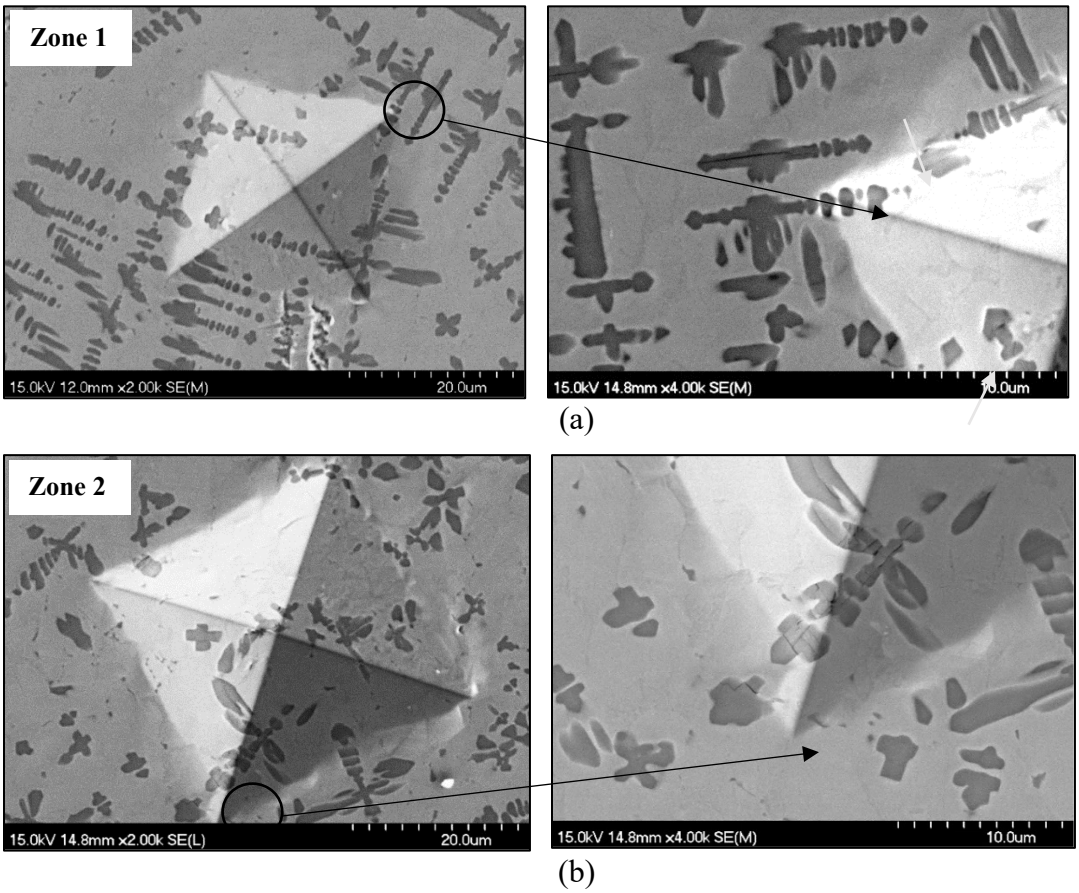

Figure 94. SEM images of Vickers indents obtained under 5 N applied normal force: (a) at top of the clad coating, and (b) at the coating/substrate interface.

Figure 95 presents the results of micro-Vickers indentation measurements on the cross sections of the TiC-Ni_3Al clads on D2 hard tool steel as a function of depth into the clad layer. The average *HV* values have been plotted in relation to the measurement location from the clad surface under the range of applied loads examined. Regardless of the value of applied normal load, the highest hardness values were recorded at the top surface of the examined cross section. In the middle section of the clad, a slight decrease in hardness values was observed. At the clad substrate interface, a value of 658.7 HV is recorded for the applied load of 5 N.

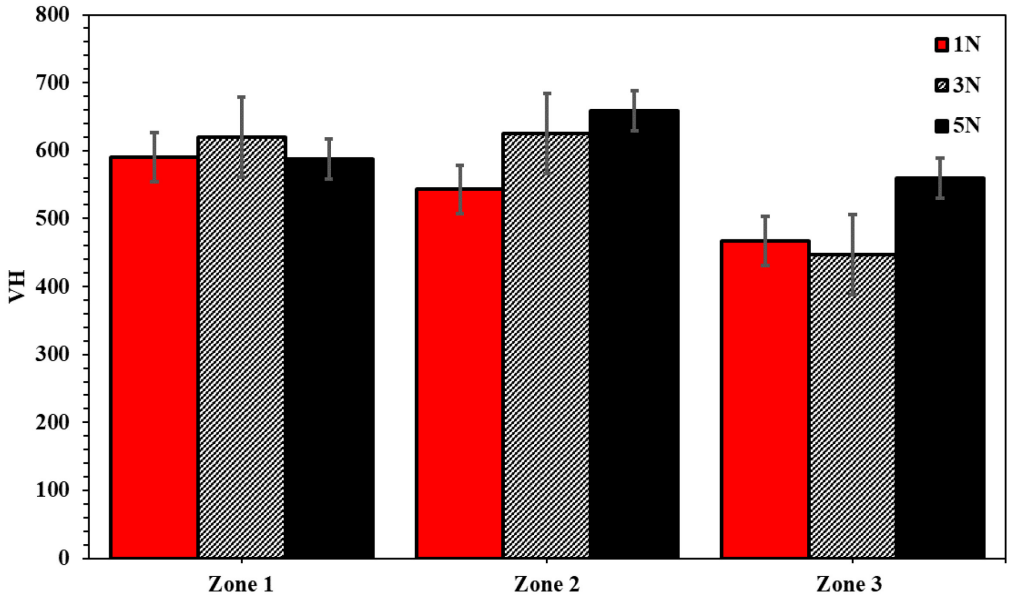

Figure 95. Instrumented micro-Vickers indentation results obtained from cross-sections of the TiC based clads on D2 demonstrating the calculated VH values under 1 N, 3 N, and 5 N applied force.

6.3.3. Scratch Testing

The resistance of a coated surface to penetration by a moving stylus, under a constant applied normal force, can be utilised as a preliminary evaluation of a material's wear resistance. Measuring the scratch width, one can define the sample scratch hardness [108], as follows:

Equation 20

$$H_{Sp} = \frac{k * F_z}{W^2}$$

where k is a geometrical constant, F_z is the normal force on the stylus in grams, and W is the scratch width (in μm); this equation then provides the scratch hardness number (in GPa). The scratch hardness values of the TiC-Ni_3Al based clads were determined by producing a 5 mm long scratch on the sample surface under constant applied loads of 5 N, 10 N, 20 N, 30 N, and 40 N, in orientations both parallel and perpendicular to the direction of the laser scan. The width of the scratches was then determined by profiling with the CLSM for scratches generated in both directions on the clad D2 substrates (Figure 96). The average width and depth of the scratch profiles did not demonstrate any significant variation when they were compared in relation to the direction of the laser scan. This is attributed to a homogeneously solidified microstructure for the fabricated clads and an absence of gross microstructural segregation between the overlapping layers.

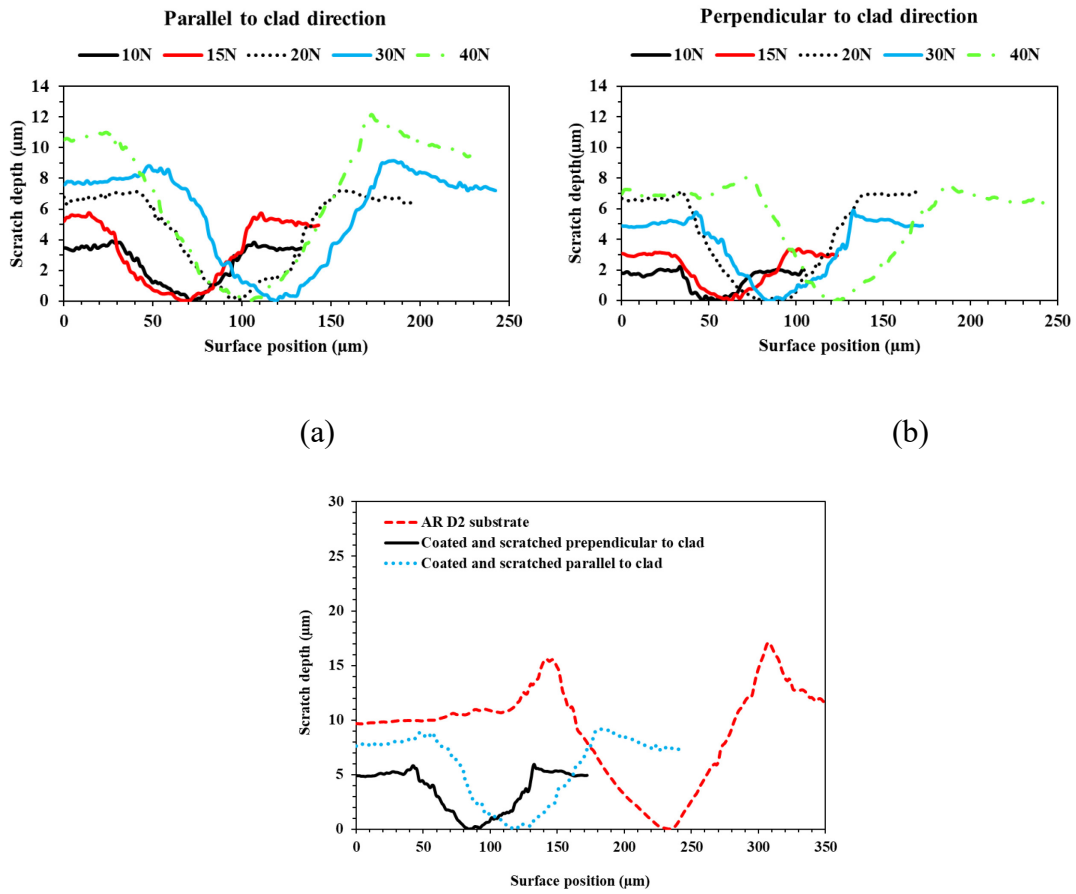

Figure 96. Scratch profiles obtained via CLSM from the post scratch surfaces of the TiC-Ni_3Al clad D2 substrate with scratch orientations: (a) in the direction of the laser scan, and (b) perpendicular to the direction of the laser scan. (c) Comparison of both scratch directions to the scratch profile obtained for the as-received D2 substrate under the applied load of 40N. Note that the x-axis is offset for clarity.

Figure 97 demonstrates the mean values of scratch hardness and COF obtained following scratch testing of TiC-Ni_3Al (30 vol.%) clads on D2 tool steel substrates, as a function of the applied normal force. Both the mean coefficient of friction (COF) and H_{Sp} exhibit a

small increase in magnitude when increasing the applied load, reaching the highest value of H_{Sp} = 7.58 ± 0.59 GPa, with an associated COF of 0.23 ± 0.04, when testing at 40 N applied normal load. Scratch hardness represents the amount of work required to create a scratch on a specimen and, in principle, eventually fracture the coating (adhesively or cohesively) for thin coatings. Therefore, a coating with greater scratch hardness exhibits better adhesion and thus it can be expected to show enhanced tribological performance. COF represents the interfacial friction at the indenter-surface contact, which generates elastic and plastic strain with progression of the indenter tip along the scratch track. The highest COF was recorded for the as-received (i.e., uncoated) D2 substrate, regardless of the applied load, while the friction response improves drastically after applying the clad layer. As is demonstrated in Figure 97, at higher applied loads, an increased scratch hardness is observed, in contrast with slight increase in COF which can be related to increase contact area at higher loads.

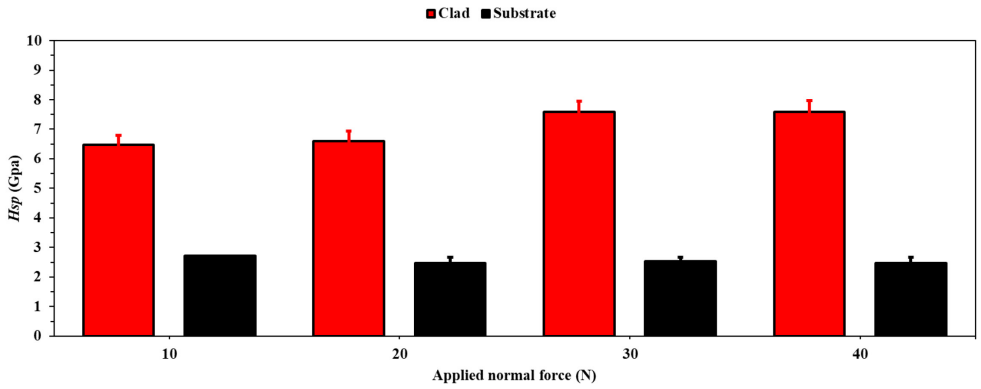

(a)

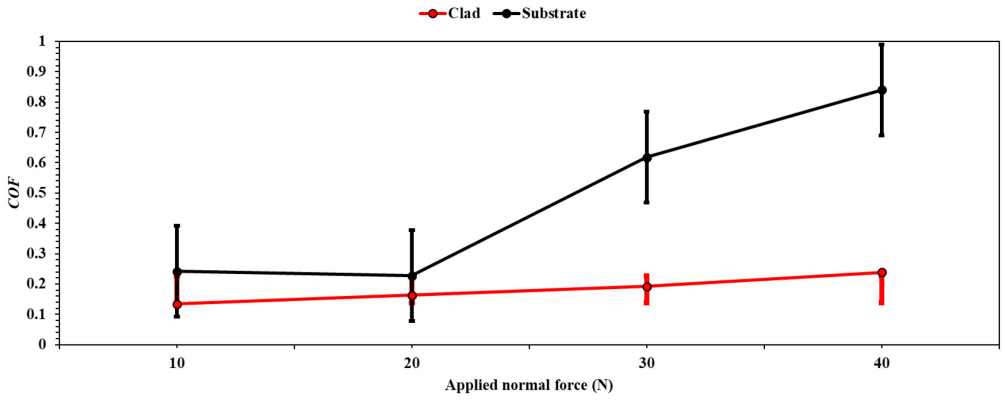

(b)

Figure 97. (a) Calculated scratch hardness (H_{Sp}) and (b) COF values obtained from scratch testing of TiC-Ni_3Al (30 vol.%) clad onto D2 tool steel (scratch orientation is parallel to the direction of the laser scan).

Figure 98 illustrates example micrographs related to scratch damage arising on the surfaces for a coating processed at P = 350 W and τ = 0.6 s, under constant applied loads of 10 N, 20 N, 30 N, and 40 N. The plastic deformation of traditional polycrystalline metals through the movement of lattice dislocations within individual grains is well known [455–457]. The progression of scratch damage on the clad D2 substrate, under an applied load of 10 N (Figure 98 (a)), shows that slight plastic deformation of the surface was accompanied by the formation of Hertz-type tensile cracks at the edges of the scratch track. By increasing the applied normal force to 20 N (Figure 98 (b)), the appearance of conformal cracks within the structure of the hard carbide phases was observed, in accordance with the initiation of buckling cracks at the edges of the scratch track. Under an applied load of 30 N, buckling cracks were again observed at the edges of the scratch track, which was combined with cohesive spallation of the clad coating at 40 N.

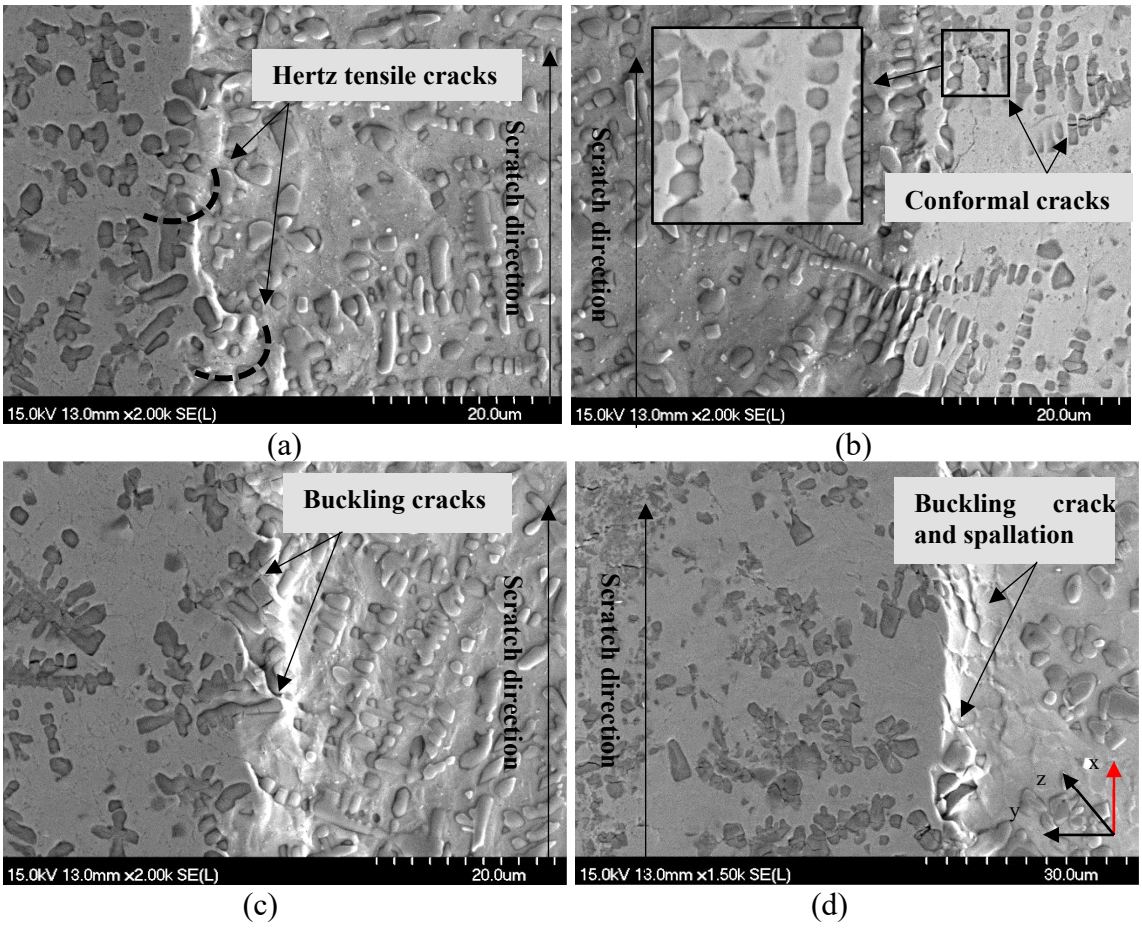

Figure 98. Post scratch micrographs from TiC-Ni_3Al (30 vol.%) clad onto D2 steel under conditions of P = 350 W and τ = 0.6 s (i.e., ED = 253.14 J/mm^2), under applied normal loads of: (a) 10 N, (b) 20 N, (c) 30 N, and (d) 40 N. Note that the scratch area is on the right-hand side in each image.

Figure 99 represents the values obtained for H_{Sp} and COF from scratch testing of TiC based composite coatings as a function of applied *ED* values. As might be anticipated, improved surface properties and reduced surface roughness was observed in contrast to overall reduction of COF for specimens fabricated under *ED* values up to 379.5 J/mm^3. When the *ED* values exceeded these values, an increase in the resultant surface roughness also resulted in increasing COF which was more noticeable at higher applied loads.

Subsequently, computed values for H_{Sp} exhibited a general increase in relation to the increasing values of *ED* which again began to decrease once *ED* values reached 379.5 J/mm^3.

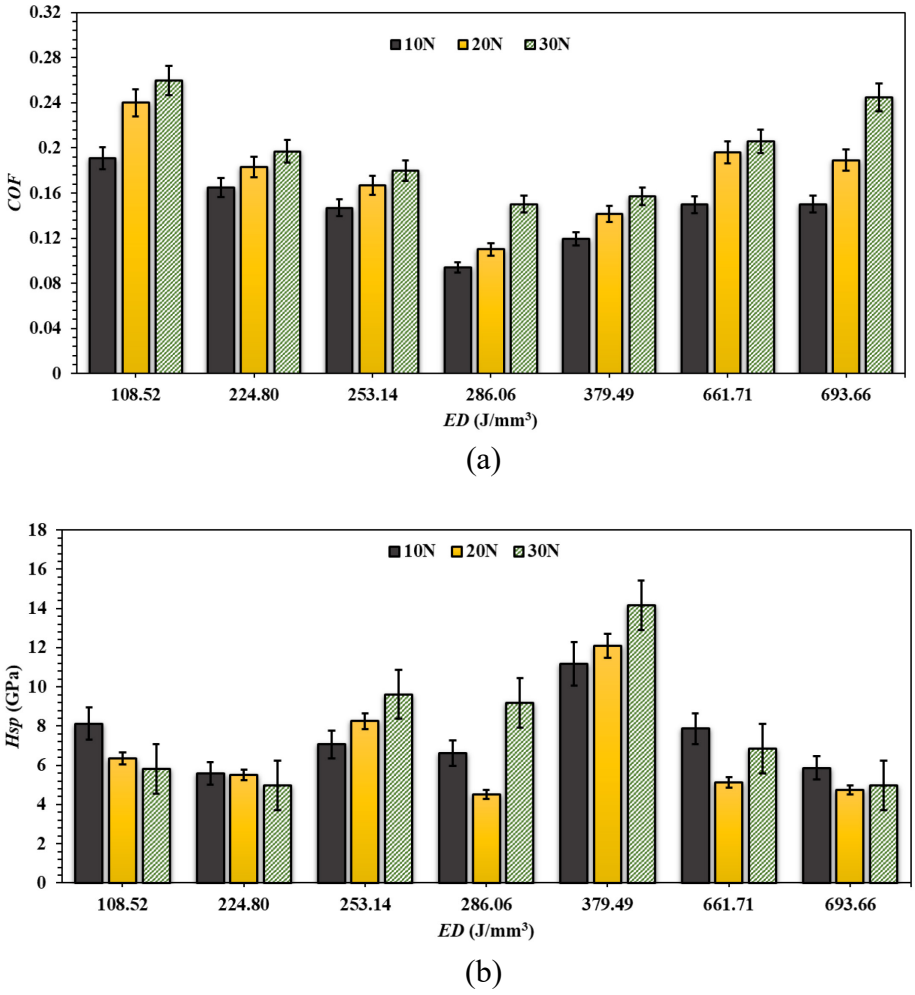

Figure 99. Results of abrasive scratch testing under applied constant normal loads on TiC-Ni_3Al composite clad coatings as a function of applied ED: (a) Coefficient of friction, and (b) scratch hardness.

Information gained through acoustic emission (AE) measurements, was also used to locate surface and sub-surface cracking, as well as possible crack propagation, that was associated with scratch testing damage. Scratches parallel to the direction of laser scan showed relatively few AE events. In contrast, a substantial increase in the fluctuations of AE was detected where scratches were generated perpendicular to the direction of the laser scan. This correlates with crack formation perpendicular to the scratch direction. Collected AE data, as a function of its detected location on the scratch track, is presented in Figure 100; these scratches were generated under an applied force of 40 N, with the scratches both parallel and perpendicular to the laser scan direction. During microstructural analysis of the corresponding scratch tracks, it was found that the periodic repetition of the AE events corresponds to the location of the existing track-bands perpendicular to the direction of moving indenter tip. Preliminary microscopical analysis of potential subsurface damage was subsequently achieved by performing FIB sectioning at the edges of scratch tracks, with approximate locations verified by the occurrence of the AE measurements in relation to the overall location within the scratch track length.

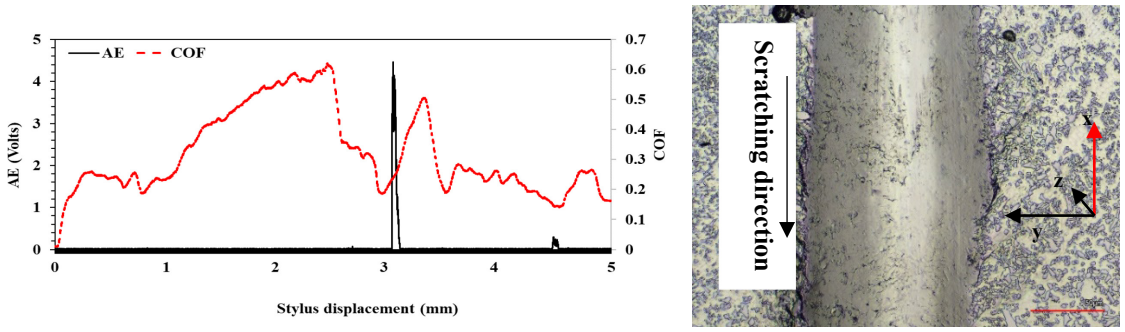

(a)

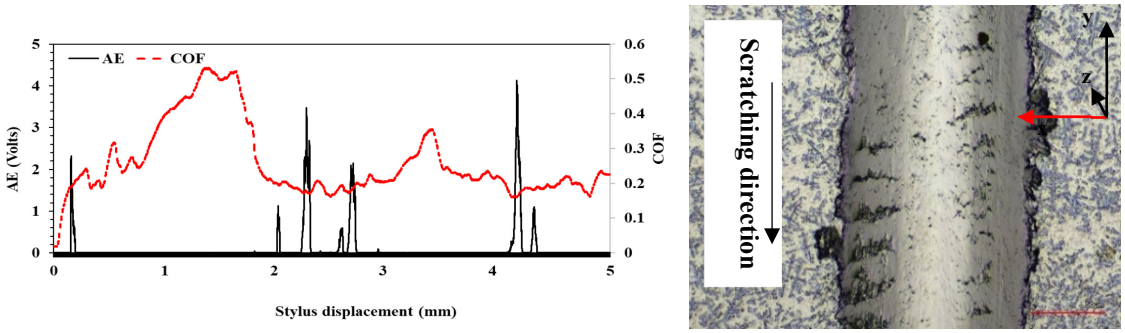

(b)

Figure 100. Plots of the AE events occurring for scratch hardness tests obtained under applied force of 40 N: (a) parallel to the direction of the laser scan, and (b) normal to the direction of the laser scan.

Figure 101 illustrates examples of SEM images obtained from post-FIB sectioning of scratch tracks generated under a 40 N applied load at various magnifications. The microstructures of the sub-surface revealed that cracking happened within the interface of the hard and soft phases in the composite structure.

It was repeatedly observed in post-FIB micrographs that buckling and spallation occurred at higher loads, especially in cases where the scratch orientation was perpendicular to the direction of the laser pass. This results in extension of damage to the sub-surface region of the composite clads and results in separation of the metallic phase from the hard ceramic particles.

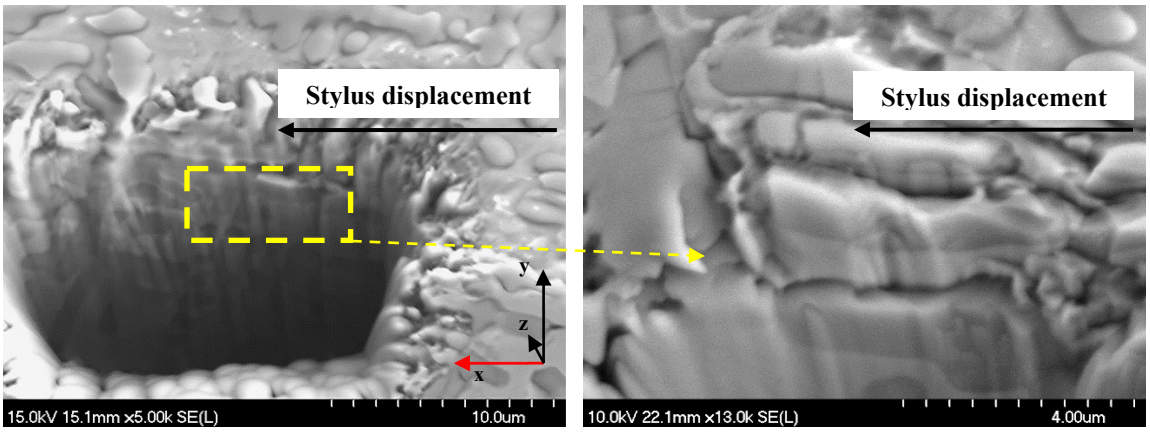

(a) (b)

Figure 101. SEM micrographs obtained by performing FIB sectioning at (a) the edges of scratch tracks generated perpendicular to the direction of laser scan and (b) higher magnification imaging of the edges of scratch tracks, highlighting the location of subsurface cracking shown in (a).

Several scratch damage techniques have been reported within the literature for evaluation of the adhesion/cohesion bond strength in thick coatings, such as scratching the top surface under constantly increasing applied load [108,458,459]. However, as with the case reported for thermal spray coatings, due to the high thickness and surface roughness, this technique was found inadequate [449], and therefore was not applied in the present work. Cross sectional scratch analysis was proposed for assessing plasma spray coatings, which was examined by sliding stylus the from the substrate towards the coating surface under a constant applied load [107]. Consequently, in the present work, an approach utilising this cross-sectional scratch analysis technique was conducted. This was performed in association with subsequent microstructural and topographical investigations of the cross-sectional scratches generated under constant applied loads from 10 N to 40 N. Figure 102

presents an example of such a cross-sectional scratch analysis for the TiC-Ni_3Al clad D2 tool steel, highlighting the change in scratch depth, which was constructed by stitching a sequence of CLSM images. Track cross-section measurements revealed a significant decrease in both the width and depth of the scratch tracks as the stylus was moved from the substrate towards the surface of clad. Moreover, increasing the applied normal force was observed to increase the projected scratch depth and the width within the substrate region. However, within the clad area, the depth of scratch track remained essentially unchanged up to 30 N applied normal force. Cohesive fracture of the coating at the end of scratch track was only observed for tests performed under a 40 N applied normal force.

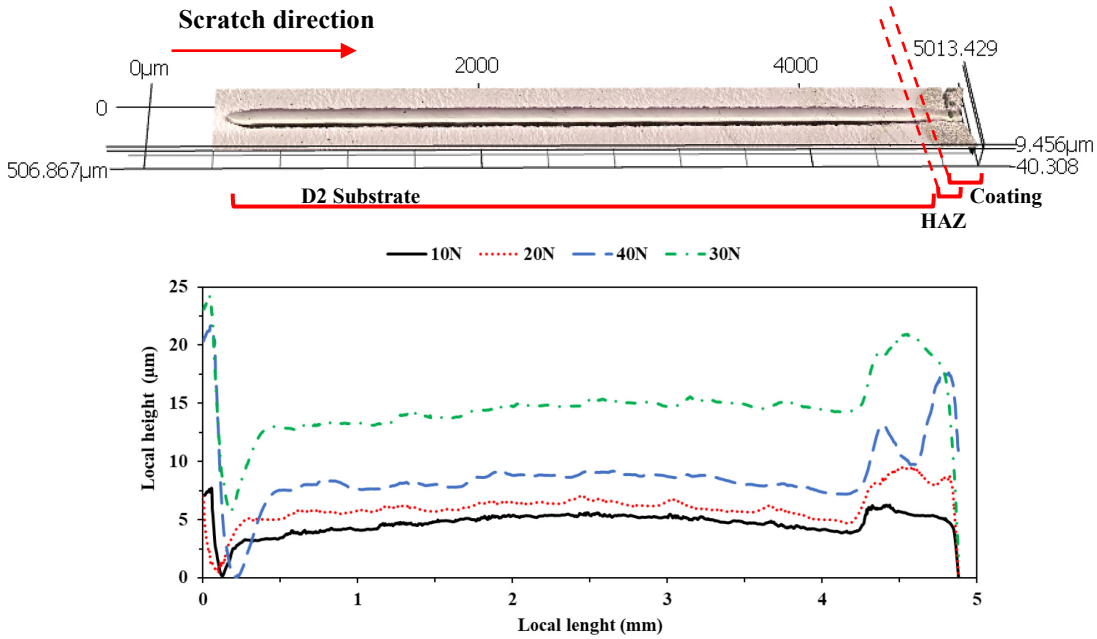

Figure 102. An example of cross-sectional scratch depth profile on the clad D2 tool steel under applied loads of 10 N, 20 N, 30 N, and 40 N. The overall image was generated by stitching sequential CLSM images. Note that the bulk material is shown on the left-hand side of the image, with the clad layer and free surface on the right-hand side.

Figure 103 presents a series of SEM micrographs obtained from a single scratch track on the cross-section of a TiC-Ni_3Al clad D2 tool steel sample, highlighting the change in scratch width (and hence the scratch hardness) when transitioning from the bulk D2 material into the clad layer itself. Images obtained from various portions of the cross-sectional scratch track clearly demonstrate the impact of the applied clads on the observed damage mechanism(s) and scratch resistivity of the D2 substrate. Lateral- and tensile-type crack formation occurs on the edges of the scratch track within the substrate region, the extent of which was significantly reduced as the stylus moved toward the surface of clad. As highlighted in Figure 103, the presence of primary and secondary hard carbide phases hinders the deformation of the projected area during scratching, by both inhibiting movement of dislocations and increasing the local hardness/elastic modulus through the presence of the hard carbide phases.

Consequently, the morphology of the scratch edges within the heat affected zone and the through the thickness of the clad exhibits a transition in deformation mechanism characterized by buckling and conformal cracking due to the increase of overall hardness. No adhesive failure was observed between the coating and substrate due to a high degree of diffusion occurring between them during laser processing.

Two types of failure may be expected during the cross-sectional scratch evaluation of hard coatings, namely adhesive and cohesive [107]. During adhesive failure, a cone-shaped fracture takes place at the interface between the substrate and coating.

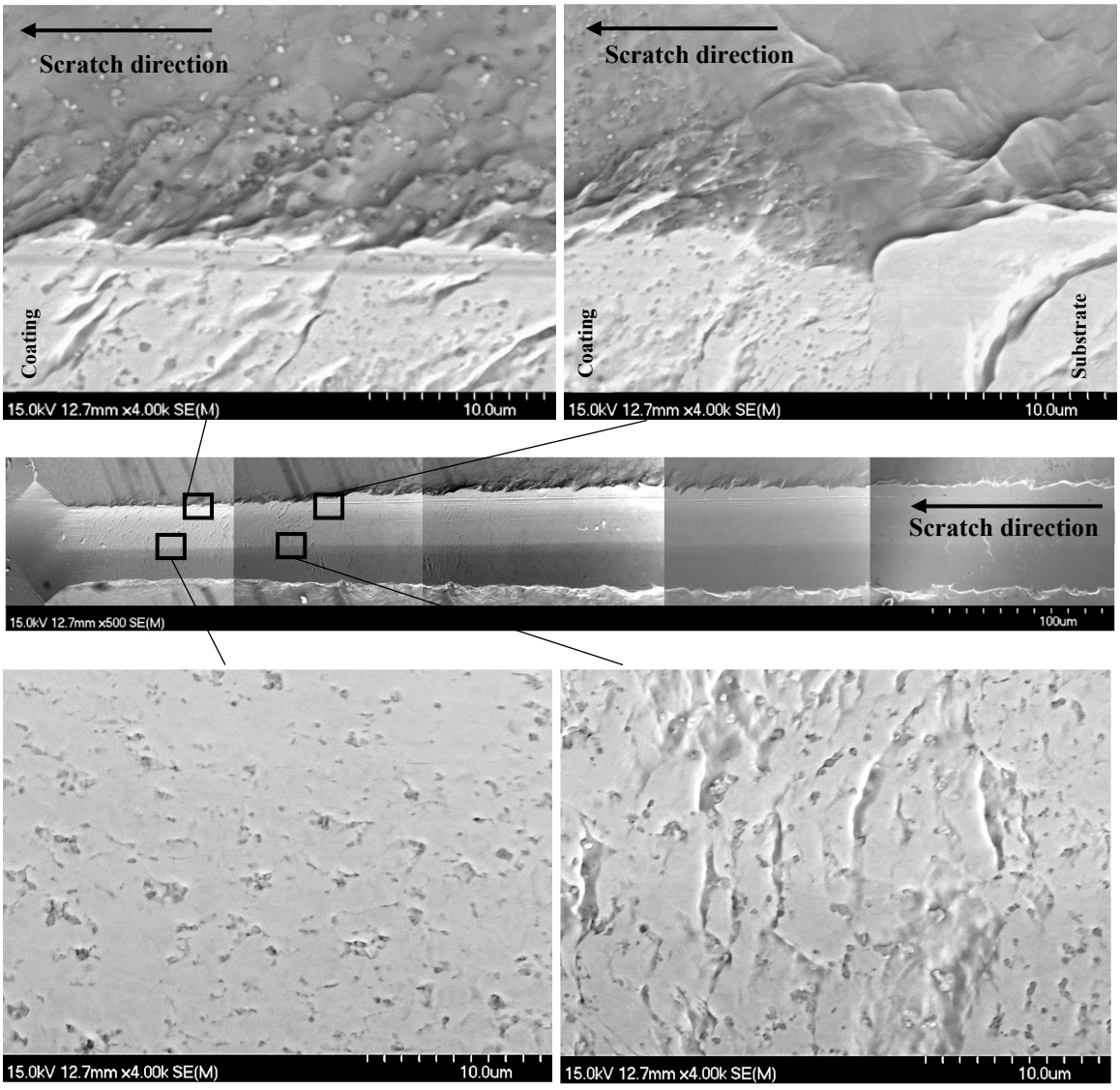

Figure 103. Microstructural evaluation of a scratch track through the bulk/cladding cross section, generated for a TiC-Ni_3Al clad on D2 substrate (processed at P = 350 W and τ = 0.6 s, with a resultant ED = 253.14 J/mm^3).

Cohesive failure, on the other hand, is an indication of failure within the coating itself, rather than at the interface. In the currently presented work, the geometry of the resulting cone shaped fracture at the tip of the scratch was measured and the area of the fracture was calculated following [449]:

Equation 21

$$A_{cn} = L_x x L_y$$

where A_{cn} is the cone area, L_x is cone diameter, and L_y refers to the depth of formed cone. The formation of cone-shaped fractures in the TiC-based clads on D2 substrates was observed once the constant applied scratch load exceeded 30 N, (Figure 104). At loads of 30 N and 40 N, cone shaped fracture was observed to originate within the coatings, which suggests a cohesive failure mode predominates above this critical load. During high magnification imaging of the projected conical areas, it was also noticed that most of the widening of the cone base is related to movement of the stylus through the porous layer that contains the top surface porosity for the as fabricated clad coatings (Figure 103). Thus, a general increase in the measured conical area was noticed as a function of increasing surface roughness.

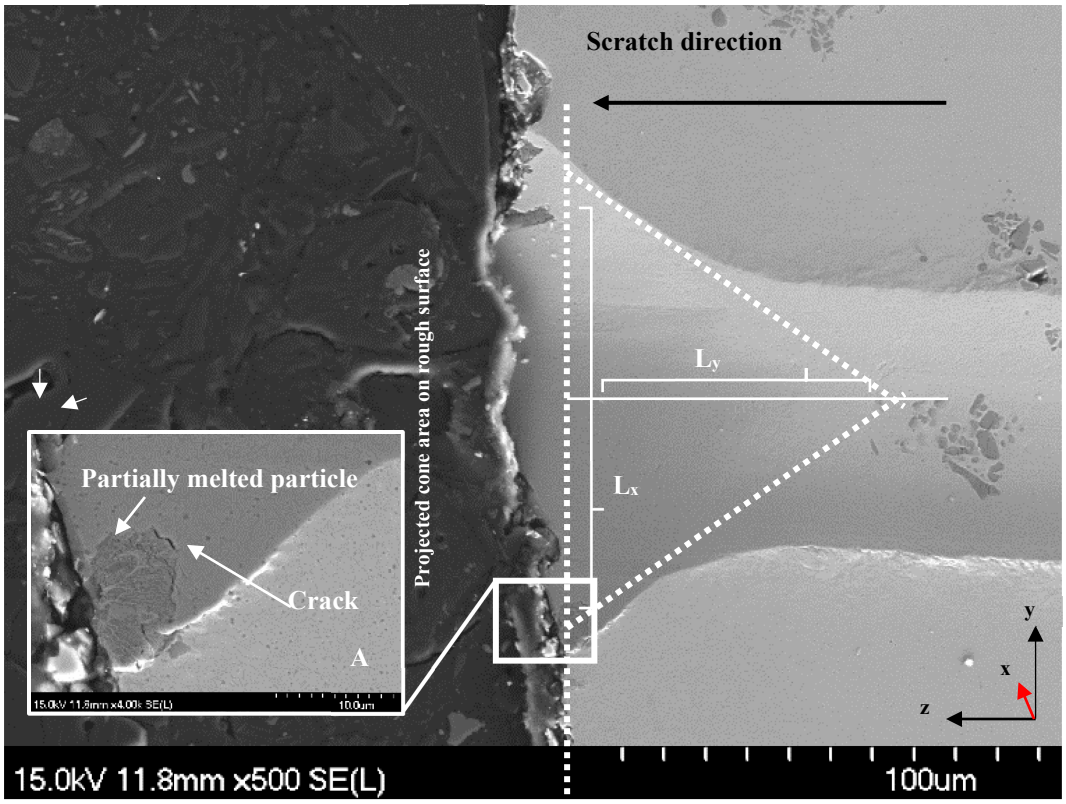

(a)

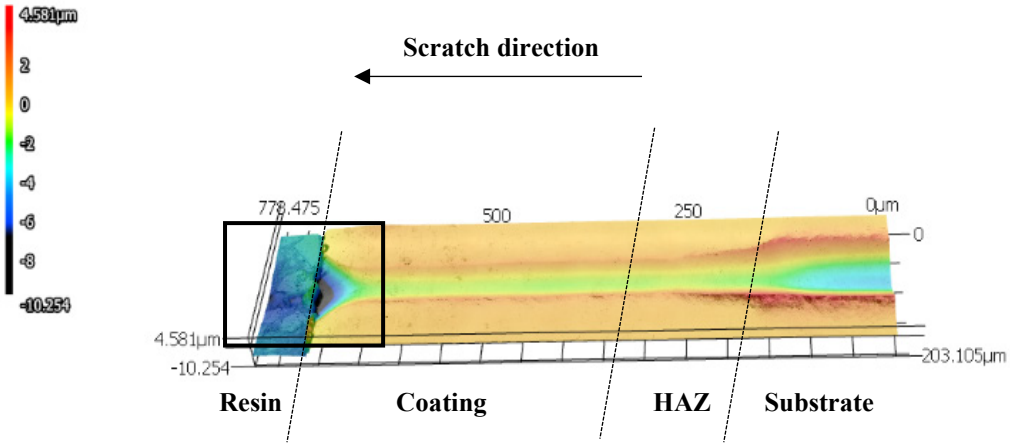

Figure 104. (a) SEM image of the tip of a through thickness scratch, for TiC-Ni_3Al cermet coating on D2 steel under 30 N applied normal force. (b) CLSM image of conical fracture arising within the scratch cross section. The associated x-axis denotes the laser scanning direction during DED fabrication.

Any potential oscillations arising for either the COF or the AE events were recorded simultaneously during cross sectional scratch tests; examples of the recorded data are provided in Figure 105. Detected AE peaks were generally sensed during the movement of the stylus through the HAZ layer which increased in intensity proportionally to the value of applied force. A constant increase in the value of COF was recorded for scratches generated within the substrate portion of the sample. However, once the stylus entered the clad layer, the COF values were significantly reduced. The COF was found to remain essentially constant within the clad portion of the scratch, regardless of the applied load.

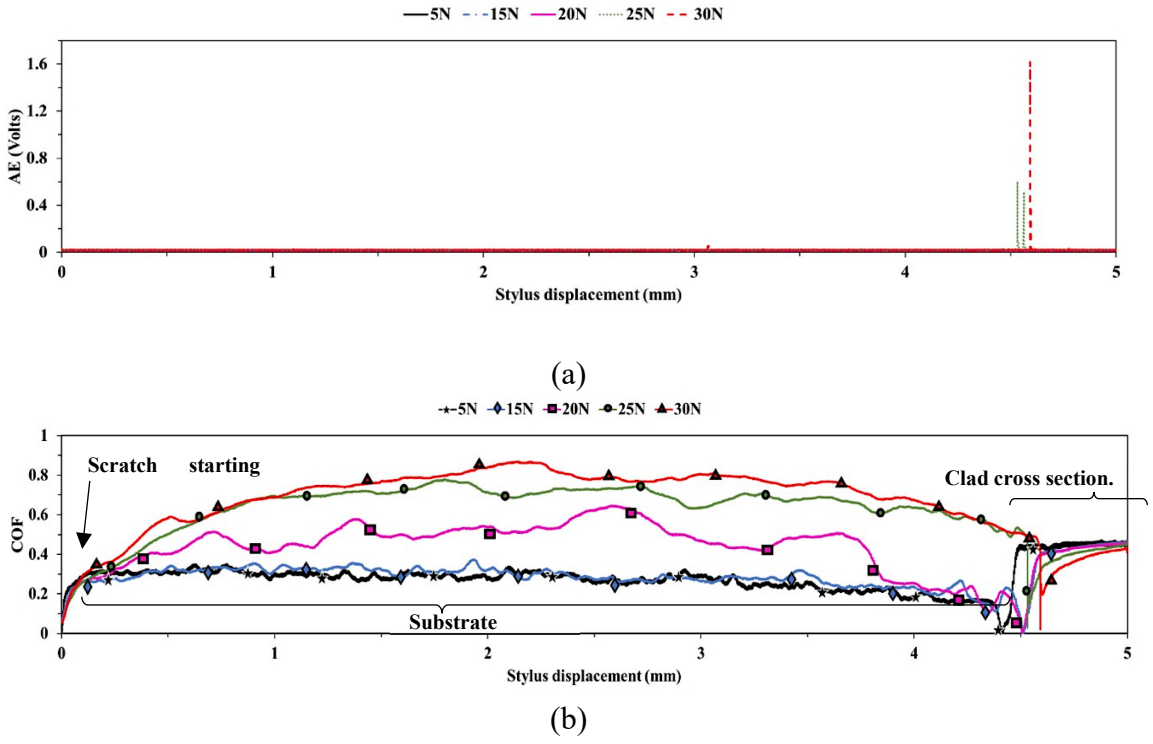

Figure 105. Representative AE events (a), and COF (b), curves obtained from scratch testing of TiC-Ni_3Al clad onto a D2 substrate under applied normal loads ranging from 5 N to 40 N. Samples were processed at P = 350 W and τ = 0.6 s, with an ED = 253.1 J/mm^2.

6.4. Conclusions

TiC-Ni_3Al based clads were successfully applied onto high Cr-containing, cold work D2 tool steel substrates using laser direct energy deposition (DED). To achieve this, a suspension-based preplacement method was used for the coating feedstock prior to DED. A well-adhered, preplaced TiC-Ni_xAl_y-Ni coating composition, with a uniform thickness, was then subjected to laser DED processing using various laser powers and scanning speeds. Microstructural examinations confirmed fabrication of high density clads with a refined microstructure and minimal levels of porosity. The efficiency of the proposed technique and its impact on mechanical enhancement of D2 hard work tool steel surface, was subsequently validated in relation to laser processing parameters. Within the narrow range of 300-350 W laser power, high quality clads were fabricated at range of scanning speeds for evaluation of the solidification dynamics and a relationship between *ED* and surface roughness was confirmed.

In terms of the mechanical behaviour, the maximum values for VH were recorded at the top surface of the examined cross section, with an average value of VH = 659. In the middle section of the clad, a slight decrease in hardness values was observed. At the clad substrate interface 560 HV was reported for the applied load of 5 N. Substantial decrease in hardness was observed with increasing depth into the substrate, with respect to the clad surface, due to the reduced concentration of the hard carbide phases.

Single-pass scratch testing approaches were undertaken for qualitative and quantitative evaluation of the micro tribological properties of the clads. Post-scratch morphology of the cermet clads demonstrated that abrasive damage is generated in the clad layer, which can be anticipated to progress by plastic deformation through dislocation motion and lattice

distortion. Within the range of 10 N to 40 N applied normal force, the scratch hardness of the cermet clad coatings (H_{Sp}) varied within the range of 4.9 to 7.6 GPa, whereas the D2 substrate exhibited a consistent value of $H_{Sp} \approx 3$ GPa.

Chapter 7. Aqueous Corrosion Performance of Gel based TiC-based Laser DED Clads on D2 Tool Steel Substrates

Zhila Russell and Kevin P. Plucknett*

Dalhousie University, Department of Mechanical Engineering, 1360 Barrington Street, Halifax, Nova Scotia, CANADA, B3H 4R2

*Corresponding author: kevin.plucknett@dal.ca

Keywords: cladding; laser directed energy deposition; metal matrix composites; additive manufacturing; potentiodynamic polarisation; electrochemical impedance spectroscopy

Abstract

Application of titanium carbide (TiC) based coatings, via laser directed energy cladding (LDED), has been examined for enhancement of the corrosion characteristics of the surface of D2 grade tool steel substrates. The TiC coatings are based on a nominal feedstock composition of TiC-Ni_3Al, which is applied using a preplacement approach through dip coating. Various LDED processing parameters were then examined, relating to both the feed stock preparation and laser processing conditions, with the aim of fabricating defect-free, thick clads (up to ~250 μm in thickness), with optimal adhesion to the D2 substrate and significantly improved corrosion properties. The development of a composite clad microstructure, with a heavily alloyed metallic matrix based on α- (Fe, Cr) and uniformly distributed TiC grains, led to a significant increase of the corrosion resistance in artificial seawater. Increased laser power resulted in increased *energy density (ED)*, resulted in reduced surface roughness for *ED* up to ~257 J/mm^2 and clad thickness of ~140 μm, visibly

improving the surface finish of the clad substrate. It is demonstrated that the corrosion behavior of the TiC-based, coated D2 steel is primarily determined by the synergistic impact of laser processing parameters associated with the coating process. The optimised laser clad steels exhibited a dense oxide layer based on α-Al_2O_3, Cr_2O_3, and NiO, which was repeteadly observed for a range of cladding parameters.

7.1. Introduction

Series D steels are one of the most popular families of high-carbon high-chromium cold work tool steels, which are often characterized by their high wear resistance and mechanical stability under thermal cycling. The presence of a large volume fraction of alloyed carbides within this family of steels provides high degrees of hardenability and the possibility of martensite formation through air cooling from the austenitizing temperature. One of the commonly used examples of Series D steels in the D2 grade. Wear-resistant forming dies, punches, trimming equipment, shear blades, and cutting tools are just a few of the industrial applications that benefit from the desirable mechanical characteristics of D2 tool steel. The corrosion performance of this alloy, on the other hand, is susceptible degradation in severe operational environments [460]. Consequently, a number of techniques have been examined in recent years to resolve or decrease the extent of losses that arise from corrosion/oxidation of the parts in-service [461,462].

The increase of chromium concentration, present in solid solution, that obtained by laser surface melting of bare D2 steel, has been shown to increase not only the resistance to corrosion, but also the resistance of the surface to wear [463–465]. However, laser processing of D2 steel is challenging, due to the segregation of C, and Cr alloy elements

and the high potential for formation of cracks [466,467], thus degrading the mechanical performance. Undesired segregation of alloying elements results in inhomogeneity of the equiaxed microstructure and pearlite transformation, which results in reduced mechanical characteristics of the surfaces and increased rates of wear and corrosion [468].

As an alternative, the application of composite coating materials offers several benefits due to their potential for high hardness, strength, and fracture toughness [469]. Ceramic metal composites, or 'cermets', as well as related metal matrix composites (MMCs), are commonly used in industrial coating applications due to their high wear and corrosion resistance [470,471]. Cermet composite coatings containing titanium carbide (TiC) are of particular interest for applications with significant weight restrictions, especially when compared to the more traditional 'hardmetals', based on heavy tungsten carbide (WC). A wide variety of metallic-based binder systems have already been developed for TiC based cermets [472]. The materials exhibit excellent performance advantages, such as high hardness and thermal stability [473], exceptional wear resistance properties, along with low coefficients of friction [474,475], high thermal shock resistance [476], and a desirable processing compatibility with the iron-based matrixes [477]. This last feature has made TiC one of the most common reinforcement particles used in the steel industry. In terms of binder developments for TiC-based cermets, the use of ductile intermetallic nickel aluminides (Ni_3Al) has been examined in recent years, due to their high yield strength and corrosion resistance, combined with an anomalous yielding response that results in increased strength at elevated temperatures [478]. As a consequence, TiC-Ni_3Al cermets have shown excellent high temperature strength, combined with wear resistance comparable to WC-Co [286].

The processing of these cermet materials by high power lasers is a potential processing technique that can be applied in industry. Within this context, additive manufacturing techniques based on laser heating has emerged as a strong candidate in recent years for many fields of application (e.g., prototyping, repair, surface modification, direct manufacturing, etc.) [469]. This is due to the method's flexibility, ability to manufacture high density materials/clads, and the excellent metallurgical bonding that can be achieved [469]. Notably, the corrosion response of TiC-based composite coatings, applied via laser processing, has been investigated by several researchers [479,480]with a view to improving the substrate response.

The present study examines the corrosion performance of coatings based on TiC, with a nominal Ni_3Al binder, deposited onto D2 tool steel substrates using LDED. Bulk cermets based on the combination of TiC and Ni_3Al have been previously shown to exhibit excellent wear and corrosion characteristics[16,285], highlighting the potential for such a system when using laser cladding. A novel, suspension-based approach is used for preplacement of the coating material onto the substrate, which is then laser treated to form a high density, metallurgically bonded clad layer on the D2 substrate. A variety of material processing and DED conditions have been examined to assess the clad development. Microstructural assessment of the clads has been performed, while an overall focus has been placed upon evaluation of their aqueous corrosion response in a simulated seawater environment. A comparison has also been made to the response of the unclad D2 steel surface.

7.2. Experimental Procedures

A composite TiC-Ni_xAl_y-Ni cermet composition was clad on AISI D2 tool steel using a preplaced mixture of TiC powder (lot #PL20126240; D_{50} = 1.0 - 2.0 μm), Ni_xAl_y powder (lot #D28X029; D_{50} = 32 μm), and Ni powder (lot #L10W013; particle size of 2.2 - 3.0 μm). The TiC was supplied by Pacific Particulate Materials Ltd. (Vancouver, BC, Canada), while the Ni_xAl_y and Ni were supplied by Alfa Aesar (Tewksbury, MA, US). Appropriate compositions were prepared for final clad composition of cermets with 30 vol% Ni_3Al metallic phase; in this respect, the Ni_xAl_y exhibits a 1:1 weight ratio. The details of powder preparation and preplacement of the composites have been discussed in greater detail in a recent publication [160]. Precision ground and annealed D2 tool steel plates were supplied from McMaster-Carr (Douglasville, GA, US), and were used as the substrate material for LDED processing. The substrate specimens were sectioned into a final geometry of 20 x 50 x 5 mm and then subjected to abrasive grit blasting with 300 μm zirconia shot prior to pre-placement of the cermet feed material.

Laser processing of the coatings was conducted using an Optomec 500 MTS-Ca LENS® LDED system (Albuquerque, NM. US). The LDED was operated in continuous mode, with a maximum operational laser power of 1kW, using ytterbium-doped fiber laser (IPG Photonics; λ=1,070 nm) with focusing optics tuned for a spot size of ~700 μm. The laser processing parameters that were used for deposition of the TiC-based clads are presented in Table 19. An argon shielding gas was delivered through a nozzle at 10 l/min to protect the melt pool from possible oxidation, which (along with an argon chamber environment) resulted in an oxygen content that was less than 10 ppm. Optimal processing parameters were verified by cladding at 200, 250, 300 and 350 W laser power (P) and with scanning

speeds (*V*) of 1.7, 3.4, 6.7, or 13.5 mm/sec.

Microstructural evaluation was performed on sectioned LDED plates using a field emission scanning electron microscopy (FE-SEM; Model S-4700, Hitachi High Technologies, Tokyo, Japan), equipped with energy dispersive X-ray spectroscopy (EDS; Inca X-maxN, Oxford Instruments, Concord, MA, USA) for subsequent compositional analysis.

Table 19. Specific build parameters utilized during the DED of preplaced TiC based cermet on D2 tool steel.

Sample	*P* (W)	*V* (mm/s)
TiC-Ni_3Al/D2	300	0.84
TiC-Ni_3Al/D2	300	3.38
TiC-Ni_3Al/D2	300	6.77
TiC-Ni_3Al/D2	300	13.54
TiC-Ni_3Al/D2	350	0.84
TiC-Ni_3Al/D2	350	3.38
TiC-Ni_3Al/D2	350	6.77
TiC-Ni_3Al/D2	350	13.54
D2- Wrought	-	-
D2-LR	300	6.77

The LDED processed coatings were sectioned perpendicularly, in relation to their planar surface, and then were mounted for grinding/polishing down to a 0.25 μm final diamond

paste particle size. The overall appearance of the clads, along with three-dimensional metrology measurements of the surfaces both prior to and after corrosion measurements, was performed using a 3D confocal laser scanning microscope (CLSM; VK-X200/X210, Keyence, Mississauga, ON, Canada). In addition, Java-based image processing software (Image J, National Institute of Health, Laboratory for Optical and Computational Instrumentation, LOCI, University of Wisconsin, WI, USA) was utilised for the phase and particle morphology analysis performed on cross sections of the examined clads.

Corrosion measurements were carried out at room temperature (21 ± 2 °C), using a standard three-electrode flat cell (Gamry Instruments, PA, USA), with the laser clad sample as the working electrode, a graphite plate as the counter electrode, and a saturated calomel electrode (SCE; −0.241 V vs. a standard hydrogen electrode) as the reference. Measurements were recorded using a potentiostat/galvanostat/zero resistance ammeter (Gamry interface, Model 1010E, Gamry Instruments, PA, USA). All of the evaluated LDED specimens were initially allowed to reach a nominally steady state condition by immersing them for 2 hours in 3.5 wt% NaCl aqueous media, while the material's open circuit potential (OCP) was recorded. Electrochemical impedance spectroscopy was performed to a frequency of up to 2 MHz. Potentiodynamic polarization experiments were subsequently performed by applying a potential sweep from -0.3 V relative to the measured OCP, up to a potential of +1.0 V vs. the reference electrode, at a voltage scan rate of 0.1667 mV/seconds.

The boundaries of the experiments were controlled during the test using the Gamry Framework software package (Gamry Framework for Windows 11, Gamry Instruments, PA, USA). The corrosion current density (I_{corr}) and potential (E_{corr}) were estimated using

an iterative, instantaneous Tafel-type fit corrosion analysis software. A Tafel curve is then modelled through the software by fitting both anodic and cathodic Tafel slopes (i.e., β_a and β_c, respectively), prior to recording the I_{corr} and E_{corr}. Based on the measured values, the extrapolated corrosion rates (in mm/year) were determined for the clads by applying the ASTM standard (G102-89) protocol [27]. Subsequently, the linear polarization resistance (R_p) was calculated in order to determine the resistance of the material under investigation against corrosion following:

Equation 22

$$\boldsymbol{R_P = \frac{B}{I_{corr}}}$$

Equation 23

$$B = \frac{\beta_a \beta_c}{2.3\ (\beta_a + \beta_c)}$$

where the various parameters have been defined above [481]. Compositional analysis of the recovered post-corrosion solutions was subsequently performed using inductively coupled plasma atomic emission spectroscopy (ICP-OES; model Thermo iCap 7400 Dual View, MA, USA), with an applied internal calibration standard (scandium), while corroded surfaces were examined using the FE-SEM and associated EDS.

7.3. Results and discussion

7.3.1. Macrostructural characterization of the LDED processed clads.

Figure 106 demonstrates representative FE-SEM micrographs obtained from TiC-based

clad coatings on D2 steel; in this instance the initial feedstock material was prepared with a nominal 30 vol.% Ni_3Al intermetallic binder. Microstructural analysis shows that a high-density layer is produced within the surface zone of the substrate, which is well bonded with essentially no microcracks. A series of macro and micro analyses were performed for geometric characterization of the fabricated clads, which were then related to the various LDED processing parameters.

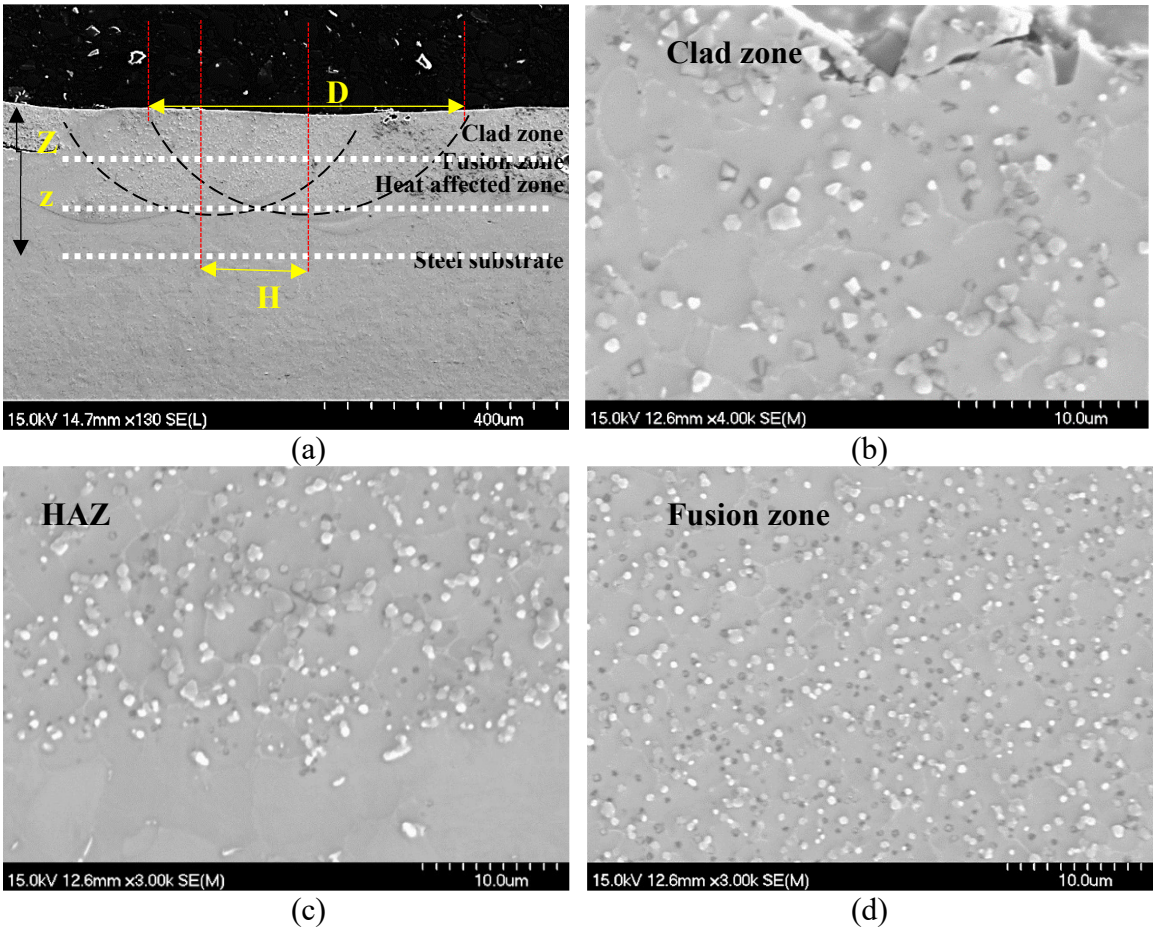

Figure 106. (a) Low magnification SEM micrograph of a TiC-Ni_3Al clad on D2 steel, highlighting the various geometrical measurements that were taken for each clad. Higher magnification SEM micrographs obtained from TiC-Ni_3Al LDED coatings on D2 steel, highlighting: (b) the cross-sectional view of the distinguished clad zones, (c) the top of the

clad zone, and (d) the fusion zone and heat affected zone (HAZ). This sample was processed with a laser power of 350 W and scanning speed of 3.38 mm/s.

The magnitude of energy output during LDED, within a specified unit of length, has been determined based on the volumetric energy density calculation derived from that more typically utilized in laser powder bed fusion processing [377]:

Equation 24

$$\boldsymbol{ED = \frac{P}{V H_S Z_S}}$$

where *ED* is the energy density, *P* is the laser power, *V* is the laser traverse rate, H_S is the line hatch spacing of adjacent laser raster tracks, and Z_S is the layer thickness (i.e., $Z' + z$, as in Figure 106(a)). Table 19 summarizes the cladding geometrical parameters, obtained from the microstructural characterization of successful builds with repeatable surface finish and functionality, with respect to the applied laser processing variables.

The 'main effects plot' that was determined for the total clad thickness, in relation to the calculated *ED* and the achieved surface roughness, is presented in Figure 107. Clad layers generated from the same volume of applied feedstock tended to vary in thickness when the laser power and/or scanning speed were altered. Increasing the laser power resulted in an increased *ED* which, in turn, led to a reduced surface roughness for *ED* up to 256.62 J/mm^2 and thickness (a minimum of 137.0 μm), together with a visibly improved surface roughness. Clad layers thicker than this value exhibited increased surface roughness and disqualification of the as-clad specimen for corrosion testing.

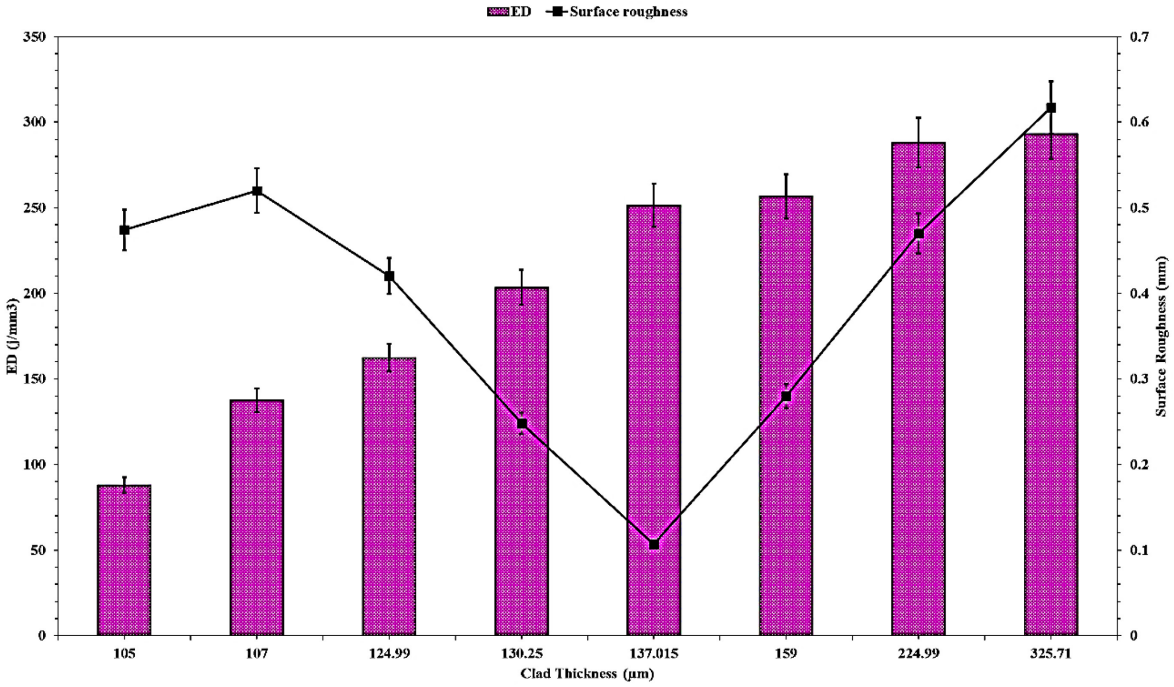

Figure 107. The calculated energy density (ED), in relation to the measured thickness of the clad layer and its associated surface roughness.

The general microstructure of the clads (shown previously in Figure 106), consists of uniformly dispersed TiC phase within a very fine (nanoscale) lamellar eutectic matrix, which distinctly varies in morphology when moving towards the mid-section of the layer. The solidified microstructure demonstrates that, following LDED processing, very fine, faceted TiC grains are present within a coarser grained metallic matrix. From visual assessment only, it is not possible to determine whether these are (primary) TiC particles retained from the original dip coating mixture or that they have selectively dissolved and reprecipitated. Variation of the evolved microstructure within different zones confirm the ultra-rapid heating and cooling rates that arise during laser processing. At the fusion zone, carbide grains exhibit minimal dendritic growth and are mainly preserved in the

cubic/polygonal morphology. At the bottom region of the clad, microalloying can provide a complete metallurgical bond between the coating and substrate and create a heat-affected zone region (HAZ) that binds permanently with the substrate. The compositional mapping in Figure 108 has been generated through EDS analysis and is obtained from the bottom section of laser deposited layer of TiC-Ni_3Al (with a laser power of 350 W and V = 6.77 mm/s). In the upper section of this region, fine TiC dendrites are surrounded by a high concentration of V and Cr that is depleted from the D2 steel substrate, suggesting the formation of secondary (or more highly alloyed) carbides.

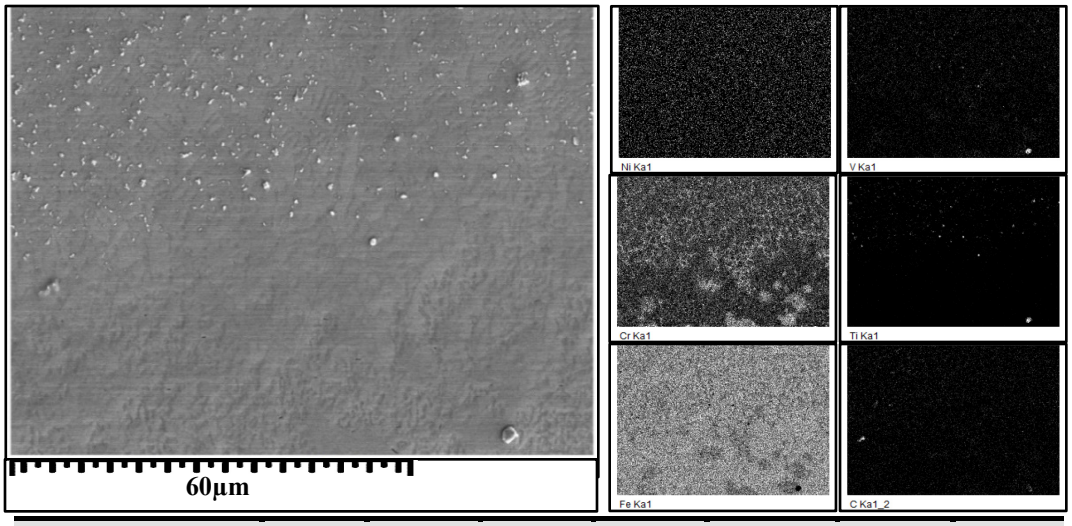

Element	C	Si	Ti	V	Cr	Fe	Ni
Weight %	6.20	0.49	0.50	0.77	11.12	80.5	0.44
Atomic %	23.23	0.78	0.47	0.68	9.63	64.87	0.34

Figure 108. An example of the TiC-Ni_3Al/D2 steel substrate clad couple, highlighting the general chemical composition of the clad zone. The associated table summarizes the overall composition for the mapped area.

Figure 109 demonstrates the results of image analysis, highlighting the structure of grain boundaries formed during austenitic transformation at eutectic temperature for clads processed at P = 350 W and V = 0.84 mm/s, 3.38 mm/s and 6.77 mm/s. In prior LDED work, the structure and the extent of the area covered by grain boundaries has been reported to vary depending on the cooling rate and austenitic grain size [465,468,482]. As is apparent in Figure 4, the extent of the formation of boundaries and the overall microstructural scale were reduced in proportion to the increased laser scanning speed.

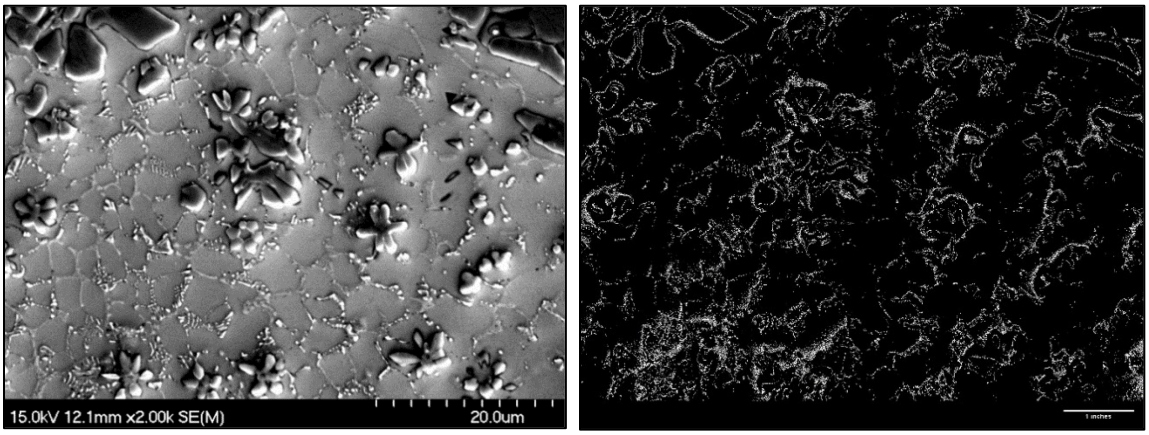

(a)

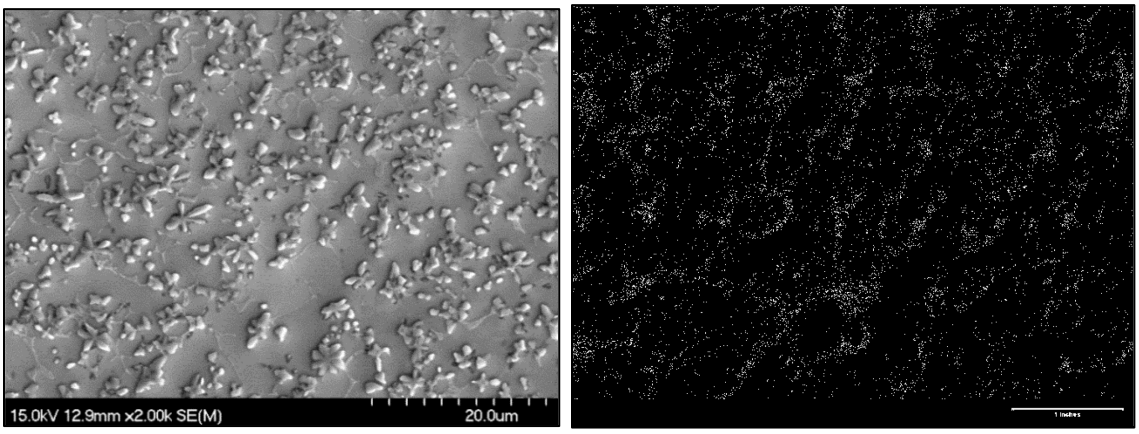

(b)

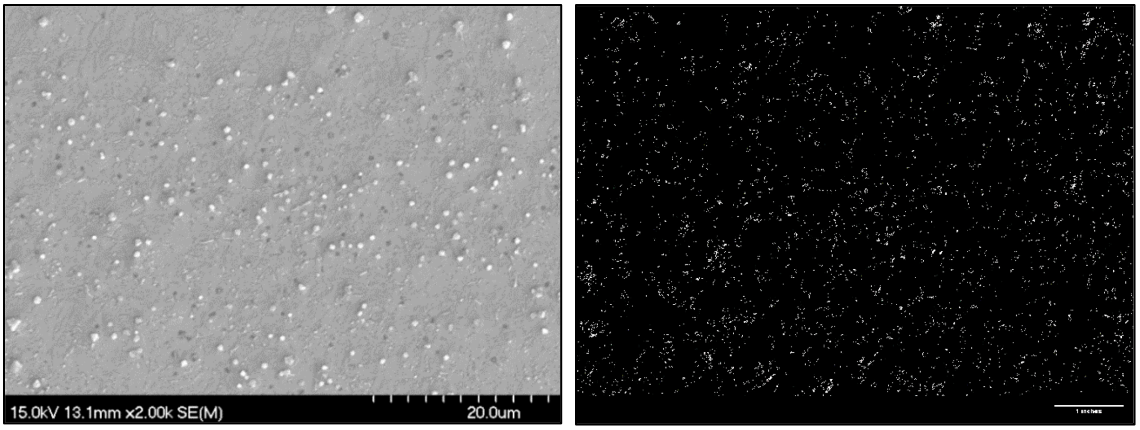

(c)

Figure 109. FE-SEM micrographs obtained from polished cross section of TiC-Ni_3Al cermet clads on D2 steel, laser processed at P = 350 W, for: (a) V = 0.84 mm/s, (b) V = 3.38 mm/s, and (c) V = 6.77 mm/s.

Analytical measurement of the surface area related to the grain boundaries showed that the fraction of surface area occupied by grain boundaries over the total surface varies with the laser scanning speed (Figure 110). At 350 W applied laser power and a scan speed of V = 0.84 mm/s, the percentage of the area (A) occupied by grain boundaries was measured as A/A_{total} = 5.53 % which was then reduced to 3.44 and finally 0.84 % as the scan speed was increased to 3.38 and then 6.77 mm/s, respectively.

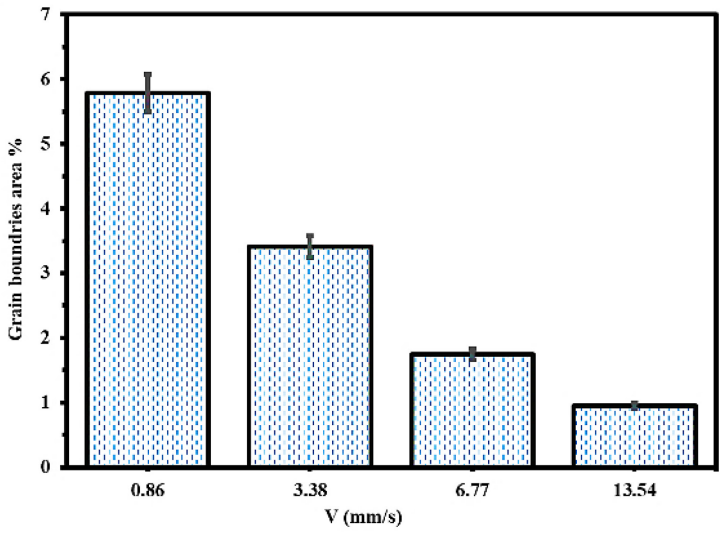

Figure 110. The average area occupied by grain boundaries measured for TiC-Ni_3Al cermet clads on D2 tool steel under various scanning speeds.

7.3.2. Microstructural characterization of the LDED clads.

Figure 111 provides a higher magnification SEM image presenting aspects of the microstructure development of the TiC based cermet, clad onto a D2 steel substrate at 350 W laser power and 3.8 mm/s scanning speed. The solidified microstructure of the clad coated D2 is composed of a uniform austenitic metallic matrix (area 1), that is a product of both substrate and NiAl from the cermet composition. The ceramic phase of the coating varied in morphology based on the concentration of alloying elements segregated from substrate during laser processing. Light color 1-2 μm MC type faceted carbide particles (area 2) contained high concentration of V and Ti and typical Cr-Fe rich lamellar phase containing Ni (area 5). The darker phase carbides (area 3), were composed of additional

alloying elements from substrate such as Si, Fe and Cr. The size and spacing of these carbide particles represent the characteristics of fast cooling dynamics of laser processing.

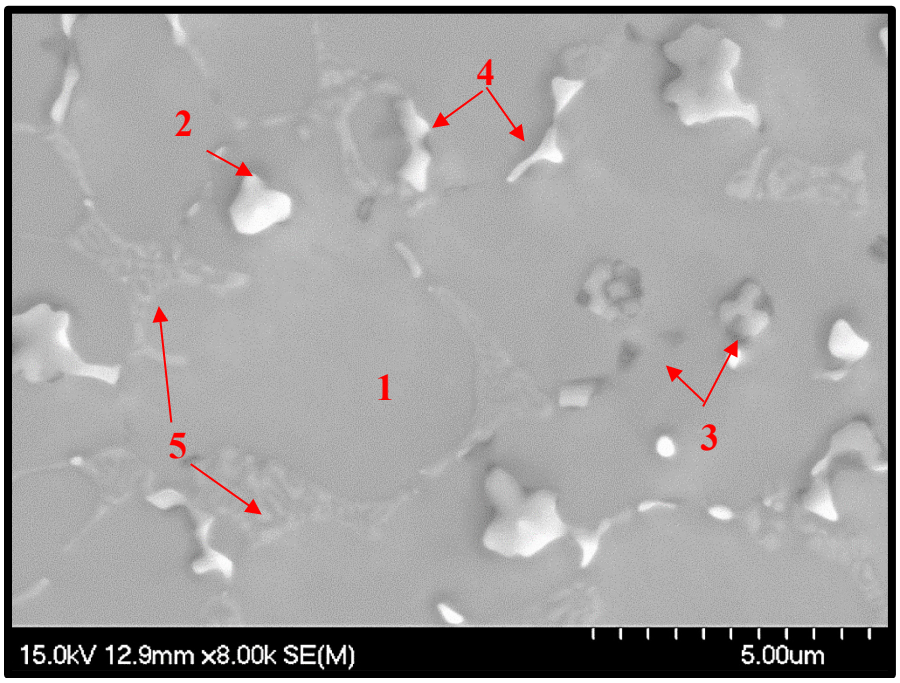

ID	Element (weight %)							
	C	Al	Si	Ti	V	Cr	Fe	Ni
#1	4.94	0.27	0.30	0.24	4.92	11.04	75.59	2.70
#2	19.88			33.27	27.01		24.38	
#3	8.88		0.27	23.39	16.06	6.32	44.18	0.90
#4	16.91		0.30	11.48	17.87	9.81	43.18	0.45
#5	7.26		0.25	0.51	5.47	23.89	61.69	0.92

Figure 111. Representative FE-SEM micrograph obtained from TiC-Ni_3Al (30 vol%) laser clad on D2 steel processed at 350 W laser power with scanning speed of 3.38 mm/s, together with EDS chemical compositions of the highlighted areas in the clad composition.

Similar microstructures have been reported previously, where the high thermal gradients in LDED result in the formation of dendrites in D2, along with M_7C_3 carbides, which are formed on the dendrite boundaries due to a eutectic reaction [483,484]. Chromium carbides, which were mainly formed within a eutectic region at the dendrite boundaries, showed an additional secondary phase, where a 'needle-type' microstructure, was noted (Figure 112).

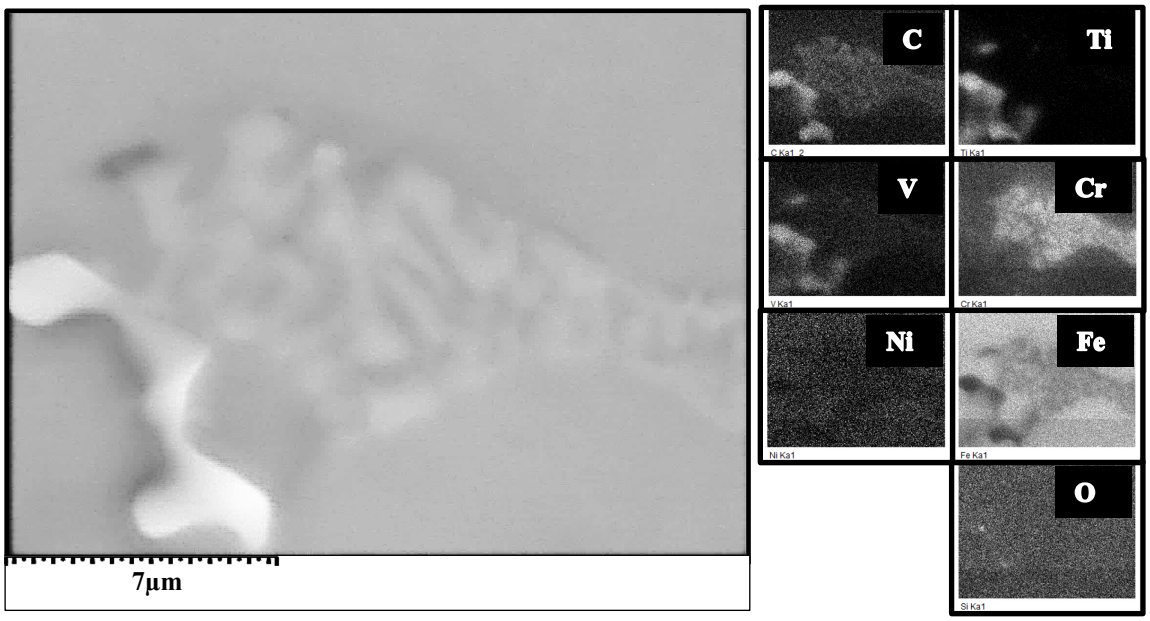

Figure 112. EDS mapping obtained from a TiC-Ni_3Al (30 vol%) composition laser clad onto D2 steel, processed at 350 W laser power with a scanning speed of 3.38 mm/s.

7.3.3. Electrochemical analysis

Examples of Nyquist plots obtained from the surface of TiC-Ni_3Al cermet clads on D2 steel is shown in Figure 113. The impedances were identified by a semicircle capacitive

loop, suggesting the presence of one time constant for the analysed frequency domain which generally is an implication of charge transfer resistance or capacitance.

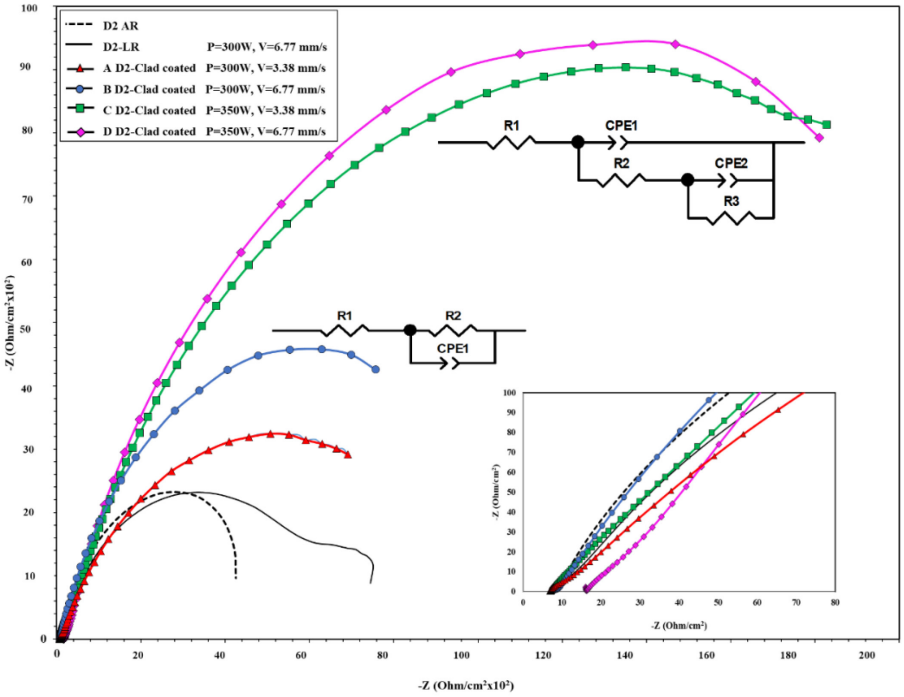

Figure 113. Results of electrochemical analysis highlighting Nyquist plots obtained from the surface of TiC-Ni_3Al cermet clads on D2 steel fabricated at various laser scanning speeds, in comparison to the as-received (AR) D2 substrate and the same substrate material after surface laser remelting (LR).

The Nyquist plots of both clad and as received samples display alike semicircle features under different conditions, while the diameters are different. The diameters of Nyquist plots related to the polarized as received (AR) and laser remelted D2 substrate (LR) were smaller than coated samples, demonstrating that the cladded samples exhibit higher impedance response and better protection against the corrosive media. Moreover, the

diameter of the capacitive reactance arc of laser remelted D2 is larger than that of the wrought AR specimens confirming the increased polarisation resistance in results of remelting the surface via surface. However, a low frequency limit is observed in steel impedance where the coating impedance reaches a capacitive state.

The equivalent circuit shown in inset of the Figure 113 was for simulation of the collected impedance data and the results are provided in Table 20 where R_1 is the resistance of the media, R_2 represents the charge transfer resistance and R_3 is referred to polarisation resistance. Subsequently, CPE_1 represents the oxide layer capacitance, CPE_2 is the electric double layer capacitor, and n is deviation parameter. The quality of the simulations was assessed by the values of chi-squared where lowest calculated values, is an indication for acceptable fits.

Table 20. Electrochemical parameters of the corrosion tested surfaces derived from EIS analysis.

ID	$R_1/\Omega.cm^2$	$R_2/\ \Omega.cm^2$	$CPE_1/F.cm^{-2}s^{n-1}$	$R_3/\ \Omega.cm^2$	$CPE_2/F.cm^{-2}s^{n-1}$	n	χ^2
D2	8.49	554.2	$7.72x10^{-3}$	-	-	0.84	$4.50\ x10^{-3}$
D2LR	7.43	768.5	$1.50\ x10^{-3}$	-	-	0.72	$8.50\ x10^{-3}$
A	6.856	1164	$3.00\ x10^{-3}$	-	-	0.65	$4.70\ x10^{-3}$
B	8.22	1319	$4.60\ x10^{-3}$	-	-	0.78	$3.90\ x10^{-3}$
C	13.15	1792	$10.29\ x10^{-3}$	2613	$4.42\ x10^{-3}$	0.71	$1.33\ x10^{-3}$
D	16.98	2464	$11.94\ x10^{-3}$	305.2	$1.28\ x10^{-11}$	0.75	$11.23x10^{-3}$

Examples of typical potentiodynamic polarisation (PD) curves obtained from the surfaces of TiC-Ni_3Al clads on D2 steel are shown in Figure 114, along with both the as-received

and laser remelted D2 substrate material. It is apparent that the application of the composite clad onto the D2 steel clearly improves the corrosion behavior of the substrate, by increasing the corrosion potential (E_{corr}) and decrease in corrosion current (I_{corr}); it is notable that this improvement arises across a range of LDED process conditions. Reduction of the corrosion current and shifting of corrosion potential toward nobler values indicates that the clad coatings provide higher corrosion resistance than that of substrate alone. Sample A only shows a 'passive-like' region at an I_{corr} value of 6.21 x 10^{-06}, while sample B, C and D showed spontaneous passivation with a wide passivity region near to 17, 140, and 460 mV respectively. Although the thermodynamic stability of the laser processed (i.e., remelted) D2 substrate in the absence of the TiC composite coating was not as noble as the coated specimens, there is still a reduction of I_{corr} in comparison to that measured for the untreated D2 substrate. This implies that improvement of the corrosion characteristics is a result of the laser processing steps. Negligible changes of the anodic current of the clad samples over a vast potential range depict the stability of the coatings. However, the stability of the coatings did vary with changing clad LDED process parameters. Specimens fabricated at the highest applied scanning speed (i.e., samples B and D) provided higher stability, while the lowest stability among the clad samples was determined for those fabricated at lowest scanning speed. The anodic current of various clad samples above their breakdown potential reached a value similar to the substrate. In this case, breakdown of the clad leads to penetration of the electrolyte into the clad coating, reaching the substrate/clad interface, where the anodic dissolution of substrate is more dominant in electrochemical reactions. Average electrochemical parameters obtained from OCP, and PD measurements are presented in Table 21.

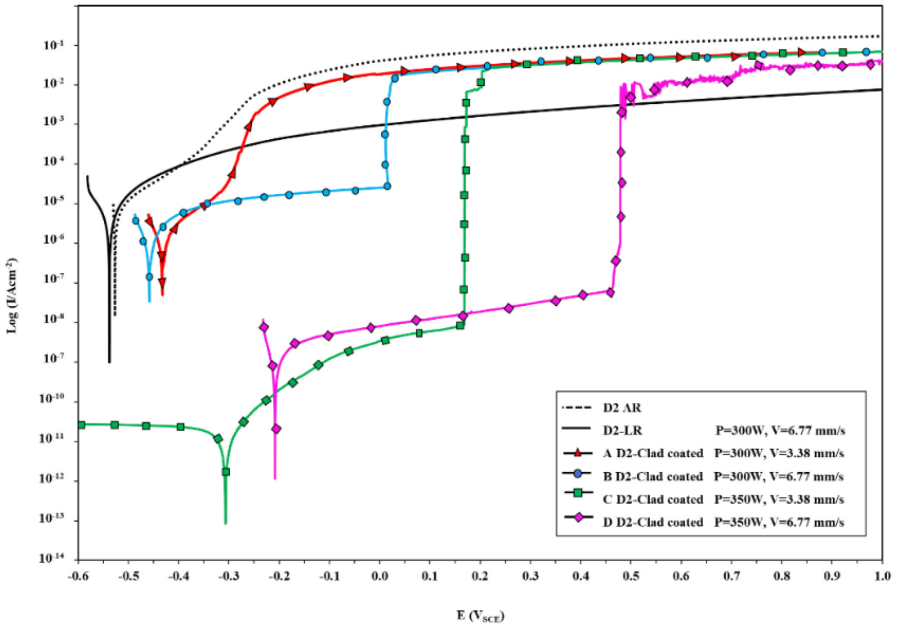

Figure 114. Results of electrochemical analyses highlighting potentiodynamic polarisation curves obtained from the surface of TiC-Ni_3Al cermet clads on D2 steel fabricated at various laser scan speeds and powers. Comparison is also made with the as-received (AR) D2 substrate and the same substrate material following laser surface remelting (LR).

Table 21. The measured electrochemical parameters following corrosion testing of the unclad and clad surfaces, derived from potentiodynamic polarisation curves.

Sample ID	OCP (Volts)	β_a (mV)	β_c (mV)	E_{corr} (Volts)	I_{corr} (A/cm^2)	Corrosion Rate (mm/yr)	Rp (Ω)
D2	-0.49	124.50	5.00	-0.51	1.94×10^{-05}	2.29×10^{-01}	1.08×10^{5}
LR	-0.48	138.73	100.81	-0.49	1.85×10^{-05}	2.19×10^{-01}	1.37×10^{6}
A	-0.52	98.50	27.18	-0.53	6.21×10^{-06}	7.34×10^{-02}	1.49×10^{6}
B	-0.46	98.09	31.96	-0.47	1.07×10^{-06}	1.27×10^{-02}	9.76×10^{6}
C	-0.44	143.52	10.10	-0.31	4.98×10^{-11}	5.89×10^{-07}	8.23×10^{10}
D	-0.16	171.80	28.60	-0.21	1.48×10^{-09}	1.75×10^{-05}	7.19×10^{9}

The results of potentiodynamic polarisation testing, in relation to the specific cladding parameters, are provided in Figure 115. The value of E_{corr} for the base metal was found to be –0.57 V vs. SCE which remained unchanged for the laser remelted D2 surfaces. Consequently, a marginal shift toward more noble potentials was observed for polarized specimens with the preplaced TiC based LDED coatings, with the largest shift relating to clads processed at the highest scanning speed, with E_{corr} = -0.31 V (vs. SCE). Consequently, it was observed that the I_{corr} at this potential experience a large drop by a margin of three order of magnitudes in contrast to clads processed at lower scanning speed and *Rp* reaches its optimal capacity. Therefore, the processing parameters resulting in *ED* value of ~256.6 J/mm^{-3} result in fabrication of coatings with optimal possible corrosion resistance without further modification.

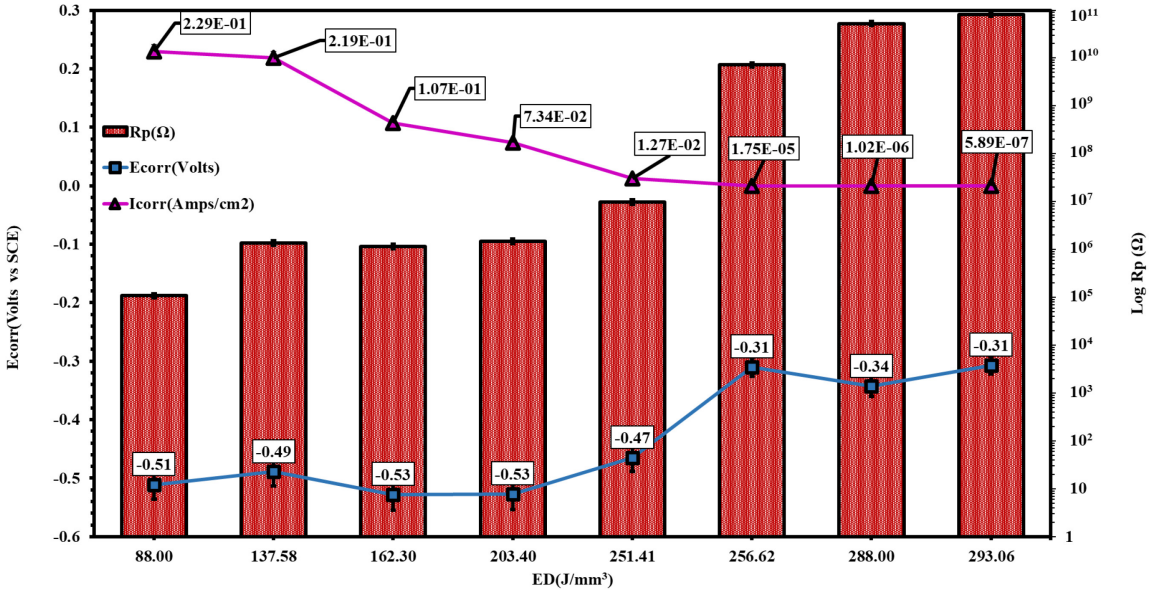

Figure 115. Identified corrosion parameters for TiC-Ni_3Al cermet clads onto D2 steel laser processed at various laser processing parameters.

7.3.4. Post corrosion surface morphology

The post-corrosion microstructure of the LR substrate was analysed to distinguish between the interactive effects of the laser processing parameters and the application of a ceramic-metal composite barrier layer, on the corrosion behavior of the D2 steel substrate. Figure 116 presents typical SEM images obtained from the cross section of the post-corroded LR, D2 steel substrate and the results of EDS compositional analysis of the surface, polarized to its corrosion potential and then to +1.0 V vs. SCE (Figure 116(a) and (b), respectively) in aqueous media containing 3.5 wt% NaCl. During the laser processing step, Cr compounds precipitate at the grain boundaries and leave the adjacent zones depleted of Cr (Figure 116(a)). Consistent with previous findings on corrosion behavior of high Cr steel, the formation of the Cr-depleted zones was observed, due to elemental segregation, which in turn can induce intragranular attack [485,486].

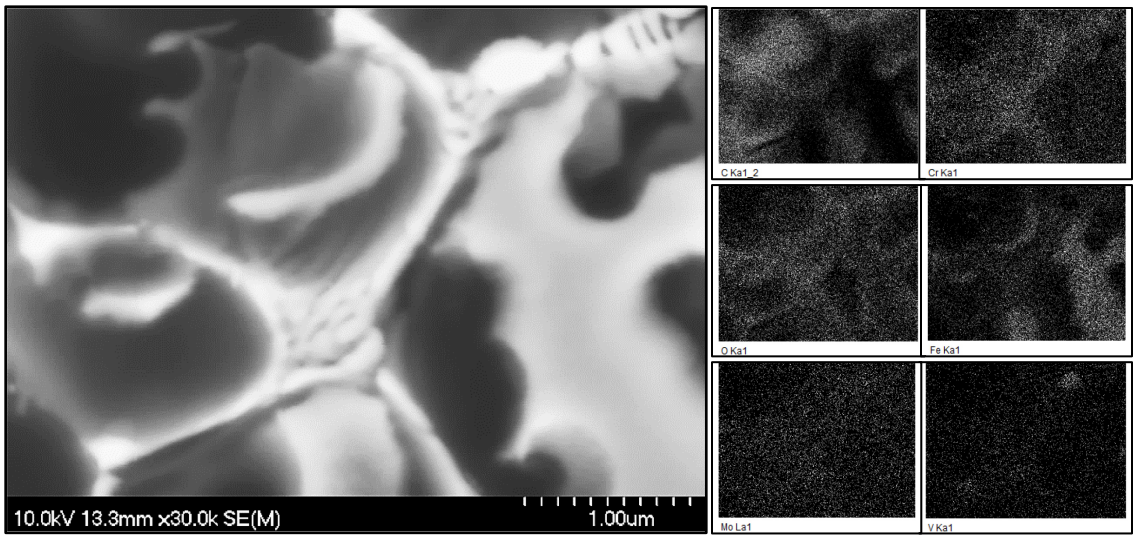

(a)

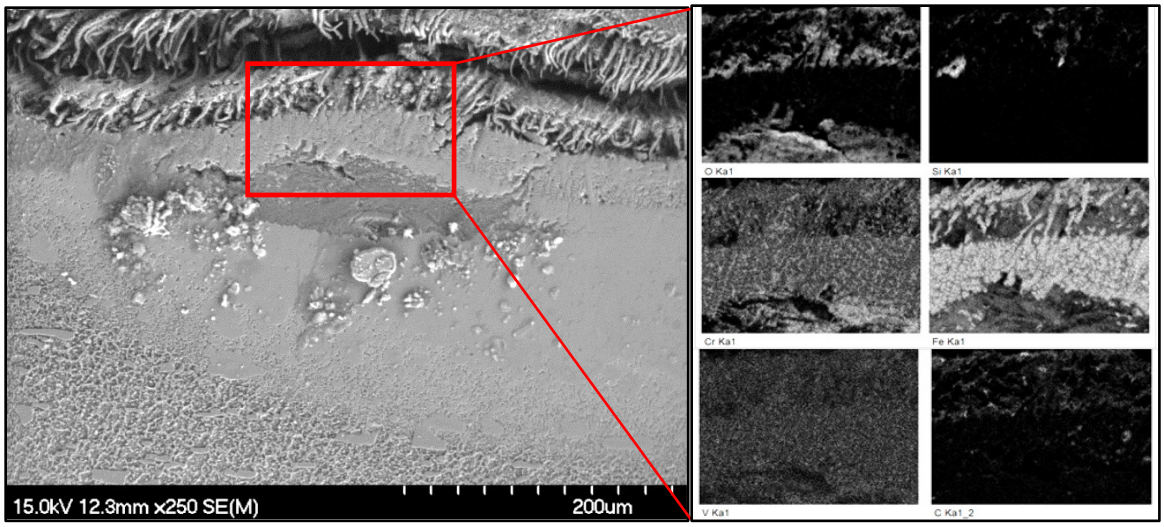

(b)

Figure 116. Post-corrosion cross section of the LR processed, D2 steel substrate, highlighting the results of EDS compositional analysis of the oxidized layer polarized to: (a) slightly above corrosion potential (E_{corr}), and (b) up to +1.0V vs. SCE. Samples were tested in an aqueous solution containing 3.5 wt% NaCl.

Thus, Cr-depleted zones develop into initiation sites for corrosion adjacent to the intergranular precipitates, where the electrochemical potential difference between the Cr depleted zone and matrix leads to intergranular corrosion and loss of material (Figure 116(b)). Figure 117 presents the post corrosion microstructure of the clad surfaces processed at P=300 W and V = 3.38 mm/s. It was noted during the electrochemical polarisation of the coatings fabricated with lower cooling rates that the post corrosion microstructure reveals selective removal of the binder phase has taken place, throughout the surface in contact with corrosive media, leaving residual TiC grains. This type of response can be anticipated through galvanic attack.

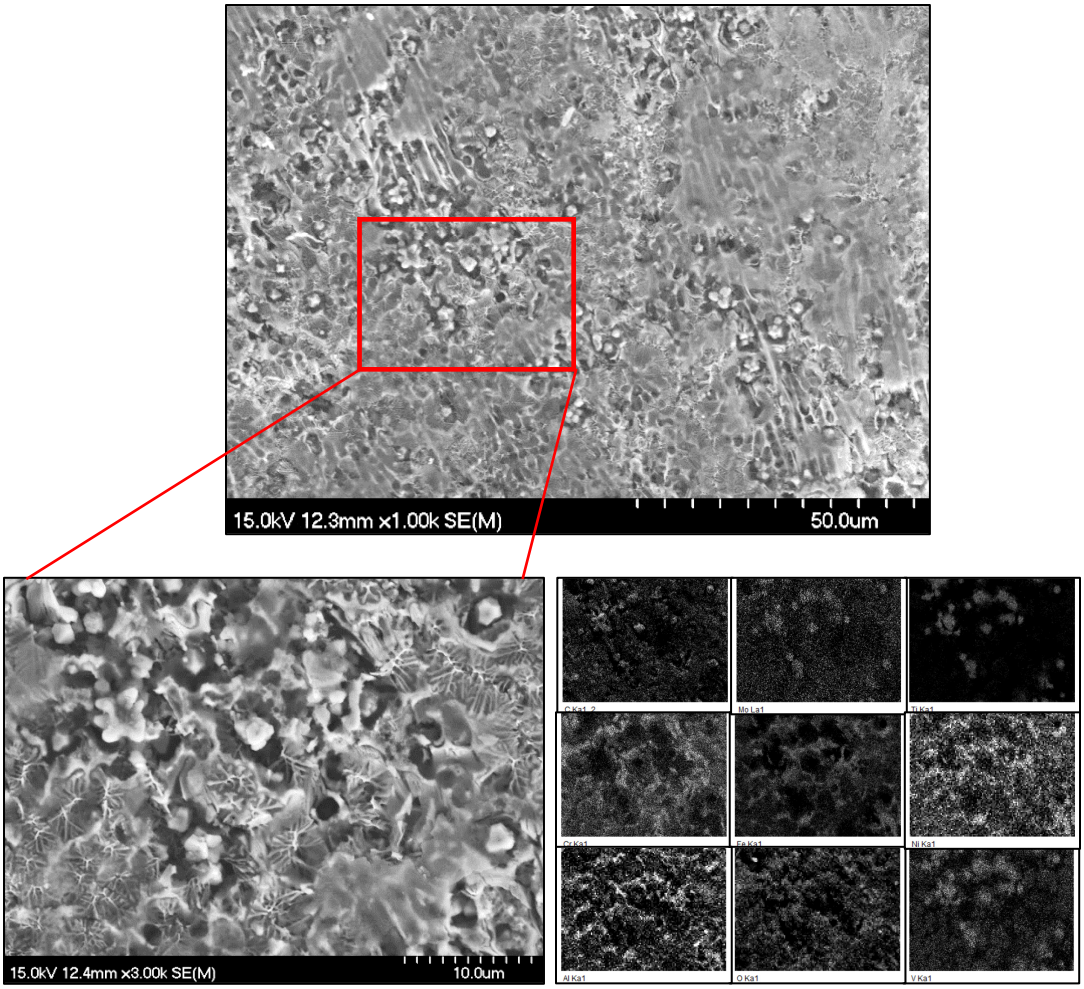

Element	C	O	Al	Si	Ti	V	Cr	Fe	Ni	Mo
Weight%	17.06	4.99	0.53	0.21	11.29	2.19	20.53	34.19	6.89	2.12
Atomic%	44.59	9.8	0.62	0.23	7.4	1.35	12.4	19.23	3.69	0.69

Figure 117. SEM micrographs obtained from post corrosion clad surfaces processed at P = 300 W and V = 3.38 mm/s and related compositional mapping generated through EDS. The associated EDS data, for the area shown, is presented in the table.

Moreover, the cross-sectional post corrosion microstructures confirmed that while anodic dissolution of the metallic phase is the basic form of the corrosion mechanism, due to galvanic attack, at lower scanning speeds a higher concentration of the Cr-rich grain

boundaries induces intragranular attack at localized Cr-depleted zones (Figure 118). Thus, the corrosive media will reach further into the coating structure, resulting in an increased rate of corrosion by removing larger volumes of the coating.

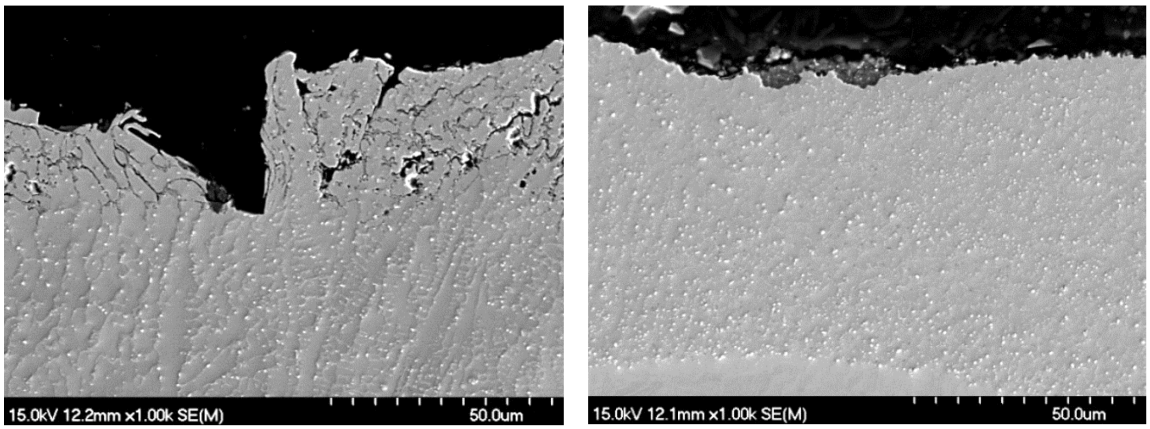

(a) (b)

Figure 118. Post-corrosion SEM images obtained from cross section of TiC-Ni_3Al (30 vol.%) metallic phase cermet clad coatings on D2 steel, fabricated at 350 W laser power, with: (a) 0.846 mm/s scanning speed, and (b) 1.69 mm/s scanning speed.

Figure 119 demonstrates the post-corrosion microstructure of the clad surfaces processed at P = 350 W and V = 3.38 mm/s. The post-corrosion morphologies clearly indicate formation of an unstable oxide layer, which is susceptible to corrosive attack at the location of galvanic couples formed as a result of the Cr segregation around the grain boundaries. As noted earlier, the highest level of elemental segregation was observed to arise at the lowest LDED scanning speed and, consequently, a larger volume of the metallic matrix has been subjected to Cr depletion. In contrast, fine TiC and Cr based precipitates form along the path of grain boundaries. The segregation of Cr near fine MC carbides has been proposed by Suzuki and colleagues [487]. Intragranular corrosion of ferritic steel

containing 11% Cr has also been reported previously, due to the formation of fine carbide precipitates at grain boundaries, and the associated creation of Cr depleted zones [485]. As highlighted in Figure 119(a), the post-polarisation surface contains a large crevice (area #1) along the solidification path of the overlapping clads, where longer cooling times result in further elemental segregation (shown in Figure 119(b)) and the formation of Cr depleted zones (Figure 119(c)). Higher magnification imaging (Figure 15) revealed that the crevice is formed from a number of microcracks within the oxide layer. The formation of Cr depleted zones, in particular, contributes to galvanic coupling of the metallic and ceramic phases within the composite coating. Eventually, a number of localized attack sites formed stable corrosion pits, due to anodic dissolution of Cr depleted zones in the vicinity of the carbide precipitates. An example of EDS mapping of the formed pits is provided in Figure 120.

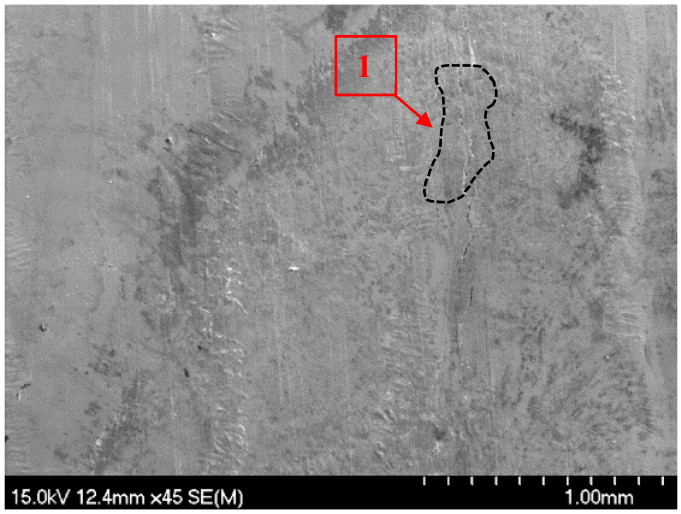

(a)

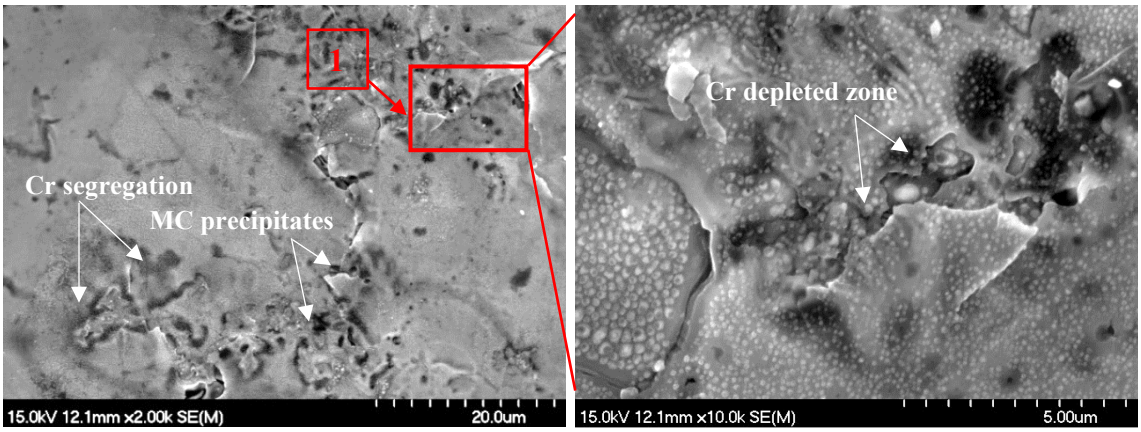

(b) (c)

Figure 119. SEM micrographs obtained from post corrosion surface of the TiC-Ni_3Al (30 vol%) clads on D2 steel processed at P = 350 W and V = 3.38 mm/s and after polarization to +1.0V vs. SCE in 3.5 wt% NaCl containing simulated seawater at various magnification (a), (b) and (c).

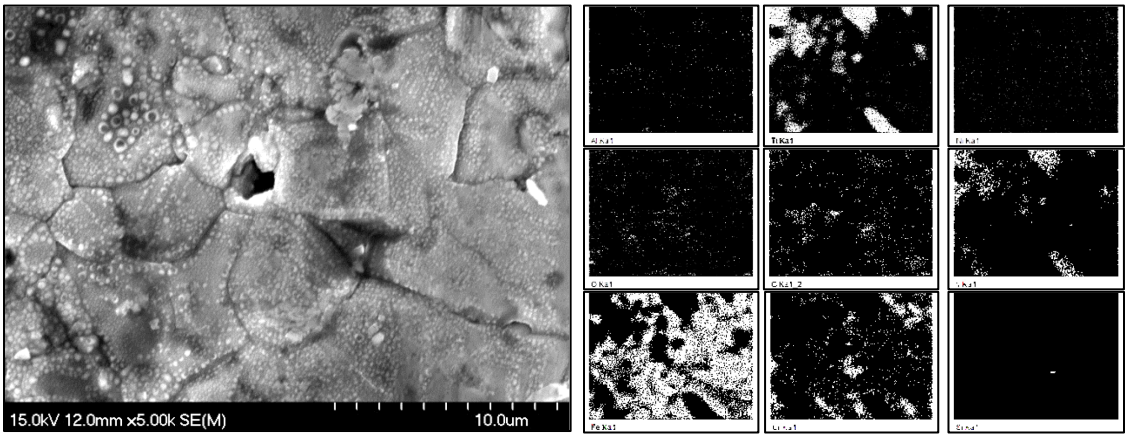

Figure 120. FE-SEM images and associated EDS mapping on the post-corrosion surface of a TiC-Ni_3Al (30 vol%) clads on D2 steel substrate, processed at P = 350 W and V = 3.38 mm/s, after polarization to +1.0 V vs. SCE in an aqueous solution containing 3.5 wt% NaCl.

Cross sectional microstructural analysis of the corroded composite clads revealed anodic dissolution of the Cr depleted metallic regions, adjacent to networks of segregated Cr containing and fine carbide precipitates (Figure 121). As it is demonstrated in this figure, after polarisation to +1.0 V vs. SCE, the the top portion of the clad has been subjected to a combination of intragranular and galvanic corrosion, to the depth of aproximately 50 μm. In this instance, disolution of the metallic compounds has left behind a semi-porous skeleton, that is now largely comprised of the hard ceramic phase. As a consequence, the overall system can be viewed as a porous electrode with different electrochemical activities between the bottom and the walls of the pits.

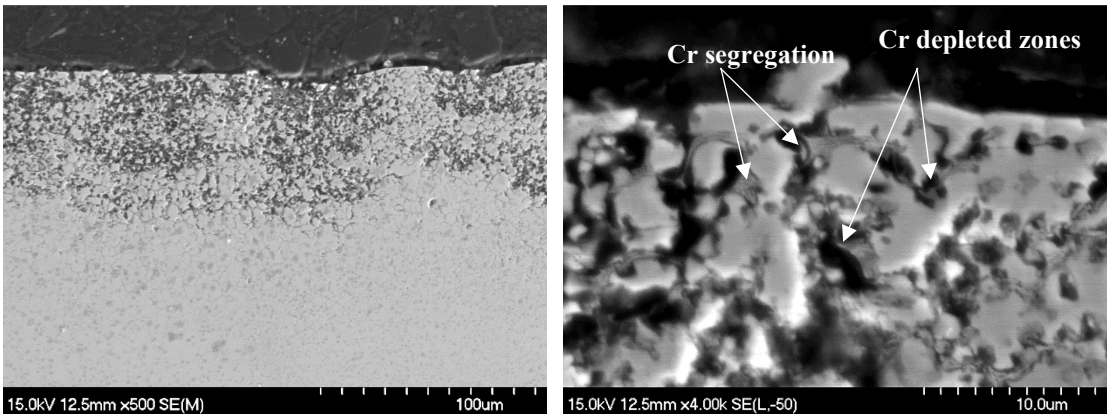

Figure 121. (a) Cross sectional FE_SEM image of the microstructure of the post-polarization TiC-based cermet clads on D2 steel, laser processed at P = 350 W, and V = 3.38 mm/s, after polarization to +1.0V vs. SCE in an aqueous solution containing 3.5 wt% NaCl. (b) Higher magnification FE-SEM image of the surface of the same sample as (a), showing Cr-rich and depleted zones.

Figure 122 shows an example of the post-corrosion microstructure of the clad surfaces processed with LDED conditions of P = 350 W and V = 6.77 mm/s. As anticipated from the results of the electrochemical measurements, clads fabricated under these described conditions displayed excellent protection against corrosion over the range of applied potentials. Nevertheless, the presence of defects and pores along the laser scan lines, which are formed during the LDED cladding process, permits the electrolyte to reach the inner layer of the composite clad and provide localized oxidation sites. The general surface of the clads fabricated at 6.77 mm/s laser scanning speed exhibited minimal variation of the surface roughness, while no local corrosion sites were detected under low magnification FE-SEM analysis.

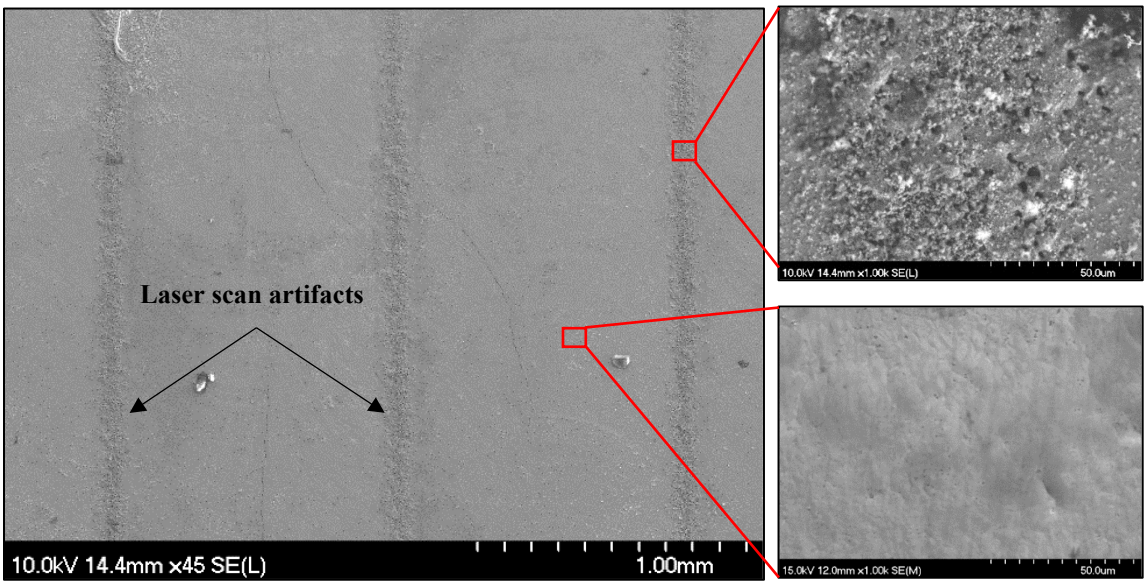

Figure 122. FE-SEM micrograph obtained from post corrosion surface of the TiC-Ni_3Al (30 vol%) clads on D2 steel processed at P = 350 W and V = 6.77 mm/s and after polarization to +1.0 V vs. SCE in an aqueous solution containing 3.5 wt% NaCl. The inset images show higher magnification FE-SEM images of areas relating to the laser scans.

Following from the images in Figure 122, Figure 123 presents a higher magnification FE-SEM image, along with related EDS compositional maps, of the post-corrosion surface of the TiC-Ni_3Al based clads LDED processed on D2 steel, after polarization to +1.0 V vs. SCE in 3.5 wt% NaCl containing water; in this instance the samples were laser processed at P = 350 W, and V = 6.77 mm/s. The results of compositional analysis of the post-corrosion surface, clad at 6.77 mm/s laser scan speed, reveals the occurrence of a multi-component oxide layer, based on α-Al_2O_3, Cr_2O_3, and NiO. Enhancement of corrosion properties by Al addition to stainless steels has been investigated in previous studies [488].

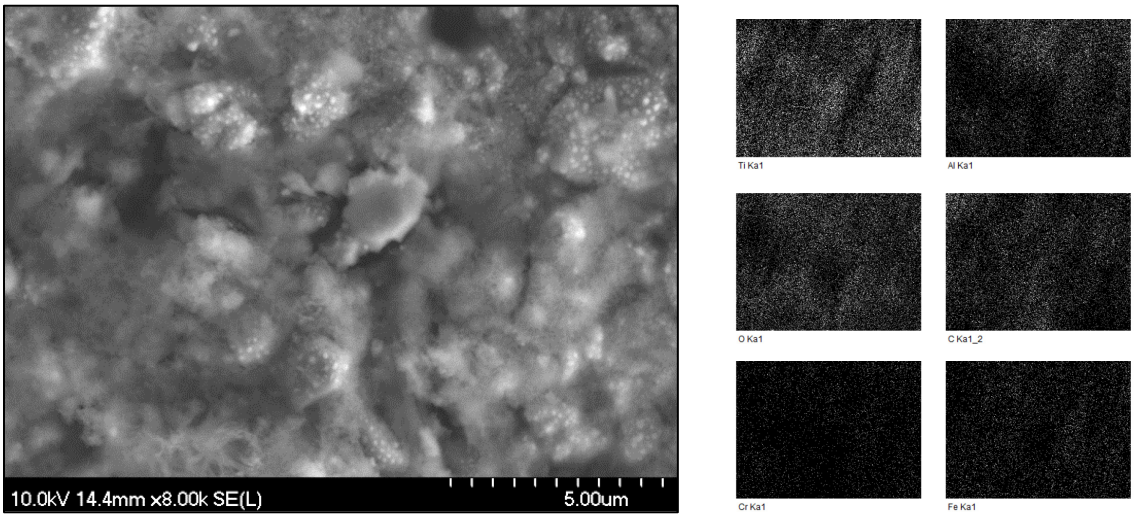

Element	C	O	Al	Si	Ti	Cr	Fe	Ni
Weight%	14.46	21.22	3.33	0.23	30.78	4.97	24.94	0.06
Atomic%	31.27	34.46	3.21	0.21	16.72	2.48	11.6	0.03

Figure 123. Higher magnification FE-SEM image of the post polarization surface of a TiC-Ni_3Al based clads on D2 steel, laser processed at P = 350 W, and V = 6.77 mm/s after polarization to +1.0 V vs. SCE in an aqueous 3.5 wt% NaCl containing solution. Also shown are examples of the EDS compositional maps obtained from the area shown in the FE-SEM image, along with the mean composition of the overall area.

Notably, Yun and colleagues reported that presence of the Al improved the adhesion of the oxide scale, through formation of oxide 'pegs' and a layer consisting of $(Cr,Al)_2O_3$ acting as a strong diffusion barrier [489].

Consequently it has been indicated that a surface Cr_2O_3-rich outer layer does not fully protect the metallic matrix from further oxidation, and the presence of Al in the composition of the layer significantly influences the corrosion resistance, due to the reaction of Al with oxygen for the formation of Al_2O_3 in the early stages of the corrosion reaction [490].

Examination of the cross sectional microstructure of the the TiC-Ni_3Al based clads deposited onto D2 steel (Figure 124) after polarization confirmed that achieving a submicron particle size, with minimal dendritic growth and an absence of elemental segregation, has resulted in the formation of dense oxide protective layer, with no evidence of corrosive media permeation; this sample was laser processed at $P = 350$ W and $V = 6.77$ mm/s,.

Furthermore, the results of compositional EDS analysis of the post-corrosion cross-section of the clad specimen processed under these conditions further confirms the formation of a dense, protective oxide layer that is based on α-Al_2O_3, Cr_2O_3, and NiO (Figure 125). It is clear from the comparison of processing effects that it is feasible with LDED to obtain highly corrosion protective coatings under carefully selected processing conditions, while at the same time retaining a fine carbide structure that will enhance wear resistance of the clad surface.

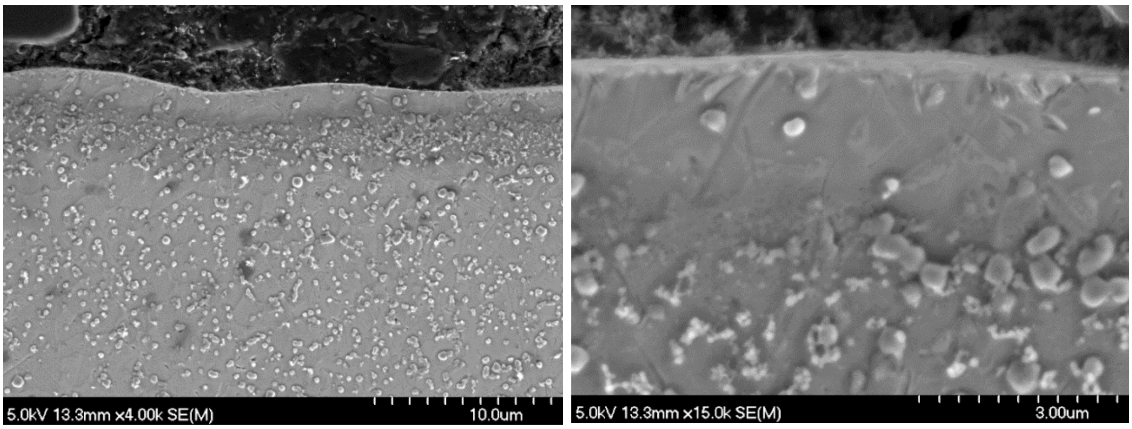

Figure 124. (a) FE-SEM image of the post-corrosion cross-section of the TiC-Ni_3Al cermet clads on D2 steel, laser processed at P = 350 W, V = 6.77 mm/s after polarization up to 1.0 V vs. SCE in an aqueous solution prepared with 3.5 wt% NaCl. (b) Higher magnification FE-SEM image of the surface cross-section of the same sample.

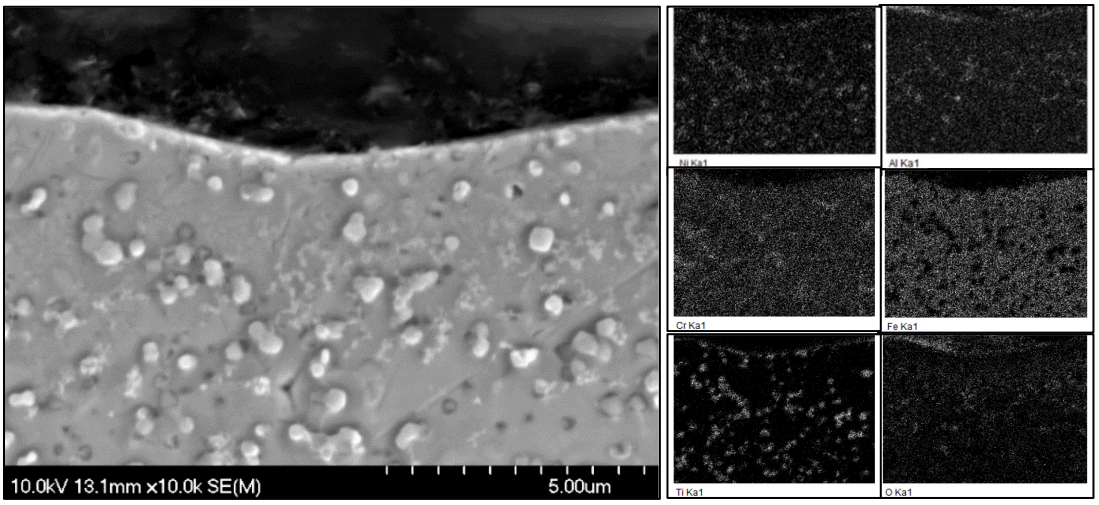

Figure 125. EDS compositional mapping of post corrosion cross section of the TiC-Ni_3Al cermet clads on D2 steel, laser processed at P = 350 W, V = 6.77 mm/s after polarization up to 1.0 V vs. SCE in an aqueous solution containing 3.5 wt% NaCl.

7.4. Conclusions

In present work, novel TiC-Ni_3Al based composite coatings, with enhanced corrosion resistance, were successfully manufactured through laser-based cladding of preplaced feedstock onto D2-grade tool steel substrates. The effects of the LDED processing parameters upon the aqueous corrosion behavior were subsequently studied. The findings from this work may be summarized as follows:

- A significant increase of the corrosion resistance of D2 tool steel in an 'artificial seawater' (containing 3.5 wt% NaCl) was obtained by fabrication of a composite structure with a heavily alloyed metallic matrix based on Ni_3Al, α-(Fe,Cr), and uniformly distributed TiC grains.
- A minimum coating thickness processed within the identified range of processing parameters, has been determined as a requirement to safeguard against degradation in corrosive media.
- Under identical corrosion testing conditions, the corroded D2 substrate only subjected to laser remelting (i.e., no cladding), showed the formation of Fe_2O_3 as the primary corrosion product. In contrast, the optimised laser clad steels exhibited a dense oxide layer based on α-Al_2O_3, Cr_2O_3, and NiO, which was repeteadly observed for a range of cladding parameters.
- Increased laser power resulted in increased *ED*, which led to a reduced surface roughness for *ED* up to ~257 J/mm^3 and clad thickness of ~140 μm, visibly improving the surface finish of the clad substrate.
- The corrosion resistance was found to be the greatest for the case of clad surfaces

processed under LDED conditions of P = 350 W and V = 6.77 mm/s. The general surface of the clads fabricated at 6.77mm/s laser scanning speed exhibited minimal variation of the surface roughness.

- The presence of defects and pores along the laser scan lines, which are formed during the cladding process itself, can potentially permit the electrolyte to reach the inner layer of the composite clad and therefore provide localized oxidation sites.
- Intragranular corrosion was induced as an artifact of laser processing by formation of Cr depletion zone due to Cr segregation within the grain boundaries.

Chapter 8. Conclusions

8.1. Research Outline

The main objectives of the current thesis were the design, development, and reliable/reproducible manufacture of novel TiC-Ni_3Al based composite feedstock and associated coatings. These materials are targeted at enhancement, modification, and/or repair of steel surfaces, with a view to improvement in the wear and/or corrosion properties of the substrate steel. Gelation-based fabrication with sodium alginate was proposed as an aid to preparation of aqueous TiC-Ni_3Al suspensions, comprised of micron-sized ceramic and metal particles, into either micron-sized spherical 'cermet' feed-stock powders or as a dip coating precursor. The physical attributes of the gelation-derived coatings were assessed for two deposition routes; (i) high velocity oxy-fuel (HVOF) thermal spraying, and (ii) laser directed energy deposition (DED). The research objectives were fulfilled by undertaking the following actions:

- The polysaccharide, sodium alginate, was examined as a gelation aid to 'solidify' aqueous TiC-Ni_3Al suspensions into micro-composite 'cermet' feedstock powders. A variety of gelation agents were examined, including calcium chloride ($CaCl_2$), calcium acetate, aluminium nitrate, methanol, acetic acid, and 5 % hydrochloric acid. Furthermore, a theoretical understanding of interparticle forces was gained through rheological assessment of the colloidal suspensions, both prior to and during the gelling stage. Subsequently, the spraying of sodium alginate containing ceramic-metal particle suspension was achieved with a suitable air atomising nozzle. Suspensions were sprayed into an aqueous bath, where replacement of Na^{1+}

within the alginate by Ca^{2+} results in cross-linking/gelation and the production of nominally spherical 'cermet' feedstock particles from the original sprayed droplets. With the intent of further optimization of the feed stock powder and improved flowability, the effects of pre-sintering heat treatments were also examined. As a preliminary 'proof-of-principle', these feedstock powders were subsequently used for the preparation of HVOF coatings and the associated optimization of the thermal spray process parameters (Section 3).

- Once the powder feedstock process was successfully developed, attention was placed on process development and characterization of the associated coatings. The fabricated feedstock particles, with sufficient mechanical strength in the gelled form, were subsequently fractionated into a narrow size range. These 'sized' micro-composite particles were subsequently used for HVOF thermal spray of TiC-Ni_3Al coatings onto a variety of substrates, including ferrous alloys; note that while these coatings were successfully sprayed onto Ti-6Al-4V and a variety of steel grades, only those HVOF deposited onto AISI 4130 steel substrates are discussed in the present thesis. The HVOF fabricated coatings then were characterized for their wear and corrosion properties, as a function of spraying 'stand-off' distance, and the results were compared to those obtained from HVOF coatings fabricated from a more conventionally produced TiC-Ni_3Al feedstock powder (i.e., agglomerated and sintered), together with both WC-Co and WC-CoCr HVOF deposited coatings (Section 4).
- For the laser DED cladding of TiC-Ni_3Al based composites onto D2 tool steel, a feedstock powder preplacement approach was proposed, in order to position the

feedstock material on the substrate prior to laser treatment. This was achieved by dip coating the substrate into an aqueous colloidal suspension, again containing sodium alginate. Initial emphasis was placed upon optimizing both the suspension and dip coating conditions, examining a variety of sodium alginate contents, suspension compositions (i.e., TiC:Ni_3Al volume ratios), suspension solids contents, and deposition temperatures. Once the dip coating process was optimized, a variety of laser DED fabrication conditions, as well as coating compositions, were then assessed via in depth macro and microstructural evaluation for the fabrication of the TiC-Ni_3Al clads onto D2 steel (Section 5). This allowed further optimization of the microstructural and mechanical characteristics of the laser DED clads, as discussed in subsequent chapters.

- Cermet-derived preplaced coatings were then subjected to a series of appropriate mechanical characterization techniques. These evaluation procedures included hardness, scratch hardness, and corrosion testing. The results were then summarized in relation to the impact of selected processing parameters utilised for the fabrication of the TiC-Ni_3Al composite clad coatings (Sections 6 and 7).

8.2. Conclusions

A number of general conclusions can be drawn from the present work, which are outlined in the following subsections:

8.2.1. Gelation based feed stock technologies for HVOF and DED deposited composite coatings

The polysaccharide sodium alginate was successfully used as a gelation aid to 'solidify' aqueous suspensions into micro-composite 'cermet' feedstock powders, which could be readily handled and subsequently classified (i.e., fractionated by size). An air atomising nozzle was used to produce these nominally spherical particles, with a mean size below 100 μm. The fabricated particles exhibited sufficient mechanical strength in their gelled form to be efficiently fractionated, by sieving, into relatively narrow size ranges and be used to produce high quality HVOF thermal spray coatings; typically, these would be sized between 45 and 75 μm, and were broadly spherical in shape.

A variety of alternative cross-linking agents were also examined for sodium alginate. In terms of the options evaluated, in addition to calcium chloride, calcium acetate, aluminium nitrate, methanol, acetic acid, and 5 % hydrochloric acid all allowed the production of roughly spherical gelled particles, at least on the macro scale; however, some of these particles were unstable and often exhibited degradation if rinsed with water. It was observed that particles made by air atomising spray technique can be sintered to improve their mechanical strength and flowability prior to subsequent HVOF processing. However, at elevated temperatures some localized 'necking' can occur between adjacent small

particles, resulting in the fabrication of non-spherical feedstock particles. This is undesirable in terms of powder flow characteristics. The theoretical perception of interparticle forces, which was obtained through rheological analysis, has also given some preliminary understanding of the physical process using one of the suggested chelating agents. However, to better understand the interaction of the particles within the gel systems there is a need for further analysis, such as direct force measurements, absorbed layer chemistry, and solution composition.

The fabricated feedstock particles were subsequently used for HVOF thermal spray of TiC-Ni_3Al coatings onto AISI 4130 steel substrates. The fabricated coatings were then characterized for their wear and corrosion properties as a function of spraying distance. It was demonstrated that TiC-based cermets, with a ductile Ni_3Al intermetallic matrix, offer a viable alternative for the development of high-performance wear and corrosion resistance hard coatings processed via HVOF. Notably, the gelation-based TiC-Ni_3Al coatings showed significantly better corrosion resistance than current industry standard WC-Co and WC-CoCr HVOF coatings, while maintaining similar wear resistance, and weighing only 50% of the WC-Co and WC-CoCr options.

In contrast, for laser DED prepared coatings, a preplacement approach was used to position the feedstock material prior to laser treatment. However, on this occasion a 'self-gelling' approach for the sodium alginate was employed, whereby Ni^{2+} and Al^{3+} are slowly leached from the TiC-Ni_3Al suspension (over a ~1 μm length scale), resulting in ion exchange with Na^{1+} and associated crosslinking/gelation.

Consequently, dip coating has been proposed as an efficient method for preplacement of feedstock material prior to laser processing. Successfully preplaced coatings were

subjected to DED and metallographic examination of cross sections of the single clad and its interface with the substrate were used to explain the quality of fabricated cermet coatings. Based on the results of the experimental observations, increasing laser power was found to increase the probability of forming a high quality clad, but it is not the only effective parameter.

8.2.2. Characterisation of the fabricated MMC coatings deposited by HVOF and DED

The aqueous corrosion resistance and tribological characteristics of TiC-Ni_3Al cermet coatings, fabricated via deposition of micro-composite gelation-based feedstock by high-velocity oxy-fuel (HVOF) thermal spray onto AISI 4130 steel substrates, was investigated. The results of this analysis were compared to coatings deposited from a TiC-Ni_3Al feedstock produced by a more typical 'agglomerated and sintered' route, processed under identical HVOF parameters and operational settings. Further, comparison was also made with more conventional WC-Co and WC-CoCr HVOF coatings. It was observed that the development-stage TiC-Ni_3Al based cermet coatings, regardless of their powder production route, provide a higher degree of aqueous corrosion resistance when compared to both WC based coatings, with the additional advantages of considerably lower density and an absence of Cr in their overall composition. However, the full passivation response of the TiC-Ni_3Al HVOF coatings was deterred by physical defects (i.e., residual porosity), which is associated with the preliminary, developmental stage of these coatings. Subsequently the calculated specific wear rates obtained from the examined HVOF

coatings based on TiC-Ni_3Al were compared closely with those frequently reported for WC-based thermal spray coatings. Cermet coatings fabricated using the commercially available TiC based feed stock material displayed slightly lower wear rates than the ones fabricated from the gelation-based feedstock material, which generally increased when the value of applied load was increased.

The efficiency of the proposed feedstock preplacement technique, prior to laser DED processing, and its impact on mechanical enhancement of D2 hard work tool steel surface, was validated by detailed structural characterization in relation to the laser processing parameters. In laser DED processing, the scan speed affects the dilution and cooling rate which are the two main factors in establishing the desired carbide morphology and microstructure. Moreover, it was observed that the heat generated by employing varied scan speeds results in different carbide morphologies and distributions. The observations show that cooling rate has the most dominant effect on the morphology and size of the TiC particles. Results of tensile failure analysis showed that the clad specimens possessed a very low elongation (<0.1%) and a low toughness (<43 J/m^3), although exhibiting an excellent tensile strength (up to 404.8 MPa). The low toughness in laser DED processed tensile parts can be attributed to the heterogeneous microstructures and grain size nucleated in different zones of the melt pool, which may lead to different extents of the strengthening effects. Substantial improvement in the microhardness properties of the clad D2 surface, relative to the unclad material, was reflected by results of micro-Vickers indentation. It was demonstrated that an increase in average hardness from 142.78 HV for as received substrate to 333.2 HV, was achieved, with further improvement under larger applied loads (up to 887.6 HV under 5 N). Moreover, the maximum values for VH were recorded at the

top surface of the examined cross section, with an average value of 659 VH (a roughly four times increase over the as-received substrate). In the middle section of the clad, a slight decrease in hardness value was observed. At the clad substrate interface 560 HV was reported for the applied load of 5 N. Substantial decrease in hardness was observed with increasing depth into the substrate, with respect to the clad surface, due to the reduced concentration of the hard carbide phases.

As a preliminary assessment of the tribological properties, and a qualitative evaluation of interfacial strength between coating and substrate material, single pass scratch testing was conducted on both the clad surface and the polished cross section of the cermet clads. This was found to be an effective technique for the determination of the wear-related failure modes and damage mechanisms. The post scratch morphologies of the cermet clads demonstrated that abrasive damage is generated within clad layer and progressed by plastic deformation through dislocations and associated lattice distortions. Within the range of 10-40 N applied normal force, the scratch hardness of the cermet clad coatings (Hs) varied within the range of 4.88-7.58 GPa, for coatings processed under various laser DED processing conditions. In comparison, the as-received D2 substrate exhibited a steady value of Hs ≈ 3 GPa. Mechanical performance of the modified D2 steel surfaces was found to vary considerably, depending on the implemented laser-processing parameters and its resultant solidified microstructure.

The electrochemical responses of the TiC based cermet clads revealed that addition of the cermet clad on D2 steel have clearly improved the corrosion behavior of the substrate by increasing the corrosion potential, E_{corr}, and decreasing the corrosion current, I_{corr}. Additionally, it was observed that variation of the laser processing parameters and

compositional content of the cermet feed, led to fabrication of clads with different thickness and thus various degrees of corrosion protection. Subsequent microstructural and compositional examination of the post-corroded sites at the surface and through the cross section of the post-polarized specimens identified the main corrosion mechanism as galvanic attack and failure of the in-service part due to dissolution of the metallic phase within the composition of the MMC clad coatings. This was generally similar to what has previously been observed for bulk TiC-Ni_3Al cermets and those deposited via HVOF, in terms of the primary corrosion mechanism. However, it was also apparent that elemental segregation of the metallic matrix, arising as a consequence of laser processing, may significantly influence the rate of galvanic attack, and increased dissolution of the metallic phase arises through the formation of numerous local and intragranular degradation sites with various electrochemical potentials through the thickness of the protective layer. A general overview summarizing the mechanical and electrochemical performance of the compositions fabricated throughout the presented work is provided in Table 22.

Table 22. Mechanical and electrochemical performance of cermet composites processed via various feed processing and sintering techniques [16,288,324,491].

	ID	Feedstock	Processing route	Corrosion rate (mm/year)	Wear rate$_{40N}$ (mm^3/Nm)	Hardness ($VH_{0.5}$)	Substrate
Bulk	**TiC-Ni_3Al (bulk)**	Ball milled	Press/sinter	3.1×10^{-4}	0.5×10^{-7}	-	N/A
	WC-Co (bulk)	-	Press/sinter	3.8×10^{-1}	0.2×10^{-7}	-	N/A
Lab-made	**TiC-Ni_3Al (coating)**	**Gel based powder**	**HVOF**	**4.1×10^{-2}**	**2.6×10^{-7}**	**320.40**	**4130**
	TiC-Ni_3Al (coating)	**Gel based suspension**	**DED**	**8.8×10^{-2}**	-	**612.16**	**D2**
Commercial	**TiC-Ni_3Al (coating)**	Agglomerate& sintered	HVOF	3.4×10^{-2}	1.3×10^{-7}	341.40	4130
	WC-Co (coating)	Agglomerate& sintered	HVOF	3.0×10^{-1}	9.8×10^{-8}	405.60	4130
	WC-CoCr (coating)	Agglomerate& sintered	HVOF	1.4×10^{-1}	8.2×10^{-8}	385.20	4130

8.3. Recommendations for future work

The current study included design, development, and manufacturing of gelation-based TiC-Ni_3Al composite feedstock materials, for subsequent HVOF and DED deposition routes. In both cases the processing parameters were optimised for application of wear and corrosion resistant protective coatings onto steel substrates with good physical properties. The impact of the evaluated coating deposition routes on the physical and electrochemical properties of the coatings was assessed via a number of micro- and macroanalysis methods. Based on the findings from this work, several additional future steps are suggested to increase the manufacturing capabilities and quality of the MMC coatings on steel substrates when used under harsh operational environments:

- Residual stress is important for the reliability of the coating/substrate system and its performance. Residual stresses in thermally deposited composite coatings originate from rapid heating and cooling rates that are experienced by the substrate/feedstock during and after deposition action, where thermal mismatch stress is developed due to the difference in thermal expansion between the coating and the substrate and can lead to cracking, delamination and destruction of the protective layer and may undermine the performance of the entire system and lead to limited fatigue life. As a consequence, it would be valuable to determine the residual stress state, and ideally its evolution as a function of processing route/stage, for both the HVOF and laser DED coatings. This can be potentially achieved through X-ray diffraction methods.

- During the high temperature processing of the ferrous alloys with high enough cooling rates, retained austenite will transform to martensite with a body centered tetragonal crystal structure, and a larger volume than the face centered cubic austenite which may lead to crack initiation within the body of the composite coatings. Therefore, implementation of heat treatment has been suggested to achieve low levels of retained austenite and fine austenitic grain sizes where finely dispersed grains prevent the nucleation of fatigue cracks. Such heat treatments are thus proposed for future work.
- Layer by layer deposition, by dip coating, for fabrication of thin films prior to laser cladding, was found an effective method for preplacement of added layer where maximum 'clad-able' thickness was obtained using minimum required feed and regardless of geometrical dimensions of the substrate. Nevertheless, once laser processed, the fabrication of clads with higher thickness can be accomplished by repetition of the preplacement rounds through dip coating and sequential LDED. Moreover, the assessment of alteration of the gel/feed-stock suspension(s) is recommended to allow the deposition of varying compositions in terms of feedstock layers with the potential then to generate functionally graded characteristics. It is to be determined if this can be achieved with multiple dip coating steps (i.e., sequentially modifying composition), followed by a single LDED treatment, or if multiple LDED cycles would be required; This will likely depend upon the individual dip coating layer thicknesses.
- In surface science, macroscopic processes such as wetting, adhesion, and friction are often correlated with the response of the surfaces at their molecular-level fine

structure. Moreover, atomic-scale crystallographic defects and potential irregularities within a crystal structure can immensely alter the performance of materials with novel functionalities. Therefore, use of nano-scale characterization techniques such as transmission electron microscopy (TEM) have previously been found critical for visual identification of the defects such as impurities, interstitial bodies, stacking faults, and their path of distribution. It is thus recommended that future work engages with this technique; it should be stressed that Dalhousie does not presently have a materials TEM.

- Microstructural examination of the cermet clads revealed the presence of multi-phase submicron crystalline structures where substantial variation of hardness were observed, depending on the location of indentation taking place on ceramic grains or metal matrix, which can be identified through nanoindentation technology. Subsequently, in terms of depth correlation of the hardness profile of the laser processed cermet clads, it is suggested that the possibility of work hardening occurs, which can be analysed via nanoindentation (for example, nanoindentation adjacent to macro-Vickers indentation). Such mechanical response can also be measured through cross sectional nanoindentation below the surface of scratch or wear tracks. Additionally, nanoindentation technology provides rate, temperature, and plasticity dependent measurement such as measurement of fracture toughness (i.e., with a cube-corner indenter geometry) which was not covered within the timeline of presented project.

References

[1] S.J. Algodi, J.W. Murray, P.D. Brown, A.T. Clare, Wear performance of TiC/Fe cermet electrical discharge coatings, Wear. 402–403 (2018) 109–123. doi:10.1016/j.wear.2018.02.007.

[2] L. Fouilland-Paille, S. Ettaqi, S. Benayoun, J.J.J. Hantzpergue, Structural and mechanical characterization of Ti/TiC cermet coatings synthesized by laser melting, Surf. Coatings Technol. 88 (1997) 204–211. doi:10.1016/S0257-8972(96)02925-8.

[3] M. Xiao, Y. Zhang, Y. Wu, Z. Qiu, C. Zhou, S. Zhuo, M. Liu, D. Zeng, Preparation, mechanical properties and enhanced wear resistance of TiC-Fe composite cermet coating, Int. J. Refract. Met. Hard Mater. 101 (2021) 105672. doi:10.1016/j.ijrmhm.2021.105672.

[4] J. Nie, Y. Wu, P. Li, H. Li, X. Liu, Morphological evolution of TiC from octahedron to cube induced by elemental nickel, CrystEngComm. 14 (2012) 2213–2221. doi:10.1039/c1ce06205k.

[5] R.L. Sun, J.F. Mao, D.Z. Yang, Microscopic morphology and distribution of TiC phase in laser clad NiCrBSiC-TiC layer on titanium alloy substrate, Surf. Coatings Technol. 155 (2002) 203–207. doi:10.1016/S0257-8972(02)00006-3.

[6] Y. Chen, H.M. Wang, Microstructure and wear resistance of a laser clad TiC reinforced nickel aluminides matrix composite coating, Mater. Sci. Eng. A. 368 (2004) 80–87. doi:10.1016/j.msea.2003.09.104.

[7] S. Zafar, A.K. Sharma, Development and characterisations of WC-12Co microwave clad, Mater. Charact. 96 (2014) 241–248. doi:10.1016/j.matchar.2014.08.015.

[8] S.Y. Yoon, S.Y. Yoon, W.S. Chung, K.H. Kim, Impact-wear behaviors of TiN and Ti-Al-N coatings on AISI D2 steel and WC-Co substrates, Surf. Coatings Technol. 177–178 (2004) 645–650. doi:10.1016/j.surfcoat.2003.08.067.

[9] D.K. Shetty, I.G. Wright, P.N. Mincer, A.H. Clauer, Indentation fracture of WC-Co cermets, J. Mater. Sci. 20 (1985) 1873–1882. doi:10.1007/BF00555296.

[10] S. Mi, T.H. Courtney, Synthesis of WC and WC-Co cermets by mechanical alloying and subsequent hot isostatic pressing, Scr. Mater. 38 (1997) 171–176. doi:10.1016/S1359-6462(97)00410-7.

[11] A.H. Dent, S. DePalo, S. Sampath, Examination of the wear properties of HVOF sprayed nanostructured and conventional WC-Co cermets with different binder phase contents, J. Therm. Spray Technol. 11 (2002) 551–558. doi:10.1361/105996302770348691.

[12] Q. Yang, W. Xiong, S. Zhou, M. Zhang, B. Huang, S. Chen, Magnetization of TiC–10TiN–xMC–yNi (MC = Mo2C, WC) cermets, Mater. Des. 115 (2017) 255–261. doi:10.1016/j.matdes.2016.11.026.

[13] P. Suresh Babu, Y. Madhavi, L. Rama Krishna, D. Srinivasa Rao, G. Padmanabham, Thermally-Sprayed WC-Based Cermet Coatings for Corrosion Resistance Applications, JOM. 70 (2018) 2636–2649. doi:10.1007/s11837-018-3131-6.

[14] A. Rajabi, M.J. Ghazali, J. Syarif, A.R. Daud, Development and application of tool wear: A review of the characterization of TiC-based cermets with different binders, Chem. Eng. J. 255 (2014) 445–452. doi:10.1016/j.cej.2014.06.078.

[15] S. Cardinal, A. Malchère, V. Garnier, G. Fantozzi, Microstructure and mechanical properties of TiC-TiN based cermets for tools application, Int. J. Refract. Met. Hard Mater. 27 (2009) 521–527. doi:10.1016/j.ijrmhm.2008.10.006.

[16] Z. Memarrashidi, K.P. Plucknett, The effects of C:N ratio on the aqueous corrosion response of TiC and Ti(C,N) cermets with a Ni_3Al-based binder, Int. J. Refract. Met. Hard Mater. 61 (2016) 162–172. doi:10.1016/j.ijrmhm.2016.09.010.

[17] P.F. Becher, K.P. Plucknett, Properties of Ni_3Al-bonded Titanium Carbide Ceramics, J. Eur. Ceram. Soc. 18 (1998) 395–400. doi:10.1016/S0955-2219(97)00124-6.

[18] J. Liu, TiC/Fe cermet coating by plasma cladding using asphalt as a carbonaceous precursor, Prog. Nat. Sci. 18 (2008) 447–454. doi:10.1016/j.pnsc.2007.12.004.

[19] Q. Wu, N. Zhong, B. Liu, C. Fan, W. Li, Y. Yin, Microstructure and corrosion behaviour of laser-clad TiC–Cr_7 C_3 –CNTs cermet coating on 304 stainless steel substrate, Corros. Eng. Sci. Technol. 51 (2016) 136–145. doi:10.1179/1743278215Y.0000000039.

[20] Y.P. Kathuria, Nd-YAG laser cladding of Cr_3C2 and TiC cerments, Surf. Coatings Technol. 140 (2001) 195–199. doi:10.1016/S0257-8972(01)01046-5.

[21] S. Yang, W. Liu, M. Zhong, Z. Wang, TiC reinforced composite coating produced by powder feeding laser cladding, Mater. Lett. 58 (2004) 2958–2962. doi:10.1016/j.matlet.2004.03.051.

[22] X.H. Wang, S.Y. Qu, B.S. Du, Z.D. Zou, In situ synthesised TiC particles reinforced Fe based composite coating produced by laser cladding, Mater. Sci. Technol. 25 (2009) 388–392. doi:10.1179/174328408X265631.

[23] K. Bochenek, M. Basista, Advances in processing of NiAl intermetallic alloys and composites for high temperature aerospace applications, Pergamon, 2015. doi:10.1016/j.paerosci.2015.09.003.

[24] B. Wang, S.W. Lee, Erosion-corrosion behaviour of HVOF NiAl-Al_2O_3 intermetallic-ceramic coating, Wear. 239 (2000) 83–90. doi:10.1016/S0043-1648(00)00309-4.

[25] N. Abu-warda, M.D. López, M. V. Utrilla, High temperature corrosion and wear behavior of HVOF-sprayed coating of Al_2O_3-NiAl on AISI 304 stainless steel, Surf. Coatings Technol. 359 (2019) 35–46. doi:10.1016/j.surfcoat.2018.12.047.

[26] E.P. Busso, F.A. McClintock, Mechanisms of cyclic deformation of NiAl single crystals at high temperatures, Acta Metall. Mater. 42 (1994) 3263–3275. doi:10.1016/0956-7151(94)90459-6.

[27] G.K. Dey, Physical metallurgy of nickel aluminides, Sadhana - Acad. Proc. Eng. Sci. 28 (2003) 247–262. doi:10.1007/BF02717135.

[28] C.P. Bergmann, J. Vicenzi, Protection against Erosive Wear Using Thermal Sprayed Cermet: A Review, in: Prot. against Erosive Wear Using Therm. Sprayed Cermet, Springer, Berlin, Heidelberg, 2011: pp. 1–77. doi:10.1007/978-3-642-21987-0_1.

[29] G. Cliche, S. Dallaire, Synthesis and deposition of TiC-Fe coatings by plasma spraying, Surf. Coatings Technol. 46 (1991) 199–206. doi:10.1016/0257-8972(91)90162-P.

[30] N.J. Archer, The plasma-assisted chemical vapour deposition of TiC, TiN and TiCxN1-x, Thin Solid Films. 80 (1981) 221–225. doi:10.1016/0040-6090(81)90225-X.

[31] J. Xu, B. Zou, S. Tao, M. Zhang, X. Cao, Fabrication and properties of Al_2O_3–TiB_2–TiC/Al metal matrix composite coatings by atmospheric plasma spraying of SHS powders, J. Alloys Compd. 672 (2016) 251–259. doi:10.1016/j.jallcom.2016.02.116.

[32] S. Dilek, H. Algül, A. Akyol, A. Alp, H. Akbulut, M. Uysal, Pulse electro co-deposition of submicron-sized TiC reinforced Ni–W coatings: tribological and corrosion properties, J. Asian Ceram. Soc. 9 (2021) 673–685. doi:10.1080/21870764.2021.1911058.

[33] C. Ma, D. Zhao, W. Liu, F. Xia, P. Jin, C. Sun, Magnetic assisted pulse electrodeposition and characterization of Ni–TiC nanocomposites, Ceram. Int. 46 (2020) 17631–17639. doi:10.1016/j.ceramint.2020.04.065.

[34] N. Selvakumar, H.C. Barshilia, Review of physical vapor deposited (PVD) spectrally selective coatings for mid- and high-temperature solar thermal applications, Sol. Energy Mater. Sol. Cells. 98 (2012) 1–23. doi:10.1016/j.solmat.2011.10.028.

[35] J. Singh, D.E. Wolfe, Nanostructured component fabrication by electron beam-physical vapor deposition, in: J. Mater. Eng. Perform., Springer, 2005: pp. 448–459. doi:10.1361/105994905X56223.

[36] J. Singh, F. Quli, D.E. Wolfe, J. Schriempf, An Overview: Electron Beam-Physical Vapor Deposition Technology-Present and Future Applications, Surf. Eng. Sci. Technol. I. (1999) 59–74. http://www.p2pays.org/ref%5C02/01162.pdf (accessed February 14, 2023).

[37] W. Schintlmeister, W. Wallgram, J. Kanz, K. Gigl, Cutting tool materials coated by chemical vapour deposition, Wear. 100 (1984) 153–169. doi:10.1016/0043-1648(84)90011-5.

[38] M. Azadi, A.S. Rouhaghdam, S. Ahangarani, H.H. Mofidi, Mechanical behavior of TiN/TiC multilayer coatings fabricated by plasma assisted chemical vapor deposition on AISI H13 hot work tool steel, Surf. Coatings Technol. 245 (2014) 156–166. doi:10.1016/j.surfcoat.2014.02.055.

[39] C.R. Ciubotariu, D. Frunzeverde, G. Merginean, V.A. Serban, A.V. Bîrdeanu, Optimization of the laser remelting process for HVOF-sprayed Stellite 6 wear resistant coatings, Opt. Laser Technol. 77 (2016) 98–103. doi:10.1016/j.optlastec.2015.09.005.

[40] L.R. Liu, T. Jin, N.R. Zhao, X.F. Sun, H.R. Guan, Z.Q. Hu, L.R. Liu, T. Jin, N.R. Zhao, X.F. Sun, H.R. Guan, Z.Q. Hu, Formation of carbides and their effects on stress rupture of a Ni-base single crystal superalloy, Mater. Sci. Eng. A. 361 (2003) 191–197. doi:10.1016/S0921-5093(03)00517-3.

[41] M. Jones, a. . J. Horlock, P.. H. Shipway, D.. G. McCartney, J.. V. Wood, A comparison of the abrasive wear behaviour of HVOF sprayed titanium carbide- and titanium boride-based cermet coatings, Wear. 250 (2001) 1009–1016. doi:10.1016/S0043-1648(01)00702-5.

[42] D. Chuanxian, H. Bingtang, L. Huiling, Plasma-sprayed wear-resistant ceramic and cermet coating materials, Thin Solid Films. 118 (1984) 485–493. doi:10.1016/0040-6090(84)90277-3.

[43] M. Mohanty, R.W. Smith, M. De Bonte, J.P. Celis, E. Lugscheider, Sliding wear behavior of thermally sprayed 75/25 Cr3C2/NiCr wear resistant coatings, Wear. 198 (1996) 251–266. doi:10.1016/0043-1648(96)06983-9.

[44] B. Gérard, Application of thermal spraying in the automobile industry, Surf. Coatings Technol. 201 (2006) 2028–2031. doi:10.1016/j.surfcoat.2006.04.050.

[45] J.M. Guilemany, J. Nutting, N. Llorca-Isern, Microstructural examination of HVOF chromium carbide coatings for high-temperature applications, J. Therm. Spray Technol. 5 (1996) 483–489. doi:10.1007/BF02645280.

[46] L. Hirt, A. Reiser, R. Spolenak, T. Zambelli, Additive Manufacturing of Metal Structures at the Micrometer Scale, Adv. Mater. 29 (2017) 1604211. doi:10.1002/adma.201604211.

[47] L. Yang, O. Harrysson, D. Cormier, H. West, H. Gong, B. Stucker, Additive Manufacturing of Metal Cellular Structures: Design and Fabrication, JOM. 67 (2015) 608–615. doi:10.1007/s11837-015-1322-y.

[48] C.A. Terrazas, S.M. Gaytan, E. Rodriguez, D. Espalin, L.E. Murr, F. Medina, R.B. Wicker, Multi-material metallic structure fabrication using electron beam melting, Int. J. Adv. Manuf. Technol. 71 (2014) 33–45. doi:10.1007/s00170-013-5449-0.

[49] A. Angrish, A critical analysis of additive manufacturing technologies for aerospace applications, in: IEEE Aerosp. Conf. Proc., IEEE Computer Society, 2014. doi:10.1109/AERO.2014.6836456.

[50] G. Wu, Y. Hu, W. Zhu, C. Song, H. Han, Research status and development trend of laser additive manufacturing technology, in: Proc. - 2017 4th Int. Conf. Inf. Sci. Control Eng. ICISCE 2017, Springer London, 2017: pp. 1210–1213. doi:10.1109/ICISCE.2017.251.

[51] S. Bengtsson, S. Dizdar, K. Gong, Dry-sliding wear of laser clad nickel aluminide/chromium carbide coatings against cast iron, in: Proc. Int. Therm. Spray Conf., 2017: pp. 184–189. https://www.hoganas.com/globalassets/download-media/technical-papers/sco/pm17_13_itsc2017_dry_sliding_wear_of_laser_clad_bengtsson.pdf (accessed June 24, 2020).

[52] D. Verdi, C.J. Múnez, M.A. Garrido, P. Poza, Process parameter selection for Inconel 625-Cr_3C_2 laser cladded coatings, Int. J. Adv. Manuf. Technol. 92 (2017) 3033–3042. doi:10.1007/s00170-017-0372-4.

[53] A. Emamian, S.F. Corbin, A. Khajepour, Tribology characteristics of in-situ laser deposition of Fe-TiC, Surf. Coatings Technol. 206 (2012) 4495–4501. doi:10.1016/j.surfcoat.2012.01.051.

[54] E.S. Processes, T. Cold, S. Process, V. Low, P. Plasma, T.S. Markets, S. Manufacture, A.G. Turbines, Key Research Challenges in Thermal Spray Science and Technology, Therm. Spray Technol. (2022) 20–29. doi:10.31399/asm.tb.tstap.t56040020.

[55] Specifications and Standards - Thermal Spray Society, (n.d.). https://www.asminternational.org/web/tss/technical/specifications (accessed March 14, 2023).

[56] S. Liu, Y. Zhang, R. Kovacevic, Numerical Simulation and Experimental Study of Powder Flow Distribution in High Power Direct Diode Laser Cladding Process, Lasers Manuf. Mater. Process. 2 (2015) 199–218. doi:10.1007/s40516-015-0015-2.

[57] D. Poirier, J.G. Legoux, P. Vo, B. Blais, J.D. Giallonardo, P.G. Keech, Powder Development and Qualification for High-Performance Cold Spray Copper Coatings on Steel Substrates, J. Therm. Spray Technol. 28 (2019) 444–459. doi:10.1007/s11666-019-00833-9.

[58] A. Memarpour, V. Brabie, P. Jönsson, Studies of effect of glass/silicon powder coatings on clogging behaviour of submerged entry nozzles when using REM alloyed stainless steels, Ironmak. Steelmak. 38 (2011) 229–239. doi:10.1179/1743281210Y.0000000005.

[59] L.M. Berger, Application of hardmetals as thermal spray coatings, Int. J. Refract. Met. Hard Mater. 49 (2015) 350–364. doi:10.1016/j.ijrmhm.2014.09.029.

[60] A. Nouri, A. Sola, Powder morphology in thermal spraying, J. Adv. Manuf. Process. 1 (2019) e10020. doi:10.1002/amp2.10020.

[61] A. Ikesue, Y. Lin Aung, (No Title), 2008. www.nature.com/naturephotonics.

[62] J. Sanghera, W. Kim, G. Villalobos, B. Shaw, C. Baker, J. Frantz, B. Sadowski, I. Aggarwal, Ceramic laser materials: Past and present, Opt. Mater. (Amst). 35 (2013) 693–699. doi:10.1016/j.optmat.2012.04.021.

[63] J. Sanghera, W. Kim, G. Villalobos, B. Shaw, C. Baker, J. Frantz, B. Sadowski, I. Aggarwal, Ceramic laser materials, Materials (Basel). 5 (2012) 258–277. doi:10.3390/ma5020258.

[64] Q. Yang, T. Senda, A. Ohmori, Effect of carbide grain size on microstructure and sliding wear behavior of HVOF-sprayed WC-12% Co coatings, Wear. 254 (2003) 23–34. doi:10.1016/S0043-1648(02)00294-6.

[65] D. a. Stewart, P.H. Shipway, D.G. McCartney, Abrasive wear behaviour of conventional and nanocomposite HVOF-sprayed WC–Co coatings, Wear. 225–229 (1999) 789–798. doi:10.1016/S0043-1648(99)00032-0.

[66] H.. Hawthorne, B. Arsenault, J.. Immarigeon, J.. Legoux, V.. Parameswaran, Comparison of slurry and dry erosion behaviour of some HVOF thermal sprayed coatings, Wear. 225–229 (1999) 825–834. doi:10.1016/S0043-1648(99)00034-4.

[67] L. Russo, M.D.-H.T.S. of Japan, U. 1995, Thermal spraying: current status and future trends, (n.d.).

[68] L.M. Berger, P. Vuoristo, T. Mantyla, W. Gruner, A study of oxidation behaviour of WC-Co, Cr_3C_2-NiCr and TiC-Ni-based materials in thermal spray processes, in: Proc. Fifteenth Int. Therm. Spray Conf. Nice, Fr., 1998: pp. 75–82.

[69] R. Nieminen, K. Vuoristo, K. Neimi, T. Mantyla, Thermal Spray Science and Technology, 1995.

[70] J.R. Davis, Handbook of Thermal Spray Technology, 2004. https://web-p-ebscohost-com.ezproxy.library.dal.ca/ehost/ebookviewer/ebook/ZTA (accessed February 21, 2023).

[71] D.W. PARKER, G.L. KUTNER, HVOF-spray technology : poised for growth, Adv. Mater. Process. 139 (1991) 68–74.

[72] B.Q. Wang, A. Verstak, Elevated temperature erosion of HVOF Cr_3C_2/TiC-NiCrMo cermet coating, in: Wear, Elsevier, 1999: pp. 342–351. doi:10.1016/S0043-1648(99)00242-2.

[73] Y. Zhao, M. Lu, Z. Fan, P. McCormick, Q. Tan, N. Mo, H. Huang, Microstructures and mechanical properties of wear-resistant titanium oxide coatings deposited on Ti-6Al-4V alloy using laser cladding, J. Eur. Ceram. Soc. 40 (2020) 798–810. doi:10.1016/j.jeurceramsoc.2019.10.037.

[74] J.M. Lourenço, S. Da Sun, K. Sharp, V. Luzin, A.N. Klein, C.H. Wang, M. Brandt, Fatigue and fracture behavior of laser clad repair of AerMet® 100 ultra-high strength steel, Int. J. Fatigue. 85 (2016) 18–30. doi:10.1016/j.ijfatigue.2015.11.021.

[75] Q. Wu, W. Li, N. Zhong, W. Gang, W. Haishan, Microstructure and wear behavior of laser cladding VC-Cr7C3 ceramic coating on steel substrate, Mater. Des. 49 (2013) 10–18. doi:10.1016/j.matdes.2013.01.067.

[76] B. Du, Z. Zou, X. Wang, S. Qu, Laser cladding of in situ TiB_2 /Fe composite coating on steel, Appl. Surf. Sci. 254 (2008) 6489–6494. doi:10.1016/j.apsusc.2008.04.051.

[77] A. Aramian, S.M.J. Razavi, Z. Sadeghian, F. Berto, A review of additive manufacturing of cermets, Addit. Manuf. 33 (2020) 101130. doi:10.1016/j.addma.2020.101130.

[78] L. Lu, J.Y.H. Fuh, Z.D. Chen, C.C. Leong, Y.S. Wong, In situ formation of TiC composite using selective laser melting, Mater. Res. Bull. 35 (2000) 1555–1561. doi:10.1016/S0025-5408(00)00339-1.

[79] Y. Zhao, T. Yu, J. Sun, S. Jiang, Microstructure and properties of laser cladded B4C/TiC/Ni-based composite coating, Int. J. Refract. Met. Hard Mater. 86 (2020) 105112. doi:10.1016/j.ijrmhm.2019.105112.

[80] S.A.M. Tofail, E.P. Koumoulos, A. Bandyopadhyay, S. Bose, L. O'Donoghue, C. Charitidis, Additive manufacturing: scientific and technological challenges, market uptake and opportunities, Mater. Today. 21 (2018) 22–37. doi:10.1016/j.mattod.2017.07.001.

[81] A. Vafadar, F. Guzzomi, A. Rassau, K. Hayward, Advances in metal additive manufacturing: A review of common processes, industrial applications, and current challenges, Appl. Sci. 11 (2021) 1–33. doi:10.3390/app11031213.

[82] I.E. Anderson, E.M.H. White, R. Dehoff, Feedstock powder processing research needs for additive manufacturing development, Curr. Opin. Solid State Mater. Sci. 22 (2018) 8–15. doi:10.1016/j.cossms.2018.01.002.

[83] M. Cauchetier, O. Croix, M. Luce, M. Michon, J. Paris, S. Tistchenko, Laser synthesis of ultrafine powders, Ceram. Int. 13 (1987) 13–17. doi:10.1016/0272-8842(87)90033-2.

[84] M. Bhuvanesh Kumar, P. Sathiya, Methods and materials for additive manufacturing: A critical review on advancements and challenges, Thin-Walled Struct. 159 (2021) 107228. doi:10.1016/j.tws.2020.107228.

[85] S. Amin, H. Panchal, A. Professor, A Review on Thermal Spray Coating Processes, Int. J. Curr. Trends Eng. Res. Sci. J. Impact Factor. 2 (2016) 556–563. http://www.ijcter.com (accessed February 18, 2023).

[86] C.J. Li, Y.Y. Wang, Effect of particle state on the adhesive strength of HVOF sprayed metallic coating, J. Therm. Spray Technol. 11 (2002) 523–529. doi:10.1361/105996302770348655.

[87] A. Ohmori, Thermal spray technology, Japanese J. Tribol. 41 (1996) 1192–1203. www.asminternational.org (accessed February 20, 2023).

[88] G. Bolelli, L. Lusvarghi, T. Varis, E. Turunen, M. Leoni, P. Scardi, C.L. Azanza-Ricardo, M. Barletta, Residual stresses in HVOF-sprayed ceramic coatings, Surf. Coatings Technol. 202 (2008) 4810–4819. doi:10.1016/j.surfcoat.2008.04.066.

[89] A.S.M. Ang, C.C. Berndt, A review of testing methods for thermal spray coatings, Int. Mater. Rev. 59 (2014) 179–223. doi:10.1179/1743280414Y.0000000029.

[90] S. Kuroda, Y. Tashiro, H. Yumoto, S. Taira, H. Fukanuma, Peening action and residual stresses in HVOF thermal spraying of 316L stainless steel, in: Proc. Int. Therm. Spray Conf., Springer, 1998: pp. 569–574. doi:10.31399/asm.cp.itsc1998p0569.

[91] J. Pina, A. Dias, J.L. Lebrun, Study by X-ray diffraction and mechanical analysis of the residual stress generation during thermal spraying, Mater. Sci. Eng. A. 347 (2003) 21–31. doi:10.1016/S0921-5093(02)00580-4.

[92] M. Li, P.D. Christofides, Multi-scale modeling and analysis of an industrial HVOF thermal spray process, Chem. Eng. Sci. 60 (2005) 3649–3669. doi:10.1016/j.ces.2005.02.043.

[93] I.A. Alnaser, M. Yunus, R. Alfattani, T. Alamro, High-temperature corrosion of aps- and hvof-coated nickel-based super alloy under air oxidation and melted salt domains, Materials (Basel). 14 (2021) 5119. doi:10.3390/ma14185119.

[94] J. Stokes, L. Looney, HVOF system definition to maximise the thickness of formed components, Surf. Coatings Technol. 148 (2001) 18–24. doi:10.1016/S0257-8972(01)01272-5.

[95] S. Vignesh, K. Shanmugam, V. Balasubramanian, K. Sridhar, Identifying the optimal HVOF spray parameters to attain minimum porosity and maximum hardness in iron based amorphous metallic coatings, Def. Technol. 13 (2017) 101–110. doi:10.1016/j.dt.2017.03.001.

[96] Z.Y. Taha-al, M.S. Hashmi, B.S. Yilbas, Effect of WC on the residual stress in the laser treated HVOF coating, J. Mater. Process. Technol. 209 (2009) 3172–3181. doi:10.1016/j.jmatprotec.2008.07.027.

[97] L. Lohmann, An overview of industrial tree, (2012).

[98] R.D. Holbrook, A.A. Galyean, J.M. Gorham, A. Herzing, J. Pettibone, Overview of Nanomaterial Characterization and Metrology, in: Front. Nanosci., Elsevier, 2015: pp. 47–87. doi:10.1016/B978-0-08-099948-7.00002-6.

[99] ASTM E2109-01, Standard Test Methods for Determining Area Percentage Porosity in Thermal Sprayed Coatings, in: Stand. Test Methods Determ. Area Percent. Porosity Therm. Sprayed Coatings, 2006. https://www-astm-org.ezproxy.library.dal.ca/e2109-01r21.html (accessed March 15, 2023).

[100] I.Y. Konyashin, T. V. Chukalovskaya, A technique for measurement of porosity in protective coatings, Surf. Coatings Technol. 88 (1997) 5–11. doi:10.1016/S0257-8972(95)02758-0.

[101] G.S. Schajer, Hole-drilling residual stress measurements at 75: Origins, advances, opportunities, Exp. Mech. 50 (2010) 245–253. doi:10.1007/s11340-009-9285-y.

[102] J. GUO, H. FU, B. PAN, R. KANG, Recent progress of residual stress measurement methods: A review, Chinese J. Aeronaut. 34 (2021) 54–78. doi:10.1016/j.cja.2019.10.010.

[103] S.T. Method, Standard Test Method for Adhesion or Cohesion Strength of Thermal Spray Coatings 1, Current. 03 (2001) 1–7.

[104] K.A. Harries, M.E. Sweriduk, Factors affecting direct tension pull-off test results of materials bonded to concrete, Adv. Civ. Eng. Mater. 5 (2016) 353–370. doi:10.1520/ACEM20160046.

[105] S. Siegmann, M. Dvorak, H. Grützner, K. Nassenstein, A. Walter, Shear Testing for Characterizing the Adhesive and Cohesive Coating Strength Without the Need of Adhesives, in: Therm. Spray 2005 Proc. from Int. Therm. Spray Conf., ASM International, 2005: pp. 823–829. doi:10.31399/asm.cp.itsc2005p0823.

[106] M. Sexsmith, T. Troczynski, Peel adhesion test for thermal spray coatings, J. Therm. Spray Technol. 3 (1994) 404–411. doi:10.1007/BF02658986.

[107] ISO, ISO 27307-15 - Thermal spraying, evaluation of adhesion/cohesion of thermal sprayed ceramic coatings by transverse scratch testing, 2015. https://www.iso.org/standard/51692.html (accessed January 23, 2023).

[108] ASTM, ASTM G 171 - Standard Test Method for Scratch Hardness of Materials Using a Diamond Stylus 1, Annu. B. ASTM Stand. 03 (2009) 1–7. doi:10.1520/G0171-03R17.2.

[109] S.J. Bull, E.G. Berasetegui, An overview of the potential of quantitative coating adhesion measurement by scratch testing, Tribol. Int. 39 (2006) 99–114. doi:10.1016/j.triboint.2005.04.013.

[110] G. Marot, J. Lesage, P. Démarécaux, M. Hadad, S. Siegmann, M.H. Staia, Interfacial indentation and shear tests to determine the adhesion of thermal spray coatings, Surf. Coatings Technol. 201 (2006) 2080–2085. doi:10.1016/j.surfcoat.2006.04.046.

[111] A. International, Standard Test Methods for Vickers Hardness and Knoop Hardness of Metallic Materials, ASM Int. (2017) 1–27. https://www-astm-org.ezproxy.library.dal.ca/e0092-17.html (accessed March 15, 2023).

[112] ASTM G99, Standard Test Method for Wear Testing with a Pin-on-Disk Standard Test Method for Wear Testing with a Pin-on-Disk Apparatus, ASTM Int. 14 (2017) 1–6. https://www-astm-org.ezproxy.library.dal.ca/g0099-17.html (accessed March 16, 2023).

[113] ASTM D4060, Standard Test Method for Abrasion Resistance of Organic Coatings by the Taber Abraser, 2014. https://www-astm-org.ezproxy.library.dal.ca/d4060-19.html (accessed March 16, 2023).

[114] E. Celik, I. Ozdemir, E. Avci, Y. Tsunekawa, Corrosion behaviour of plasma sprayed coatings, Surf. Coatings Technol. 193 (2005) 297–302. doi:10.1016/j.surfcoat.2004.08.143.

[115] D. Toma, W. Brandl, G. Marginean, Wear and corrosion behaviour of thermally sprayed cermet coatings, Surf. Coatings Technol. 138 (2001) 149–158. doi:10.1016/S0257-8972(00)01141-5.

[116] ASTM B117-19, Standard Practice for Operating Salt Spray (FOG) Apparatus., Water. 03 (2003) 1–15. https://www-astm-org.ezproxy.library.dal.ca/b0117-19.html (accessed March 16, 2023).

[117] R.C. Tucker, Introduction to Coating Design and Processing, ASM Handbook, Therm. Spray Technol. 5A (2013) 76–88. www.asminternational.org (accessed February 24, 2023).

[118] D.J. Varacalle, D.P. Guillen, D.M. Deason, W. Rhodaberger, E. Sampson, Effect of grit-blasting on substrate roughness and coating adhesion, J. Therm. Spray Technol. 15 (2006) 348–355. doi:10.1361/105996306X124347.

[119] J.A. Gan, C.C. Berndt, Nanocomposite coatings: Thermal spray procebing, microstructure and performance, Int. Mater. Rev. 60 (2015) 195–244. doi:10.1179/1743280414Y.0000000048.

[120] H. Chen, A. Rushworth, Effects of oxide stringers on the β-phase depletion behaviour in thermally sprayed CoNiCrAlY coatings during isothermal oxidation, J. Mater. Sci. Technol. 45 (2020) 108–116. doi:10.1016/j.jmst.2019.11.018.

[121] M. Gaier, T.Z.Z. Todorova, Z. Russell, Z.N.N. Farhat, J.W.W. Zwanziger, K.P.P. Plucknett, The influence of intermetallic ordering on wear and indentation properties of TiC-Ni_3 Al cermets, Wear. 426–427 (2019) 390–400. doi:10.1016/j.wear.2018.12.034.

[122] K.P. Plucknett, C. Jin, C.C. Onuoha, T.L. Stewart, Z. Memarrashidi, The sliding wear response of high-performance cermets, in: Handb. Mech. Mater., Springer Singapore, 2019: pp. 2249–2290. doi:10.1007/978-981-10-6884-3_56.

[123] J.G. Odhiambo, W.G. Li, Y.T. Zhao, C.L. Li, Porosity and its significance in plasma-sprayed coatings, Coatings. 9 (2019) 460. doi:10.3390/coatings9070460.

[124] A. Scrivani, S. Ianelli, A. Rossi, R. Groppetti, F. Casadei, G. Rizzi, A contribution to the surface analysis and characterisation of HVOF coatings for petrochemical application, Wear. 250 (2001) 107–113. doi:10.1016/S0043-1648(01)00621-4.

[125] L. Gil, M.H. Staia, Influence of HVOF parameters on the corrosion resistance of NiWCrBSi coatings, in: Thin Solid Films, Elsevier, 2002: pp. 446–454. doi:10.1016/S0040-6090(02)00815-5.

[126] W. Riggs, D. Rucker, K. Couch, Testing of Coatings, in: Therm. Spray Technol., ASM International, 2018: pp. 214–237. doi:10.31399/asm.hb.v05a.a0005730.

[127] M.R. Dorfman, Thermal spray coatings, in: Handb. Environ. Degrad. Mater. Third Ed., ASM International, 2018: pp. 469–488. doi:10.1016/B978-0-323-52472-8.00023-X.

[128] C.K. Lin, C.C. Berndt, Measurement and analysis of adhesion strength for thermally sprayed coatings, J. Therm. Spray Technol. 3 (1994) 75–104. doi:10.1007/BF02649003.

[129] Y. Inoue, A. Noutomi, T. Ono, A. Izuha, M. Toyoda, M. Tsukamoto, Applicability of Stress Singularity Parameter for Evaluating Adhesive Strength of Coating Film (Phase 1) Adhesive Strength Evaluation of Plasma Sprayed Coatings by Tesile Pin Test, Q. J. JAPAN Weld. Soc. 9 (1991) 167–173. doi:10.2207/qjjws.9.167.

[130] B. Tekyeh-Marouf, R. Bagheri, Fracture behavior of multi-layered composites under impact loading, Mater.Sci.Eng.A.448(2007)20–24. doi:10.1016/j.msea.2006.11.078.

[131] M. Naka, International Workshop on Designing of Interfacial Structures in Advanced Materials and their Joints, DIS 2006, Solid State Phenom. 127 (2007) 1–355.

[132] S.Q. Guo, D.R. Mumm, A.M. Karlsson, Y. Kagawa, Measurement of interfacial shear mechanical properties in thermal barrier coating systems by a barb pullout method, Scr. Mater. 53 (2005) 1043–1048. doi:10.1016/j.scriptamat.2005.07.012.

[133] S.T. Method, Standard Test Method for Adhesion or Cohesion Strength of Thermal Spray Coatings, Current. 03 (2001) 1–7. doi:10.1520/C0633-13R21.2.

[134] M. Watanabe, S. Kuroda, K. Yokoyama, T. Inoue, Y. Gotoh, Modified tensile adhesion test for evaluation of interfacial toughness of HVOF sprayed coatings, Surf. CoatingsTechnol. 202 (2008) 1746–1752. doi:10.1016/j.surfcoat.2007.07.028.

[135] L. Jacobs, M.M. Hyland, M. De Bonte, Comparative Study of WC-Cermet Coatings Sprayed via the HVOF and the HVAF Process, J. Therm. Spray Technol. 7 (1998) 213–218. doi:10.1361/105996398770350954.

[136] D. Chicot, H. Ageorges, M. Voda, G. Louis, M.A. Ben Dhia, C.C. Palacio, S. Kossman, Hardness of thermal sprayed coatings: Relevance of the scale of measurement, Surf. Coatings Technol. 268 (2015) 173–179. doi:10.1016/j.surfcoat.2014.04.043.

[137] C.K. Lin, C.C. Berndt, Statistical analysis of microhardness variations in thermal spray coatings, J. Mater. Sci. 30 (1995) 111–117. doi:10.1007/BF00352139.

[138] M. Xie, S. Zhang, M. Li, Comparative investigation on HVOF sprayed carbide-based coatings, Appl. Surf. Sci. 273 (2013) 799–805. doi:10.1016/j.apsusc.2013.03.010.

[139] D. Zhang, S.J. Harris, D.G. McCartney, Microstructure formation and corrosion behaviour in HVOF-sprayed inconel 625 coatings, Mater. Sci. Eng. A. 344 (2003) 45–56. doi:10.1016/S0921-5093(02)00420-3.

[140] B. Wielage, A. Wank, H. Pokhmurska, T. Grund, C. Rupprecht, G. Reisel, E. Friesen, Development and trends in HVOF spraying technology, Surf. Coatings Technol. 201 (2006) 2032–2037. doi:10.1016/j.surfcoat.2006.04.049.

[141] L. Fedrizzi, L. Valentinelli, S. Rossi, S. Segna, Tribocorrosion behaviour of HVOF cermet coatings, Corros. Sci. 49 (2007) 2781–2799. doi:10.1016/j.corsci.2007.02.003.

[142] M.M. Verdian, K. Raeissi, M. Salehi, Corrosion performance of HVOF and APS thermally sprayed NiTi intermetallic coatings in 3.5% NaCl solution, Corros. Sci. 52 (2010) 1052–1059. doi:10.1016/j.corsci.2009.11.034.

[143] J.M. Guilemany, N. Espallargas, P.H. Suegama, A. V. Benedetti, Comparative study of Cr3C2-NiCr coatings obtained by HVOF and hard chromium coatings, Corros. Sci. 48 (2006) 2998–3013. doi:10.1016/j.corsci.2005.10.016.

[144] R.Q. Guo, C. Zhang, Q. Chen, Y. Yang, N. Li, L. Liu, Study of structure and corrosion resistance of Fe-based amorphous coatings prepared by HVAF and HVOF, Corros. Sci. 53 (2011) 2351–2356. doi:10.1016/j.corsci.2010.12.022.

[145] M. V. Diamanti, F. Bolzoni, M. Ormellese, E.A. Pérez-Rosales, M.P. Pedeferri, Characterisation of titanium oxide films by potentiodynamic polarisation and electrochemical impedance spectroscopy, Corros. Eng. Sci. Technol. 45 (2010) 428–434. doi:10.1179/147842208X373191.

[146] R.G. Kelly, J.R. Scully, D. Shoesmith, R.G. Buchheit, Electrochemical Techniques in Corrosion Science and Engineering, CRC Press LLC, 2002. doi:10.1201/9780203909133.

[147] K. Thulasiraman, M.N.S. Swamy, Circuit Analysis: A Graph-Theoretic Foundation, in: Electr. Eng. Handb., Elsevier Inc., 2005: pp. 31–41. doi:10.1016/B978-012170960-0/50005-0.

[148] G.W. Walter, A review of impedance plot methods used for corrosion performance analysis of painted metals, Corros. Sci. 26 (1986) 681–703. doi:10.1016/0010-938X(86)90033-8.

[149] J. Matejícek, S. Sampath, J. Dubsky, X-ray Residual Stress Measurement in Metallic and Ceramic Plasma Sprayed Coatings, J. Therm. Spray Technol. 7 (1998) 489–496. doi:10.1361/105996398770350701.

[150] ASTM E 837:2008, Standard Test Method for Determining Residual Stresses by the Hole-Drilling Strain-Gages, 1 (2008) 1–17. doi:10.1520/E0837-20.1.

[151] W. Reitz, Surface cleaning and coating removal by lasers, ASM Handb. Vol. 5 Surf. Eng. (1994) 431–464.

[152] P.S. Prevey, X-RAY Diffraction residual stress techniuqes, (n.d.).

[153] C.U. Hardwicke, Y.C. Lau, Advances in thermal spray coatings for gas turbines and energy generation: A review, J. Therm. Spray Technol. 22 (2013) 564–576. doi:10.1007/s11666-013-9904-0.

[154] N. Espallargas, F. Mubarok, Thermal Spraying of Ceramic Materials, 2014. http://www.google.com/patents/ (accessed February 18, 2023).

[155] H. Herman, S. Sampath, R. McCune, Thermal spray: Current status and future trends, MRS Bull. 25 (2000) 17–25. doi:10.1557/MRS2000.119/METRICS.

[156] R.C. Dykhuizen, Review of impact and solidification of molten thermal spray droplets, J. Therm. Spray Technol. 3 (1994) 351–361. doi:10.1007/BF02658980.

[157] F. Tarasi, E. Alebrahim, A. Dolatabadi, C. Moreau, A Comparative study of YSZ suspensions and coatings, Coatings. 9 (2019) 188. doi:10.3390/COATINGS9030188.

[158] A.J. Horlock, Z. Sadeghian, D.G. McCartney, P.H. Shipway, High-velocity oxyfuel reactive spraying of mechanically alloyed Ni-Ti-C powders, J. Therm. Spray Technol. 14 (2005) 77–84. doi:10.1361/10599630522747.

[159] C.A. da Cunha, N.B. de Lima, J.R. Martinelli, A.H. de A. Bressiani, A.G.F. Padial, L.V. Ramanathan, Microstructure and mechanical properties of thermal sprayed nanostructured Cr_3C_2-$Ni_{20}Cr$ coatings, Mater. Res. 11 (2008) 137–143. doi:10.1590/s1516-14392008000200005.

[160] Z. Russell, W.A. Sparling, T.L. Stewart, P. Gray, M. Gaier, M.J. Froning, G. Mazzanti, K.P. Plucknett, Gelation-based feed-stock technologies for HVOF thermal spray development: Micro-composite powder preparation and HVOF coating microstructure, Surf. Coatings Technol. 452 (2023) 129089. doi:10.1016/j.surfcoat.2022.129089.

[161] J. Wang, E.H. Jordan, M. Gell, Plasma sprayed dense MgO-Y_2O_3 nanocomposite coatings using sol-gel combustion synthesized powder, J. Therm. Spray Technol. 19 (2010) 873–878. doi:10.1007/s11666-010-9496-x.

[162] D. Yan, Y. Dong, Y. Yang, L. Wang, X. Chen, J. He, J. Zhang, Microstructure characterization of the FeAl 2O 4-based nanostructured composite coating synthesized by plasma spraying Fe_2O_3/Al powders, J. Therm. Spray Technol. 20 (2011) 1269–1277. doi:10.1007/s11666-011-9673-6.

[163] Herbert Herman, Powders for Thermal Spray Technology, Stony Brook, 1991.

[164] J.M. Guilemany, J. Nutting, N. Llorca-Isern, N. Llorcalsern, Microstructural examination of HVOF chromium carbide coatings for high-temperature applications, J. Therm. Spray Technol. 5 (1996) 483–489. doi:10.1007/BF02645280.

[165] A.K. Maiti, N. Mukhopadhyay, R. Raman, Effect of adding WC powder to the feedstock of WC-Co-Cr based HVOF coating and its impact on erosion and abrasion resistance, Surf. Coatings Technol. 201 (2007) 7781–7788. doi:10.1016/j.surfcoat.2007.03.014.

[166] D. Lioma, N. Sacks, I. Botef, Cold gas dynamic spraying of WC-Ni cemented carbide coatings, Int. J. Refract. Met. Hard Mater. 49 (2015) 365–373. doi:10.1016/j.ijrmhm.2014.08.017.

[167] J.M. Guilemany, J. Nutting, N. Llorca-Isern, Microstructural examination of HVOF chromium carbide coatings for high-temperature applications, J. Therm. Spray Technol. 5 (1996) 483–489. doi:10.1007/BF02645280.

[168] B.Q. Wang, Z.R. Shui, The hot erosion behavior of HVOF chromium carbide-metal cermet coatings sprayed with different powders, Wear. 253 (2002) 550–557. doi:10.1016/S0043-1648(02)00049-2.

[169] G. Taillon, F. Pougoum, S. Lavigne, L. Ton-That, R. Schulz, E. Bousser, S. Savoie, L. Martinu, J.E. Klemberg-Sapieha, Cavitation erosion mechanisms in stainless steels and in composite metal–ceramic HVOF coatings, Wear. 364–365 (2016) 201–210. doi:10.1016/j.wear.2016.07.015.

[170] E.R. Ault, R.S. Bradford, M.L. Bhaumik, High-power xenon fluoride laser, Appl. Phys. Lett. 27 (1975) 413–415. doi:10.1063/1.88496.

[171] A.J. Alcock, P.B. Corkum, D.J. James, A fast scalable switching technique for high-power CO2 laser radiation, Appl. Phys. Lett. 27 (1975) 680–682. doi:10.1063/1.88336.

[172] B.H. Ripin, P.G. Burkhalter, F.C. Young, J.M. McMahon, D.G. Colombant, S.E. Bodner, R.R. Whitlock, D.J. Nagel, D.J. Johnson, N.K. Winsor, C.M. Dozier, R.D. Bleach, J.A. Stamper, E.A. McLean, X-ray emission spectra from high-power-laser-produced plasmas, Phys. Rev. Lett. 34 (1975) 1313–1316. doi:10.1103/PhysRevLett.34.1313.

[173] H. Tan, Y. Fang, C. Zhong, Z. Yuan, W. Fan, Z. Li, J. Chen, X. Lin, Investigation of heating behavior of laser beam on powder stream in directed energy deposition, Surf. Coatings Technol. 397 (2020) 126061. doi:10.1016/j.surfcoat.2020.126061.

[174] E. Toyserkani, A. Khajepour, S. Corbin, Laser Cladding, CRC Press, 2004. doi:10.1201/9781420039177.

[175] A. Ikesue, Y.L. Aung, Ceramic laser materials, Nat. Photonics. 2 (2008) 721–727. doi:10.1038/nphoton.2008.243.

[176] A.S. Khanna, S. Kumari, S. Kanungo, A. Gasser, Hard coatings based on thermal spray and laser cladding, Int. J. Refract. Met. Hard Mater. 27 (2009) 485–491. doi:10.1016/j.ijrmhm.2008.09.017.

[177] E. Cuce, S.B. Riffat, A state-of-the-art review on innovative glazing technologies, Renew. Sustain. Energy Rev. 41 (2015) 695–714. doi:10.1016/j.rser.2014.08.084.

[178] C.W. Draper, C.A. Ewing, Laser surface alloying: a bibliography, J. Mater. Sci. 19 (1984) 3815–3825. doi:10.1007/BF00980743.

[179] E. Toyserkani, A. Khajepour, S. Corbin, Laser Cladding, 2017. doi:10.2351/1.521888.

[180] J.L. Koch, J. Mazumder, Rapid prototyping by laser cladding, in: Int. Congr. Appl. Lasers Electro-Optics, Laser Institute of America LIA, 2018: pp. 556–565. doi:10.2351/1.5058617.

[181] H. Paydas, A. Mertens, R. Carrus, J. Lecomte-Beckers, J. Tchoufang Tchuindjang, Laser cladding as repair technology for Ti–6Al–4V alloy: Influence of building strategy on microstructure and hardness, Mater. Des. 85 (2015) 497–510. doi:10.1016/J.MATDES.2015.07.035.

[182] R. Vilar, Laser cladding, Int. J. Powder Metall. (Princeton, New Jersey). 37 (2001) 64. doi:10.2351/1.521888.

[183] T.N. S. Nowotny, S. Scharek, R. Zieris, E. Beyer, Laser Materials Processing , ICALEO 2000 Proceedings - Laser Institute, 2000. https://books.google.ca/books (accessed May 31, 2018).

[184] W.P.. Jüptner, LIA handbook of laser materials processing, Opt. Lasers Eng. 38 (2002) 608–610. doi:10.1016/S0143-8166(01)00176-2.

[185] Q. Meng, L. Geng, D. Ni, Laser cladding NiCoCrAlY coating on Ti-6Al-4V, Mater. Lett. 59 (2005) 2774–2777. doi:10.1016/j.matlet.2005.03.056.

[186] J. Xu, W. Liu, Y. Kan, M. Zhong, Microstructure and wear properties of laser cladding Ti-Al-Fe-B coatings on AA2024 aluminum alloy, Mater. Des. 27 (2006) 405–410. doi:10.1016/j.matdes.2004.11.011.

[187] J. Nurminen, J. Näkki, P. Vuoristo, Microstructure and properties of hard and wear resistant MMC coatings deposited by laser cladding, Int. J. Refract. Met. Hard Mater. 27 (2009) 472–478. doi:10.1016/j.ijrmhm.2008.10.008.

[188] P.C. Yu, X.B. Liu, X.L. Lu, S.J. Qiao, Y.J. Zhai, G.X. Zhu, Y.G. Wang, Y. Chen, Tribology and high-temperature oxidation behaviors of NiCrBSiFe composite coatings on Ti6Al4V alloy by laser cladding, RSC Adv. 5 (2015) 76516–76525. doi:10.1039/c5ra14732h.

[189] I. Mahmud U, X. Lijue, M. Gavin, Process for manufacturing or reparing turbine engine or compressor componants, 2001. doi:10.1074/JBC.274.42.30033.(51).

[190] M. Gäumann, S. Henry, F. Cléton, J.-D. Wagnière, W. Kurz, Epitaxial laser metal forming: analysis of microstructure formation, Mater. Sci. Eng. A. 271 (1999) 232–241. doi:10.1016/S0921-5093(99)00202-6.

[191] J. Leunda, C. Soriano, C. Sanz, V.G. Navas, Laser cladding of vanadium-carbide tool steels for die repair, in: Phys. Procedia, Elsevier, 2011: pp. 345–352. doi:10.1016/j.phpro.2011.03.044.

[192] L. Sexton, S. Lavin, G. Byrne, A. Kennedy, Laser cladding of aerospace materials, J. Mater. Process. Technol. 122 (2002) 63–68. doi:10.1016/S0924-0136(01)0121-9.

[193] R.Housholder,_Molding_process,1981. https://patents.google.com/patent/US4247508B1/en (accessed October 14, 2018).

[194] M. Shellabear, O. Nyrhilä, Dmls – Development History and State of the Art, (2004). https://www.i3dmfg.com/wp-content/uploads/2015/07/History-of DMLS.pdf (accessed October 14, 2018).

[195] A. Dass, A. Moridi, State of the art in directed energy deposition: From additive manufacturing to materials design, Coatings 9(2019)418. doi:10.3390/COATINGS9070418.

[196] M. John, U.B. Kuruveri, P.L. Menezes, Laser Cladding-Based Surface Modification of Carbon Steel and High-Alloy Steel for Extreme Condition Applications, Coatings. 12 (2022) 1444. doi:10.3390/coatings12101444.

[197] Y.. Kathuria, Laser-cladding process: a study using stationary and scanning CO_2 laser beams, Surf. Coatings Technol. 97 (1997) 442–447. doi:10.1016/S0257-8972(97)00165-5.

[198] M. Bianco, C. Rivela, S. Talentino, On-line surface treatment feasibility of industrial components by means of CO_2 power laser, in: E. Beyer, M. Cantello, A. V. La Rocca, L.D. Laude, F.O. Olsen, G. Sepold (Eds.), International Society for Optics and Photonics, 1994: p. 53. doi:10.1117/12.184760.

[199] Y. Yang, Microstructure and properties of laser-clad high-temperature wear-resistant alloys, Appl. Surf. Sci. 140 (1999) 19–23. doi:10.1016/S0169-4332(98)00320-1.

[200] J.D. Majumdar, I. Manna, Laser-Assisted Fabrication of Materials, Springer Berlin Heidelberg, Berlin, Heidelberg, 2012. doi:10.1007/978-3-642-28359-8.

[201] K.P. Driedger, R.M. Ifflander, H. Weber, Multirod Resonators for High-Power Solid-State Lasers with Improved Beam Quality, IEEE J. Quantum Electron. 24 (1988) 665–674. doi:10.1109/3.176.

[202] S. Zhang, D. Zhao, Aerospace materials handbook, CRC Press, 2016. doi:10.1201/b13044.

[203] J. Lin, Concentration mode of the powder stream in coaxial laser cladding, Opt. Laser Technol. 31 (1999) 251–257. doi:10.1016/S0030-3992(99)00049-3.

[204] Oerlikon - Powder Feeder TWIN 150 | Kaufen auf Ricardo, (n.d.). https://www.ricardo.ch/de/a/oerlikon-powder-feeder-twin-150-1149392946/ (accessed June 2, 2023).

[205] A. Hansel, M. Mori, M. Fujishima, Y. Oda, G. Hyatt, E. Lavernia, J.P. Delplanque, Study on Consistently Optimum Deposition Conditions of Typical Metal Material Using Additive/Subtractive Hybrid Machine Tool, in: Procedia CIRP, Elsevier, 2016: pp. 579–582. doi:10.1016/j.procir.2016.04.113.

[206] M. Rafiee, F. Granier, D. Therriault, Advances in Coaxial Additive Manufacturing and Applications, Adv.Mater.Technol. 6(2021)2100356. doi:10.1002/admt.202100356.

[207] J. Xu, X. Zhang, Y. Liu, Y. Zhang, H.Y. Nie, G. Zhang, W. Gao, Selective coaxial ink 3D printing for single-pass fabrication of smart elastomeric foam with embedded stretchable sensor, Addit. Manuf. 36 (2020) 101487. doi:10.1016/j.addma.2020.101487.

[208] H. Koehler, K. Partes, T. Seefeld, F. Vollertsen, Laser reconditioning of crankshafts: From lab to application, in: Phys. Procedia, Elsevier, 2010: pp. 387–397. doi:10.1016/j.phpro.2010.08.160.

[209] C. Stauter, J. Fontaine, T. Engel, A. Biernaux, Optical and Acoustical Techniques for the Characterization of Material Ablation by Q-Switched ND:YAG and Excimer Laser Radiation, in: Laser Process. Surf. Treat. Film Depos., Springer Netherlands, Dordrecht, 1996: pp. 881–894. doi:10.1007/978-94-009-0197-1_48.

[210] T.M. Bloomstein, S.T. Palmacci, R.H. Mathews, N. Nassuphis, D.J. Ehrlich, Advances in Laser Direct Writing, in: Laser Process. Surf. Treat. Film Depos., Springer Netherlands, Dordrecht, 1996: pp. 895–906. doi:10.1007/978-94-009-0197-1_49.

[211] A. Mukherjee, B.J. Eapen, S.K. Baral, Laser Processing of Integrated Optic Waveguides for Photonic Applications, in: Laser Process. Surf. Treat. Film Depos., Springer Netherlands, Dordrecht, 1996: pp. 869–880. doi:10.1007/978-94-009-0197-1_47.

[212] P.A. Vetter, T. Engel, J. Fontaine, Laser cladding: the relevant parameters for process control, in: E. Beyer, M. Cantello, A. V. La Rocca, L.D. Laude, F.O. Olsen, G. Sepold (Eds.), Proc. SPIE, Vol. 2207, p. 452-462 (1994)., 1994: p. 452. doi:10.1117/12.184751.

[213] H.S. (Horatio S. Carslaw, J.C. (John C. Jaeger, Conduction of heat in solids, Clarendon Press, 1959. https://global.oup.com/academic/product/conduction-of-heat-in-solids- (accessed October 20, 2018).

[214] J.P. Kruth, M.C. Leu, T. Nakagawa, Progress in additive manufacturing and rapid prototyping, CIRP Ann. - Manuf. Technol. 47 (1998) 525–540. doi:10.1016/S0007-8506(07)63240-5.

[215] C.C. Renaud, H.L. Offerhaus, J.A. Alvarez-Chavez, J. Nilsson, W.A. Clarkson, P.W. Turner, D.J. Richardson, A.B. Grudinin, Characteristics of Q-switched cladding-pumped ytterbium-doped fiber lasers with different high-energy fiber designs, IEEE J. Quantum Electron. 37 (2001) 199–206. doi:10.1109/3.903069.

[216] Institute of Electrical and Electronics Engineers. Electron Devices Group., IEEE Microwave Theory and Techniques Group., IEEE Quantum Electronics Council., IEEE Quantum Electronics and Applications Society., Lasers and Electro-optics Society (Institute of Electrical and Electronics Engineers), IEEE Photonics Society, IEEE journal of quantum electronics., [Institute of Electrical and Electronics Engineers, 1965.

[217] J. Nilsson, W.A. Clarkson, R. Selvas, J.K. Sahu, P.W. Turner, S.U. Alam, A.B. Grudinin, High-power wavelength-tunable cladding-pumped rare-earth-doped silica fiber lasers, Opt. Fiber Technol. 10 (2004) 5–30. doi:10.1016/j.yofte.2003.07.001.

[218] S.D. Jackson, T.A. King, High-power diode-cladding-pumped Tm-doped silica fiber laser, Opt. Lett. 23 (1998) 1462. doi:10.1364/OL.23.001462.

[219] High-speed laser cladding makes wear-resistant coatings more cost-efficient - Industrial Laser Solutions, (n.d.). https://www.industrial-lasers.com/articles/2017/04/high-speed-laser-cladding-makes-wear-resistant-coatings-more-cost-efficient.html (accessed October 14, 2018).

[220] H.M. Wang, Y.F. Liu, Microstructure and wear resistance of laser clad Ti5Si3/NiTi2intermetallic composite coating on titanium alloy, Mater. Sci. Eng. A. 338 (2002) 126–132. doi:10.1016/S0921-5093(02)00076-X.

[221] A. Clare, O. Oyelola, J. Folkes, P. Farayibi, Laser cladding for railway repair and preventative maintenance, J. Laser Appl. 24 (2012) 032004. doi:10.2351/1.4710578.

[222] S. Da Sun, Q. Liu, M. Brandt, V. Luzin, R. Cottam, M. Janardhana, G. Clark, Effect of laser clad repair on the fatigue behaviour of ultra-high strength AISI 4340 steel, Mater. Sci. Eng. A. 606 (2014) 46–57. doi:10.1016/j.msea.2014.03.077.

[223] A.J. Pinkerton, W. Wang, L. Li, Component repair using laser direct metal deposition, Proc. Inst. Mech. Eng. Part B J. Eng. Manuf. 222 (2008) 827–836. doi:10.1243/09544054JEM1008.

[224] P. Bendeich, N. Alam, M. Brandt, D. Carr, K. Short, R. Blevins, C. Curfs, O. Kirstein, G. Atkinson, T. Holden, R. Rogge, Residual stress measurements in laser clad repaired low pressure turbine blades for the power industry, Mater. Sci. Eng. A. 437 (2006) 70–74. doi:10.1016/J.MSEA.2006.04.065.

[225] X. Yan, P. Gu, A review of rapid prototyping technologies and systems, CAD Comput. Aided Des. 28 (1996) 307–318. doi:10.1016/0010-4485(95)00035-6.

[226] E.C. Santos, M. Shiomi, K. Osakada, T. Laoui, Rapid manufacturing of metal components by laser forming, Int. J. Mach. Tools Manuf. 46 (2006) 1459–1468. doi:10.1016/J.IJMACHTOOLS.2005.09.005.

[227] V. Bagaria, D. Rasalkar, S. Jain, J. Ilyas, Medical Applications of Rapid Prototyping - A New Horizon, in: Adv. Appl. Rapid Prototyp. Technol. Mod. Eng., 2011. doi:10.5772/20058.

[228] S. Zhou, X. Dai, Laser induction hybrid rapid cladding of WC particles reinforced NiCrBSi composite coatings, Appl. Surf. Sci. 256 (2010) 4708–4714. doi:10.1016/J.APSUSC.2010.02.078.

[229] Y.. Pei, V. Ocelik, J.T.. De Hosson, SiCp/Ti6Al4V functionally graded materials produced by laser melt injection, Acta Mater. 50 (2002) 2035–2051. doi:10.1016/S1359-6454(02)00049-6.

[230] F. Weng, C. Chen, H. Yu, Research status of laser cladding on titanium and its alloys: A review, Mater. Des. 58 (2014) 412–425. doi:10.1016/j.matdes.2014.01.077.

[231] T.M. Yue, Y.P. Su, H.O. Yang, Laser cladding of $Zr_{65}Al_{7.5}Ni10Cu1_{7.5}$ amorphous alloy on magnesium, Mater. Lett. 61 (2007) 209–212. doi:10.1016/J.MATLET.2006.04.033.

[232] C. Chan, J. Mazumder, M.M. Chen, Three-dimantional model forconvection in laser melted pool., in: LIA (Laser Inst. Am., 1985: pp. 17–27. doi:10.2351/1.5057601.

[233] Z.D. Dai, S.C. Pan, M. Wang, S.R. Yang, X.S. Zhang, Q.J. Xue, Improving the fretting wear resistance of titanium alloy by laser beam quenching, Wear. 213 (1997) 135–139. doi:10.1016/S0043-1648(97)00160-9.

[234] Y. Fu, A.W. Batchelor, Laser nitriding of pure titanium with Ni, Cr for improved wear performance, Wear. 214 (1998) 83–90. doi:10.1016/S0043-1648(97)00204-4.

[235] X. Wu, B. Zhu, X. Zeng, X. Hu, K. Cui, Critical state of laser cladding with powder auto-feeding, Surf. Coatings Technol. 79 (1996) 200–204. doi:10.1016/0257-8972(95)02452-2.

[236] J. Przybylowicz, J. Kusinski, Laser cladding and erosive wear of Co-Mo-Cr-Si coatings, in: Surf. Coatings Technol., Elsevier, 2000: pp. 13–18. doi:10.1016/S0257-8972(99)00563-0.

[237] S. Sircar, C. Ribaudo, J. Mazumder, Laser Clad Nickel Based Superalloys: Microstructure Evolution And High Temperature Oxidation Studies, in: G. Sepold (Ed.), International Society for Optics and Photonics, 1988: p. 29. doi:10.1117/12.947700.

[238] L.. C. Lim, Q. Ming, Z.. D. Chen, Microstructures of laser-clad nickel-based hardfacing alloys, Surf. Coatings Technol. 106 (1998) 183–192. doi:10.1016/S0257-8972(98)00525-8.

[239] S. Wulin, J. Echigoya, Z. Beidi, X. Changsheng, H. Wei, C. Kun, Vacuum laser cladding and effect of Hf on the cracking susceptibility and the microstructure of

Fe-Cr-Ni laser-clad layer, Surf. Coatings Technol. 126 (2000) 76–80. doi:10.1016/S0257-8972(00)00532-6.

[240] W. Niu, R. Sun, Y. Lei, Microstructure and wear properties of laser clad NiCrBSi-MoS2 coating, Frict. Wear Res. 2 (2014) 1–5. doi:10.2351/1.5058666.

[241] S. Yang, N. Chen, W. Liu, M. Zhong, In situ formation of MoSi2/SiC composite coating on pure Al by laser cladding, Mater. Lett. 57 (2003) 3412–3416. doi:10.1016/S0167-577X(03)00086-7.

[242] Y.T. Pei, J.H. Ouyang, T.C. Lei, Y. Zhou, Microstructure of laser-clad SiC-(Ni alloy) composite coating, Mater. Sci. Eng. A. 194 (1995) 219–224. doi:10.1016/0921-5093(94)09653-8.

[243] L.R. Katipelli, A. Agarwal, N.B. Dahotre, Laser surface engineered TiC coating on 6061 Al alloy: Microstructure and wear, Appl. Surf. Sci. 153 (2000) 65–78. doi:10.1016/S0169-4332(99)00368-2.

[244] Q. Zhang, J. He, W. Liu, M. Zhong, Microstructure characteristics of ZrC-reinforced composite coating produced by laser cladding, Surf. Coatings Technol. 162 (2003) 140–146. doi:10.1016/S0257-8972(02)00697-7.

[245] S. Yang, M. Zhong, W. Liu, TiC particulate composite coating produced in situ by laser cladding, Mater. Sci. Eng. A. 343 (2003) 57–62. doi:10.1016/S0921-5093(02)00361-1.

[246] F. Norton, Fine ceramics: technology and applications, (1970). https://www.bcin.ca/bcin/detail.app?id=81762 (accessed March 31, 2020).

[247] F. Norton, Elements of ceramics, (1974). (accessed March 31, 2020).

[248] R. Moreno, Colloidal processing of ceramics and composites, Adv. Appl. Ceram. 111 (2012) 246–253. doi:10.1179/1743676111Y.0000000075.

[249] G. Messing, J. McCauley, K. Mazdiyasni, R. Haber, Ceramic powder science, (1987). https://www.osti.gov/biblio/5525472 (accessed March 31, 2020).

[250] I.A.-A.O.P.O. THE, U. 1988, Forming of ceramic matrix composites with colloids, Chem. SOC 1155 16TH ST, NW …. (n.d.).

[251] M.J.-C.T.A.C. Soc., undefined 1988, Ceramic Powder Science II, Ci.Nii.Ac.Jp. (n.d.). https://ci.nii.ac.jp/naid/10024353161/ (accessed March 31, 2020).

[252] Messing: Ceramicpowderscience, (n.d.). 1988&pages=66374& (accessed March 31, 2020).

[253] H.N. Shsh, a V Rao, Rheological Properties of Sodium Alginate, Indian J. Technol. 7 (1969) 261.

[254] W.E. Rochefort, T. Rehg, P.C. Chau, Trivalent cation stabilization of alginate gel for cell immobilization, Biotechnol. Lett. 8 (1986) 115–120. doi:10.1007/BF01048468.

[255] E. Hermansson, E. Schuster, L. Lindgren, A. Altskär, A. Ström, Impact of solvent quality on the network strength and structure of alginate gels, Carbohydr. Polym. 144 (2016) 289–296. doi:10.1016/j.carbpol.2016.02.069.

[256] Y. Zhou, ichiro Kajiyama, H. Masuhara, Y. Hosokawa, T. Kaji, K. Fukui, A new size and shape controlling method for producing calcium alginate beads with immobilized proteins, J. Biomed. Sci. Eng. 2 (2009) 287–293. doi:10.4236/jbise.2009.25043.

[257] A. Nussinovitch, A. Nussinovitch, Bead Formation, Strengthening, and Modification, in: Polym. Macro- Micro-Gel Beads Fundam. Appl., Springer New York, 2010: pp. 27–52. doi:10.1007/978-1-4419-6618-6_2.

[258] E.S. Chan, T.K. Lim, P. Ravindra, R.F. Mansa, A. Islam, The effect of low air-to-liquid mass flow rate ratios on the size, size distribution and shape of calcium alginate particles produced using the atomization method, J. Food Eng. 108 (2012) 297–303. doi:10.1016/j.jfoodeng.2011.08.010.

[259] K.Y. Lee, D.J. Mooney, Alginate: Properties and biomedical applications, Prog. Polym. Sci. 37 (2012) 106–126. doi:10.1016/j.progpolymsci.2011.06.003.

[260] W.A. Sparling, K.P. Plucknett, The effects of Mo_2C additions on the sintering response of TiC0.3N0.7–Ni_3Al cermets, Int. J. Refract. Met. Hard Mater. 61 (2016) 98–106. doi:10.1016/j.ijrmhm.2016.08.013.

[261] J.H. Cui, J.S. Goh, S.Y. Park, P.H. Kim, B.J. Lee, Preparation and physical characterization of alginate microparticles using air atomization method, Drug Dev. Ind. Pharm. 27 (2001) 309–319. doi:10.1081/DDC-100103730.

[262] S. Abang, P.E. Loh, P. Ravindra, Z.H. Yim, E.S. Chan, Production of Alginate Microbeads through Air Atomisation Technique, n.d.

[263] J. Li, Y. Wu, J. He, Y. Huang, A new insight to the effect of calcium concentration on gelation process and physical properties of alginate films, J. Mater. Sci. 51 (2016) 5791–5801. doi:10.1007/s10853-016-9880-0.

[264] Y. Senuma, C. Lowe, Y. Zweifel, J.G. Hilborn, I. Marison, Alginate hydrogel microspheres and microcapsules prepared by spinning disk atomization, Biotechnol. Bioeng. 67 (2000) 616–622. doi:10.1002/(SICI)1097-0290(20000305)67:5<616::AID-BIT12>3.0.CO;2-Z.

[265] S.W. Huang, M. Samandi, M. Brandt, Abrasive wear performance and microstructure of laser clad WC/Ni layers, Wear. 256 (2004) 1095–1105. doi:10.1016/S0043-1648(03)00526-X.

[266] B.. Kooi, Y.. Pei, J.T.. De Hosson, The evolution of microstructure in a laser clad TiB–Ti composite coating, Acta Mater. 51 (2003) 831–845. doi:10.1016/S1359-6454(02)00475-5.

[267] J. Singh, J. Mazumder, Microstructure and wear properties of laser clad Fe-Cr-Mn-C alloys, Metall. Trans. A. 18 (1987) 313–322. doi:10.1007/BF02825712.

[268] R.L. Sun, D.Z. Yang, L.X. Guo, S.L. Dong, Microstructure and wear resistance of NiCrBSi laser clad layer on titanium alloy substrate, Surf. Coatings Technol. 132 (2000) 251–255. doi:10.1016/S0257-8972(00)00904-X.

[269] Y. Yang, H.C. Man, Microstructure evolution of laser clad layers of W-C-Co alloy powders, Surf. Coatings Technol. 132 (2000) 130–136. doi:10.1016/S0257-8972(00)00909-9.

[270] H.M. Wang, F. Cao, L.X. Cai, H.B. Tang, R.L. Yu, L.Y. Zhang, Microstructure and tribological properties of laser clad Ti2Ni3Si/NiTi intermetallic coatings, Acta Mater. 51 (2003) 6319–6327. doi:10.1016/S1359-6454(03)00465-8.

[271] K. Van Acker, D. Vanhoyweghen, R. Persoons, J. Vangrunderbeek, Influence of tungsten carbide particle size and distribution on the wear resistance of laser clad WC/Ni coatings, in: Wear, Elsevier, 2005: pp. 194–202. doi:10.1016/j.wear.2004.09.041.

[272] V. Ocelík, I. Furár, J.T.M. De Hosson, Microstructure and properties of laser clad coatings studied by orientation imaging microscopy, Acta Mater. 58 (2010) 6763–6772. doi:10.1016/j.actamat.2010.09.002.

[273] Y.. Pei, T.. Zuo, Gradient microstructure in laser clad TiC-reinforced Ni-alloy composite coating, Mater. Sci. Eng. A. 241 (1998) 259–263. doi:10.1016/S0921-5093(97)00501-7.

[274] K.A. Chiang, Y.C. Chen, Microstructural characterization and microscopy analysis of laser cladding Stellite12 and tungsten carbide, J. Mater. Process. Technol. 182 (2007) 297–302. doi:10.1016/j.jmatprotec.2006.08.007.

[275] C.J. Li, Y.Y. Wang, G.J. Yang, A. Ohmori, K.A. Khor, Effect of solid carbide particle size on deposition behaviour, microstructure and wear performance of HVOF cermet coatings, Mater. Sci. Technol. 20 (2004) 1087–1096. doi:10.1179/026708304225019722.

[276] N. Ma, L. Guo, Z. Cheng, H. Wu, F. Ye, K. Zhang, Improvement on mechanical properties and wear resistance of HVOF sprayed WC-12Co coatings by optimizing feedstock structure, Appl. Surf. Sci. 320 (2014) 364–371. doi:10.1016/j.apsusc.2014.09.081.

[277] C.A. Poblano-Salas, J.A. Cabral-Miramontes, A. Gallegos-Melgar, H. Ruiz-Luna, J.D. Aguilar-Escobar, D.G. Espinosa-Arbelaez, F. Espinoza-Beltrán, G. Trapaga-Martínez, J. Muñoz-Saldaña, Effects of VC additions on the mechanical properties of bimodal WC-Co HVOF thermal sprayed coatings measured by nanoindentation, Int. J. Refract. Met. Hard Mater. 48 (2015) 167–178. doi:10.1016/j.ijrmhm.2014.08.016.

[278] V. Crespo, I.G. Cano, S. Dosta, J.M. Guilemany, The influence of feedstock powders on the CGS deposition efficiency of bond coats for TBCs, J. Alloys Compd. 622 (2015) 394–401. doi:10.1016/j.jallcom.2014.09.216.

[279] X. Wang, Z. Xie, Y. Huang, Y.C.-C. international, undefined 2002, Gelcasting of silicon carbide based on gelation of sodium alginate, Elsevier. (n.d.). https://www.sciencedirect.com/science/article/pii/S0272884202000664 (accessed March 31, 2020).

[280] T. Nozaki, T. Arima, K. Idemitsu, Y. Inagaki, Synthesis of zirconia sphere particles based on gelation of sodium alginate, J. Nucl. Mater. 412 (2011) 184–189. doi:10.1016/j.jnucmat.2011.02.056.

[281] C.J.E. Santos, T.S. Wei, B. Cho, W.M. Kriven, A forming technique to produce spherical ceramic beads using sodium alginate as a precursor binder phase, J. Am. Ceram. Soc. 96 (2013) 3379–3388. doi:10.1111/jace.12584.

[282] R.H. Plovnick, S. Louis Park, Application Data Division of Ser, 1994.

[283] US5665279A - Low density silicon nitride-containing beads, aggregates thereof, and method for preparing same, (n.d.). https://patents.google.com/patent/US5665279A/en (accessed March 31, 2020).

[284] C. Hu, W. Lu, A. Mata, K. Nishinari, Y. Fang, Ions-induced gelation of alginate: Mechanisms and applications, Int. J. Biol. Macromol. 177 (2021) 578–588. doi:10.1016/j.ijbiomac.2021.02.086.

[285] T.L. Stewart, K.P. Plucknett, The sliding wear of TiC and Ti(C,N) cermets prepared with a stoichiometric Ni_3Al binder, Wear. 318 (2014) 153–167. doi:10.1016/j.wear.2014.06.025.

[286] T.L. Stewart, K.P. Plucknett, The effects of Mo2C additions on the microstructure and sliding wear of TiC0.3N0.7-Ni3Al cermets, Int. J. Refract. Met. Hard Mater. 50 (2015) 227–239. doi:10.1016/j.ijrmhm.2015.01.013.

[287] Z. Memarrashidi, The Aqueous Corrosion Response of Ti (C,N), TiC and WC Based Ceramic-Metal Composites by Zhila Memarrashidi Submitted in partial fulfillment of the requirements for the degree of Master of Applied Science at, 2015.

[288] Z. Memarrashidi, K.P. Plucknett, Factors influencing the aqueous electrochemical response of TiC–Ni_3Al cermets, J. Mater. Res. 32 (2017) 1–11. doi:10.1557/jmr.2017.178.

[289] R.B. Collier, K.P. Plucknett, A comparison of the colloidal stabilization of aqueous titanium carbide suspensions using anionic and cationic dispersants, Int. J. Refract. Met. Hard Mater. 29 (2011) 298–305. doi:10.1016/j.ijrmhm.2010.12.005.

[290] A. Koike, N. Nemoto, M. Takahashi, K. Osaki, Dynamic viscoelasticity of end-linking α,ω-dimethyl silyl poly(propylene oxide) solutions near the gel point, Polymer (Guildf). 35 (1994) 3005–3010. doi:10.1016/0032-3861(94)90413-8.

[291] M.K. KEOGH, B.T. O'KENNEDY, Rheology of Stirred Yogurt as Affected by Added Milk Fat, Protein and Hydrocolloids, J. Food Sci. 63 (1998) 108–112. doi:10.1111/j.1365-2621.1998.tb15687.x.

[292] T. Funami, Y. Fang, S. Noda, S. Ishihara, M. Nakauma, K.I. Draget, K. Nishinari, G.O. Phillips, Rheological properties of sodium alginate in an aqueous system during gelation in relation to supermolecular structures and Ca^{2+} binding, Food Hydrocoll. 23 (2009) 1746–1755. doi:10.1016/j.foodhyd.2009.02.014.

[293] D. Gómez-Díaz, J.M. Navaza, Rheology of aqueous solutions of food additives: Effect of concentration, temperature and blending, J. Food Eng. 56 (2003) 387–392. doi:10.1016/S0260-8774(02)00211-X.

[294] F. Belalia, N.E. Djelali, Rheological properties of sodium alginate solutions, Rev. Roum. Chim. 59 (2014) 135–145.

[295] M.M. Ahmadi, S. Mohammadi, A.N. Hayati, Analytical derivation of tortuosity and permeability of monosized spheres: A volume averaging approach, Phys. Rev. E - Stat. Nonlinear, Soft Matter Phys. 83 (2011). doi:10.1103/PhysRevE.83.026312.

[296] M.M. Ahmadi, S. Mohammadi, A.N. Hayati, Physical Review E - Statistical, Nonlinear, and Soft Matter Physics, 2011. doi:10.1103/PhysRevE.83.026312.

[297] L. Pisani, Simple Expression for the Tortuosity of Porous Media, Transp. Porous Media. 88 (2011) 193–203. doi:10.1007/s11242-011-9734-9.

[298] K. Hilpert, D. Kobertz, V. Venugopal, M. Miller, H. Gerads, F.J. Bremer, H. Nickel, Phase Diagram Studies on the Al-Ni System, Zeitschrift Fur Naturforsch. - Sect. A J. Phys. Sci. 42 (1987) 1327–1332. doi:10.1515/zna-1987-1117.

[299] S. Miura, Liquidus and solidus temperatures of Ni-Solid solution in Ni-AI-X(X: Ti, Zr, and Hf) ternary systems, J. Phase Equilibria. 20 (1999) 193–198. doi:10.1361/105497199770335712.

[300] W.O. Alexander, N.B. Vaughan, Phase Diagram Updates: Section HI Phase Diagram Updates AI-Ni (Aluminum-Nickel), J. Phase Equilibria. 37 (1937) 257.

[301] H.S. Ni, X.H. Liu, X.C. Chang, W.L. Hou, W. Liu, J.Q. Wang, High performance amorphous steel coating prepared by HVOF thermal spraying, J. Alloys Compd. 467 (2009) 163–167. doi:10.1016/j.jallcom.2007.11.133.

[302] W. Brandl, D. Toma, J. Krüger, H.J. Grabke, G. Matthäus, The oxidation behaviour of HVOF thermal-sprayed MCrAlY coatings, Surf. Coatings Technol. 94–95 (1997) 21–26. doi:10.1016/S0257-8972(97)00470-2.

[303] W.J. Oh, W.J. Lee, M.S. Kim, J.B. Jeon, D.S. Shim, Repairing additive-manufactured 316L stainless steel using direct energy deposition, Opt. Laser Technol. 117 (2019) 6–17. doi:10.1016/j.optlastec.2019.04.012.

[304] C.J. Li, A. Ohmori, Y. Harada, Effect of powder structure on the structure of thermally sprayed WC-Co coatings, J. Mater. Sci. 31 (1996) 785–794. doi:10.1007/BF00367900.

[305] J. Stokes, L. Looney, Residual stress in HVOF thermally sprayed thick deposits, Surf. Coatings Technol. 177–178 (2004) 18–23. doi:10.1016/j.surfcoat.2003.06.003.

[306] A. Karimi, C. Verdon, J.L. Martin, R.K. Schmid, Slurry erosion behaviour of thermally sprayed WC-M coatings, Wear. 186–187 (1995) 480–486. doi:10.1016/0043-1648(95)07154-7.

[307] C. Verdon, a Karimi, J.-L.L. Martin, A study of high velocity oxy-fuel thermally sprayed tungsten carbide based coatings. Part 1: Microstructures, Mater. Sci. Eng. A. 246 (1998) 11–24. doi:10.1016/S0921-5093(97)00759-4.

[308] B.R. Marple, J. Voyer, J.F. Bisson, C. Moreau, Thermal spraying of nanostructured cermet coatings, in: J. Mater. Process. Technol., 2001: pp. 418–423. doi:10.1016/S0924-0136(01)00798-1.

[309] J.C. Sn miguel Castro, M. Lara-Banda, F.H. Estupiñán Lopez, C.G. Tiburcio, F. Almeraya Calderon, J.Á. Cabral Miramontes, Wear Resistance of WC-Co Bimodal Coatings Manufactured By HVOF With Different Types of Flames as an Alternative to Hexavalent Chromium for Landing Gears, ECS Trans. 106 (2022) 151–161. doi:10.1149/10601.0151ecst.

[310] T. Sahraoui, N.E. Fenineche, G. Montavon, C. Coddet, Structure and wear behaviour of HVOF sprayed Cr_3C_2-NiCr and WC-Co coatings, Mater. Des. 24 (2003) 309–313. doi:10.1016/S0261-3069(03)00059-1.

[311] S. Watanabe, T. Tajiri, N. Sakoda, J. Amano, Fatigue cracks in HVOF thermally sprayed WC-Co coatings, J. Therm. Spray Technol. 7 (1998) 93–96. doi:10.1007/s11666-006-5009-3.

[312] P. Mi, T. Wang, F. Ye, Influences of the compositions and mechanical properties of HVOF sprayed bimodal WC-Co coating on its high temperature wear performance, Int. J. Refract. Met. Hard Mater. 69 (2017) 158–163. doi:10.1016/j.ijrmhm.2017.08.012.

[313] Z. Geng, S. Li, D.L. Duan, Y. Liu, Wear behaviour of WC-Co HVOF coatings at different temperatures in air and argon, Wear. 330–331 (2015) 348–353. doi:10.1016/j.wear.2015.01.035.

[314] B. Casas, X. Ramis, M. Anglada, J.M. Salla, L. Llanes, Oxidation-induced strength degradation of WC-Co hardmetals, in: Int. J. Refract. Met. Hard Mater., Elsevier, 2001: pp. 303–309. doi:10.1016/S0263-4368(01)00033-6.

[315] S. Hochstrasser(-Kurz), Y. Mueller, C. Latkoczy, S. Virtanen, P. Schmutz, Analytical characterization of the corrosion mechanisms of WC-Co by electrochemical methods and inductively coupled plasma mass spectroscopy, Corros. Sci. 49 (2007) 2002–2020. doi:10.1016/j.corsci.2006.08.022.

[316] V.A.D.D. Souza, A. Neville, Using In Situ Atomic Force Microscopy to Investigate the Kinetics of Corrosion of WC–Co–Cr Cermet Coatings Applied by High-Velocity Oxy-Fuel, J. Eng. Mater. Technol. 129 (2007) 55. doi:10.1115/1.2400258.

[317] S. Zhang, Titanium carbonitride-based cermets: processes and properties, Mater. Sci. Eng. A. 163 (1993) 141–148. doi:10.1016/0921-5093(93)90588-6.

[318] B. Meredith, D.R. Milner, The liquid–phase sintering of titanium carbide, Powder Metall. 19 (1976) 162–170. doi:10.1179/pom.1976.19.3.162.

[319] R. Sepúlveda, F. Arenas, TiC-VC-Co: A study on its sintering and microstructure, in: Int. J. Refract. Met. Hard Mater., Elsevier, 2001: pp. 389–396. doi:10.1016/S0263-4368(01)00013-0.

[320] W.D. Kaplan, D. Rittel, M. Lieberthal, N. Frage, M.P. Dariel, Static and dynamic mechanical damage mechanisms in TiC-1080 steel cermets, Scr. Mater. 51 (2004) 37–41. doi:10.1016/j.scriptamat.2004.03.021.

[321] C.C. Onuoha, G.J. Kipouros, Z.N. Farhat, K.P. Plucknett, The reciprocating wear behaviour of TiC-304L stainless steel composites prepared by melt infiltration, Wear. 303 (2013) 321–333. doi:10.1016/j.wear.2013.03.040.

[322] K.P. Plucknett, P.F. Becher, Processing and Microstructure Development of Titanium Carbide-Nickel Aluminide Composites Prepared by Melt Infiltration/Sintering (MIS), J.Am.Ceram.Soc. 84(2001) 55–61. doi:10.1111/j.1151-2916.2001.tb00607.x.

[323] K.P. Plucknett, P.F. Becher, S.B. Waters, Flexure strength of melt-infiltration-processed titanium carbide/nickel aluminide composites, J. Am. Ceram. Soc. 81 (1998) 1839–1844. doi:10.1111/j.1151-2916.1998.tb02555.x.

[324] Z. Memarrashidi, K.P. Plucknett, The influence of Ni_3Al binder content on the aqueous corrosion response of TiC and Ti(C,N) cermets, Int. J. Refract. Met. Hard Mater. 64 (2017) 113–121. doi:10.1016/j.ijrmhm.2017.01.009.

[325] S. Wirojanupatump, P.H. Shipway, D.G. McCartney, The influence of HVOF powder feedstock characteristics on the abrasive wear behaviour of CrxCy-NiCr coatings, Wear. 249 (2001) 829–837. doi:10.1016/S0043-1648(01)00821-3.

[326] L.M. Berger, S. Saaro, T. Naumann, M. Wiener, V. Weihnacht, S. Thiele, J. Suchánek, Microstructure and properties of HVOF-sprayed chromium alloyed WC-Co and WC-Ni coatings, Surf. Coatings Technol. 202 (2008) 4417–4421. doi:10.1016/j.surfcoat.2008.04.019.

[327] G. Mittal, S. Paul, Suspension and Solution Precursor Plasma and HVOF Spray: A Review, J. Therm. Spray Technol. 31 (2022) 1443–1475. doi:10.1007/s11666-022-01360-w.

[328] S. Hochstrasser-Kurz, D. Reiss, T. Suter, C. Latkoczy, D. Günther, S. Virtanen, P.J. Uggowitzer, P. Schmutz, ICP-MS, SKPFM, XPS, and Microcapillary Investigation of the Local Corrosion Mechanisms of WC–Co Hardmetal, J. Electrochem. Soc. 155 (2008) C415. doi:10.1149/1.2929822.

[329] ASTM Standard G102-89, “Standard Practice for Calculation of Corrosion Rates and Related Information,” ASTM International, West Conshohocken, PA, 1999. doi:10.1520/G0102-89R10.

[330] K.P. Plucknett, P.F. Becher, R. Subramanian, Melt-infiltration processing of TiC/Ni_3Al composites, J.Mater. Res.12(1997) 2515–2517 .doi:10.1557/JMR.1997.0332.

[331] G. Bolelli, A. Colella, L. Lusvarghi, S. Morelli, P. Puddu, E. Righetti, P. Sassatelli, V. Testa, TiC–NiCr thermal spray coatings as an alternative to WC-CoCr and Cr3C2–NiCr, Wear. 450–451 (2020) 203273. doi:10.1016/j.wear.2020.203273.

[332] H. Doi, Y. Fujiwara, K. Miyake, Y. Oosawa, A systematic investigation of elastic moduli of WC-Co alloys, Metall. Trans. 3 (1972) 606. doi:10.1007/BF02642078.

[333] R. Chang, L.J. Graham, Low-temperature elastic properties of ZrC and TiC, J. Appl. Phys. 37 (1966) 3778–3783. doi:10.1063/1.1707923.

[334] T.Z. Todorova, M. Gaier, J.W. Zwanziger, K.P. Plucknett, Understanding the elastic and thermal response in TiC-based ceramic-metal composite systems: First-principles and mechanical studies, J. Alloys Compd. 789 (2019) 712–719. doi:10.1016/j.jallcom.2019.03.092.

[335] R. Mahmoodian, M. Hamdi, M.A. Hassan, A. Akbari, Mechanical and chemical characterization of a TiC/C system synthesized using a focus plasma arc, PLoS One. 10 (2015). doi:10.1371/journal.pone.0130836.

[336] J. Ding, C.J. Deng, W.J. Yuan, H.X. Zhu, J. Li, Preparation of porous TiC/C ceramics using wooden template in molten salt media, Adv. Appl. Ceram. 112 (2013) 131–135. doi:10.1179/1743676112Y.0000000052.

[337] T.C. Lei, J.H. Ouyang, Y.T. Pei, Y. Zhou, Microstructure and wear resistance of laser clad TiC particle reinforced coating, Mater. Sci. Technol. (United Kingdom). 11 (1995) 520–525. doi:10.1179/mst.1995.11.5.520.

[338] R.M. Mahamood, E.T. Akinlabi, M. Shukla, S. Pityana, Scanning velocity influence on microstructure, microhardness and wear resistance performance of laser deposited Ti6Al4V/TiC composite, Mater. Des. 50 (2013) 656–666. doi:10.1016/j.matdes.2013.03.049.

[339] F. Sergejev, E. Kimmari, M. Viljus, Residual stresses in TiC-based cermets measured by indentation, Procedia Eng. 10 (2011) 2873–2881. doi:10.1016/j.proeng.2011.04.477.

[340] D. Jiang, C. Hong, M. Zhong, M. Alkhayat, A. Weisheit, A. Gasser, H. Zhang, I. Kelbassa, R. Poprawe, Fabrication of nano-TiCp reinforced Inconel 625 composite coatings by partial dissolution of micro-TiCp through laser cladding energy input control, Surf. Coatings Technol. 249 (2014) 125–131. doi:10.1016/j.surfcoat.2014.03.057.

[341] L. Chen, T. Yu, X. Chen, Y. Zhao, C. Guan, Process optimization, microstructure and microhardness of coaxial laser cladding TiC reinforced Ni-based composite coatings, Opt. Laser Technol. 152 (2022) 108129. doi:10.1016/j.optlastec.2022.108129.

[342] S. V. Dudiy, B.I. Lundqvist, Wetting of TiC and TiN by metals, Phys. Rev. B. 69 (2004) 125421. doi:10.1103/PhysRevB.69.125421.

[343] M. Baumers, P. Dickens, C. Tuck, R. Hague, The cost of additive manufacturing: Machine productivity, economies of scale and technology-push, Technol. Forecast. Soc. Change. 102 (2016) 193–201. doi:10.1016/j.techfore.2015.02.015.

[344] F. Klocke, K. Arntz, M. Teli, K. Winands, M. Wegener, S. Oliari, State-of-the-art Laser Additive Manufacturing for Hot-work Tool Steels, in: Procedia CIRP, Elsevier, 2017: pp. 58–63. doi:10.1016/j.procir.2017.03.073.

[345] M. Leino, J. Pekkarinen, R. Soukka, The role of laser additive manufacturing methods of metals in repair, refurbishment and remanufacturing - Enabling circular economy, in: Phys. Procedia, Elsevier, 2016: pp. 752–760. doi:10.1016/j.phpro.2016.08.077.

[346] A. Zocca, P. Colombo, C.M. Gomes, J. Günster, Additive Manufacturing of Ceramics: Issues, Potentialities, and Opportunities, J. Am. Ceram. Soc. 98 (2015) 1983–2001. doi:10.1111/jace.13700.

[347] L. He, X. Song, Supportability of a High-Yield-Stress Slurry in a New Stereolithography-Based Ceramic Fabrication Process, JOM. 70 (2018) 407–412. doi:10.1007/s11837-017-2657-3.

[348] F.T. Cheng, K.H. Lo, H.C. Man, A preliminary study of laser cladding of AISI 316 stainless steel using preplaced NiTi wire, Mater. Sci. Eng. A. 380 (2004) 20–29. doi:10.1016/j.msea.2004.01.056.

[349] W.C. Tseng, J.N. Aoh, Simulation study on laser cladding on preplaced powder layer with a tailored laser heat source, Opt. Laser Technol. 48 (2013) 141–152. doi:10.1016/j.optlastec.2012.09.014.

[350] J. Powell, P.S. Henry, W.M. Steen, Laser cladding with preplaced powder: Analysis of thermal cycling and dilution effects, Surf. Eng. 4 (1988) 141–149. doi:10.1179/sur.1988.4.2.141.

[351] A. Heinrich, M. Rank, P. Maillard, A. Suckow, Y. Bauckhage, P. Rößler, J. Lang, F. Shariff, S. Pekrul, Additive manufacturing of optical components, Adv. Opt. Technol. 5 (2016) 293–301. doi:10.1515/aot-2016-0021.

[352] S. Hengsbach, A.D. Lantada, Rapid prototyping of multi-scale biomedical microdevices by combining additive manufacturing technologies, Biomed. Microdevices. 16 (2014) 617–627. doi:10.1007/s10544-014-9864-2.

[353] S. Bose, S.F. Robertson, A. Bandyopadhyay, Surface modification of biomaterials and biomedical devices using additive manufacturing, Acta Biomater. 66 (2018) 6–22. doi:10.1016/j.actbio.2017.11.003.

[354] K. Dixit, A. Raichur, N. Sinha, Polymer-Coated and Nanofiber-Reinforced Functionally Graded Bioactive Glass Scaffolds Fabricated Using Additive Manufacturing, IEEE Trans. Nanobioscience. 21 (2022) 380–386. doi:10.1109/TNB.2021.3083278.

[355] A. Motealleh, S. Eqtesadi, F.H. Perera, A. Pajares, F. Guiberteau, P. Miranda, Understanding the role of dip-coating process parameters in the mechanical performance of polymer-coated bioglass robocast scaffolds, J. Mech. Behav. Biomed. Mater. 64 (2016) 253–261. doi:10.1016/j.jmbbm.2016.08.004.

[356] M. Alhabeb, K. Maleski, B. Anasori, P. Lelyukh, L. Clark, S. Sin, Y. Gogotsi, Guidelines for Synthesis and Processing of Two-Dimensional Titanium Carbide ($Ti_3C_2T_x$ MXene), Chem. Mater. 29 (2017) 7633 –7644. doi:10.1021/acs.chemmater.7b02847.

[357] C.J. Brinker, G.C. Frye, A.J. Hurd, C.S. Ashley, Fundamentals of sol-gel dip coating, Thin Solid Films. 201 (1991) 97–108. doi:10.1016/0040-6090(91)90158-T.

[358] D. Gailevičius, V. Padolskytė, L. Mikoliūnaitė, S. Šakirzanovas, S. Juodkazis, M. Malinauskas, Additive-manufacturing of 3D glass-ceramics down to nanoscale resolution, Nanoscale Horizons. 4 (2019) 647–651. doi:10.1039/c8nh00293b.

[359] I. Cooperstein, E. Shukrun, O. Press, A. Kamyshny, S. Magdassi, Additive Manufacturing of Transparent Silica Glass from Solutions, ACS Appl. Mater. Interfaces. 10 (2018) 18879–18885. doi:10.1021/acsami.8b03766.

[360] W. Xi, B. Song, Y. Zhao, T. Yu, J. Wang, Geometry and dilution rate analysis and prediction of laser cladding, Int. J. Adv. Manuf. Technol. 103 (2019) 4695–4702. doi:10.1007/s00170-019-03932-7.

[361] I. Hemmati, V. Ocelík, J.T.M. De Hosson, Dilution effects in laser cladding of Ni-Cr-B-Si-C hardfacing alloys, Mater. Lett. 84 (2012) 69–72. doi:10.1016/j.matlet.2012.06.054.

[362] J. Liao, H. Li, W. Zeng, D.B. Sauer, R. Belmares, Y. Jiang, Structural insight into the ion-exchange mechanism of the sodium/calcium exchanger, Science (80-.). 335 (2012) 686–690. doi:10.1126/science.1215759.

[363] J. Brus, M. Urbanova, J. Czernek, M. Pavelkova, K. Kubova, J. Vyslouzil, S. Abbrent, R. Konefal, J. Horský, D. Vetchy, J. Vysloužil, P. Kulich, Structure and Dynamics of Alginate Gels Cross-Linked by Polyvalent Ions Probed via Solid State NMR Spectroscopy, Biomacromolecules. 18 (2017) 2478–2488. doi:10.1021/acs.biomac.7b00627.

[364] P. Jozwik, W. Polkowski, Z. Bojar, Applications of Ni_3Al based intermetallic alloys-current stage and potential perceptivities, Materials (Basel). 8 (2015) 2537–2568. doi:10.3390/ma8052537.

[365] R.B. Collier, K.P. Plucknett, Spherical indentation damage in TiC-Ni_3Al composites, Int. J. Refract. Met. Hard Mater. 30 (2012) 188–195. doi:10.1016/j.ijrmhm.2011.08.008.

[366] B.L. He, Y.F. Zhu, Microstructure and properties of TiC/Ni_3Al composites prepared by pressureless melt infiltration with porous TiC/Ni_3Al preforms, Mater. Manuf. Process. 26 (2011) 586–591. doi:10.1080/10426910903229339.

[367] L.M. Zhang, J. Liu, R.Z. Yuan, T. Hirai, Properties of $TiCNi_3Al$ composites and structural optimization of $TiCNi_3Al$ functionally gradient materials, Mater. Sci. Eng. A. 203 (1995) 272–277. doi:10.1016/0921-5093(95)09823-2.

[368] A. Interanational, Standard Guide for Preparation of Metallographic Specimens Standard Guide for Preparation of Metallographic Specimens 1, ASTM Int. 03.01 (2012) 1–12. doi:10.1520/E0003-11R17.1.

[369] J. Ion, Laser Processing of Engineering Materials, 2005. doi:10.1016/0301-679x(77)90212-2.

[370] C. Ouwerx, N. Velings, M.M. Mestdagh, M.A.V. Axelos, Physico-chemical properties and rheology of alginate gel beads formed with various divalent cations, Polym. Gels Networks. 6 (1998) 393–408. doi:10.1016/S0966-7822(98)00035-5.

[371] Q. Zhou, H. Kang, M. Bielec, X. Wu, Q. Cheng, W. Wei, H. Dai, Influence of different divalent ions cross-linking sodium alginate-polyacrylamide hydrogels on antibacterial properties and wound healing, Carbohydr. Polym. 197 (2018) 292–304. doi:10.1016/j.carbpol.2018.05.078.

[372] A. Haug, O. Smidsrød, The effect of divalent metals on the properties of alginate solutions, Acta Chem. Scand. 19 (1965) 341–351.

[373] Z. jian Shao, X. lian Huang, F. Yang, W. feng Zhao, X. zhi Zhou, C. sheng Zhao, Engineering sodium alginate-based cross-linked beads with high removal ability of toxic metal ions and cationic dyes, Carbohydr. Polym. 187 (2018) 85–93. doi:10.1016/j.carbpol.2018.01.092.

[374] C. Jeong, S. Kim, C. Lee, S. Cho, S.B. Kim, Changes in the physical properties of calcium alginate gel beads under a wide range of gelation temperature conditions, Foods. 9 (2020) 180. doi:10.3390/foods9020180.

[375] G.A.W. Sweet, I.W. Donaldson, C.T. Schade, M.Y. Amegadzie, D.P. Bishop, Laser free-form fabrication of dual phase DP600 steel using water atomized feedstock powder, Addit. Manuf. 47 (2021). doi:10.1016/j.addma.2021.102357.

[376] W. Wang, S. Kelly, A Metallurgical Evaluation of the Powder-Bed Laser Additive Manufactured 4140 Steel Material, JOM. 68 (2016) 869–875. doi:10.1007/s11837-015-1804-y.

[377] D. Gu, Y. Shen, Effects of processing parameters on consolidation and microstructure of W-Cu components by DMLS, J. Alloys Compd. 473 (2009) 107–115. doi:10.1016/j.jallcom.2008.05.065.

[378] C.T. Tran, T.N. Dinh, The effective convectivity model for simulation of melt pool heat transfer in a light water reactor pressure vessel lower head. Part I: Physical processes, modeling and model implementation, Prog. Nucl. Energy. 51 (2009) 849–859. doi:10.1016/j.pnucene.2009.06.007.

[379] J.I. Arrizubieta, A. Lamikiz, F. Klocke, S. Martínez, K. Arntz, E. Ukar, Evaluation of the relevance of melt pool dynamics in Laser Material Deposition process modeling, Int. J. Heat Mass Transf. 115 (2017) 80–91. doi:10.1016/j.ijheatmasstransfer.2017.07.011.

[380] P. Promoppatum, S.C. Yao, P.C. Pistorius, A.D. Rollett, A Comprehensive Comparison of the Analytical and Numerical Prediction of the Thermal History and Solidification Microstructure of Inconel 718 Products Made by Laser Powder-Bed Fusion, Engineering. 3 (2017) 685–694. doi:10.1016/J.ENG.2017.05.023.

[381] Harry Chandler, Heat Treater's Guide: Practices and Procedures for Irons and Steels, ASM International, 2006.

[382] A. Emamian, S.F. Corbin, A. Khajepour, Effect of laser cladding process parameters on clad quality and in-situ formed microstructure of Fe-TiC composite coatings, Surf. Coatings Technol. 205 (2010) 2007–2015. doi:10.1016/j.surfcoat.2010.08.087.

[383] G.Z. Wang, J.H. Chen, A comparison of fracture behavior of low alloy steel with different sizes of carbide particles, Metall. Mater. Trans. A Phys. Metall. Mater. Sci. 27 (1996) 1909–1917. doi:10.1007/BF02651940.

[384] W. Liu, Y. Guo, Y. Cao, J. Wang, Z. Hou, M. Sun, B. Xu, D. Li, Transformation behavior of primary MC and M_2C carbides in Cr_4Mo_4V steel, J. Alloys Compd. 889 (2022) 161755. doi:10.1016/j.jallcom.2021.161755.

[385] X. Zhou, F. Fang, L.I. Gang, J. Jiang, Morphology and properties of M_2C eutectic carbides in AISI M2 steel, ISIJ Int. 50 (2010) 1151–1157. doi:10.2355/isijinternational.50.1151.

[386] A. Khalili, M. Goodarzi, M. Mojtahedi, M.J. Torkamany, Solidification microstructure of in-situ laser-synthesized Fe-TiC hard coating, Surf. Coatings Technol. 307 (2016) 747–752. doi:10.1016/j.surfcoat.2016.09.051.

[387] X. Wang, G.T. MacLennan, S. Zhang, R. Montironi, A. Lopez-Beltran, P.H. Tan, S. Foster, L.A. Baldridge, L. Cheng, Sarcomatoid carcinoma of the upper urinary tract: clinical outcome and molecular characterization, Hum. Pathol. 40 (2009) 211–217. doi:10.1016/j.humpath.2008.07.003.

[388] H. Nowotny, P. Rogl, J.C. Schuster, Structural chemistry of complex carbides and related compounds, J. Solid State Chem. 44 (1982) 126–133. doi:10.1016/0022-4596(82)90409-1.

[389] W. Xiang, M. Xuliang, L. Xinlin, D. Lihua, W. Mingjia, Effect of boron addition on microstructure and mechanical properties of TiC/Ti6Al4V composites, Mater. Des. 36 (2012) 41–46. doi:10.1016/j.matdes.2011.10.040.

[390] T. Xu, W. Wang, H. Jiang, G. He, Study on micro crack propagation mechanism of ferrite–pearlite gas transmission pipeline steel with lamellar structure, Sci. Rep. 12 (2022) 1–26. doi:10.1038/s41598-022-23405-4.

[391] S. Wang, X. Zhao, P. Liu, J. Pan, C. Chen, R. Ren, Investigation of the Relation between Rolling Contact Fatigue Property and Microstructure on the Surface Layer of D2 Wheel Steel, Mater. Sci. Appl. 10 (2019) 509–526. doi:10.4236/msa.2019.108037.

[392] T.I. El Wardany, M.A. Elbestawi, Prediction of tool failure rate in turning hardened steels, Int. J. Adv. Manuf. Technol. 13 (1997) 1–16. doi:10.1007/BF01179225.

[393] Y. Murakami, N.N. Yokoyama, J. Nagata, Mechanism of fatigue failure in ultralong life regime, Fatigue Fract. Eng. Mater. Struct. 25 (2002) 735–746. doi:10.1046/j.1460-2695.2002.00576.x.

[394] K.H.Z. Gahr, Wear by hard particles, Tribol. Int. 31 (1998) 587–596. doi:10.1016/S0301-679X(98)00079-6.

[395] M. Nagumo, M. Nakamura, K. Takai, Hydrogen thermal desorption relevant to delayed-fracture susceptibility of high-strength steels, Metall. Mater. Trans. A Phys. Metall. Mater. Sci. 32 (2001) 339–347. doi:10.1007/s11661-001-0265-9.

[396] J.I. Verdeja, J. Asensio, J.A. Pero-Sanz, Texture, formability, lamellar tearing and HIC susceptibility of ferritic and low-carbon HSLA steels, Mater. Charact. 50 (2003) 81–86. doi:10.1016/S1044-5803(03)00106-2.

[397] M. Cabeza, G. Castro, P. Merino, G. Penaa, M. Roman, A study of laser melt injection of TiN particles to repair maraging tool steels, Surf. Interface Anal. 46 (2014) 861–864. doi:10.1002/sia.5373.

[398] M. Vedani, Microstructural evolution of tool steels after Nd-YAG laser repair welding, J. Mater. Sci. 39 (2004) 241–249. doi:10.1023/B:JMSC.0000007750.16970.4e.

[399] P. Kattire, S. Paul, R. Singh, W. Yan, Experimental characterization of laser cladding of CPM 9V on H13 tool steel for die repair applications, J. Manuf. Process. 20 (2015) 492–499. doi:10.1016/j.jmapro.2015.06.018.

[400] Y. Wang, Z. Jiang, Z. Yao, H. Tang, Microstructure and corrosion resistance of ceramic coating on carbon steel prepared by plasma electrolytic oxidation, Surf. Coatings Technol. 204 (2010) 1685–1688. doi:10.1016/j.surfcoat.2009.10.023.

[401] R. Mallick, R. Kumar, A. Panda, A.K. Sahoo, Performance characteristics of hardened AISI D2 steel turning: A review, in: Mater. Today Proc., Elsevier, 2019: pp. 2685–2690. doi:10.1016/j.matpr.2020.02.565.

[402] S. Chinchanikar, S.K. Choudhury, Machining of hardened steel - Experimental investigations, performance modeling and cooling techniques: A review, Int. J. Mach. Tools Manuf. 89 (2015) 95–109. doi:10.1016/j.ijmachtools.2014.11.002.

[403] K. Aslantas, T.I. Ucun, A. Çicek, Tool life and wear mechanism of coated and uncoated Al 2O 3/TiCN mixed ceramic tools in turning hardened alloy steel, Wear. 274–275 (2012) 442–451. doi:10.1016/j.wear.2011.11.010.

[404] P.B. Kadolkar, T.R. Watkins, J.T.M. De Hosson, B.J. Kooi, N.B. Dahotre, State of residual stress in laser-deposited ceramic composite coatings on aluminum alloys, Acta Mater. 55 (2007) 1203–1214. doi:10.1016/j.actamat.2006.07.049.

[405] A.A. Voevodin, M.S. Donley, J.S. Zabinski, Pulsed laser deposition of diamond-like carbon wear protective coatings: A review, Surf. Coatings Technol. 92 (1997) 42–49. doi:10.1016/S0257-8972(97)00007-8.

[406] D.G. Teer, J. Hampshire, V. Fox, V. Bellido-Gonzalez, The tribological properties of MoS_2/metal composite coatings deposited by closed field magnetron sputtering, Surf. Coatings Technol. 94–95 (1997) 572–577. doi:10.1016/S0257-8972(97)00498-2.

[407] L. Benea, P.L. Bonora, A. Borello, S. Martelli, F. Wenger, P. Ponthiaux, J. Galland, Composite Electrodeposition to Obtain Nanostructured Coatings, J. Electrochem. Soc. 148 (2001) C461. doi:10.1149/1.1377279.

[408] I. Gurrappa, L. Binder, Electrodeposition of nanostructured coatings and their characterization - A review, Sci. Technol. Adv. Mater. 9 (2008) 43001–43012. doi:10.1088/1468-6996/9/4/043001.

[409] M. Van Stappen, L.M. Stals, M. Kerkhofs, C. Quaeyhaegens, State of the art for the industrial use of ceramic PVD coatings, Surf. Coatings Technol. 74–75 (1995) 629–633. doi:10.1016/0257-8972(95)08296-4.

[410] X. Huang, S. Sun, G. Tu, Investigation of mechanical properties and oxidation resistance of CVD TiB_2 ceramic coating on molybdenum, J. Mater. Res. Technol. 9 (2020) 282–290. doi:10.1016/j.jmrt.2019.10.056.

[411] R. Naslain, F. Langlais, CVD-Processing of Ceramic-Ceramic Composite Materials, in: Tailoring Multiph. Compos. Ceram., Springer, Boston, MA, 1986: pp. 145–164. doi:10.1007/978-1-4613-2233-7_12.

[412] K.L. Choy, Chemical vapour deposition of coatings, Prog. Mater. Sci. 48 (2003) 57–170. doi:10.1016/S0079-6425(01)00009-3.

[413] G. Li, L.F. Xia, Structural characterization of TiCx films prepared by plasma based ion implantation, Thin Solid Films. 396 (2001) 16–22. doi:10.1016/S0040-6090(01)01227-5.

[414] E. Kusano, A. Satoh, M. Kitagawa, H. Nanto, A. Kinbara, Titanium carbide film deposition by DC magnetron reactive sputtering using a solid carbon source, Thin Solid Films. 343–344 (1999) 254–256. doi:10.1016/S0040-6090(98)01638-1.

[415] N. Balasubramanyam, S.G. Prasanthi, M. Yugandhar, Study o f Coated TiN and TiC on Cutting Tools f or t he PVD and CVD Coated Tungsten Carbide by Sand Blasting Pretreatment o f Nickel and Carbon, Int. J. Adv. Sci. Technol. 75 (2015) 51–58. doi:10.14257/ijast.2015.75.06.

[416] S. Kinkel, G.N. Angelopoulos, W. Dahl, Formation of TiC coatings on steels by a fluidized bed chemical vapour deposition process, Surf. Coatings Technol. 64 (1994) 119–125. doi:10.1016/S0257-8972(09)90012-3.

[417] J. Morimoto, Y. Sasaki, S. Fukuhara, N. Abe, M. Tukamoto, Surface modification of Cr_3C_2-NiCr cermet coatings by direct diode laser, Vacuum. 80 (2006) 1400–1405. doi:10.1016/j.vacuum.2006.01.070.

[418] J. Xu, B. Zou, S. Zhao, Y. Hui, W. Huang, X. Zhou, Y. Wang, X. Cai, X. Cao, Fabrication and properties of ZrC-ZrB2/Ni cermet coatings on a magnesium alloy by atmospheric plasma spraying of SHS powders, Ceram. Int. 40 (2014) 15537–15544. doi:10.1016/j.ceramint.2014.07.029.

[419] Y. Arata, A. Kobayashi, Y. Habara, Ceramic coatings produced by means of a gas tunnel-type plasma jet, J. Appl. Phys. 62 (1987) 4884–4889. doi:10.1063/1.338995.

[420] L. Qiao, Y. Wu, S. Hong, W. Long, J. Cheng, Wet abrasive wear behavior of WC-based cermet coatings prepared by HVOF spraying, Ceram. Int. 47 (2021) 1829–1836. doi:10.1016/j.ceramint.2020.09.009.

[421] A. Möller, H. Hahn, Synthesis and characterization of nanocrystalline Ni/ZrO_2 composite coatings, Nanostructured Mater. 12 (1999) 259–262. doi:10.1016/S0965-9773(99)00112-9.

[422] R. Koc, C. Meng, G.A. Swift, Sintering properties of submicron TiC powders from carbon coated titania precursor, J. Mater. Sci. 35 (2000) 3131–3141. doi:10.1023/A:1004876121000.

[423] N. Li, W. Liu, H. Xiong, R. Qin, S. Huang, G. Zhang, C. Gao, In-situ reaction of Ti-Si-C composite powder and formation mechanism of laser deposited Ti6Al4V/(TiC+Ti_3SiC_2) system functionally graded material, Mater. Des. 183 (2019). doi:10.1016/j.matdes.2019.108155.

[424] Y. Li, D. Zhang, Z. Ye, G. Ye, R. He, H. Wang, W. Cong, The reinforcement mechanisms of graphene oxide in laser-directed energy deposition fabricated metal and ceramic matrix composites: a comparison study, Int. J. Adv. Manuf. Technol. (2021) 1–14. doi:10.1007/s00170-021-08337-z.

[425] D.I. Pantelis, E. Bouyiouri, N. Kouloumbi, P. Vassiliou, A. Koutsomichalis, Wear and corrosion resistance of laser surface hardened structural steel, Surf. Coatings Technol. 161 (2002) 125–134. doi:10.1016/S0257-8972(02)00495-4.

[426] I.R. Pashby, S. Barnes, B.G. Bryden, Surface hardening of steel using a high power diode laser, J. Mater. Process. Technol. 139 (2003) 585–588. doi:10.1016/S0924-0136(03)00509-0.

[427] P.D. Babu, K.R. Balasubramanian, G. Buvanashekaran, Laser surface hardening: A review, Int. J. Surf. Sci. Eng. 5 (2011) 131–151. doi:10.1504/IJSURFSE.2011.041398.

[428] E. Kennedy, G. Byrne, D.N. Collins, A review of the use of high power diode lasers in surface hardening, J. Mater. Process. Technol. 155–156 (2004) 1855–1860. doi:10.1016/j.jmatprotec.2004.04.276.

[429] S. Buchholz, Z.N. Farhat, G.J. Kipouros, K.P. Plucknett, The reciprocating wear behaviour of TiC-Ni_3Al cermets, Int. J. Refract. Met. Hard Mater. 33 (2012) 44–52. doi:10.1016/j.ijrmhm.2012.02.008.

[430] K.I. Parashivamurthy, R.K. Kumar, S. Seetharamu, M.N. Chandrasekharaiah, Review on TiC reinforced steel composites, J. Mater. Sci. 36 (2001) 4519–4530. doi:10.1023/A:1017947206490.

[431] I. Hussainova, J. Kubarsepp, J. Pirso, Mechanical properties and features of erosion of cermets, Wear. 250–251 (2001) 818–825. doi:10.1016/S0043-1648(01)00737-2.

[432] C. Jin, C.C. Onuoha, Z.N. Farhat, G.J. Kipouros, K.P. Plucknett, Reciprocating wear behaviour of TiC-stainless steel cermets, Tribol. Int. 105 (2017) 250–263. doi:10.1016/j.triboint.2016.10.012.

[433] S. Jhavar, C.P. Paul, N.K. Jain, Causes of failure and repairing options for dies and molds: A review, Eng. Fail. Anal. 34 (2013) 519–535. doi:10.1016/j.engfailanal.2013.09.006.

[434] M.A.S. Bin Abdul Rahim, M. Bin Minhat, N.I.S.B. Hussein, M.S. Bin Salleh, A comprehensive review on cold work of AISI D2 tool steel, Metall. Res. Technol. 115 (2018) 104. doi:10.1051/metal/2017048.

[435] K.N. Lyon, T.J. Marrow, S.B. Lyon, Influence of milling on the development of stress corrosion cracks in austenitic stainless steel, J. Mater. Process. Technol. 218 (2015) 32–37. doi:10.1016/j.jmatprotec.2014.11.038.

[436] R.S. Tresder, T.M. SWANSON, Factors in Sulfide Corrosion Cracking of High Strength Steels, Corrosion. 24 (1968) 31–37. doi:10.5006/0010-9312-24.2.31.

[437] N. Eliaz, A. Shachar, B. Tal, D. Eliezer, Characteristics of hydrogen embrittlement, stress corrosion cracking and tempered martensite embrittlement in high-strength steels, Eng. Fail. Anal. 9 (2002) 167–184. doi:10.1016/S1350-6307(01)00009-7.

[438] D.A. Lesyk, S. Martinez, B.N. Mordyuk, V. V. Dzhemelinskyi, Lamikiz, G.I. Prokopenko, Y. V. Milman, K.E. Grinkevych, Microstructure related enhancement in wear resistance of tool steel AISI D2 by applying laser heat treatment followed by ultrasonic impact treatment, Surf. Coatings Technol. 328 (2017) 344–354. doi:10.1016/j.surfcoat.2017.08.045.

[439] R. Šturm, M. Štefanikova, D.S. Petrovič, Influence of pre-heating on the surface modification of powder-metallurgy processed cold-work tool steel during laser surface melting, Appl. Surf. Sci. 325 (2015) 203–210. doi:10.1016/j.apsusc.2014.11.050.

[440] D.A. Lesyk, S. Martinez, V. V. Dzhemelinskyy, A. Lamikiz, B.N. Mordyuk, G.I. Prokopenko, Surface microrelief and hardness of laser hardened and ultrasonically peened AISI D2 tool steel, Surf. Coatings Technol. 278 (2015) 108–120. doi:10.1016/j.surfcoat.2015.07.049.

[441] M. seob Kim, W. jin Oh, G. yoon Baek, Y. kwan Jo, K. yong Lee, S. hu Park, D. sik Shim, Ultrasonic nanocrystal surface modification of high-speed tool steel (AISI M4) layered via direct energy deposition, J. Mater. Process. Technol. 277 (2020) 116420. doi:10.1016/j.jmatprotec.2019.116420.

[442] D.D. Gu, W. Meiners, K. Wissenbach, R. Poprawe, Laser additive manufacturing of metallic components: Materials, processes and mechanisms, Int. Mater. Rev. 57 (2012) 133–164. doi:10.1179/1743280411Y.0000000014.

[443] M.S. Sohn, X.Z. Hu, J.K. Kim, L. Walker, Impact damage characterization of carbon fibre/epoxy composites with multi-layer reinforcement, Compos. Part B Eng. 31 (2000) 681–691. doi:10.1016/S1359-8368(00)00028-7.

[444] R. Jendrzejewski, A. Conde, J. de Damborenea, G. Sliwinski, Characterisation of the laser-clad stellite layers for protective coatings, Mater. Des. 23 (2002) 83–88. doi:10.1016/S0261-3069(01)00074-7.

[445] S. Sreekanth, E. Ghassemali, K. Hurtig, S. Joshi, J. Andersson, Effect of direct energy deposition process parameters on single-track deposits of alloy 718, Metals (Basel). 10 (2020) 96. doi:10.3390/met10010096.

[446] J. Do Kim, Y. Peng, Melt pool shape and dilution of laser cladding with wire feeding, J. Mater. Process. Technol. 104 (2000) 284–293. doi:10.1016/S0924-0136(00)00528-8.

[447] ASTM E2546-15, Standard Practice for Instrumented Indentation Testing ASTM E2546-15, ASTM B. Stand. 1 (2015) 1–23. doi:10.1520/E2546-15.2.

[448] A. C1624-05 (2015), Standard Test Method for Adhesion Strength and Mechanical Failure Modes of, ASTM Int. C1624-05 (2012) 1–29. doi:10.1520/C1624-22.

[449] A. Vencl, S. Arostegui, G. Favaro, F. Zivic, M. Mrdak, S. Mitrović, V. Popovic, Evaluation of adhesion/cohesion bond strength of the thick plasma spray coatings by scratch testing on coatings cross-sections, in: Tribol. Int., Elsevier, 2011: pp. 1281–1288. doi:10.1016/j.triboint.2011.04.002.

[450] L. Tonelli, A. Fortunato, L. Ceschini, CoCr alloy processed by Selective Laser Melting (SLM): effect of Laser Energy Density on microstructure, surface morphology, and hardness, J. Manuf. Process. 52 (2020) 106–119. doi:10.1016/j.jmapro.2020.01.052.

[451] X. Zhou, K. Li, D. Zhang, X. Liu, J. Ma, W. Liu, Z. Shen, Textures formed in a CoCrMo alloy by selective laser melting, J. Alloys Compd. 631 (2015) 153–164. doi:10.1016/j.jallcom.2015.01.096.

[452] P. Kadolkar, N.B. Dahotre, Variation of structure with input energy during laser surface engineering of ceramic coatings on aluminum alloys, Appl. Surf. Sci. 199 (2002) 222–233. doi:10.1016/S0169-4332(02)00799-7.

[453] T. Chande, J. Mazumder, Estimating effects of processing conditions and variable properties upon pool shape, cooling rates, and absorption coefficient in laser welding, J. Appl. Phys. 56 (1984) 1981–1986. doi:10.1063/1.334231.

[454] Y.S. Tian, C.Z. Chen, L.B. Chen, L.X. Chen, Study on the microstructure and wear resistance of the composite coatings fabricated on Ti-6Al4V under different processing conditions, Appl. Surf. Sci. 253 (2006) 1494–1499. doi:10.1016/j.apsusc.2006.02.026.

[455] H. Zhao, F. Qiu, S. Jin, Q. Jiang, High room-temperature plastic and work-hardening effect of the NiAl-matrix composites reinforced by particulates, Intermetallics. 19 (2011) 376–381. doi:10.1016/j.intermet.2010.10.023.

[456] J.R. Weertman, D. Farkas, K. Hemker, H. Kung, M. Mayo, R. Mitra, H. Van Swygenhoven, Structure and mechanical behavior of bulk nanocrystalline materials, MRS Bull. 24 (1999) 44–50. doi:10.1557/s088376940005154x.

[457] S. Pauly, J. Das, C. Duhamel, J. Eckert, Effect of titanium on microstructure and mechanical properties of Cu50Zr50-xTix (2.5 ≤ × ≤ 7.5) glass matrix composites, in: Metall. Mater. Trans. A Phys. Metall. Mater. Sci., Springer Boston, 2008: pp. 1868–1873. doi:10.1007/s11661-007-9291-6.

[458] K.D. Bouzakis, A. Asimakopoulos, N. Michailidis, S. Kompogiannis, G. Maliaris, G. Giannopoulos, E. Pavlidou, G. Erkens, The inclined impact test, an efficient method to characterize coatings' cohesion and adhesion properties, Thin Solid Films. 469–470 (2004) 254–262. doi:10.1016/j.tsf.2004.08.093.

[459] R. Lacombe, Adhesion Measurement Methods, CRC Press, 2005. doi:10.1201/9781420028829.

[460] M.H. Staia, Y. Pérez-Delgado, C. Sanchez, A. Castro, E. Le Bourhis, E.S. Puchi-Cabrera, Hardness properties and high-temperature wear behavior of nitrided AISI D2 tool steel, prior and after PAPVD coating, Wear. 267 (2009) 1452–1461. doi:10.1016/j.wear.2009.03.045.

[461] J. Hardell, B. Prakash, High-temperature friction and wear behaviour of different tool steels during sliding against Al-Si-coated high-strength steel, Tribol. Int. 41 (2008) 663–671. doi:10.1016/j.triboint.2007.07.013.

[462] A. Pauschitz, M. Roy, F. Franek, Mechanisms of sliding wear of metals and alloys at elevated temperatures, Tribol. Int. 41 (2008) 584–602. doi:10.1016/j.triboint.2007.10.003.

[463] N. Yasavol, A. Abdollah-Zadeh, M. Ganjali, S.A. Alidokht, Microstructure and mechanical behavior of pulsed laser surface melted AISI D2 cold work tool steel, Appl. Surf. Sci. 265 (2013) 653–662. doi:10.1016/j.apsusc.2012.11.070.

[464] A. Moradiani, Z.M. Beiranvand, R.M.C. Ratnayake, A. Aliabadi, M. Rasoulinia, The effect of laser surface melting on the retained austenite and wear properties of AISI D2 tool steel, Optik (Stuttg). 252 (2022). doi:10.1016/j.ijleo.2021.168469.

[465] S.E. Offerman, N.H. Van Dijk, M.T. Rekveldt, J. Sietsma, S. Van der Zwaag, Ferrite/pearlite band formation in hot rolled medium carbon steel, Mater. Sci. Technol. 18 (2002) 297–303. doi:10.1179/026708301225000752.

[466] A. Bhattacharyya, G. Subhash, N. Arakere, Evolution of subsurface plastic zone due to rolling contact fatigue of M-50 NiL case hardened bearing steel, Int. J. Fatigue. 59 (2014) 102–113. doi:10.1016/j.ijfatigue.2013.09.010.

[467] A. Gasser, G. Backes, I. Kelbassa, A. Weisheit, K. Wissenbach, Laser Additive Manufacturing, Laser Tech. J. 7 (2010) 58–63. doi:10.1002/latj.201090029.

[468] Y. long Wang, Y. li Chen, W. Yu, Effect of Cr/Mn segregation on pearlite—martensite banded structure of high carbon bearing steel, Int. J. Miner. Metall. Mater. 28 (2021) 665–675. doi:10.1007/S12613-020-2035-Y/METRICS.

[469] J. Sampedro, I. Pérez, B. Carcel, J.A. Ramos, V. Amigó, Laser cladding of TiC for better titanium components, in: Phys. Procedia, Elsevier, 2011: pp. 313–322. doi:10.1016/j.phpro.2011.03.040.

[470] I. Hussainova, Microstructure and erosive wear in ceramic-based composites, in: Wear, Elsevier, 2005: pp. 357–365. doi:10.1016/j.wear.2004.01.024.

[471] I. Hussainova, Effect of microstructure on the erosive wear of titanium carbide-based cermets, Wear. 255 (2003) 121–128. doi:10.1016/S0043-1648(03)00198-4.

[472] A. Rajabi, M.J.G. et al., M.J. Ghazali, A.R. Daud, M.J.G. et al., Chemical composition, microstructure and sintering temperature modifications on mechanical properties of TiC-based cermet - A review, Mater. Des. 67 (2015) 95–106. doi:10.1016/j.matdes.2014.10.081.

[473] H.J. Boving, H.E. Hintermann, Wear-resistant hard titanium carbide coatings for space applications, Tribol. Int. 23 (1990) 129–133. doi:10.1016/0301-679X(90)90045-Q.

[474] A.K. Srivastava, K. Das, The abrasive wear resistance of TiC and (Ti,W)C-reinforced Fe-17Mn austenitic steel matrix composites, Tribol. Int. 43 (2010) 944–950. doi:10.1016/j.triboint.2009.12.057.

[475] H. Berns, B. Wewers, Development of an abrasion resistant steel composite with in situ TiC particles, Wear. 250–251 (2001) 1386–1395. doi:10.1016/S0043-1648(01)00790-6.

[476] X.Q. You, T.Z. Si, N. Liu, P.P. Ren, Y.D. Xu, J.P. Feng, Effect of grain size on thermal shock resistance of Al2O 3-TiC ceramics, Ceram. Int. 31 (2005) 33–38. doi:10.1016/j.ceramint.2004.02.009.

[477] G. Radhakrishnan, P.M. Adams, D.M. Speckman, Low temperature pulsed laser deposition of titanium carbide on bearing steels, Thin Solid Films. 358 (2000) 131–138. doi:10.1016/S0040-6090(99)00681-1.

[478] Z. Memarrashidi and K. P. Plucknett, The Effect of Binder Content on the Aqueous Corrosion Response of WC-Co Cermets-com2015, 2014 (2014). http://www.programmaster.org/PM/PM.nsf/ApprovedAbstracts/1D194ABA75CABD6A85257C9B005ABAED?OpenDocument.

[479] D. Kong, C. Dong, X. Ni, L. Zhang, C. Man, G. Zhu, J. Yao, L. Wang, X. Cheng, X. Li, Effect of TiC content on the mechanical and corrosion properties of Inconel 718 alloy fabricated by a high-throughput dual-feed laser metal deposition system, J. Alloys Compd. 803 (2019) 637–648. doi:10.1016/j.jallcom.2019.06.317.

[480] H. Zhang, D. Gu, L. Xi, H. Zhang, M. Xia, C. Ma, Anisotropic corrosion resistance of TiC reinforced Ni-based composites fabricated by selective laser melting, J. Mater. Sci. Technol. 35 (2019) 1128–1136. doi:10.1016/j.jmst.2018.12.020.

[481] A.L.G. Stern, M., Electrochemical Polarization: I . A Theoretical Analysis of the Shape of Polarization Curves, J. Electrochem. Soc. 104 (1957) 56.

[482] H. Wang, Y. ping Bao, M. Zhao, M. Wang, X. ming Yuan, S. Gao, Effect of Ce on the cleanliness, microstructure and mechanical properties of high strength low alloy steel Q690E in industrial production process, Int. J. Miner. Metall. Mater. 26 (2019) 1372–1384. doi:10.1007/s12613-019-1871-0.

[483] J.-H. Park, K.-S. Kim, J.-Y. Kim, J.-B. Jeon, Y.-M. Koo, K.-A. Lee, Microstructure and Tensile Properties of Bulk Aisi D2 Tool Steel Fabricated by Direct Energy Deposition, SSRN Electron. J. (2022). doi:10.2139/ssrn.4034576.

[484] K. Zelič, J. Burja, P.J. McGuiness, M. Godec, Effect of Rare Earth Elements on the Morphology of Eutectic Carbides in AISI D2 Tool Steels: Experimental and Modelling Approaches, Sci. Rep. 8 (2018). doi:10.1038/S41598-018-27658-W.

[485] J.K. Kim, Y.H. Kim, S.H. Uhm, J.S. Lee, K.Y. Kim, Intergranular corrosion of Ti-stabilized 11 wt% Cr ferritic stainless steel for automotive exhaust systems, Corros. Sci. 51 (2009) 2716–2723. doi:10.1016/j.corsci.2009.07.008.

[486] B. Poulson, The sensitization of ferritic steels containing less than 12% Cr, Corros. Sci. 18 (1978) 371–395. doi:10.1016/S0010-938X(78)80051-1.

[487] V. Kuzucu, M. Aksoy, M.H. Korkut, M.M. Yildirim, The effect of niobium on the microstructure of ferritic stainless steel, Mater. Sci. Eng. A. 230 (1997) 75–80. doi:10.1016/s0921-5093(97)00010-5.

[488] Y. Xu, H. Fu, L. Fan, B. Lu, H. Zhao, H. Dong, Oxidation kinetics and mechanisms of aluminum modified ultra-pure low chromium ferritic stainless steels, Corros. Sci. 161 (2019) 108192. doi:10.1016/j.corsci.2019.108192.

[489] D.W. Yun, S.M. Seo, H.W. Jeong, Y.S. Yoo, The effects of the minor alloying elements Al, Si and Mn on the cyclic oxidation of Ni-Cr-W-Mo alloys, Corros. Sci. 83 (2014) 176–188. doi:10.1016/j.corsci.2014.02.015.

[490] X. Guo, K. Chen, W. Gao, Z. Shen, L. Zhang, Corrosion behavior of alumina-forming and oxide dispersion strengthened austenitic 316 stainless steel in supercritical water, Corros. Sci. 138 (2018) 297–306. doi:10.1016/j.corsci.2018.04.026.

[491] Z. Memarrashidi, The Aqueous Corrosion Response of Ti(C,N), TiC and WC Based Ceramic-Metal Composites,(2015). http://dalspace.library.dal.ca:8080/bitstream/handle/10222/56840/Memarrashidi-Zhila-MASc-MATL-May-2015.pdf (accessed September 30, 2017).

APPENDIX A RESEARCH DISSEMINATION

The NSERC HI-AM network required semi-annual internal progress reports comprised of the project progress and results of the latest findings. Published documents based on the later findings are listed below. The data collection, preparation of specimens, material characterization, manuscripts preparation of journal articles and presented thesis was completed by the author, unless otherwise stated, with the guidance of the PhD supervisor Dr Kevin Paul Plucknett

- Z. Russell, W.A. Sparling, T.L. Stewart, P. Gray M. Gaier, M.J. Froning, G. Mazzanti, K.P. Plucknett, Gelation-based feed-stock technologies for HVOF thermal spray development: Micro-composite powder preparation and HVOF coating microstructure, *Surface & Coatings Technology, 2023*
- Z. Russell, K.P. Plucknett, Scratch resistance and damage mechanisms in TiC-Ni_3Al cermet coatings fabricated by pre-placement laser directed energy deposition, *HIAM database, 2022.*
- Z. Russell, K.P. Plucknett, Corrosion performance of laser DED TiC-Ni_3Al cermet coatings on D2 substrate, *Extended abstract COM2021*
- T. Street, Z. Russell, D. Griffin, and K.P. Plucknett, Deep cryogenic treatment of Titanium-based alloys, *Extended abstract COM2021*
- Zhila Russell, Kevin Plucknett, Gianfranco Mazzanti, *Laser cladding of high-performance Titanium cermets from sol gel structure, HIAM database, 2020*
- Zhila Russell, Kevin Plucknett, Gianfranco Mazzanti. *Laser DED Cladding of Dip-Coated TiC-Ni_3Al Cermets on D2 Tool Steel, HIAM database, 2019.*

APPENDIX B COPYRIGHT PERMISSION LETTER

June23, 2023
Dear chair of Journal of Surface coatings and technology, I am preparing my PhD thesis for submission to the Faculty of Graduate Studies at Dalhousie University, Halifax, Nova Scotia, Canada. I am seeking your permission to include a manuscript version of the following paper(s) as a chapter in the thesis:
Z. Russell, W.A. Sparling, T.L. Stewart, P. Gray, M. Gaier, M.J. Froning, G. Mazzanti, K.P. Plucknett, Gelation-based feed-stock technologies for HVOF thermal spray development: Micro-composite powder preparation and HVOF coating microstructure, Surf. Coatings Technol. 452 (2023).
Canadian graduate theses are reproduced by the Library and Archives of Canada (formerly National Library of Canada) through a non-exclusive, world-wide license to reproduce, loan, distribute, or sell theses. I am also seeking your permission for the material described above to be reproduced and distributed by the LAC(NLC). Further details about the LAC(NLC) thesis program are available on the LAC(NLC) website (www.nlc-bnc.ca). Full publication details and a copy of this permission letter will be included in the thesis. Yours sincerely, Samer Omar Permission is granted for: a) the inclusion of the material described above in your thesis. b) for the material described above to be included in the copy of your thesis that is sent to the Library and Archives of Canada (formerly National Library of Canada) for reproduction and distribution.
Yours sincerely
Zhila Russell
Permission is granted for: a) the inclusion of the material described above in your thesis. b) for the material described above to be included in the copy of your thesis that is sent to the Library and Archives of Canada (formerly National Library of Canada) for reproduction and distribution.
Name: Title:
Signature: Date: